



**PACIFIC EARTHQUAKE ENGINEERING
RESEARCH CENTER**

**Seismic Performance of
Column-to-Drilled-Shaft Connections in
Reinforced Concrete Bridges**

Michelle Chang

John Stanton

Marc Eberhard

**Department of Civil and Environmental Engineering
University of Washington**

PEER Report No. 2021/10

Pacific Earthquake Engineering Research Center
Headquarters at the University of California, Berkeley
September 2021

Disclaimer

The opinions, findings, and conclusions or recommendations expressed in this publication are those of the author(s) and do not necessarily reflect the views of the study sponsor(s), the Pacific Earthquake Engineering Research Center, or the Regents of the University of California.

Seismic Performance of Column-to-Drilled-Shaft Connections in Reinforced Concrete Bridges

Michelle Chang

John Stanton

Marc Eberhard

Department of Civil and Environmental Engineering
University of Washington, Seattle, Washington

PEER Report 2021/10
Pacific Earthquake Engineering Research Center
Headquarters at the University of California, Berkeley

September 2021

ABSTRACT

Drilled shaft foundations are often used to support reinforced concrete bridge columns founded in soft soils or in locations where a small footprint is desired. Increasingly, the shaft is being built with a diameter larger than that of the column, to allow tolerance in the column placement and to facilitate plastic hinge formation in the column rather than in the shaft. The column–shaft connection, which involves a noncontact splice between the column and shaft bars, is a key component in this structural system. However, there is limited research on the behavior of these connections under seismic loads. In order to understand the force-transfer mechanism of column–shaft connections under seismic loading, one quasi-static cyclic experimental test was conducted on a column–shaft subassembly. Measured results were compared with those from three previous experiments performed at the University of Washington and others conducted at the University of California San Diego.

The study found that the amount of shaft transverse reinforcement in the connection region was critical in determining the failure mode of the connection. In specimens with relatively low amounts of transverse reinforcement, including the specimen tested during this study and a previous specimen tested at the University of Washington, the connection failed through a shaft prying failure mode; the specimens developed large vertical cracks between the confined column core and the annular shaft transition region, and the shaft transverse reinforcement eventually fractured at large drift ratios. Therefore, three methodologies for detailing the shaft transverse reinforcement were evaluated, and a new analysis procedure using a strut-and-tie model was proposed. It is consistent with the measured and observed performances of the tested connections and is applicable to shafts supporting either precast or cast-in-place columns. The new procedure allows engineers to (a) more accurately predict the behavior of a column–shaft connection and (b) prevent an undesirable below-ground failure in the shaft transition region. Lastly, a set of design equations based on the strut-and-tie findings and existing design models is proposed for use in practice.

ACKNOWLEDGMENTS

This research was funded by the Pacific Earthquake Engineering Research Center (PEER) and the Accelerated Bridge Construction University Transportation Center at Florida International University (ABC-UTC). Any opinions, findings, and conclusions or recommendations expressed in this material are those of the authors and do not necessarily reflect those of PEER or the Regents of the University of California.

This research built upon the University of Washington doctoral dissertation work of Vietnam National University of Civil Engineering Professor Hung Viet Tran, who provided technical support during the duration of this project. Professor Juan Murcia-Delso also provided data from column–shaft connection experiments conducted at the University of California San Diego (UCSD).

The experiments presented in this report were conducted in the Large-Scale Structural Engineering Testing Laboratory at the University of Washington. Vongsant (Vince) Chaijaroen, lab manager, and Professor Dawn Lehman, lab director, provided technical support. Several graduate and undergraduate students at the University of Washington provided labor and resources.

Concrete Technology Corporation donated their time and labor. Several bridge consultants in the Seattle and Northern California areas, as well as WSDOT and Caltrans bridge engineers, shared their time and knowledge.

CONTENTS

ABSTRACT	iii
ACKNOWLEDGMENTS	v
TABLE OF CONTENTS	vii
LIST OF TABLES	xiii
LIST OF FIGURES	xv
DEFINITIONS AND ACRONYMS	xxi
NOTATION	xxiii
1 INTRODUCTION	1
1.1 Motivation	1
1.2 Objectives and Scope	2
1.3 Report Organization	2
2 LITERATURE REVIEW	5
2.1 Force-Transfer Models	5
2.1.1 Noncontact Lap Splice Model: McLean and Smith [1997]	5
2.1.2 Bond-Based Model: Murcia-Delso et al. [2013].....	7
2.1.3 Strut-and-Tie Model: Tran [2015]	8
2.2 Design Provisions	9
2.2.1 AASHTO LRFD Bridge Design Specifications [2017] and AASHTO LRFD Seismic Guide Specifications [2015].....	10
2.2.2 Caltrans Seismic Design Criteria [2019]	11
2.2.3 WSDOT Bridge Design Manual [2020]	11
2.2.4 AASHTO Guide Specifications for Accelerated Bridge Construction [2018].....	12
2.3 Experimental Tests of Column-Drilled Shaft Connections	14
2.3.1 Reduced-Scale Column–Shaft Test: McLean and Smith [1997]	14
2.3.2 Full-Scale Column–Shaft Tests with Large Bars: Murcia-Delso et al. [2013].....	17

2.3.3	Full-Scale Column–Shaft Test with Grade 80 Bars: Lotfizadeh and Restrepo [2019].....	20
2.3.4	Precast Column–Shaft Tests for Accelerated Bridge Construction: Tran [2015]	21
2.4	Finite-Element Analyses	24
2.4.1	Connections with Cast-in-Place Components.....	24
2.4.2	Connections with Precast Components for Accelerated Bridge Construction	24
3	DESIGN AND CONSTRUCTION OF TEST SPECIMEN	26
3.1	Characteristics of Previous Column–shaft Connection Specimens	26
3.2	Design of Fourth Column–shaft Connection Specimen	29
3.3	Construction	31
3.4	Material Properties	32
4	EXPERIMENTAL PROGRAM.....	33
4.1	Experimental Setup	33
4.2	Instrumentation.....	36
4.2.1	Instrumentation for Measuring Global Deformations.....	36
4.2.2	Instrumentation for Curvature Measurements	38
4.2.3	Instrumentation for Concrete Surface Measurements.....	38
4.2.4	Internal Instrumentation: Strain Gauges	40
4.3	Load and Displacement History	42
5	EXPERIMENTAL RESULTS.....	45
5.1	Sign Conventions and Terminology	45
5.2	Damage Progression	45
5.3	Global Measured Response.....	55
5.3.1	Force-Displacement Response.....	55
5.3.2	Moment-Drift Response.....	57
5.4	Deformation Profiles.....	59
5.4.1	Displacement Profiles	59
5.4.2	Rotation Profiles	61
5.4.3	Curvature Profiles	62

	5.4.4	Contributions to Total Displacement	63
5.5		Strain Profiles.....	65
	5.5.1	Strains in Column Longitudinal Bars	68
	5.5.2	Strains in Shaft Longitudinal Bars.....	68
	5.5.3	Strains in Shaft Transverse Reinforcement.....	69
	5.5.4	Circumferential Surface Strains in Shaft Concrete.....	73
5.6		Inferred Axial and Bond Stress Profiles	75
	5.6.1	Axial Stress-Strain Relation.....	75
	5.6.2	Experimental Bond Stress.....	76
	5.6.3	Inferred Axial and Bond Stress Profiles	76
6		COMPARISON OF EXPERIMENTAL RESPONSES	81
	6.1	Discussion of Key Parameters.....	81
	6.2	Specimen Characteristics	83
	6.3	Damage Progression	84
	6.4	Moment-Drift Response	93
	6.5	Strains in Column Longitudinal Bars.....	95
	6.6	Strains in Shaft Longitudinal Bars.....	97
	6.7	Strains in Shaft Transverse Reinforcement	99
	6.8	Discussion of Experimental Responses	101
7		EVALUATION OF MODELS AND DESIGN EQUATIONS	103
	7.1	Strategy for Evaluating Model Accuracy	103
	7.2	Noncontact Lap Splice Model: McLean and Smith [1997]	107
	7.3	Bond-Based Model: Murcia-Delso et al. [2013]	109
	7.4	Strut-and-Tie Model: Tran [2015]	111
	7.5	Discussion of Model Evaluation Results	113
8		STRUT-AND-TIE MODEL FOR COLUMN-SHAFT CONNECTIONS	117
	8.1	Introduction of Proposed Model.....	117
	8.2	Modeling and Analysis Procedure.....	120
	8.3	Verification of Proposed Model.....	125
	8.4	Concrete Contribution to Shear Transfer	128

8.5	Additional Concrete Contribution	130
8.6	Discussion.....	132
8.7	Design Recommendations	133
9	SUMMARY AND CONCLUSIONS	139
9.1	Summary.....	139
9.2	Conclusions.....	140
9.3	Recommendations for Future Work.....	141
	REFERENCES.....	143
APPENDIX A	SPECIMEN DESIGN DRAWINGS.....	145
APPENDIX B	SPECIMEN CONSTRUCTION AND SETUP PHOTOGRAPHS ...	163
APPENDIX C	MATERIAL TESTS	171
C.1	Concrete.....	171
C.2	Steel	172
APPENDIX D	EFFECT OF RESIDUAL STRESS ON PREMATURE SPIRAL YIELDING 179	
D.1	The Phenomenon.....	179
D.2	Method of Calculation	179
D.3	Results	181
D.4	Implications in Practice.....	183
APPENDIX E	DAMAGE PROGRESSION PHOTOGRAPHS	185
APPENDIX F	ADDITIONAL EXPERIMENTAL RESULTS.....	191
F.1	Raw Moment-Drift Response (DS-4)	191
F.2	Instantaneous Strain Profiles (DS-4).....	192
F.3	Moment-Drift Response for Specimens DS-1 through DS-4	196
APPENDIX G	FLEXURAL ANALYSIS	197
G.1	Moment-Curvature Relationship	197
G.2	Trends in Neutral Axis and Resultant Locations.....	199

**APPENDIX H DESIGN EQUATIONS FOR TRANSVERSE REINFORCEMENT
BASED ON STRUT-AND-TIE MODELING203**

LIST OF TABLES

Table 2.1	Minimum volumetric ratio of transverse reinforcement in Caltrans Type II shafts.	11
Table 2.2	Key characteristics of past specimens.....	16
Table 3.1	Key characteristics of Specimens DS-1 through DS-4.	27
Table 3.2	Concrete and steel material properties of DS-1 through DS-4.	32
Table 5.1	Maximum displacement and drift reached during each cycle.	46
Table 5.2	Damage milestone definitions.....	47
Table 5.3	Damage progression of column (C) and shaft (S).	47
Table 6.1	Key characteristics of Specimens DS-1 through DS-4.	84
Table 6.2	Damage progression in the column for Specimens DS-1 through DS-4. Milestones are defined in Table 5.2.....	88
Table 6.3	Damage progression in the shaft for Specimens DS-1 through DS-4. Milestones are defined in Table 5.2.....	88
Table 6.4	Comparison of maximum moments and imposed drifts during testing.....	93
Table 7.1	Key characteristics of specimens used in model evaluation.	105
Table 7.2	Material properties of specimens used in model evaluation.....	106
Table 7.3	Maximum measured strains in shaft transverse reinforcement at given drift ratios.....	107
Table 7.4	Evaluation of McLean and Smith’s [1997] model.....	109
Table 7.5	Evaluation of Murcia-Delso et al.’s [2013] model.	110
Table 7.6	Evaluation of Tran’s [2015] model.....	112
Table 7.7	Bond-to-axial capacity ratios.	114
Table 8.1	Calculated boundary forces and locations in the transition region.	126
Table 8.2	Strut-and-tie model results.....	127
Table 8.3	Concrete shear contribution results. See Section 8.3 for an explanation of UCSD-4.....	130
Table 8.4	Additional concrete contribution results. See Section 8.3 for an explanation of UCSD-4.....	131
Table 8.5	Column-to-shaft longitudinal bar development length ratio.....	135
Table C.1	Concrete compressive test results for DS-4.....	171

Table C.2	Steel material properties for DS-4.	172
Table G.1	Tensile resultant location in the column.	201
Table G.2	Tensile resultant location in the shaft.	201
Table G.3	Compressive resultant location in the column.	202

LIST OF FIGURES

Figure 1.1	Column–shaft connection types [Caltrans 2010].	1
Figure 2.1	McLean and Smith’s model for noncontact lap splices. “C” refers to the diagonal compression force, and “T” refers to tension. Variables are defined in Equation (2.3). (Adapted from McLean and Smith [1997].)	6
Figure 2.2	Tran’s strut-and-tie model for force transfer [Tran 2015].	9
Figure 2.3	AASHTO ABC’s three regions (A, B, C) within the height of a socket connection [AASHTO ABC 2018].	13
Figure 2.4	McLean and Smith’s experimental specimen design [1997].	15
Figure 2.5	Typical setup for UCSD experimental tests [Murcia-Delso et al. 2013].	18
Figure 2.6	Photograph of post-test damage in Specimen UCSD-2 [Murcia-Delso et al. 2013].	19
Figure 2.7	Strain profiles for transverse reinforcement (hoops) in UCSD-1 through UCSD-4 specimens [Murcia-Delso et al. 2016].	20
Figure 2.8	360° 3D point cloud model showing damage in UCSD-5 column plastic hinge [Lotfizadeh and Restrepo 2019].	21
Figure 2.9	Tran’s precast column-CIP drilled shaft concept [Tran 2015].	22
Figure 2.10	Photograph of post-test damage in Specimen DS-2 [Tran 2015].	23
Figure 3.1	Bending moment profiles of actual column–shaft-soil system vs. test specimens.	28
Figure 3.2	Design of test specimen.	30
Figure 3.3	Photograph of specimen construction.	31
Figure 4.1	Experimental test setup.	34
Figure 4.2	Roller setup at the top of the column. Numbers refer to the three components of the assembly described in Section 4.1. This setup should be modified for future use.	36
Figure 4.3	Potentiometer and inclinometer locations (east elevation).	37
Figure 4.4	Optotrak marker layout (northwest view).	39
Figure 4.5	Photograph of two strain gauges at different stages of installation.	40
Figure 4.6	Strain gauge locations: (a) cross section in connection region; (b) elevation with longitudinal gauges; and (c) elevation with transverse gauges.	42
Figure 4.7	Target lateral displacement history.	43

Figure 5.1	Photographs of damage progression at column–shaft interface (overhead view): (a) 1.0% drift (NW view); (b) 1.8% drift (SE view); (c) 3.6% drift (E view); (d) 5.2% drift (SW view); (e) 7.3% drift (SE view); and (f) 10.5% drift (NE view).....	50
Figure 5.2	Photographs of damage progression in transition region (south view): (a) 1.0% drift; (b) 1.8% drift; (c) 3.6% drift; (d) 5.2% drift; (e) 7.3% drift; and (f) 10.5% drift.	53
Figure 5.3	Photographs of specimen at end of test: (a) north view; (b) south view; (c) east view; and (d) transverse reinforcement fractured down to the level of the pencil (height of shaft = 30 in.).....	54
Figure 5.4	Photographs of interface at end of test: (a) north face; (b) south face; and (c) west face.	55
Figure 5.5	Lateral force-displacement response (before and after accounting for friction).	57
Figure 5.6	Definitions of variables to calculate base moment [Equations (5.4) through (5.6)] [Tran 2015].	58
Figure 5.7	Moment-drift response.....	58
Figure 5.8	Displacement profiles.	60
Figure 5.9	Rotation profiles.....	62
Figure 5.10	Curvature profiles.	63
Figure 5.11	Types of deformation [Tran 2015].....	64
Figure 5.12	Contributions of mechanisms to total displacement.	65
Figure 5.13	Determining strain envelopes: transverse strain vs. frame for the strain gauge on shaft transverse reinforcement at $y = -4$, close to the east face of the specimen (SG_T_04_E).....	66
Figure 5.14	Determining strain envelopes: transverse strain vs. drift for the same strain gauge as in Figure 5.13.	67
Figure 5.15	Column longitudinal bar strain profiles in transition region: (a) 1.0% drift; (b) 1.8% drift; (c) 3.6% drift; and (d) 5.2% drift. See Section 5.5 for the definition of the envelopes and NT/NC/ST/SC/E.....	70
Figure 5.16	Shaft longitudinal bar strain profiles: (a) 1.0% drift; (b) 1.8% drift; (c) 3.6% drift; and (d) 5.2% drift. See Section 5.5 for the definition of the envelopes and NT/NC/ST/SC/E.	71
Figure 5.17	Shaft transverse wire enveloped strain profiles: (a) 1.0% drift; (b) 1.8% drift; (c) 3.6% drift; and (d) 5.2% drift. See Section 5.5 for the definition of the envelopes and NT/NC/ST/SC/E.	72

Figure 5.18	Overhead view of uppermost wire strain gauge on the south end of the shaft reinforcement cage (indicated by red arrow; photograph was taken mid-installation).....	73
Figure 5.19	Hoop strains at shaft surface and in transverse reinforcement: (a) strains at top of shaft ($y \approx -4$ in.); and (b) strains and height of shaft ($y \approx -15$ in.).....	74
Figure 5.20	Raynor model for monotonic loading on reinforcing bar [Hoehler and Stanton 2006].....	75
Figure 5.21	Axial and bond stress profiles at 1.0% drift: (a) column longitudinal bars; and (b) shaft longitudinal bars.	78
Figure 5.22	Axial and bond stress profiles at 1.8% drift: (a) column longitudinal bars; and (b) shaft longitudinal bars.	79
Figure 5.23	Axial and bond stress profiles at 3.6% drift: (a) column longitudinal bars; and (b) shaft longitudinal bars.	80
Figure 6.1	Damage progression in the column for Specimens DS-1 through DS-4. Note: any points on the right-side axis indicate that the milestone did not occur by the end of testing. Figure values are reported in Table 6.2.....	86
Figure 6.2	Damage progression in the shaft for Specimens DS-1 through DS-4. Note: any points on the right-side axis indicate that the milestone did not occur by the end of testing. Figure values are reported in Table 6.3.....	87
Figure 6.3	Photographs of Specimens DS-1 through DS-4 at 1.6%-1.8% drift: (a) DS-1, (b) DS-2, (c) DS-3, and (d) DS-4.....	89
Figure 6.4	Photographs of Specimens DS-1 through DS-4 at 3.6-3.9% drift: (a) DS-1, (b) DS-2, (c) DS-3, and (d) DS-4.....	90
Figure 6.5	Photographs of Specimens DS-1 through DS-4 at 6.8-7.4% drift: (a) DS-1, (b) DS-2, (c) DS-3, and (d) DS-4.....	91
Figure 6.6	Photographs of Specimens DS-1 through DS-4 after experimental testing: (a) DS-1, (b) DS-2, (c) DS-3, and (d) DS-4.....	92
Figure 6.7	Normalized moment vs. drift curves for all DS specimens. See Appendix F for non-normalized curves. See Section 5.3 for an explanation of the DS-4 outlier peaks.....	94
Figure 6.8	Column longitudinal bar strain profiles.	96
Figure 6.9	Shaft longitudinal bar strain profiles.....	98
Figure 6.10	Shaft transverse reinforcement strain profiles.	100
Figure 6.11	Transverse strain vs. drift envelopes.....	101

Figure 7.1	Strains in shaft hoops for Specimen UCSD-4: (a) north face and (b) south face [Murcia-Delso et al. 2013].	107
Figure 7.2	Evaluation of McLean and Smith’s [1997] model.	109
Figure 7.3	Evaluation of Murcia-Delso et al.’s [2013] model.	110
Figure 7.4	Tran [2015] strut-and-tie model for force transfer.	111
Figure 7.5	Evaluation of Tran’s [2015] model.	112
Figure 8.1	Proposed strut-and-tie model.	118
Figure 8.2	Strut-and-tie configuration modes.	119
Figure 8.3	Determination of transverse component factor.	124
Figure 8.4	Evaluation of proposed strut-and-tie model.	128
Figure 8.5	Evaluation of strut-and-tie model considering concrete shear resistance.	130
Figure 8.6	Evaluation of strut-and-tie model considering additional concrete component.	132
Figure 8.7	Force-transfer lengths of column and shaft bars.	135
Figure 8.8	Evaluation of modified McLean and Smith model [Equation (8.19)].	137
Figure A.1	Column detail.	158
Figure A.2	Shaft and footing detail.	159
Figure A.3	Footing plan.	160
Figure A.4	Instrumentation.	161
Figure B.1	Shaft reinforcement cage in progress.	163
Figure B.2	Column reinforcement cage in progress.	164
Figure B.3	End of first concrete placement (base and shaft starter stub).	164
Figure B.4	Sonotube formwork for the shaft, with strain gauge leads routed out.	165
Figure B.5	Covered strain gauges on column longitudinal bar (north bar).	165
Figure B.6	Concrete placement for the shaft (pour #2).	166
Figure B.7	Formwork and embedded items for the column.	167
Figure B.8	Move-in of the specimen onto the test frame.	168
Figure B.9	Instruments attached to the specimen: (a) inclinometers, Duncan potentiometers, and string potentiometers at the column base (north side); and (b) Optotrak marker installation in progress.	169
Figure D.1	Normalized residual stress profiles.	180

Figure D.2	Normalized average (ave) axial stress-strain curves, with and without residual stress (dotted blue and solid black lines, respectively).	181
Figure D.3	Normalized residual stresses at the exterior and interior of the spiral.....	182
Figure D.4	Normalized strain at the departure from linearity.....	182
Figure D.5	Normalized axial stress when axial yield strain.....	182
Figure E.1	Crack opening at column–shaft construction joint at 3.6% drift (peak).	186
Figure E.2	Spalling and cracks at base of column at 5.2% drift.....	187
Figure E.3	Close-up photographs of shaft transverse reinforcement fracture (at end of test): (a) uppermost spiral fracture on southwest side; and (b) Line of spiral fracture on southside.	187
Figure E.4	Southwest view of specimen (at end of test).	188
Figure E.5	Overhead angled view of specimen from southwest (post-test).	189
Figure F.1	Raw vs. adjusted moment-drift response.	191
Figure F.2	Column longitudinal bar instantaneous strain profiles.	193
Figure F.3	Shaft longitudinal bar instantaneous strain profiles.....	194
Figure F.4	Shaft transverse reinforcement instantaneous strain profiles.....	195
Figure F.5	Moment vs. drift curves for all DS specimens.....	196
Figure G.1	Kent and Park model for concrete confined concrete [Kent and Park 1971].	197
Figure G.2	Material stress-strain relationships for Specimen DS-4 column flexural analysis.....	198
Figure G.3	Moment-curvature results for Specimen DS-4 column.	199
Figure G.4	Neutral axis and resultant locations.	200

DEFINITIONS AND ACRONYMS

AASHTO	American Association of State Highway and Transportation Officials
ABC	accelerated bridge construction
ACI	American Concrete Institute
ASCE	American Society of Civil Engineers
ASTM	American Society for Testing and Materials
BDM	Bridge Design Manual (WSDOT)
BDS	Bridge Design Specifications (AASHTO)
Caltrans	California Department of Transportation
CIDH	cast-in-drilled-hole (type of pile foundation)
CIP	cast-in-place
CISS	cast-in-steel-shell (type of pile foundation)
col.	column
cycle	a single displacement-controlled load sequence following a sawtooth wave pattern that starts at zero, rises to a peak, dips to a valley, and returns to zero (identified with a number format of [#]-[#], where the first number [#] is the set number, and the second number is the within-set cycle number)
DAQ	data acquisition system
dept.	department
dia.	diameter
drift (or drift ratio)	the lateral displacement at the actuator level divided by the vertical distance from the actuator centerline to the column–shaft interface
DS	drilled shaft [specimen]
E	east
enlarged shaft	a shaft whose diameter is greater than that of the adjoining column (also known as oversized shaft or Type II shaft)
FE	finite element
FEMA	Federal Emergency Management Agency
ft.	feet
Hydrostone	a gypsum product that is supplied as a powder and mixed with water to form a viscous liquid, which is then poured and which quickly sets into a solid
Hz	hertz
in.	inch[es]
kip	kilopound
lbs	pounds
LED	light-emitting diode

LRFD	Load and Resistance Factor Design
LVDT	linear variable differential transformer
Max	maximum
Min	minimum
mm	millimeters
MTS	Materials Test Systems Corporation
N:	north
NEHRP	National Earthquake Hazards Reduction Program
o.c.	on center
Optotrak Certus	product line of the motion capture system used in the experiment
oversized shaft	a shaft whose diameter is greater than that of the adjoining column (also known as enlarged shaft or Type II shaft)
peak	the maximum positive displacement or strain within a cycle, defined as positive and denoted in blue in this report
pot.	potentiometer
PTFE	polytetrafluoroethylene
reinf.	reinforcement
S	south
SDC	Seismic Design Criteria (Caltrans)
set	a group of four displacement-controlled cycles
SGS	Seismic Guideline Specifications (AASHTO)
STM	strut-and-tie model
transition region	the connection region between a column and drilled shaft where force transfer occurs
Type I shaft	a shaft whose diameter is greater than that of the adjoining column (also known as enlarged shaft or oversized shaft)
UCSD	University of California, San Diego
UTM	Universal Testing Machine (in reference to Baldwin UTM)
UW	University of Washington
valley	the maximum negative displacement or strain within a cycle, defined as negative and denoted in red in this report
vs.	versus
WSDOT	Washington State Department of Transportation
2D	two-dimensional
3D	three-dimensional

NOTATION

A_{tr}	area of shaft transverse reinforcement in transition region
A_g	gross concrete cross-sectional area
A	[1] area of reinforcing bar
A	[2] amplitude (in reference to target displacement cycle amplitudes)
A_l	total area of column longitudinal reinforcement
A_v	effective shear area
B	horizontal distance between two Δ_v measurement locations
C	compression force
C_c	compression resultant of the column
C_s	compression resultant of the shaft
C_1	parameter that defines the curvature of the strain hardening curve (used in steel model)
c	cover from top of shaft-to-shaft longitudinal bar
D	diameter or width of cross section
D_c	diameter of column
D_s	diameter of shaft
d_b	nominal diameter of reinforcing bar
d_{bl}	nominal diameter of column longitudinal bar
$d_{b,col}$	nominal diameter of column longitudinal bar
E	elastic modulus
E_y	slope of the yield plateau in the steel stress–strain relation
e	eccentricity, i.e. physical distance between shaft and column longitudinal reinforcement
e_{ef}	effective eccentricity, i.e. the horizontal distance between the column and shaft tensile resultants ($e_{ef} = x_{Ts} - x_{Tc}$)
$F_{applied}$	applied lateral load
F_c	force in concrete component
F_{fric}	friction force from axial bearing assembly
F_{max}	maximum friction force
F_{tr}	transverse force demand on shaft transverse reinforcement in the transition region
f'_c	concrete compressive strength (nominal, unless otherwise noted)
f'_{cc}	confined concrete compressive strength
f_u	ultimate strength

$f_{u,l}$	ultimate strength of longitudinal reinforcement
f_y	yield strength
$f_{y,tr}$	yield strength of transverse reinforcement
H	column height
h_A	vertical distance from the column–shaft interface to Node B
h_B	vertical distance from the column–shaft interface to Node A
h_1	vertical distance from the column–shaft interface to the line of action of the lateral load (60 in.)
h_2	vertical distance from the interface to the top of column where the axial load P is applied (72 in.)
k	[1] the factor representing the ratio of column tensile reinforcement to total column reinforcement at the nominal bending resistance
k	[2] spring stiffness in friction model
L	depth of transition region
L_A	vertical distance from the bottom of the transition region to Node A (Tran model)
L_{SP}	vertical distance from the bottom of the transition region to Node B (Tran model)
l_{ac}	development length from AASHTO SGS Section 8.8.4 for column longitudinal reinforcement
l_d	tension development length of the larger of the column and shaft longitudinal bars (see context for which procedure to use to determine l_d)
$l_{d,c}$	tension development length of column longitudinal bar
$l_{d,s}$	tension development length of shaft longitudinal bar
l_e	required embedment length of column longitudinal bar
$l_{e,PC}$	total required embedment depth of precast column in shaft
l_{ns}	noncontact lap splice length
l_s	typical (in-contact) lap splice length
M	base moment at the column–shaft interface
N_{col}	number of column longitudinal bars
P	axial load
p	perimeter of reinforcing bar (i.e., bar circumference for a single bar)
R	radius of spherical surface of the bearing
s	pitch (i.e. center-to-center spacing) of transverse reinforcement
T	tension force
T_c	tension resultant of the column
T_s	tension resultant of the shaft
V	[1] measured force from MTS actuator load cell
V	[2] column base shear force
V_c	concrete contribution to shear resistance

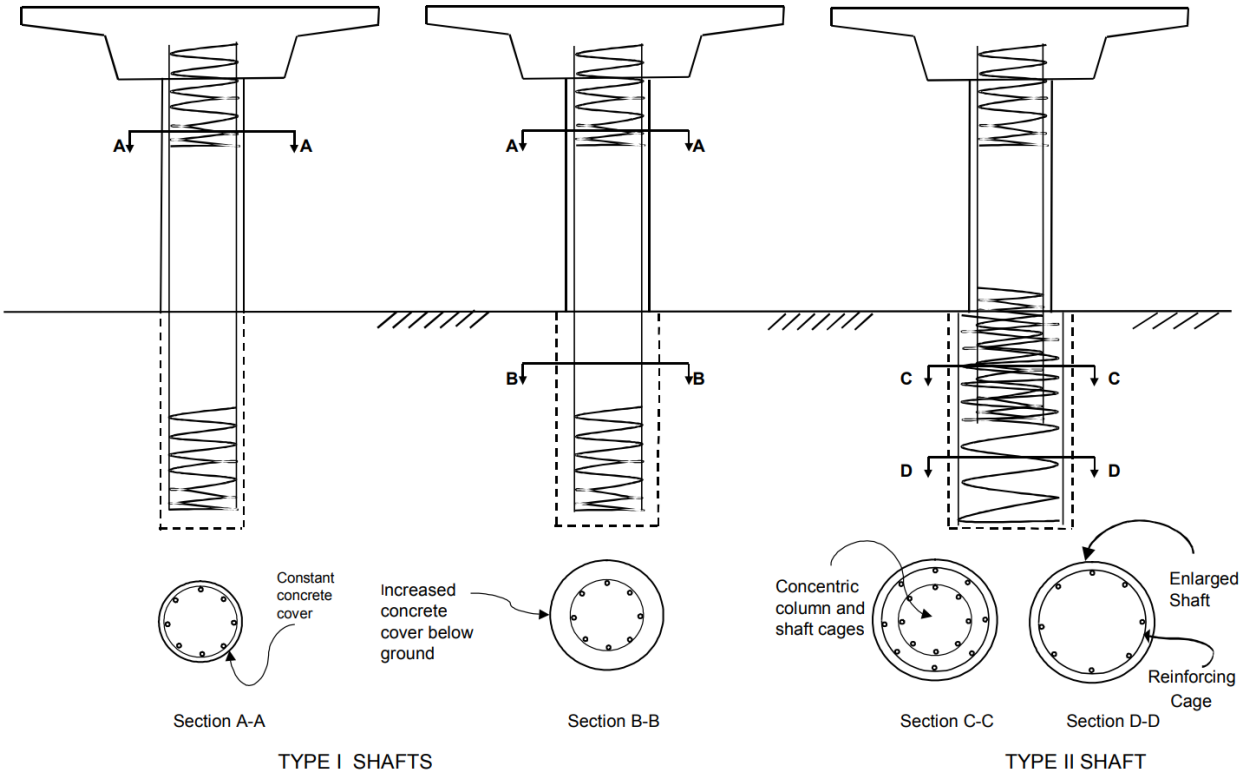
$V_{u,s}$	shear demand on the transverse reinforcement
x_{Cc}	distance from column compressive resultant force to the centroid of the column
x_{Cs}	distance from shaft compressive resultant force to the centroid of the shaft
x_{Tc}	distance from column tensile resultant force to the centroid of the column
x_{Ts}	distance from shaft tensile resultant force to the centroid of the shaft
y	elevation of instrument or measurement ($y = 0$ is the column–shaft interface, and up is positive)
α	shaft bar strain factor
β	factor indicating the ability of diagonally cracked concrete to transmit tension and shear, taken as 2.0 in this report
γ	factor representing the ratio of the tensile resultant location to the total length of the cross-section in tension
Δ_1	measured lateral displacement at the centroid of load application
Δ_2	inferred lateral displacement at the top of column
Δ_3	measured lateral displacement at the column–shaft interface
$\Delta_{v,N}$	vertical displacement on the north side of specimen
$\Delta_{v,S}$	vertical displacement on the south side of specimen
Δh	height of the segment (i.e., the vertical distance between the two instrument locations)
$\Delta\theta$	relative rotation
ε	strain
ε_{sh}	strain at onset of strain hardening
ε_{tr}	strain in shaft transverse reinforcement
ε_u	ultimate strain
ε_y	yield strain
η	factor representing the ratio of the compressive resultant location to the total length of the cross-section in compression
θ	angle of struts in strut-and-tie or truss models (measured from the horizontal)
μ	coefficient of friction between stainless steel and greased dimpled PTFE or MSM pad
μ_{eff}	effective coefficient of friction
ρ_{tr}	transverse volumetric reinforcement ratio
σ	stress
σ_{sh}	stress at onset of strain hardening
σ_u	ultimate (peak) stress

σ_y	stress at yield
τ	bond stress
τ_{max}	maximum bond stress capacity of the column longitudinal bars
ϕ	curvature
$\frac{d\sigma}{dy}$	rate of change in axial stress

1 Introduction

1.1 MOTIVATION

Drilled shafts, also known as pile shafts, are often used to support reinforced concrete bridge columns founded in soft soils or in locations where a small footprint is desired. Each shaft may have the same diameter as the column it supports (“Type I” shaft) or be larger in diameter than the column (“Type II,” “enlarged,” or “oversized” shaft); see Figure 1.1.



Enlarged shafts have several advantages over Type I shafts: the connection can be designed such that under seismic loading, the plastic hinge will form at or above the column–shaft interface, facilitating above-ground damage inspection and repair. Enlarged shafts also allow more generous construction tolerances when aligning the column in both precast and cast-in-place (CIP) applications. For these reasons, enlarged shafts have been used more commonly than Type I shafts in recent years in seismic areas such as Washington and California. Consequently, this investigation focused exclusively on column-to-enlarged-shaft connections.

The column–shaft connection, which involves a noncontact splice between the column and shaft bars, is a key component in this structural system. However, there is limited research on the behavior of these connections under seismic loads. For safe and efficient design, engineers need to understand the force-transfer mechanism of this connection.

1.2 OBJECTIVES AND SCOPE

The main objectives of this investigation were as follows:

1. Understand the force-transfer mechanism of column–shaft connections under seismic loading;
2. Evaluate existing methods for designing the connection region; and
3. Develop design recommendations to improve the efficiency and performance of column-to-shaft connections.

In order to achieve these goals, one quasi-static cyclic experimental test was conducted on a column–shaft subassembly. Experimental results were compared with those from three previous experiments performed at the University of Washington [Tran 2015]. Three methodologies for detailing the connection region were evaluated, and a new analysis procedure using a strut-and-tie model was proposed. The procedure was applied to the four University of Washington (UW) specimens and to four specimens tested at the University of California San Diego (UCSD) [Murcia-Delso 2013]. The findings of this research can be used in both precast and CIP applications.

1.3 REPORT ORGANIZATION

The components of this research study are described as follows:

- Chapter 2 provides a review of relevant literature and past experimental tests on similar column–shaft connections.
- Chapter 3 covers the design, construction, and material properties of the test specimen.
- Chapter 4 describes the experimental test setup, instrumentation, and displacement history applied to the specimen.

- Chapter 5 provides the experimental results, including the damage progression, moment-drift response, deformation profiles, strain profiles, and inferred stress profiles.
- Chapter 6 includes a discussion of key parameters that influence the connection performance and compares the specimen behavior to that of previous experimental specimens from the University of Washington.
- Chapter 7 evaluates existing models for designing the connection region.
- Chapter 8 describes a new analysis procedure based on a strut-and-tie model for detailing the connection region, with accompanying design recommendations.
- Chapter 9 provides a summary, conclusions, and recommendations.
- The appendices include more detailed information about the design, construction, and experimental response of the specimen. They also provide additional calculations to justify the proposed design procedure.

2 Literature Review

This chapter provides an overview of force-transfer models used to describe column–shaft connection behavior, current drilled shaft design provisions, and the results of previous experiments of column–shaft connections.

2.1 FORCE-TRANSFER MODELS

Several procedures have been developed to explain the force transfer and detail the transition region in column–shaft connections. The key design parameters identified in all of these procedures include: (1) the embedment length of the column reinforcement into the shaft, and (2) the amount of shaft transverse reinforcement in the transition region. Other parameters, such as the shaft–column diameter ratio, are addressed in some models but not in others. The following sections will summarize three models that can be used to design these two parameters in the transition region.

2.1.1 Noncontact Lap Splice Model: McLean and Smith [1997]

McLean and Smith [1997] developed a model to describe the three-dimensional (3D) behavior of noncontact lap splices between bars of equal size loaded in direct tension. This model is based on a truss analogy in which the forces between noncontact column and shaft longitudinal bars are transferred through compression struts at an angle θ ; see Figure 2.1. For standard in-contact spliced bars, the splice length l_s is solely based on the bar development length l_d ; for noncontact lap splices spaced apart at a distance e , the noncontact splice length l_{ns} needed for adequate force transfer per McLean and Smith is:

$$l_{ns} = l_s + \frac{e}{\tan \theta} \quad (2.1)$$

McLean and Smith assumed the angle of the struts to be 45° . The noncontact splice length required becomes:

$$l_{ns} = l_s + e \quad (2.2)$$

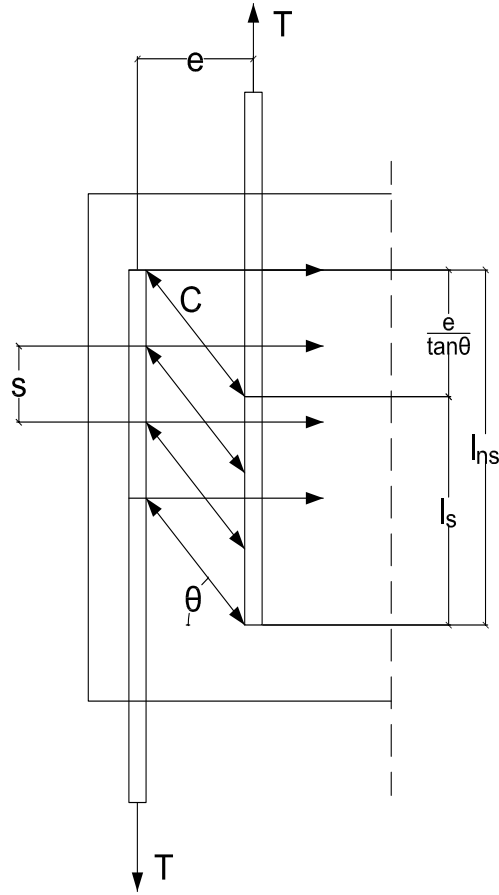


Figure 2.1 McLean and Smith’s model for noncontact lap splices. “C” refers to the diagonal compression force, and “T” refers to tension. Variables are defined in Equation (2.3). (Adapted from McLean and Smith [1997].)

For a 45° angle, the tension in the longitudinal direction and tension in the transverse direction are equal. Thus, if the amount of longitudinal reinforcement is known, the required transverse reinforcement for a circular transition region can be found using Equation (2.3).

$$\frac{A_{tr}}{s} = \frac{A_l f_{u,l}}{2\pi f_{y,tr} l_s} \quad (2.3)$$

where A_{tr} = area of shaft transverse reinforcement in transition region; s is the pitch (i.e., center-to-center spacing) of transverse reinforcement; A_l is the total area of column longitudinal reinforcement; $f_{u,l}$ is the ultimate strength of column longitudinal reinforcement; $f_{y,tr}$ is the yield strength of shaft transverse reinforcement; and l_s is the required typical (in-contact) Class C lap splice length for the larger of the shaft and column longitudinal bars per AASHTO LRFD Bridge Design Specifications [2010]. Because AASHTO lap splice length requirements had remained unchanged from 1995 through 2010, AASHTO BDS [2010] is cited here even though it was published after McLean and Smith’s study.

The model formulation implies that the diagonal strut force per unit length in the model is uniform along the lap length. Therefore, the transverse reinforcement determined from Equation (2.3) is assumed to be distributed over the full length of the noncontact splice.

Although the model was developed for bars in direct tension, McLean and Smith experimentally verified that noncontact lap splices designed using Equation (2.2) and Equation (2.3) performed adequately (withstanding repeated loading with no strength degradation) under cyclic flexural loading. Additionally, since the model assumed that the spliced bars in the noncontact splice were of the same size, they recommended that in Equation (2.3) the splice length for the larger bar should be used for determining l_s . This makes Equation (2.3) less conservative since taking the splice length for the larger bar would result in a larger l_s and less required transverse reinforcement.

2.1.2 Bond-Based Model: Murcia-Delso et al. [2013]

Murcia-Delso et al. [2013] conducted experimental tests and a finite-element (FE) study to examine the bond-slip behavior of column longitudinal bars embedded in drilled shafts; see Section 2.3.2 and Section 2.4.1. The study demonstrated that an embedment length shorter than that required in past Caltrans design manuals [Caltrans 2010] is sufficient to prevent anchorage failure of the column bars. This shorter embedment length is given by Equation (2.4). Subtracting the cover c from Equation (2.4), the noncontact lap splice length implied in Equation (2.4) is nearly identical to McLean and Smith's required noncontact lap splice length; see Equation (2.2). The only difference is in the l_d or $l_{d,c}$ term.

$$l_e = l_{d,c} + e + c \quad (2.4)$$

where l_e is the required embedment length of column longitudinal bar; $l_{d,c}$ is the development length of column longitudinal bar per AASHTO BDS [2010]; e is the eccentricity, as defined by McLean and Smith [1997]; and c is the cover from top of shaft-to-shaft longitudinal bar

Murcia-Delso et al. [2013] noted that the embedment length l_e given by Equation (2.4) may be less than the column diameter in very large columns. To avoid group pull-out failure and prying effects, they suggested that the minimum design embedment length of column reinforcement be:

$$l_e = l_{d,c} + \frac{D_s - D_{c,min}}{2} \geq D_{c,max} \quad (2.5)$$

where D_s is the diameter of shaft; $D_{c,min}$ is the minimum cross-sectional dimension of column; and $D_{c,max}$ is the maximum cross-sectional dimension of column.

The investigation also showed that the bond stress distribution of the column bar in the transition region is highly nonuniform. This nonuniformity implies that the diagonal strut force from McLean and Smith's [1997] model, which transfers forces between the column and shaft longitudinal bars, is not constant along the length of the transition region. Due to above-average local bond stress demand, the strut force and thereby the transverse force might be higher than

anticipated in McLean and Smith's model. Consequently, Murcia-Delso et al. developed a new formula to determine the required transverse reinforcement to prevent tensile splitting failure due to bond degradation:

$$\frac{A_{tr}}{s} = \frac{N_{col}d_{b,col}\tau_{max}}{2\pi f_{y,tr}} \quad (2.6)$$

where N_{col} is the number of column longitudinal bars; $d_{b,col}$ is the diameter of column longitudinal bars; and τ_{max} is the maximum bond strength capacity of the column longitudinal bars. For 5 ksi concrete, Murcia-Delso et al. took this value to be 2.4 ksi. For other concrete strengths, they recommended that this value be scaled proportionally to $f_c^{3/4}$.

This formula is based on bond stress and aims to prevent bond failure of the column bars due to concrete splitting along the longitudinal bars. To develop the formula, it was assumed that all bars were subjected to uniform tension, but that the equation can be used in flexural cases as well. Murcia-Delso et al. recommend that the transverse steel calculated with Equation (2.6) be distributed along the entire lap splice length.

2.1.3 Strut-and-Tie Model: Tran [2015]

As part of a Ph.D. dissertation at the University of Washington, Tran [2015] developed a two-dimensional (2D) strut-and-tie model to describe the force-transfer behavior and proportion the transverse reinforcement in a column–shaft transition region; see Figure 2.2. The model was based on experimental observations from three flexural tests on precast column-drilled shaft connections described in Section 2.3.4. The model sought to examine the force transfer in a bending—rather than direct tension—environment. It collapses the true 3D structure into an analogous 2D structure.

In the Tran model, the boundary forces on the transition region C_c , T_c , T_s , and C_s , along with their locations X_{C_c} , X_{T_c} , X_{T_s} , and X_{C_s} , are determined from flexural analysis. The shear force V is based on the moment capacity of the column. The depth of the transition region L is defined as such:

$$L = \begin{cases} \text{bottom of precast column,} & \text{for precast applications} \\ l_{d,c} + e + c, & \text{for CIP applications} \end{cases} \quad (2.7)$$

where L is the depth of transition region; $l_{d,c}$ is the tension development length of column bars per Priestley [1993]; e is the eccentricity, as defined by McLean and Smith [1997]; and c is the cover from top of shaft to top of shaft longitudinal bar.

For CIP applications, this depth of transition region follows the same concept as the required embedment depth of column longitudinal bars l_e determined by Murcia-Delso et al. [2013]; see Equation (2.4). The main difference is in the calculation of l_d . The definition of l_d in Murcia-Delso et al.'s equation references the AASHTO [2010] development length, which is about 1.2–1.5 times that required by Priestley [1993].

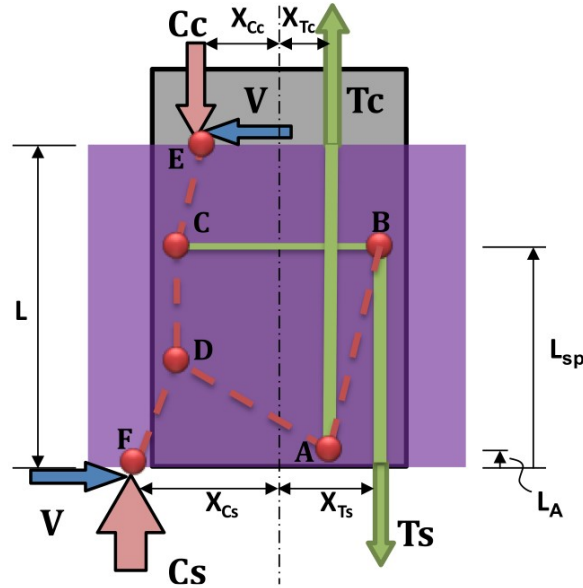


Figure 2.2 Tran's strut-and-tie model for force transfer [Tran 2015].

The tensile force from the column longitudinal bars, represented by resultant force T_c , is transferred to the shaft bars through compressive struts, which are collectively represented by strut AB . This strut has an angle that is not necessarily 45° , which differs from McLean and Smith's [1997] assumption. The transverse reinforcement in the transition region is represented by resultant tie BC . This tie is located at the centroid of the spiral or hoop forces, which are spread over a length L_{sp} . The centroid depends on an assumed strain distribution and spatial distribution of the transverse reinforcement along the height of the transition region. The other strut and node locations are based on equilibrium requirements.

Based on the strut-and-tie model, Tran recommended designing the transverse reinforcement in the transition region as follows:

1. Determine boundary forces and their locations in the connection region using flexural analysis.
2. Using the strut-and-tie model, find tie force BC (representing the resultant force acting on the transverse reinforcement).
3. Assuming a desired spatial distribution of transverse reinforcement and a certain strain distribution, distribute the resultant force among the transverse reinforcement. Design the reinforcement to resist this loading.

2.2 DESIGN PROVISIONS

Five sets of drilled-shaft design provisions were examined:

1. *AASHTO LRFD Bridge Design Specifications* [AASHTO BDS 2017].

2. *AASHTO Guide Specifications for LRFD Seismic Bridge Design* [AASHTO SGS 2015].
3. *Caltrans Seismic Design Criteria* [Caltrans SDC 2019].
4. *Washington State Department of Transportation Bridge Design Manual* [WSDOT BDM 2020].
5. *AASHTO LRFD Guide Specifications for Accelerated Bridge Construction* [AASHTO ABC 2018].

All five provisions require shafts to be capacity protected for overstrength moment and shear demands by ensuring that the shaft is stronger than the column. Additionally, all three agencies specify detailing requirements for the column longitudinal bar embedment depth and shaft transverse reinforcement in the connection region. Specific requirements will be outlined in the following subsections.

2.2.1 AASHTO LRFD Bridge Design Specifications [2017] and AASHTO LRFD Seismic Guide Specifications [2015]

This subsection outlines select design provisions found in AASHTO BDS [2017] and AASHTO SGS [2015]. These include required embedment length of the column reinforcement and minimum transverse reinforcement in the transition region.

The AASHTO BDS does not discuss the required embedment length of column reinforcement into drilled shafts. However, it does provide an equation to determine the minimum transverse reinforcement in such connections (LRFD Section 5.10.8.4.2a). This equation was adapted from the WSDOT BDM and will be later introduced and discussed in Section 2.2.3 alongside other WSDOT requirements.

The AASHTO SGS provisions include specifications for both embedment length and transverse reinforcement in SGS Sections 8.8.10 and 8.8.12, respectively. According to these specifications, the column longitudinal reinforcement is to be extended into oversized shafts with staggered embedment lengths of at least:

$$l_e = \begin{cases} D_{c,max} + l_{d,c}, & \text{every other bar} \\ D_{c,max} + 2l_{d,c}, & \text{every other bar} \end{cases} \quad (2.8)$$

where l_e is the required embedment length of column longitudinal bar (in.); $D_{c,max}$ is the largest cross-sectional dimension of the column (in.); and $l_{d,c}$ is the tension development length of the column longitudinal bars per AASHTO BDS using expected values of material properties

The AASHTO SGS provisions specify shaft transverse reinforcement requirements in terms of a minimum volumetric reinforcement ratio. They do not contain shaft transverse reinforcement requirements based on column bar embedment length or other parameters. The shaft volumetric transverse reinforcement ratio in the transition region is required to be at least 50% of that provided at the base of the column, provided the shaft is capacity designed. The provisions

recommend that this transverse reinforcement be extended along the shaft until the embedded column cage is terminated.

2.2.2 Caltrans Seismic Design Criteria [2019]

Caltrans design requirements for Type II (i.e., enlarged) shafts are found in the Caltrans SDC [2019] Sections 5.4, 6.2, 8.3, and 8.4. Caltrans requires that for non-epoxy-coated bars, the column longitudinal bar embedment length be:

$$l_e = \begin{cases} D_{c,max} + 42d_{bl}, & \text{for No. 11 and smaller} \\ D_{c,max} + 48d_{bl}, & \text{for No. 14 and No. 18} \end{cases} \quad (2.9)$$

where d_{bl} is the nominal diameter of column longitudinal bar (in.).

Caltrans provides requirements for shaft transverse reinforcement in terms of a minimum volumetric ratio and maximum allowable spacing. The volumetric ratio is specified as a percentage of that required at the base of the column and varies based on the type of shaft. Percentages are listed in Table 2.1 (Caltrans SDC Table 5.4.5-1).

Table 2.1 Minimum volumetric ratio of transverse reinforcement in Caltrans Type II shafts.

Location	Minimum volumetric ratio of transverse reinforcement	
	CISS or CIDH with permanent casing	All other shafts
Top 2 ft of shaft	50% of that required at the base of the column	Same as that required at the base of the column
Between bottom end of column cage and 2 ft below top of Type II shaft		50% of that required at the base of the column

2.2.3 WSDOT Bridge Design Manual [2020]

The WSDOT BDM [2020] provides requirements for column-drilled shaft connections primarily in Sections 7.3.5 and 7.8. These requirements are based on McLean and Smith's [1997] study with some modifications.

The WSDOT requires the column longitudinal reinforcement to be embedded similarly to McLean and Smith [1997], with a noncontact lap splice length of l_{ns} ; see Equation (2.10). The only difference between McLean and Smith's [1997] and WSDOT BDM's [2020] recommendations is the tension development length to be used for l_s . McLean and Smith recommended using a lap splice length (l_s) based on the larger of the shaft and column longitudinal bars. In contrast, the WSDOT requirement always bases the lap splice length on the column bars.

$$l_{ns} = l_s + e \quad (2.10)$$

where l_s is the larger of $1.7l_{ac}$ or $1.7l_{d,c}$. (The 1.7 factor represents a Class C lap splice modification factor from previous versions of AASHTO BDS. Class C splices were eliminated in recent years from AASHTO BDS [2017]. However, the factor remains in WSDOT BDM for this calculation in order to match McLean's [1997] recommendations); l_{ac} is the development length from AASHTO SGS Section 8.8.4 for column longitudinal reinforcement; $l_{d,c}$ is the tension development length from AASHTO BDS Section 5.11.2.1 for column longitudinal reinforcement; and e is the eccentricity, i.e., the distance between the shaft and column longitudinal reinforcement.

The WSDOT's requirement for transverse reinforcement in the transition region is based on McLean and Smith's model [Equation (2/30)] but contains an additional factor k . This equation is also used in AASHTO BDS [2017]:

$$\frac{A_{tr}}{s} = \frac{kA_l f_{u,l}}{2\pi f_{y,tr} l_s} \quad (2.11)$$

where k is the factor representing the ratio of column longitudinal reinforcement that is subject to tension at the nominal bending resistance to total column longitudinal reinforcement. In the upper half of the splice zone, WSDOT recommends using $k = 1.0$. In the lower half of the splice zone, WSDOT claims that k can be determined either from the column moment-curvature analysis or by assuming a value of $k = 0.5$; AASHTO [2017] references the same equation for transverse reinforcement design [Equation (2.11)] but suggests a value of $k = 0.5$ along the entire splice zone.

Additionally, the WSDOT BDM provides a lower limit for the shaft volumetric transverse reinforcement ratio. It recommends that the volumetric ratio in the splice zone not be less than that provided by a #6 spiral with a 6-in. pitch.

2.2.4 AASHTO Guide Specifications for Accelerated Bridge Construction [2018]

Design provisions have also been developed specifically for accelerated bridge construction (ABC) bridge elements, many of which are prefabricated. For column–shaft connections, one commonly proposed ABC concept is a socket connection. The column can be fully precast and embedded into a CIP drilled shaft, with no protruding reinforcement from either element. The interstitial space between the two elements is filled with either grout or concrete. The AASHTO ABC provisions and suggested construction sequence for this type of connection are based on experimental tests conducted by Tran [2012]. These tests are described in more detail in Section 2.3.4.

The AASHTO ABC provisions include guidelines for the minimum precast column embedment depth into the CIP shaft. Because the column longitudinal bars are terminated within the precast column (with either straight bar development or mechanical anchorages), the approximate embedment depth of column bars equals the column embedment depth less the bottom concrete cover. The column embedment depth $l_{e,PC}$ is suggested as:

$$l_{e,PC} \geq \max \left\{ \begin{array}{l} D_{c,max} \\ l_s + e + c \end{array} \right. \quad (2.12)$$

where $l_{e,PC}$ is the total required embedment depth of precast column in shaft; and l_s is the splice length of the larger bar between the column and shaft bars, defined as the larger of $1.7l_{ac}$ or $1.7l_{d,c}$. This is similar to the definition of l_s in the WSDOT BDM [2020] requirements (Section 2.2.3), where e is the eccentricity, i.e., the distance between the shaft and column longitudinal reinforcement; and c is the total bar end cover distance of both column and shaft bars.

The AASHTO ABC provisions' [2018] equation to determine the transverse reinforcement in the transition region matches that in AASHTO BDS [2017] and WSDOT BDM [2020], which is outlined in Equation (2.11). However, the efficiency factor k differs from those recommended in the other specifications. The factor k —and thus the amount of transverse reinforcement—varies over the depth of the transition region. The transition region equates to the socket depth or column embedment depth in a precast column-CIP shaft connection and is divided into three regions; see Figure 2.3. In the uppermost foot of the shaft reinforcement cage, Region C, $k = 2.0$. In the remaining upper half of the socket connection, Region B, $k = 1.0$. For the lower half of the socket connection, Region A, $k = 0.5$. The additional reinforcement in the uppermost region (Region C) is intended to control cracking; the amount is based on experimental results from Tran [2012] (see Section 2.3.4).

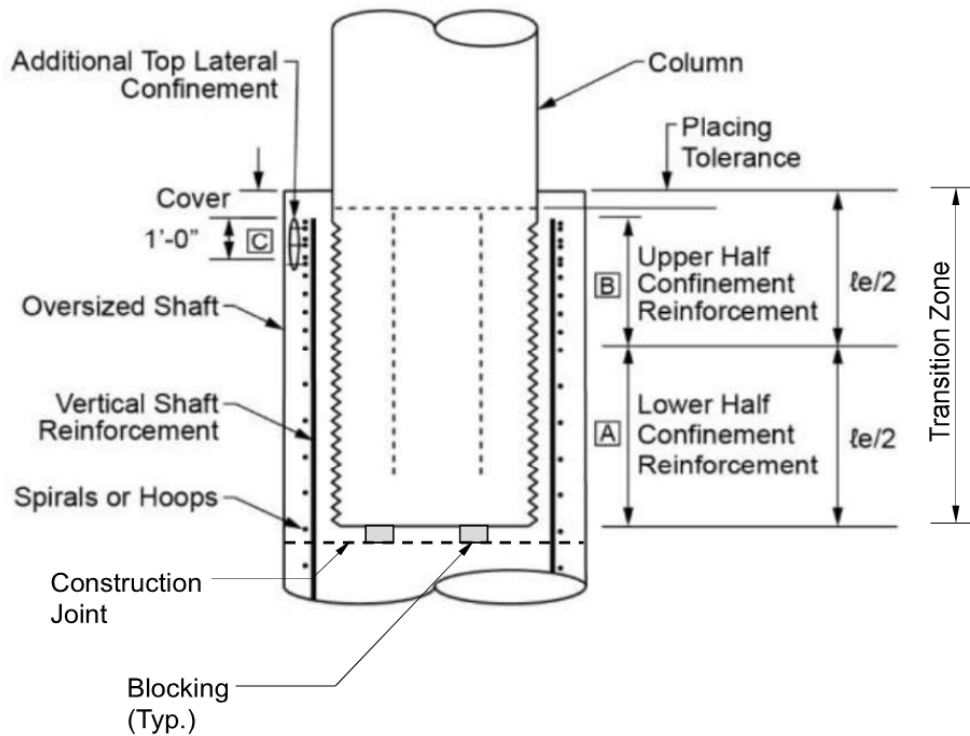


Figure 2.3 AASHTO ABC's three regions (A, B, C) within the height of a socket connection [AASHTO ABC 2018].

2.3 EXPERIMENTAL TESTS OF COLUMN-DRILLED SHAFT CONNECTIONS

A number of experimental tests of column-drilled shaft subassemblies under cyclic lateral loading have been conducted. These include reduced-scale specimens by McLean and Smith [1997] and Tran [2015], as well as full-scale column–shaft specimens by Murcia-Delso et al. [2013] and Lotfizadeh and Restrepo [2019]. The design parameters of all the specimens, including bar sizes, embedment, and transverse reinforcement, are summarized in Table 2.2.

2.3.1 Reduced-Scale Column–Shaft Test: McLean and Smith [1997]

McLean and Smith [1997] tested one ¼-scale, CIP, column–shaft specimen under cyclic lateral loading; see Figure 2.4. The column diameter was 12 in., and the shaft diameter was 24 in.

The specimen was loaded under a series of increasing displacement cycles with a maximum applied displacement of ± 3.5 in. (approx. 7% drift). The experimental report did not include any strain measurements for the transverse reinforcement, but the specimen performed well with little distress observed in the connection region. Cracks were observed radiating outward from the column to the shaft and down the sides of the shaft, but crack propagation was adequately controlled by the transverse reinforcement. The load-deflection hysteresis curves showed no strength degradation, indicating that the provided connection strength was sufficient under this load case.

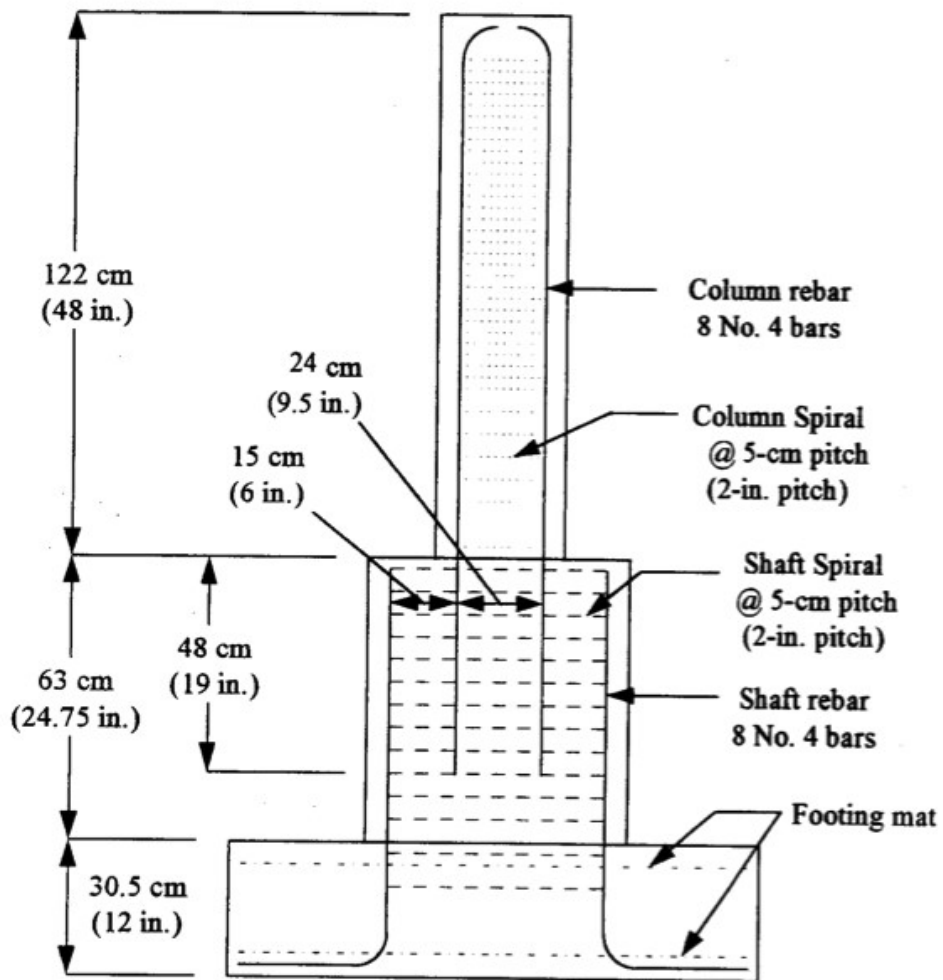


Figure 2.4 McLean and Smith's experimental specimen design [1997].

Table 2.2 Key characteristics of past specimens.

	McLean and Smith [1997]	Murcia-Delso et al. [2013]			Lotfzadeh and Restrepo [2019]	Tran [2015]		
		UCSD-1	UCSD-2	UCSD-4	UCSD-5	DS-1	DS-2	DS-3
Column diameter (in.)	12	48	48	48	48	20	20	20
Column height (in.)	48	192	216	192	216	60	60	60
Shaft diameter (in.)	24	72	72	60	72	30	30	26
Shaft height (in.)	24.75	108	96	72	96	30	30	30
Shaft-column diameter ratio	2.0	1.5	1.5	1.25	1.5	1.5	1.5	1.3
Column longitudinal reinforcement (reinf. ratio)	8 #4 (1.41%)	18 #11 (1.55%)	18 #14 (2.24%)	32 #8 (1.40%)	14 #14 (1.74%)	10 #5 (0.98%)	10 #5 (0.98%)	16 #5 (1.56%)
Shaft longitudinal reinforcement (reinf. ratio)	8 #4 (0.35%)	28 #14 (1.55%)	26 #18 (2.55%)	40 #11 (2.21%)	20 #18 (1.96%)	30 2#3 (0.94%)	30 2#3 (0.94%)	24 3#4 (2.66%)
Formula for embedment length of column reinf.	$l_s + e + c$	$D_{c,max} + l_d$	$l_{d,c} + e + c$	$l_{d,c} + e + c$	$l_{d,c} + e + c$	$l_d + e + c$	$l_d + e + c$	$l_d + e + c$
Embedment length of column reinf. (in.)	19	90	72	37	90	26	26	26
Formula for shaft transverse reinf. In transition region	McLean & Smith [Eq. (2.3)]	Compression member, AASHTO [2010]	McLean & Smith [Eq. (2.3)]	Murcia-Delso et al. [Eq. (2.6)]	Murcia-Delso et al. [Eq. (2.6)]	WSDOT BDM [2017]	50% of transverse reinf. from DS-1	300% of transverse reinf. from DS-1
Shaft transverse reinf. in transition region (vol. ratio)	gauge-4 wire at 2 in. (1.82%)	2#6 at 6.5 in. (0.82%)	2#7 at 7 in. (1.04%)	2#7 at 5.5 in. (1.62%)	#7 at 5 in. (0.74%)	2 gauge-9 wire at 3 in. (0.17%)	gauge-9 wire at 3 in. (0.09%)	3 gauge-9 wire at 1.5 in. (0.61%)
Transverse reinforcement in plastic-hinge region of column (vol. ratio)	gauge-4 wire at 2 in. (0.87%)	2#5 at 6.5 in. (0.87%)	2#5 at 4 in. (1.41%)	#6 at 4 in. (1.00%)	2#5 at 5 in. (1.14%)	gauge-3 wire at 1.25 in. (0.81%)	gauge-3 wire at 1.25 in. (0.81%)	gauge-3 wire at 1.25 in. (0.81%)

2.3.2 Full-Scale Column–Shaft Tests with Large Bars: Murcia-Delso et al. [2013]

Murcia-Delso et al. [2013] tested four full-scale column–shaft specimens with different column reinforcement sizes and embedment lengths, amounts of transverse reinforcement, and column–shaft diameter ratios; see Figure 2.5. The varying specimen designs were based on different design methodologies, including McLean and Smith’s [1997] truss model, Caltrans’ SDC [2013], and Murcia-Delso et al.’s bond-slip model, all of which were outlined in Sections 2.1 and 2.2. Key parameters are summarized in Table 2.2. One of the specimens (UCSD-3) had an engineered steel casing surrounding the shaft; therefore, it was omitted from the table.

All column–shaft specimens were loaded with a constant axial load (including self-weight) of 9.4% of the target compressive strength of the concrete at the base of the column. Each specimen was then loaded cyclically with an increasing lateral load until the lateral load resistance dropped significantly due to fracture of the column reinforcing bars.

All specimens followed similar damage progressions and ultimately failed at the base of the column. Specimens UCSD-2 and UCSD-4 had the most severe damage in the shaft, with wide radial cracks at the base of the column and top of shaft; see Figure 2.6. This observed damage was consistent with the strains measured in the reinforcing bars. For example, the maximum plastic strain penetration measured in the column longitudinal bars was deepest for UCSD-2 and UCSD-4 (in terms of both column bar diameters $d_{b,col}$ and provided embedment length l_e); among the specimens without steel casing, the strains in the hoops in the transition region were largest for UCSD-4 and smallest for UCSD-1, which had, respectively, the shortest and longest embedment for the column longitudinal reinforcement. Along the length of the transition region, the hoop strains were largest at the top and nearly zero at the bottom for almost all specimens; see Figure 2.7. In UCSD-4, the largest hoop strains were measured near mid-height of the transition region, but it is possible that the two strain gauges at this height were faulty because their measurements were an order of magnitude larger than those of surrounding gauges and strains measured in the other UCSD specimens.

In conclusion, Murcia-Delso demonstrated that a column bar embedment length significantly shorter than that required by Caltrans SDC v1.6 [2010] is sufficient to develop the tensile strength of the reinforcement and facilitate ductile failure at the column base. The transverse reinforcement provided in the connection region in all cases sufficiently protected the system from another failure mode; damage in the shaft ranged from practically no damage (UCSD-3 and UCSD-1) to a cone-shaped fracture surface at the top of shaft (UCSD-2, Figure 2.6).

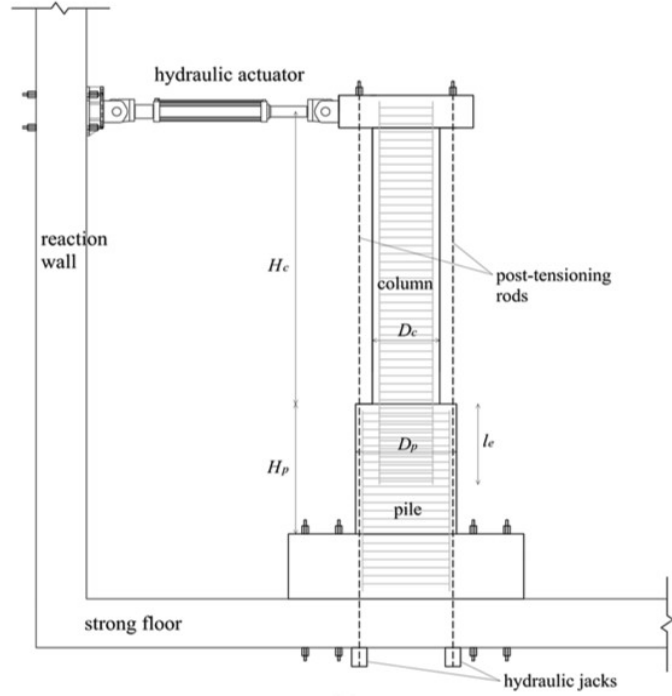


Figure 2.5 Typical setup for UCSD experimental tests [Murcia-Delso et al. 2013].



Figure 2.6 Photograph of post-test damage in Specimen UCSD-2 [Murcia-Delso et al. 2013].

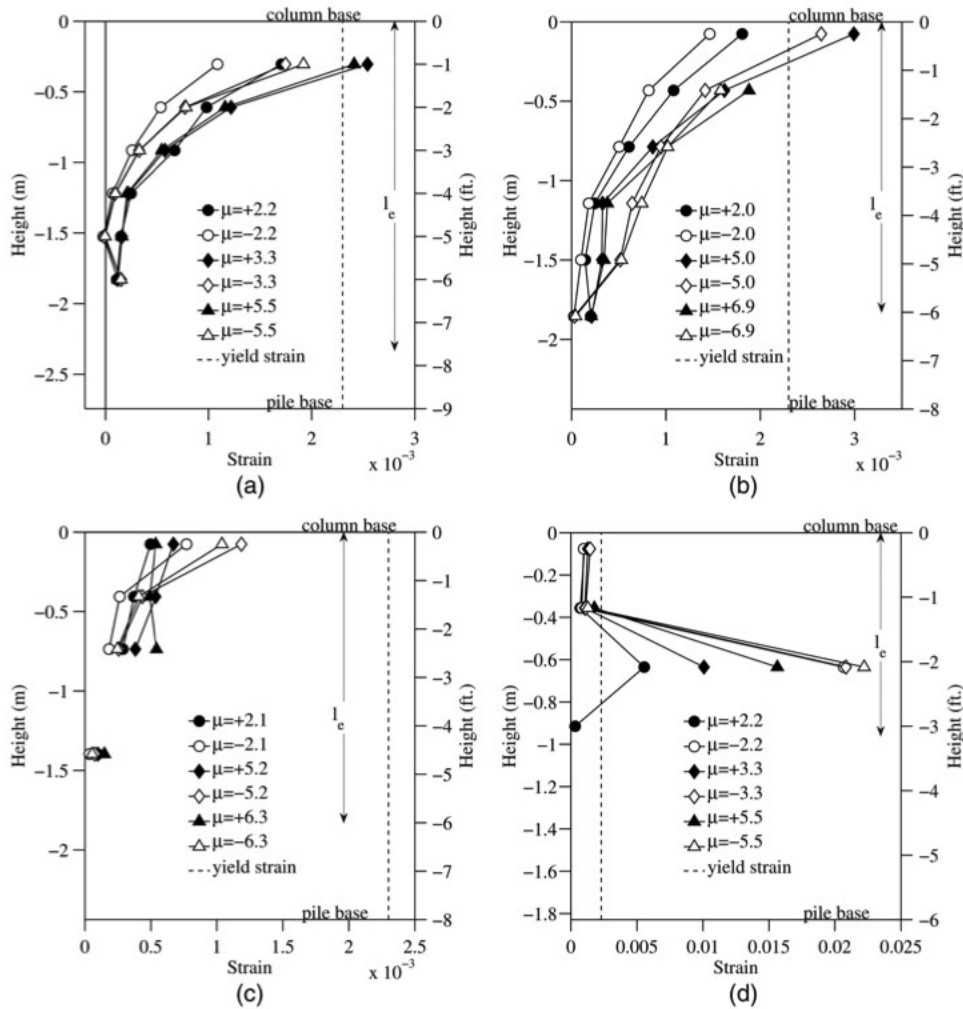


Figure 2.7 Strain profiles for transverse reinforcement (hoops) in UCSD-1 through UCSD-4 specimens [Murcia-Delso et al. 2016].

2.3.3 Full-Scale Column–Shaft Test with Grade 80 Bars: Lotfizadeh and Restrepo [2019]

Lotfizadeh and Restrepo [2019] tested one full-scale column–shaft specimen using Grade 80 reinforcement. This experiment was intended to be a proof-of-concept for Grade 80 bars in column–shaft connections, as current design guidelines only allow the use of Grade 60 bars in seismic critical members.

The experimental setup was similar to that used by Murcia-Delso et al. [2013]; see Figure 2.5. The specimen was first loaded to a constant axial force of 8.9% of the target compressive strength of the concrete at the base of the column. Then, it was loaded cyclically under a series of increasing displacement cycles until the lateral load resistance dropped significantly.

Experimental results showed that the Grade 80 specimen behaved similarly to similar Grade 60 specimens; see Figure 2.8. Along with other experimental tests and a FE model on Grade 80 bars, this experiment supports the implementation of Grade 80 bars in this type of connection.

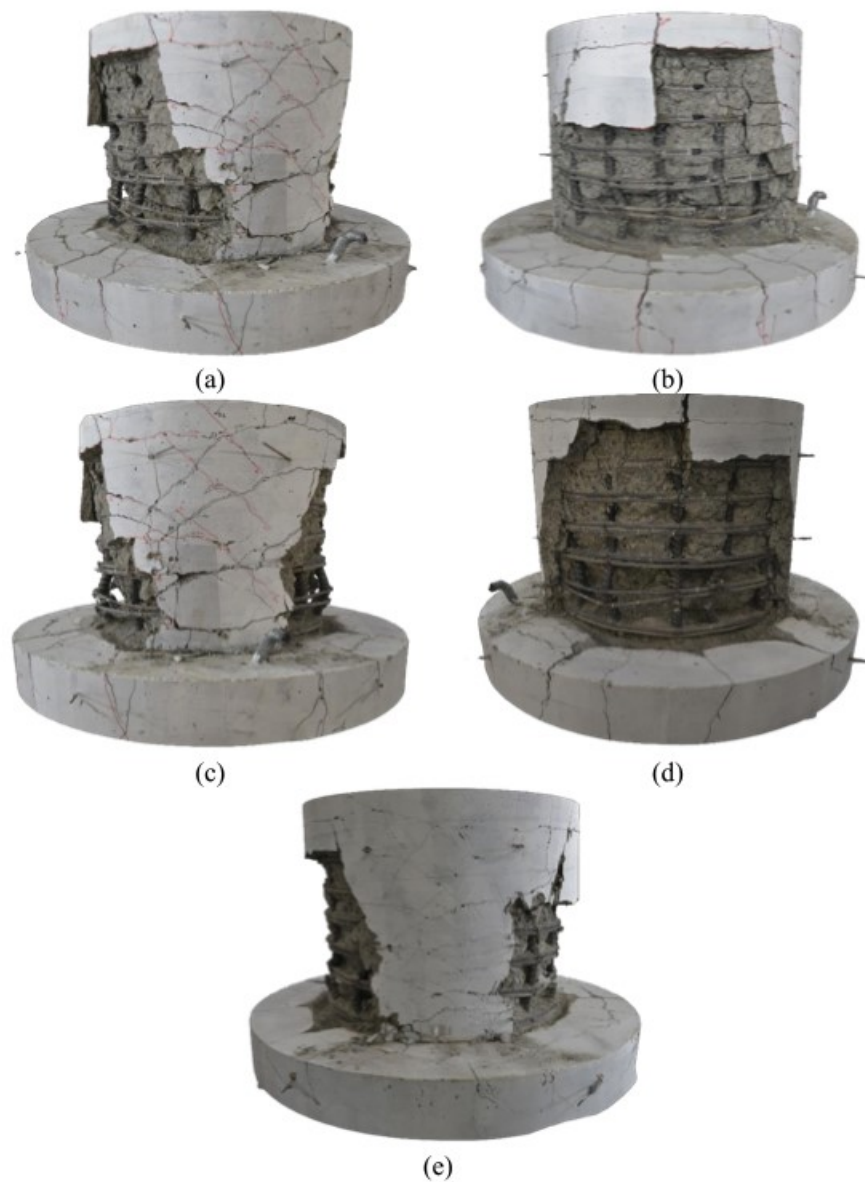


Figure 2.8 360° 3D point cloud model showing damage in UCSD-5 column plastic hinge [Lotfizadeh and Restrepo 2019].

2.3.4 Precast Column–Shaft Tests for Accelerated Bridge Construction: Tran [2015]

Tran [2015] developed and tested a concept for column–shaft connections using a precast concrete column and a CIP drilled shaft; see Figure 2.9. This concept is useful for ABC. Three column–

shaft specimens were tested until failure in order to investigate the seismic performance of this precast-CIP connection.

Tran's proposed precast column-CIP shaft construction sequence is as follows:

- Drill shaft excavation and cast drilled shaft up to the bottom of the transition region.
- Position and brace precast column.
- Cast annular transition region around the precast column.

For Tran's tests, the column longitudinal reinforcement was developed with mechanical anchors. The surface of the precast column was intentionally roughened where it was to be embedded in the drilled shaft.

Three 1/3.6-scale column-shaft subassemblies with varying transverse reinforcement and column-shaft diameter ratios were tested under cyclic lateral loading [Tran 2012; 2015]. The embedment length for all specimens remained the same and was designed according to the scaled-down noncontact lap splice length proposed by McLean and Smith [1997]. The specimen designs are summarized in Table 2.2.

The specimens were first loaded with a constant axial load of 10% of the nominal compressive strength of the concrete (excluding self-weight). They were then subjected to a lateral displacement history with generally increasing amplitudes. The specimens were loaded until failure, which occurred at a drift ratio of about 10% for all specimens. Failure was defined as the stage when the lateral load resistance dropped significantly due to fracturing of the reinforcement or bursting of the transition region.

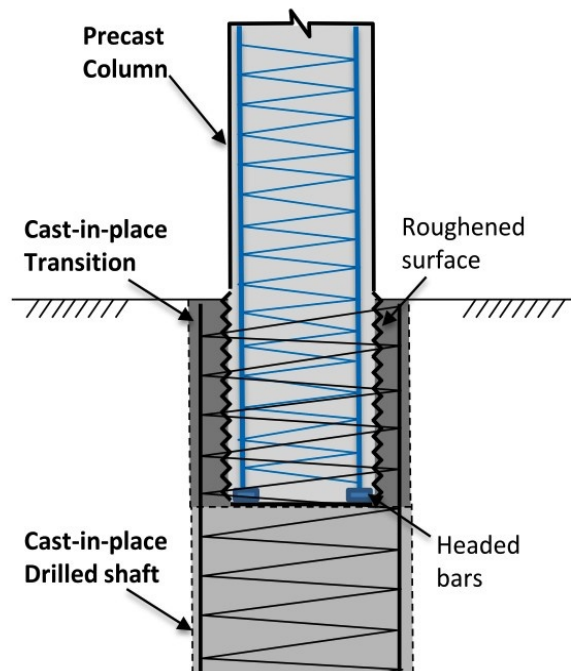


Figure 2.9 Tran's precast column-CIP drilled shaft concept [Tran 2015].

Failure in both Specimens DS-1 and DS-3 occurred by bar buckling and fracture in the column base while the transition region remained intact. In Specimen DS-2, a prying failure occurred in the transition region: the annular CIP concrete shell split open, and the precast column was able to be separated from the CIP shaft; see Figure 2.10. In all cases, the measured strain distributions in the shaft transverse reinforcement were not uniform. The uppermost spirals in all specimens yielded, while the spiral strains were nearly zero at the bottom of the transition region. This pattern is similar to the strain distributions measured by Murcia-Delso et al. [2013], and demonstrates that McLean and Smith's [1997] assumption of a uniform diagonal strut force is not true in practice.

The experimental results showed that a precast column-CIP drilled shaft connection can perform well if adequate transverse reinforcement is provided in the transition region. If inadequate transverse reinforcement is provided, an undesirable failure in the shaft may occur. The Tran [2012] and Tran [2015] results are discussed in greater detail in Chapter 6.



Figure 2.10 Photograph of post-test damage in Specimen DS-2 [Tran 2015].

2.4 FINITE-ELEMENT ANALYSES

Following the experimental tests of column-drilled shaft connections, two sets of FE models were developed to simulate the behavior of such connections. The models were first validated against experimental test results and used to obtain more detailed information. Then, they were used in parametric studies to determine the required column longitudinal bar embedment length and minimum shaft diameter to ensure plastic hinging in a precast column.

2.4.1 Connections with Cast-in-Place Components

Murcia-Delso and Shing [2018] conducted a numerical study with nonlinear FE models to examine the bond-slip behavior and development of column longitudinal reinforcement in drilled shafts. The bond-slip behavior in the FE models followed a constitutive model developed by Murcia-Delso and Shing [2015], which was based on results of their pullout tests. Nonlinear static FE analysis to model the cyclic behavior was performed in Abaqus [Dassault Systèmes 2010].

The FE analysis load-displacement curves generally matched those of Specimens UCSD-1 through UCSD-4. Numerical and experimental strains in the column longitudinal reinforcement were similar. For the shaft longitudinal reinforcement, the FE models underestimated strain levels in the bars. Correlations between the numerical and experimental hoop strains in the shaft transverse reinforcement ranged from good to poor among the four specimens. Ultimately, the FE models were not able to consistently capture strains in the shaft hoops. Murcia-Delso and Shing concluded that the FE model was unable to accurately capture prying action of the column within the shaft, and the bond-slip model underestimated the splitting force as the bond stress deteriorated, resulting in an inability to accurately capture shaft hoop strains.

Murcia-Delso and Shing also conducted a parametric study with seven additional column–shaft assemblies to determine the required column longitudinal bar embedment length for bar development. Conclusions from this analysis, including an equation to determine the minimum embedment length, are summarized in Section 2.1.2.

2.4.2 Connections with Precast Components for Accelerated Bridge Construction

Saiidi et al. [2020] conducted a numerical study with nonlinear FE models to simulate the behavior of column–shaft socket connections. The pushover analyses in their study were performed in Abaqus/Explicit [Dassault Systèmes 2014].

The FE models were first validated against DS-1 and DS-2 precast column-CIP shaft experimental results, described in Section 2.3.4. The overall moment-drift response of the numerical analysis and experimental tests were similar. The cracks in the FE model for DS-1 mostly occurred in the column, while those in the DS-2 model extended to both the column and shaft. Similarly, the model strains in the shaft spirals were much larger in DS-2 than in DS-1. These numerical results match the behavior observed in the experiments.

The models were then used to perform a parametric study examining the minimum allowable diameter of drilled shafts with socket connections to ensure that plastic hinges form in the column. The study included full-scale shafts with diameters 19 in., 27 in., 31 in., and 39 in. greater than the adjoining column's 75-in. diameter. Numerical results showed that the change in the shaft diameter had little effect on moment-drift curves. All four models failed through plastic hinging in the column. The smallest-diameter model also exhibited large cracks in the shaft, indicating that the shaft diameter was not sufficient to provide capacity protection. This is consistent with Caltrans' specifications for Type II (enlarged) shafts, which require shafts to have a diameter at least 24 in. greater than that of the column. In conclusion, Saiidi et al. [2020] determined that requirements for the seismic design of CIP column–shaft connections could be extended to similar precast connections with some modifications. The proposed specifications from this study were incorporated into AASHTO ABC, described in Section 2.2.4.

3 Design and Construction of Test Specimen

For this study, one column–shaft connection specimen was designed, constructed, and tested at the University of Washington. The specimen consisted of a 1/3.6 (28%)-scale column embedded into the top of an enlarged drilled shaft, which sat on a rectangular base fixed to the experimental testing frame. The design rationale, construction process, and material properties for the specimen will be described in this chapter. Because the specimen was the fourth in a planned series, the designs of the first three specimens (tested previously by others at the University of Washington) are reviewed before addressing the latest specimen design.

3.1 CHARACTERISTICS OF PREVIOUS COLUMN–SHAFT CONNECTION SPECIMENS

Previous tests of similar column–shaft connection specimens [Tran 2012; Tran 2015] are shown in Table 3.1. They include: a reference specimen based on a column–shaft connection with reinforcement typical of that used in Washington (DS-1); a “weak shaft” specimen with a 50% reduction in the shaft transverse reinforcement in the transition region (DS-2); and a “strong column” specimen with increased column flexural strength as well as increased shaft transverse reinforcement (DS-3). In all three specimens, a precast column was embedded in a CIP shaft. Additionally, all three specimens shared similar geometry. In Table 3.1, column height is defined as the distance between the centroid of load application and the top of the shaft.

Specimens DS-1 and DS-2 were designed to represent a 6 ft.-diameter bridge column and the connection region of a 9 ft.-diameter shaft. The scale factor of 1/3.6, or 28%, was limited by the constraints of the available testing equipment. The resulting test specimens had a 20-in.-diameter column and 30-in.-diameter shaft. Specimen DS-3 had a similar 20-in.-diameter column with a thinner 26-in.-diameter shaft. For all specimens, this column–shaft assembly was connected to a rectangular base that was anchored to the testing frame. The base was designed to remain elastic throughout the test.

Table 3.1 Key characteristics of Specimens DS-1 through DS-4.

	Tran [2015]			Current study	
	DS-1	DS-2	DS-3	DS-4	Full-Scale Equivalent of DS-4
Column diameter (in.)	20	20	20	20	72
Column height (in.)	60	60	60	60	216
Shaft diameter (in.)	30	30	26	30	108
Shaft height (in.)	30	30	30	30	108
Shaft-column diameter ratio	1.5	1.5	1.3	1.5	1.5
Column longitudinal reinforcement (reinforcement ratio)	10 #5 (0.99%)	10 #5 (0.99%)	16 #5 (1.58%)	16 #5 (1.58%)	16 #18 (1.57%)
Shaft longitudinal reinforcement (reinforcement ratio)	30 2#3 (0.93%)	30 2#3 (0.93%)	24 3#4 (2.71%)	24 3#4 (2.04%)	28 3#14 (2.06%)
Embedment length of column reinforcement (in.)	26 (42d _b)	26 (42d _b)	26 (42d _b)	26 (42d _b)	94 (42d _b)
Shaft transverse reinforcement in transition region	2 gauge-9 wire (0.148 in. dia.) at 3 in.	gauge-9 wire (0.148 in. dia.) at 3 in.	3 gauge-9 wire (0.148 in. dia.) at 1.5 in.	gauge-9 wire (0.148 in. dia.) at 0.75 in.	#6 at 5 in.
Volumetric ratio of transverse reinforcement in transition region	0.17%	0.09%	0.61%	0.35%	0.35%
Transverse reinforcement in plastic-hinge region of column	gauge-3 wire (0.244 in. dia.) at 1.25 in.	gauge-3 wire (0.244 in. dia.) at 1.25 in.	gauge-3 wire (0.244 in. dia.) at 1.25 in.	gauge-3 wire (0.244 in. dia.) at 1.25 in.	#7 at 4.5 in.
Volumetric ratio of transverse reinforcement in plastic-hinge region of column	0.81%	0.81%	0.81%	0.81%	0.78%

In an actual column–shaft system in a bridge, the shaft would extend deeper and be buried in soils rather than fixed to an essentially rigid base. The bending moment profiles for a column–shaft–soil system and a column–shaft specimen are compared in Figure 3.1. In order to approximate the behavior of the column–shaft connection in soil, the portion of the shaft to be

included in the specimens needed to be carefully considered. Liu [2012] conducted nonlinear pushover analyses to capture the soil–structure interaction of a column–shaft–soil system. Results showed that the maximum bending moment occurred at a depth between 0 and $2D_c$ from the soil surface, where D_c is the column diameter, depending on soil properties. Liu observed that the system’s peak moment magnitude and location was significantly more dependent on the column diameter than the shaft diameter. Therefore, the shaft height of Specimens DS-1, DS-2, and DS-3 was designed to be 30 in., or $1.5D_c$. This height of the specimens subjected them to a moment and shear demand that was comparable to those applied to a drilled shaft surrounded by soil.

The bending moment profile in the field has a second consequence. The peak moment in the shaft occurs below grade, but the bars required to resist it typically extend up to the top of the shaft. Thus, the flexural strength of the shaft at the transition region is larger than the demand from the column on the connection, and the shaft is already capacity protected without the need for additional measures.

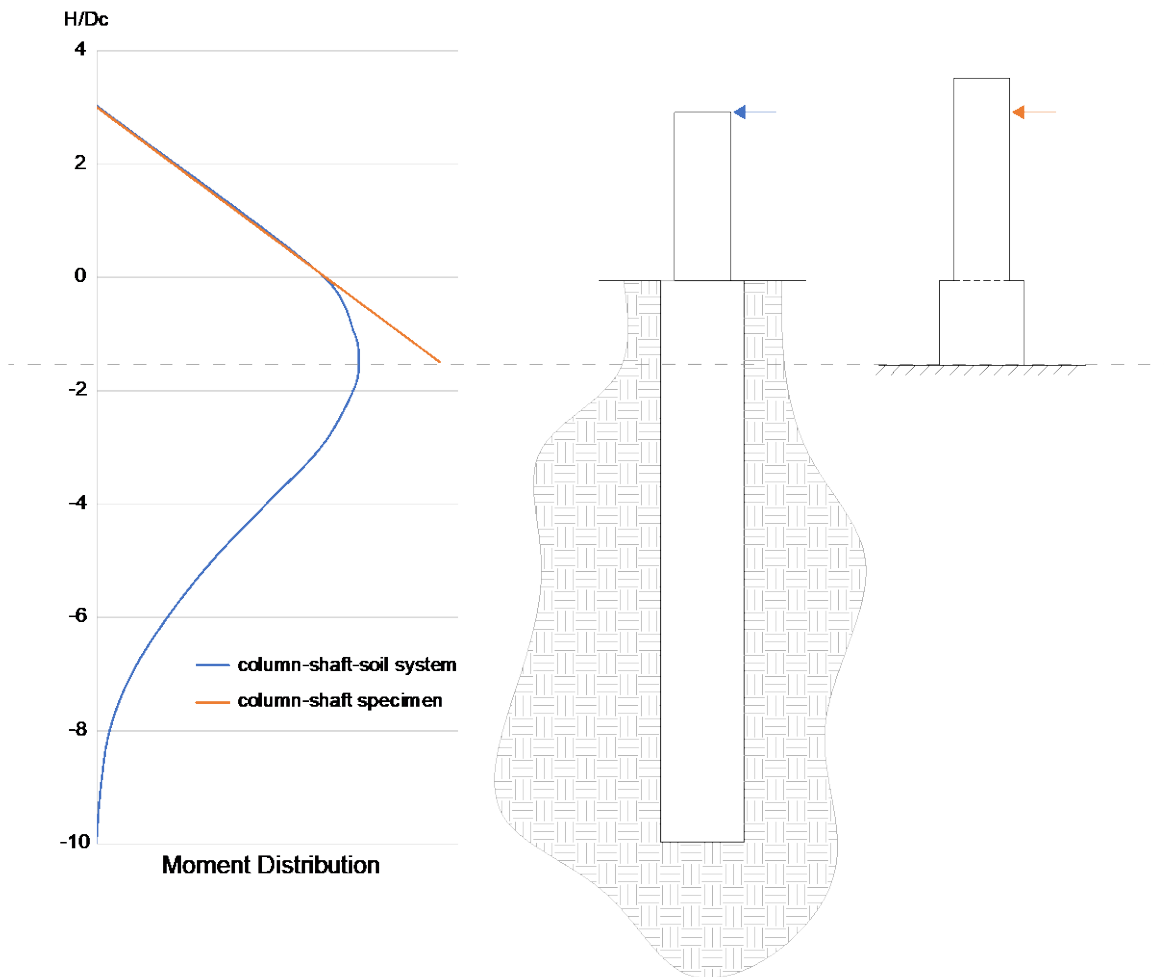


Figure 3.1 Bending moment profiles of actual column–shaft-soil system vs. test specimens.

Specimen DS-1 failed by flexure of the column, while DS-2 (whose shaft spiral was half that of DS-1) failed by prying action in the shaft at the transition region followed by fracture of the shaft spiral. Thus, three failure modes could be envisaged for future specimens with similar geometry:

- Flexural failure of the column
- Column bar pullout from the shaft
- Prying failure (and spiral fracture) of the shaft in the transition region

Shear failure of the shaft is improbable because its diameter is significantly greater than that of the column; shear failure of the column was deemed improbable because of its height-diameter ratio. The three aforementioned failure modes were considered when designing the fourth specimen.

3.2 DESIGN OF FOURTH COLUMN-SHAFT CONNECTION SPECIMEN

The fourth test specimen (DS-4) was designed to have geometry and detailing similar to those of previous specimens; see Table 3.1 in the previous section and Figure 3.2. Specimen DS-4's column was nearly identical to the column in DS-3, with two exceptions: (1) it was CIP, not precast, and (2) the longitudinal reinforcement was not terminated with mechanical anchor heads.

The 26-in. embedment length of the column bars into the transition region, which remained constant across Specimens DS-1 through DS-4, met McLean and Smith's [1997] requirement for noncontact lap splices (which is also used by WSDOT BDM [2020]). It also satisfied the tension development lengths required by Priestley [1993], Murcia-Delso et al. [2013], AASHTO BDS [2010], and ACI 318-14 [2014]. This anchorage length was significantly shorter than the development length required in AASHTO BDS [2017]. The column bars in Specimens DS-1 through DS-3 were terminated with anchor heads, but the measured bar strains near the anchors were essentially zero, so anchors were deemed unnecessary for DS-4.

Specimen DS-4's shaft (which contains the transition region) was designed as a hybrid of the DS-1 and DS-3 shafts. Specimen DS-4's shaft diameter (30 in.) was larger than DS-3's shaft diameter (26 in.) and matched the shaft diameters of DS-1 and DS-2. Specimen DS-4's shaft longitudinal reinforcement matched that of DS-3, which was designed to ensure that the shaft was capacity-protected, forcing the plastic hinge to form in the column rather than in the shaft. In DS-4, the transverse shaft reinforcement was 67% of that used in DS-3 (in terms of total area of transverse reinforcement). This reduced amount of reinforcement was 120% of that required by AASHTO BDS [2017] and 62% of that required by McLean and Smith [1997] and WSDOT BDM [2020]. This reduced level of transverse reinforcement was expected to be near the critical value at which the failure mechanism would change from flexural failure of the column to prying failure in the shaft. Therefore, the transverse strains were expected to be beyond yield but still within the reading capacity of the strain gauges by the end of the experiment, leading to a greater range of experimental results that could then be used for model calibration.

Per WSDOT BDM [2020], the shaft spirals were terminated with the scaled-down equivalent of three turns at the top of the shaft. Specifically, since every two turns of shaft spiral in the specimen represented one turn of #6 spiral at full scale, the specimen spirals were terminated with six turns. The six turns used in the test specimen provided better end anchorage than the three turns used in the field, but the test specimen used smooth wire, while field reinforcement consists of deformed hoops or spiral, so the specimen spiral had worse bond than does field reinforcement. Aside from the termination bundles at the top, the spiral was uniformly spaced in the shaft.

Figure 3.2 shows the configuration of Specimen DS-4. Key dimensions and reinforcement of the current specimen, along with those of previous specimens, were summarized in Table 3.1 in the previous section; see Section 3.1. Additional design drawings can be found in Appendix A.

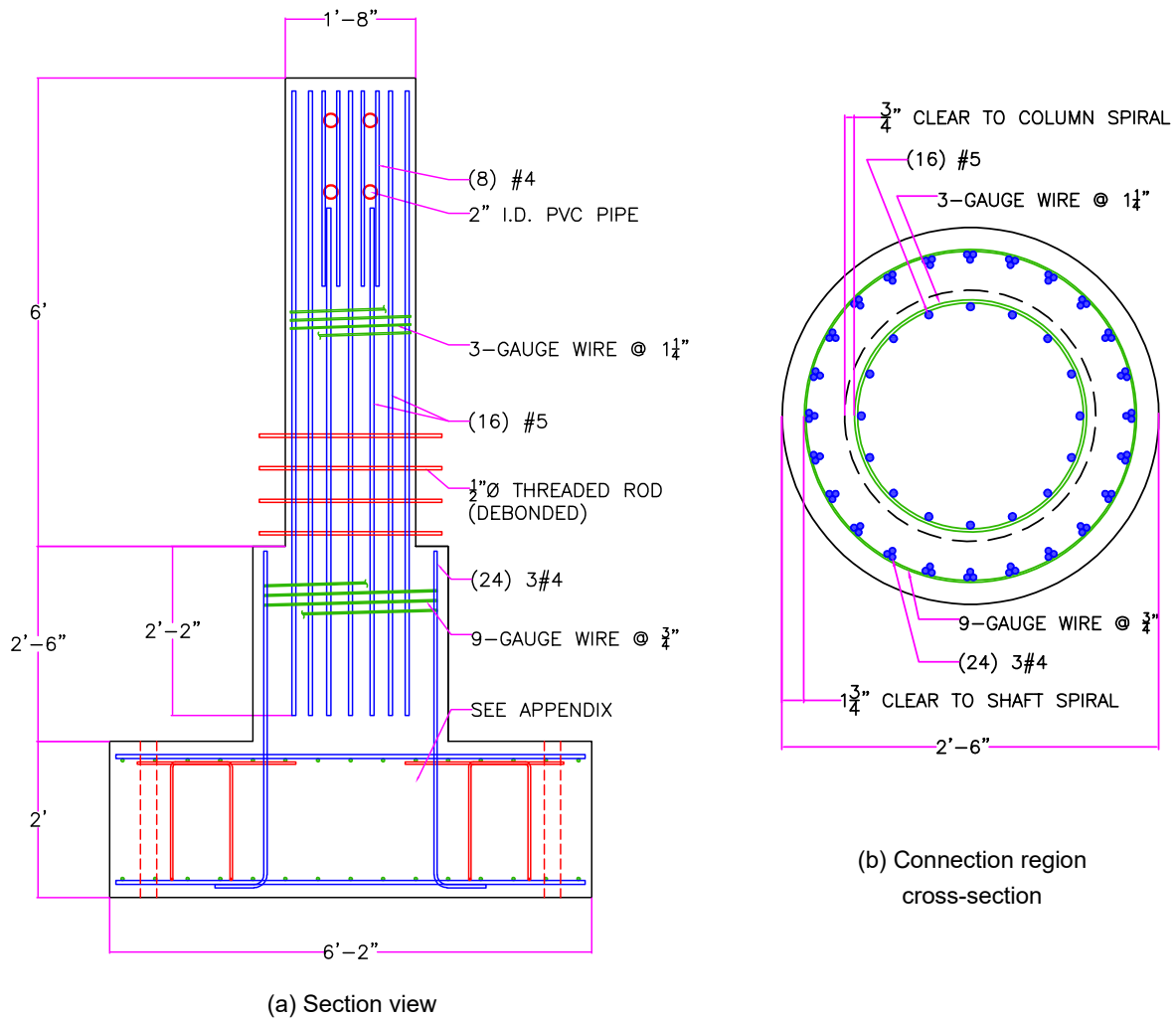


Figure 3.2 Design of test specimen.

3.3 CONSTRUCTION

The specimen was constructed in the Large-Scale Structural Engineering Testing Laboratory at the University of Washington. It was cast in three lifts using a hopper (funnel) hooked to a concrete bucket, lifted by a crane: first the rectangular base and a stub starter for the shaft were cast, then the transition region (Figure 3.3), and finally the column. The surface of each cold joint was intentionally left rough after concrete placement to partially expose the aggregate. Before the following placement, the surface was cleaned of debris. More photographs of the specimen construction are included in Appendix B.



Figure 3.3 Photograph of specimen construction.

3.4 MATERIAL PROPERTIES

The nominal and actual material properties of all specimens tested at the University of Washington are shown in Table 3.2. All reinforcing bars were ASTM A706 Grade 60 bar. The wire reinforcement complied with ASTM A1064 standards. More information on the materials is included in Appendices C and D. These material properties were used in the design and post-experimental analysis of the specimens.

Table 3.2 Concrete and steel material properties of DS-1 through DS-4.

		Tran [2015]			Current study
		DS-1	DS-2	DS-3	DS-4
f'_c (ksi), column	Nominal	6.0	6.0	6.0	5.0
	Actual	7.8	7.2	7.2	7.1
f'_c (ksi), transition region	Nominal	6.0	6.0	6.0	5.0
	Actual	7.4	6.5	8.4	6.7
f_y (ksi), column longitudinal reinforcement	Nominal	60	60	60	60
	Actual	68	68	62	65
f_u (ksi), column longitudinal reinforcement	Nominal	80	80	80	80
	Actual	106	106	86	96
f_y (ksi), shaft longitudinal reinforcement	Nominal	60	60	60	60
	Actual	66	66	67	69
f_u (ksi), shaft longitudinal reinforcement	Nominal	80	80	80	80
	Actual	101	101	92	98
f_y (ksi), shaft transverse reinforcement	Nominal	70	70	70	70
	Actual	N/A	N/A	N/A	N/A
f_u (ksi), shaft transverse reinforcement	Nominal	80	80	80	80
	Actual	110	110	110	98

4 Experimental Program

One column–shaft connection specimen was tested at the University of Washington in the Large-Scale Structural Engineering Testing Laboratory. This chapter describes the experimental setup, instrumentation, and load history of the experiment.

4.1 EXPERIMENTAL SETUP

The specimen was tested using a self-reacting test frame, as shown in Figure 4.1. A constant axial load was applied by the Baldwin Universal Testing Machine (UTM) and then a cyclic lateral load was applied by a servo-controlled MTS Systems actuator at an elevation of 60 in. above the column–shaft interface. A sliding spherical bearing allowed for both loads to be maintained simultaneously. The horizontal actuator and Baldwin UTM have capacities of 220 kips and 2400 kips, respectively.

First, the test frame was centered under the Baldwin UTM, and the specimen was placed in the frame. Next, the specimen was leveled with Hydrostone and post-tensioned to the test frame base with four 1-1/4 in. Williams Form Engineering All-Thread high-strength steel bars, each tensioned to 120 kips. The actuator was post-tensioned to the specimen using four 1-in. high-strength steel threaded rods, each of which was bolted down with 375 lb*ft of torque (which corresponds to approximately 22 kips in tension per rod). The other end of the actuator was attached to the test frame.

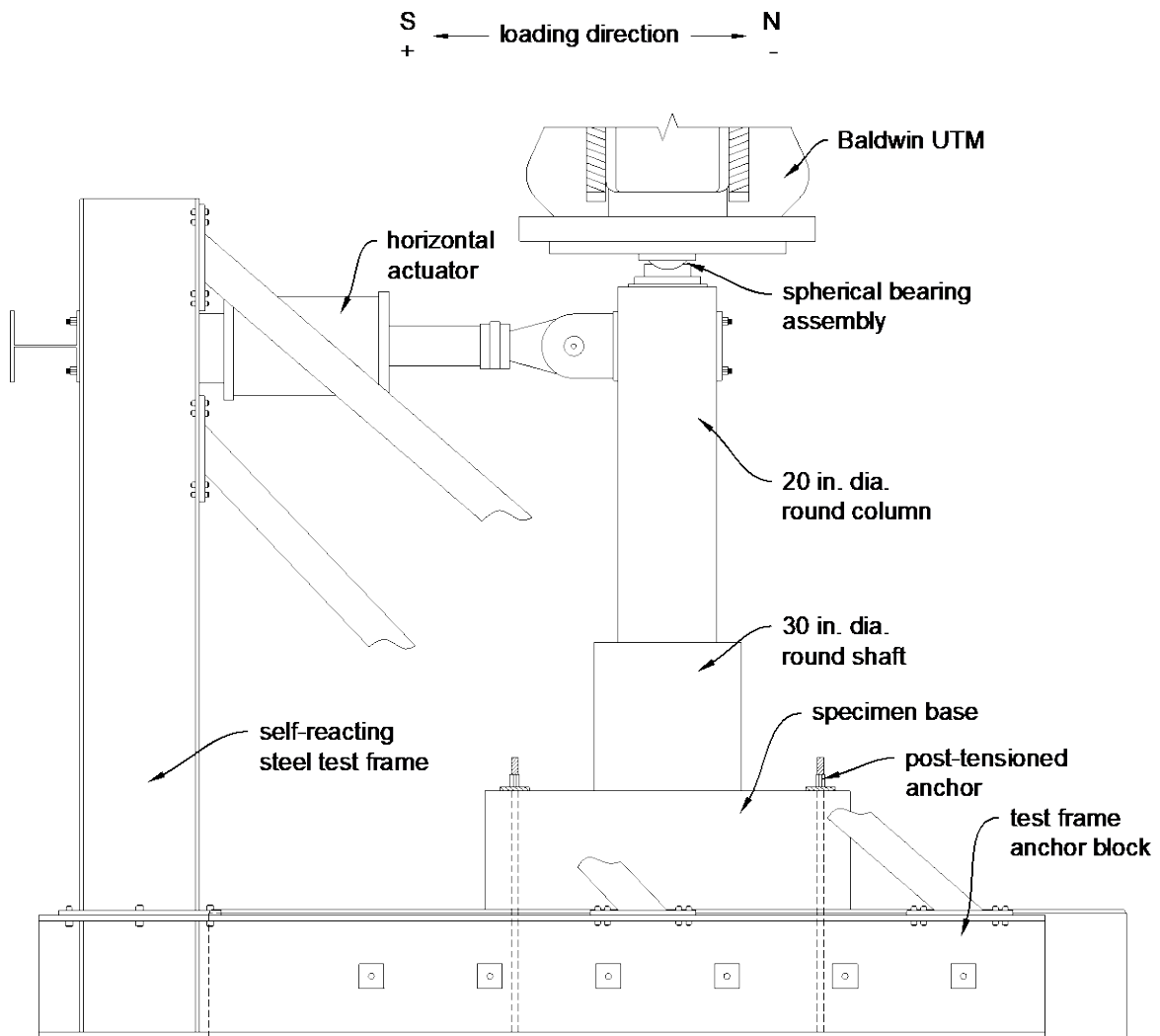


Figure 4.1 Experimental test setup.

To maintain a constant vertical force under varying lateral displacements, a spherical swivel-head bearing was seated within two steel pieces on top of the specimen; see Figure 4.2. This axial bearing assembly was intended to act as a roller support with restrictions against unintended out-of-plane (i.e., transverse) displacements. There were three main components to the assembly:

1. A 2-in.-thick steel plate sat on top of the column to distribute the axial load. To help guide the lateral displacements, 4×4 HSS tubes were welded to the top face of the plate, and the inside faces of the HSS were lined with greased dimpled PTFE to provide a smooth sliding surface.
2. A steel channel was bolted to the Baldwin UTM head. It acted as a guiding track for lateral displacements. The interior web and exterior flanges of the channel were lined with greased stainless steel, which served as low-friction sliding surfaces.
3. A two-piece spherical bearing sat between the two steel pieces. It allowed rotation and displacement of the column under varying lateral displacements. The top surface of the bearing had a greased Maurer Sliding Material (MSM) pad that enabled smooth sliding against the stainless steel-lined web of the channel. The bottom piece of the bearing was held in place by friction.

The spreader component and steel channel nested into each other with the spherical bearing sandwiched in between the two components. During the test, the top of the column, spreader plate, and bearing displaced together in the north–south direction, guided by the HSS-and-channel track formed from the two steel components. The column, spreader plate, and bottom piece of the bearing also rotated together under lateral loading. Meanwhile, the Baldwin UTM head, steel channel, and top piece of the bearing remained level throughout the test.

After the test, it was discovered that the two steel components of the assembly were binding against each other at large rotations: the top of the spreader plate rotated and contacted the flanges of the steel channel. For this reason, the aforementioned axial bearing setup should be modified for future tests. Possible solutions include: (1) adding vertical clearance between the two steel components by inserting a steel plate shim underneath the spherical bearing, or (2) removing the steel spreader component and seating the spherical bearing directly on top of the specimen (using Hydrostone to create a level contact surface between the bearing and the specimen). The implications of this issue will be described in detail in Chapter 5.

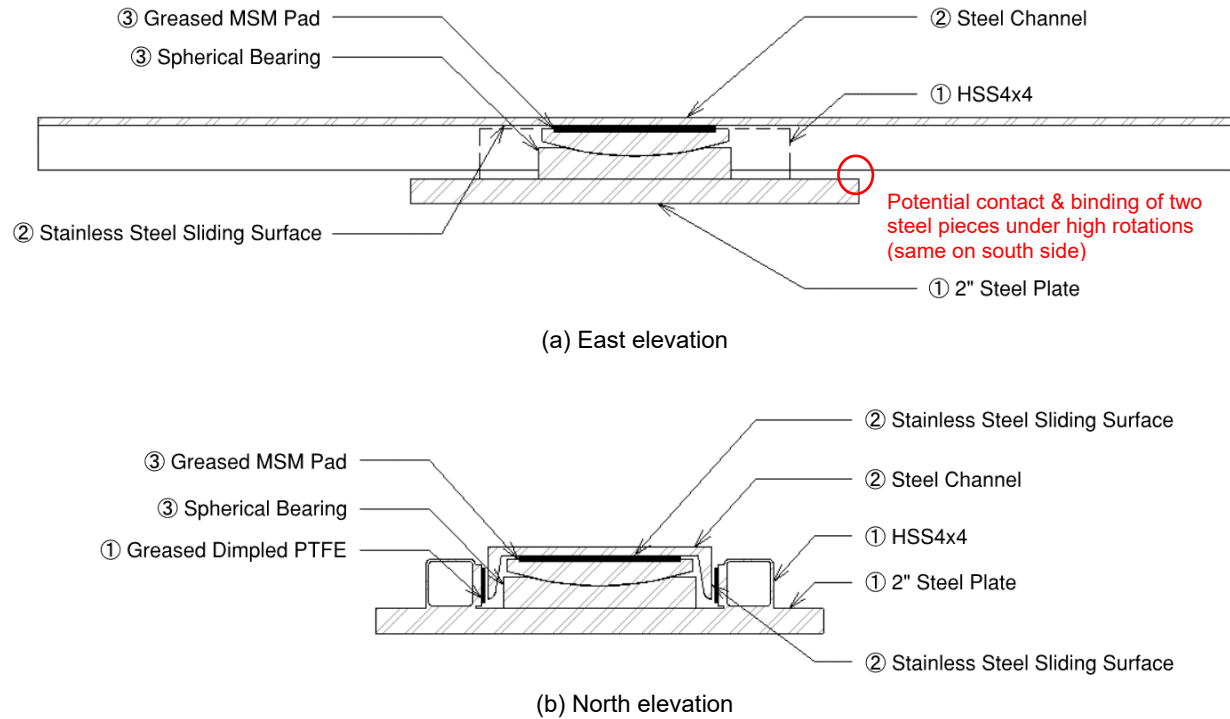


Figure 4.2 Roller setup at the top of the column. Numbers refer to the three components of the assembly described in Section 4.1. This setup should be modified for future use.

4.2 INSTRUMENTATION

The specimen was instrumented with external displacement transducers and strain gauges attached to the specimen surface, as well as internal strain gauges attached to the longitudinal and transverse reinforcement. Inclinometers on one face of the specimen measured rotations. An Optotrak Certus motion capture system was also used to measure deformations. The applied loads were monitored with load cells in the Baldwin UTM and MTS actuator. The lateral displacement of the MTS actuator was monitored using a linear variable differential transformer (LVDT). All measurements were recorded using a computer-controlled data acquisition system (DAQ) at a 5 Hz sampling rate. Specific instruments and their locations will be described in detail in the following subsections.

4.2.1 Instrumentation for Measuring Global Deformations

Six string potentiometers, five inclinometers, and eight Duncan linear potentiometers were used to measure the global deformation of the specimen and testing rig. Figure 4.3 shows the locations of this external instrumentation.

The six string potentiometers measured large horizontal displacements (with a possible range of 10 to 20 in.) in the test system. Five of the six potentiometers measured the horizontal displacement of the column and shaft relative to an unloaded reference tower. The wire ends of the potentiometers were attached to wood blocks glued to the column or shaft concrete surface or embedded rods protruding from the column base, and the spool ends of the potentiometers were clamped to the reference tower. Attaching the potentiometer ends to rods rather than directly to the concrete surface allowed accurate measurements to be taken even after concrete had spalled off. These rods were also used for curvature measurements, which will be described in Section 4.2.2. The sixth string potentiometer was used to monitor deformation of the testing rig. Specifically, it measured the horizontal displacement of the crossbeam to which the actuator was attached relative to another unloaded reference tower. This provided redundancy in the measurement system. This potentiometer is not shown in Figure 4.3.

The five inclinometers measured the absolute rotation of the column, and each had a measurement range of roughly $\pm 20^\circ$. They were attached to aluminum plates that were glued directly on the concrete surface on the east face of the column. One inclinometer was placed at the height of load application to verify consistency between string potentiometer and inclinometer measurements, and to ensure redundancy in case of instrument failure. Another inclinometer was placed at the base of the column near the same height as the embedded rods, again to verify consistency between different measurement methods. The remaining inclinometers were located at different heights from the other instruments along the column to increase density of measurements over the height of the column.

The short-stroke Duncan potentiometers measured smaller displacements (with a stroke of up to 2 in.). Eight Duncan linear potentiometers were used to monitor deformation of the test setup. Four of these potentiometers measured potential uplift and slip of the specimen from the testing rig on the north and south sides. Another four potentiometers measured potential uplift of the testing rig from the test floor: two measured vertical displacements of the rig's steel base beams on the northeast and southeast corners of the rig, and two measured vertical displacement of the rig's concrete reaction block on the north and south sides.

4.2.2 Instrumentation for Curvature Measurements

The instrumentation used to determine column curvature consisted of eight Duncan linear potentiometers. These potentiometers were used to measure relative vertical displacements between debonded embedded rods in the column plastic hinge region, called "curvature rods." The relative displacements could then be used to determine rotation, from which it was possible to calculate the average curvature of the column at its base. The configuration is shown in Figure 4.3.

4.2.3 Instrumentation for Concrete Surface Measurements

An Optotrak Certus motion capture system was used to monitor deformations of the northwest quadrant of the shaft. The system consists of a 3D optical sensor and a series of LED markers. The Optotrak system determines the 3D coordinates of each LED marker relative to the sensor through

optical tracking. Each marker emits an electronic signal that is then recorded by three cameras in the sensor and outputted as a 3D position data point. For this test, 89 LED markers were placed on the shaft to monitor deformations (Figure 4.4), three LED markers were placed on the specimen base block as stationary reference points that defined the coordinate planes, and one LED marker was temporarily placed on a Duncan potentiometer to help synchronize data from different DAQs. From the Optotrak position data, deformations of the shaft (including its deformed shape, rotations, and local strains at the concrete surface) can be calculated. These deformations were verified against measurements from the string potentiometers on the shaft. The locations of the LED markers are shown in Figure 4.4.

A homemade extensometer consisting of packing tape and strain gauges measured the average circumferential elongation in the shaft. First, one layer of packing tape was wrapped around the shaft and stuck to the concrete (with the adhesive facing into the concrete). Then, two layers of packing tape were stuck together to create a plastic band with two smooth faces (with the adhesive sides facing each other). A small adhesive tab was left overhanging on one end of the band. The two-layered band was wrapped taut around the shaft, on top of the existing single layer of tape, and secured to itself with the overhanging adhesive tab. Finally, strain gauges were installed on top of the tape at the north, south, east, and west faces, oriented in the circumferential direction. This extensometer was designed to measure average circumferential strain at the concrete surface: the strain gauges were not directly attached to the concrete to avoid capturing hyperlocal strains and lessen the risk of instrument damage from concrete cracking; the three-layered tape assembly created low-friction sliding surfaces that would stretch and not break if the shaft expanded, and would not increase the specimen's stiffness. Two of these circumferential extensometers were installed at the top and mid-height of the shaft, as seen in Figure 4.3.

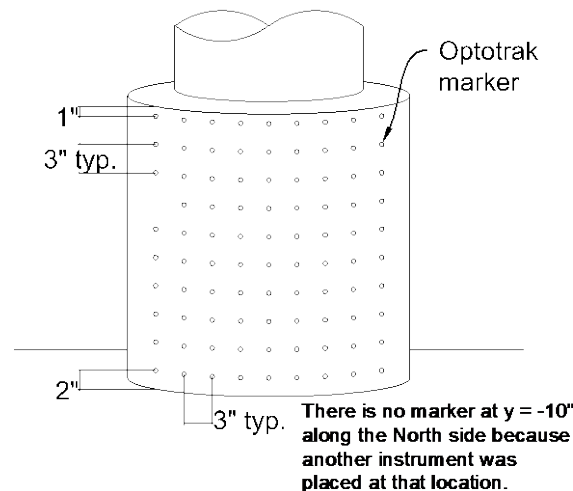


Figure 4.4 Optotrak marker layout (northwest view).

4.2.4 Internal Instrumentation: Strain Gauges

Strain gauges were attached to the longitudinal reinforcement in the column, and both the longitudinal and transverse reinforcement in the shaft. In total, 15 gauges were placed on the column longitudinal bars, 12 on the shaft longitudinal bars, and 21 on the shaft spirals. Type FLA-10-11-5LJCT gauges were used on the reinforcing bars, and FLA-5-11-5LJCT gauges were used on the spiral wire. All gauges were manufactured by Tokyo Measuring Instruments Lab and supplied by Texas Measurements.

The strain gauge installation procedure will first be introduced; then the strain gauge locations, including diagrams and placement details, will be described.

4.2.4.1 Installation Procedure

The strain gauges were installed following a previously used procedure at the University of Washington designed to protect strain gauges from damage during concrete placement and wire leads from fracturing during testing. The following procedure resulted in the loss of only two out of 48 internal strain gauges.

For each strain gauge, the longitudinal rib of the bar at the intended gauge location was ground down and sanded until the surface was flat and smooth (for wire reinforcement, this step was skipped since the wire surface was already fairly smooth). Then, each surface was wiped in an alternating sequence with acid and base solutions multiple times. Each gauge was glued to the dry, clean, and smooth reinforcement and coated with a waterproof compound per manufacturer instructions. During installation, the exposed wire leads were separated from each other and bent on a curve away from each other to provide strain relief: if inadvertently tugged, the wire leads would be able to withstand a small deformation before being pulled taut and stressed. The insulated part of the wire lead was then folded over itself (so the entire gauge assembly resembled a Z-shape) and tucked into a thin pocket made from plastic wrap (so the wire lead could slip within the pocket, providing further strain relief). One layer of electrical tape was wrapped over this assembly around the entire circumference of the bar at the gauge location. All of the lead wires were routed out of the specimen along the reinforcement cage such that falling wet concrete would not disturb the lead wires; see Figure 4.5.



Figure 4.5 Photograph of two strain gauges at different stages of installation.

This assembly ensured that the strain gauge would be well-protected against water, impact from concrete placement, inadvertent contact from a concrete vibrator, and tugging on the wire lead before and during testing; however, this installation procedure does reduce the local bond at the strain gauge location. Loss of bond was minimized by keeping the gauge-protected region as small as possible along the length of the bar. For each gauge, the debonded length was approximately 1 in.

4.2.4.2 Strain Gauge Layout

The goal of the strain gauge layout as shown in Figure 4.6 was to capture detailed strain profiles in the expected transition region without significantly affecting global bond of the reinforcing bar or wire. Gauges were placed at regular intervals in the transition region down to levels where the expected strain was zero to confirm the extent of strain penetration. These measurements would help determine behavioral mechanisms in the transition region.

Figure 4.6 shows the locations of the strain gauges. Gauges were placed on the reinforcement at various elevations near the north, east, and south faces of the specimen, with one gauge per location. Gauges on the longitudinal bars were placed on the west face of each bar, and gauges on the wire spiral were placed on the top face of the spiral, to avoid capturing local bending effects in the measurement.

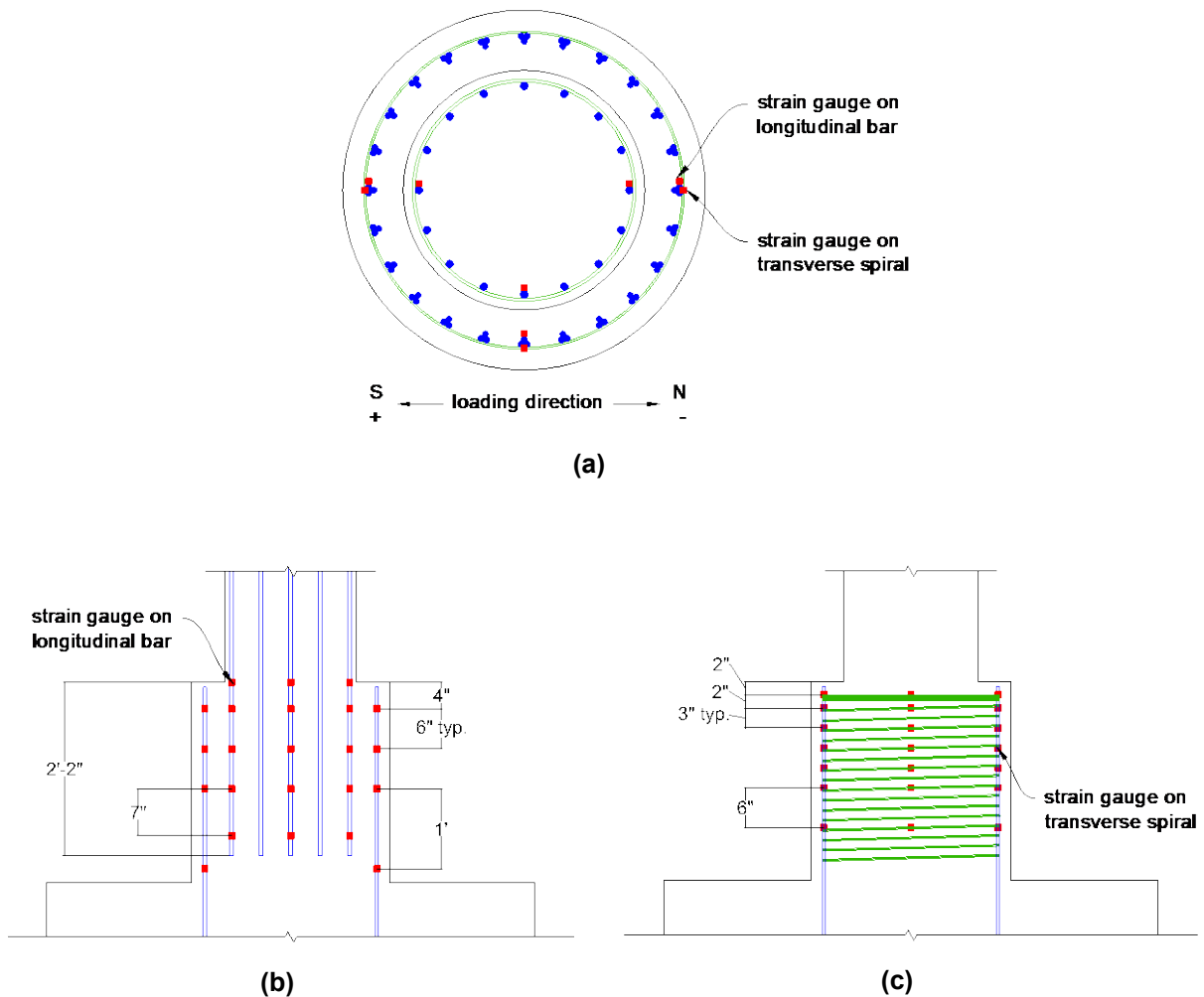


Figure 4.6 Strain gauge locations: (a) cross section in connection region; (b) elevation with longitudinal gauges; and (c) elevation with transverse gauges.

4.3 LOAD AND DISPLACEMENT HISTORY

The column was first loaded axially to 159 kips, or roughly $0.1f'_cA_g$ (where f'_c is the specified nominal concrete strength), which represents the expected unfactored dead load on a typical bridge column. This axial load was kept constant throughout testing. The specimen then was subjected to a displacement-controlled reversed cyclic lateral load. The target displacement history was the same as used in previous tests at the University of Washington [Cohagen et al. 2008; Janes 2011; Haraldsson 2015; and Tran 2015]. It is a modification of the loading history for precast structural walls recommended in NEHRP/FEMA 450 [Building Seismic Safety Council 2004].

The target displacement history is plotted in Figure 4.7. The loading consisted of sets of four cycles in which the amplitude was $1.2A$, $1.4A$, $1.4A$, and $0.5A$, where A is the maximum amplitude from the previous set. The cycle amplitudes of the first set were 0.20 in., 0.24 in., 0.24

in., and 0.08 in. The small amplitude cycle at the end of each set was intended to supply information about the residual stiffness of the specimen.

Displacements to the south were defined as positive, and displacements to the north were negative. The positive and negative peak displacements within a cycle were called “peak” and “valley,” respectively. In the third cycle of each set, the loading was paused at peak and valley displacements to allow for crack inspection, and again at zero force (towards the end of the third cycle, after the valley) to measure the maximum residual crack width. The loading was uninterrupted for all other cycles. Testing was stopped when the lateral force resistance dropped to nearly zero.

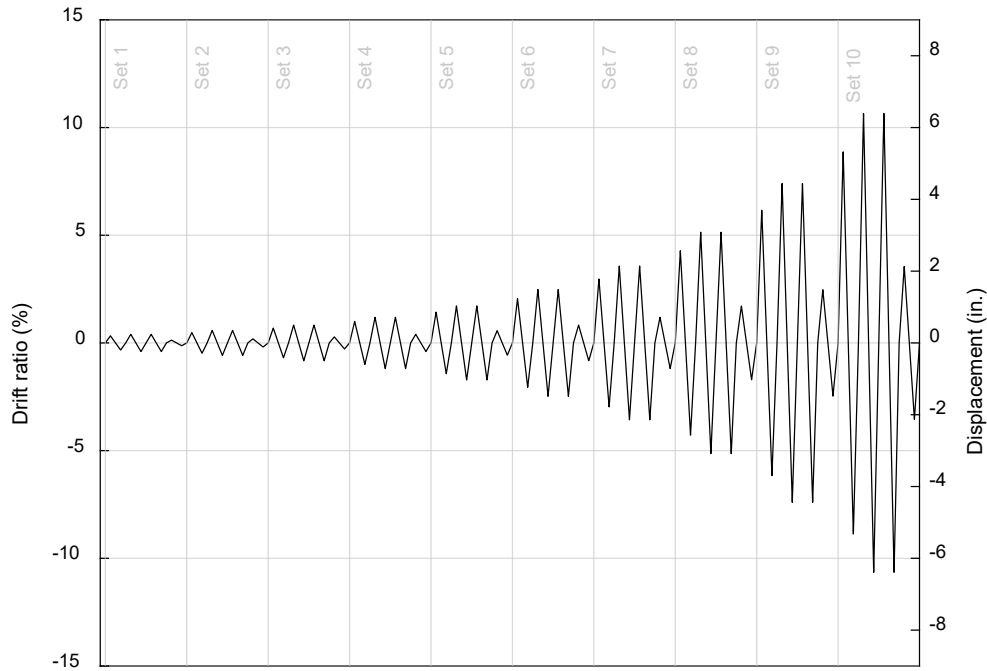


Figure 4.7 Target lateral displacement history.

5 Experimental Results

This chapter describes the results of an experiment in which a column–shaft subassembly (Chapter 3, Appendix A) was subjected to a constant axial load and increasing cyclic lateral displacements; see Chapter 4. The reported results include the observed damage progression, as well as the measured global response, local deformations, strains, and inferred stresses.

5.1 SIGN CONVENTIONS AND TERMINOLOGY

The specimen was subjected to ten sets of displacement-controlled, cyclic lateral loading under a constant axial load; see Table 5.1. Each set consisted of four displacement cycles. In this report, each cycle can be identified by the set number and the within-set cycle number. For example, Cycle 5-2 corresponds to the second cycle of Set 5. The specimen was subjected to a total of 38 cycles (up to Cycle 10-2), reaching a maximum lateral displacement of 6.55 in. (10.9% drift). Testing was stopped when the lateral force resistance dropped to nearly zero.

Displacements to the south are defined as positive, and displacements to the north are defined as negative. The maximum positive and negative displacements within a cycle will be referred to as the cycle “peak” and “valley,” respectively. In this chapter’s figures, occurrences recorded during peak/positive/south displacement (e.g., cracks) are denoted in blue, and occurrences recorded during valley/negative/north displacement are denoted in red.

The maximum displacement and drift ratio reached in each cycle are summarized in Table 5.1. In this document, the drift ratio is defined as the lateral displacement at the actuator level divided by the vertical distance from the actuator centerline to the column–shaft interface (60 in.). For all reported data, the drift ratios indicate the actual drifts reached (as opposed to the target drift ratios).

5.2 DAMAGE PROGRESSION

The specimen damage progression is documented in terms of key damage milestones that are defined in the UW/PEER Structural Performance Database and summarized in Table 5.2. A summary of the damage progression can be found in Table 5.3. This section will first describe the damage progression in writing, and then all damage photographs will be presented at the end of the section.

Table 5.1 Maximum displacement and drift reached during each cycle.

Set	Cycle	Target		Actual		
		Displacement (in.)	Drift (%)	Peak disp. (in.)	Valley disp. (in.)	Average drift (%)
1	1	0.20	0.33%	+0.33	-0.35	0.57%
	2	0.24	0.40%	+0.35	-0.37	0.60%
	3	0.24	0.40%	+0.35	-0.37	0.60%
	4	0.08	0.13%	+0.23	-0.25	0.39%
2	1	0.29	0.48%	+0.39	-0.42	0.68%
	2	0.35	0.58%	+0.43	-0.45	0.73%
	3	0.35	0.58%	+0.44	-0.46	0.75%
	4	0.11	0.19%	+0.25	-0.26	0.42%
3	1	0.41	0.69%	+0.50	-0.53	0.86%
	2	0.50	0.83%	+0.58	-0.61	0.99%
	3	0.50	0.83%	+0.58	-0.61	0.99%
	4	0.17	0.28%	+0.31	-0.32	0.53%
4	1	0.60	1.00%	+0.68	-0.70	1.15%
	2	0.71	1.19%	+0.77	-0.79	1.31%
	3	0.71	1.19%	+0.77	-0.80	1.31%
	4	0.24	0.40%	+0.35	-0.36	0.60%
5	1	0.86	1.43%	+0.92	-0.94	1.55%
	2	1.03	1.72%	+1.08	-1.10	1.81%
	3	1.03	1.72%	+1.09	-1.10	1.82%
	4	0.34	0.57%	+0.47	-0.50	0.80%
6	1	1.24	2.06%	+1.31	-1.32	2.19%
	2	1.49	2.48%	+1.54	-1.53	2.56%
	3	1.49	2.48%	+1.55	-1.56	2.59%
	4	0.50	0.83%	+0.61	-0.68	1.07%
7	1	1.78	2.97%	+1.82	-1.82	3.04%
	2	2.14	3.57%	+2.19	-2.16	3.63%
	3	2.14	3.57%	+2.19	-2.16	3.63%
	4	0.71	1.19%	+0.80	-0.87	1.40%
8	1	2.57	4.28%	+2.63	-2.57	4.33%
	2	3.08	5.14%	+3.15	-3.05	5.17%
	3	3.08	5.14%	+3.16	-3.05	5.17%
	4	1.03	1.71%	+1.12	-1.18	1.92%
9	1	3.70	6.16%	+3.77	-3.61	6.15%
	2	4.44	7.40%	+4.49	-4.26	7.29%
	3	4.44	7.40%	+4.51	-4.28	7.32%
	4	1.48	2.47%	+1.58	-1.61	2.66%
10	1	5.32	8.87%	+5.41	-5.07	8.73%
	2	6.39	10.65%	+6.47	-6.11	10.48%
	3	6.39	10.65%	+6.55	END	10.92%

Table 5.2 Damage milestone definitions.

Damage type	Damage milestone	Milestone description
Cracking	First significant horizontal crack	Crack width ≥ 0.5 mm
	First significant diagonal crack	Crack width ≥ 0.5 mm. Diagonal crack extends 5 in. (1/4 of column diameter)
	First open residual crack	Residual crack width ≥ 0.25 mm
	Large cracks in concrete core	Crack width ≥ 2.0 mm
Spalling	First spalling	Observed spalling on surface
	Significant spalling in column	Spalled height ≥ 5 in. (1/4 of column diameter)
	Fully spalled	Spalling height does not increase with incr. deformation
Yield	First yield of longitudinal reinforcement	First strain gauge that reaches yield
	First yield of transverse reinforcement	First strain gauge that reaches yield
Fracture	Exposure of longitudinal reinforcement	First observation
	Buckling of longitudinal reinforcement	First observation
	Fracture of transverse reinforcement	Observation or sound
	Fracture of longitudinal reinforcement	Observation or sound
	Loss of axial capacity	Instability of member

Table 5.3 Damage progression of column (C) and shaft (S).

Damage milestone	Drift									
	0.6%	0.7%	1.0%	1.3%	1.8%	2.6%	3.6%	5.2%	7.3%	11%
First significant horizontal crack			C S							
First significant diagonal crack						C S				
First open residual crack				S		C				
Large cracks in concrete core					S			C		
First spalling						C	S			
Significant spalling in column								C		
Fully spalled										
First yield of long. reinforcement		C								S
First yield of trans. reinforcement						S				
Exposure of long. reinforcement										S
Buckling of long. reinforcement										
Fracture of trans. reinforcement									S	
Fracture of long. reinforcement										

A small pre-test deformation cycle was applied about 20 hours before the main test to verify that the instruments were working correctly. The specimen was loaded axially up to 80 kips, and lateral loading was cycled at ± 0.1 in. (0.2% drift). No cracks were detected during these pre-test cycles.

Next, the specimen was subjected to the loading described in Table 5.1. Photographs of the specimen at key drift ratios are shown in Figure 5.1 and Figure 5.2. Up to a drift ratio of 0.7%, only hairline cracks were detected, mostly at the column base and some near the top of the shaft, and all cracks closed between cycles. Most cracks were oriented horizontally and concentrated on the north and south faces. At 0.7% drift (Cycle 2-2), the longitudinal steel in the column yielded (Section 5.5.1); cracks remained small (< 0.15 mm), and residual cracks closed.

After the column longitudinal steel yielded, cracks started appearing and growing at the column–shaft interface. Circumferential cracks appeared at the column–shaft construction joint (i.e., the joint split open to create a small vertical gap), and radial cracks grew outward from the column–shaft joint to the shaft edge. Horizontal cracks in the shaft and column grew at the base of the column. By 1.8% drift (Cycle 5-3), the column–shaft interface joint had opened up to 2.0 mm at peak loading, and vertical cracks had propagated from the interface radial cracks down to mid-height of the shaft, with a maximum crack width of 0.7 mm at the top of the shaft. On the column, horizontal cracks from the north and south faces extended to become diagonal cracks on the east and west faces.

From 1.8% to 3.6% drift, the maximum crack width grew to 3.0 mm, which occurred at the shaft–column interface. Surface spalling at the base of the column appeared at 2.6% drift (Cycle 6-3), and surface spalling at the interface appeared at 3.6% drift (Cycle 7-3). The shaft transverse reinforcement at the top of the shaft yielded at 3.6% drift (Cycle 7-2).

At 5.2% drift (Cycle 8-3), the largest interface radial crack (along the top of the shaft) measured 0.5 in. (12.7 mm) wide. Existing spalls grew in width and slightly in depth so that one small portion of the shaft transverse reinforcement was exposed. The spalling had not yet exposed the inside face of the transverse reinforcement or any of the longitudinal reinforcement.

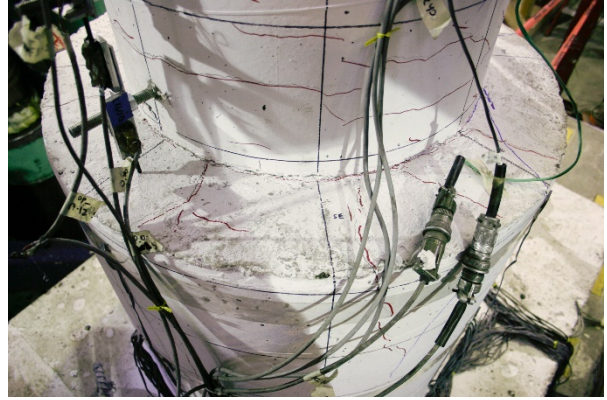
In the later sets from 5.2% drift to 8.7% drift, the column started rocking inside the connection, and the shaft noticeably started prying open, with vertical cracks widening significantly and the shaft face visibly angled outwards. Quiet creaking sounds were heard starting at 5.2% drift (Cycle 8-3). From 5.2% drift to 7.3% drift (Cycle 9-3), multiple radial cracks at the interface grew to be about 0.5 in. (12.7 mm) wide and remained as such through the full cycles, including the instant of zero load. These radial cracks propagated down the height of the shaft with a width greater than 2.0 mm until about mid-height of the shaft. Spalls grew much quicker than they had in previous sets; still, no additional shaft steel became visible. No loud or popping sounds were heard, but strain gauge readings near the top of shaft skyrocketed at 7.3% drift, so it is assumed that the shaft transverse reinforcement fractured. This interpretation could not be verified visually at this drift level as most of the concrete cover, while cracked, was still intact and obscured the shaft reinforcement from view.

Figure 5.3 and Figure 5.4 show photographs of the specimen after testing concluded. In the final cycle (Cycle 10-3), as the specimen was deformed up to 10.5% drift, the shaft quickly opened up, and a few small popping sounds were heard. Large pieces of concrete at the top of the shaft started falling off, and there was an annular gap about 4 in. wide at the column–shaft interface, separating the CIP column core from the CIP shaft shell; see Figure 5.4(b). A researcher was able to stick a measuring tape down 12 in. into this gap; see Figure 5.4(a). The shaft very clearly inclined outwards while the column remained intact, indicating a prying failure in the connection region. The shaft reinforcement was clearly visible at multiple locations, the concrete cover having fallen off around most of the shaft. The shaft transverse reinforcement mainly fractured along one vertical line: the majority of the fractures occurred near the southeast face and extended from the top of shaft down 22.25 in., or 86% of the column longitudinal bar embedment depth; see Figure 5.3(d). One other fracture occurred in the uppermost turn of spiral near the southwest face.

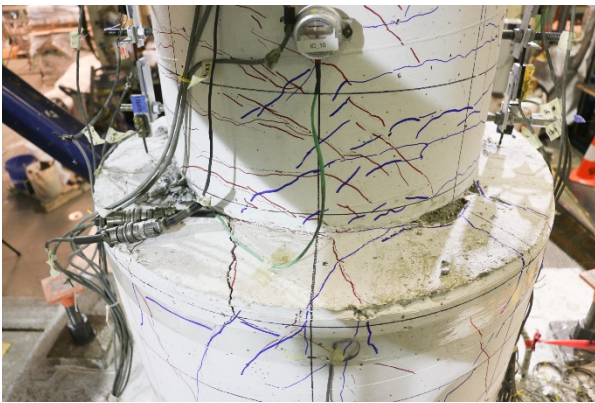
Researchers later tried to separate the column from the rest of the specimen (as was possible for Specimen DS-2) by lifting the specimen by the column only, subjecting the connection to the self-weight of the specimen base, but the specimen remained in one piece.



(a)



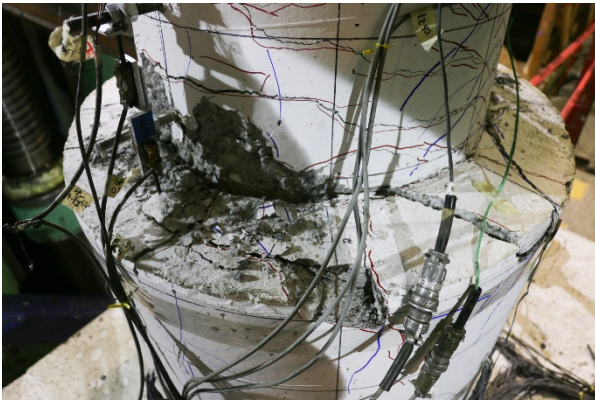
(b)



(c)



(d)

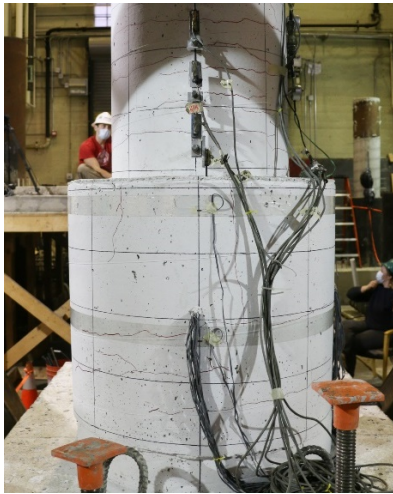


(e)

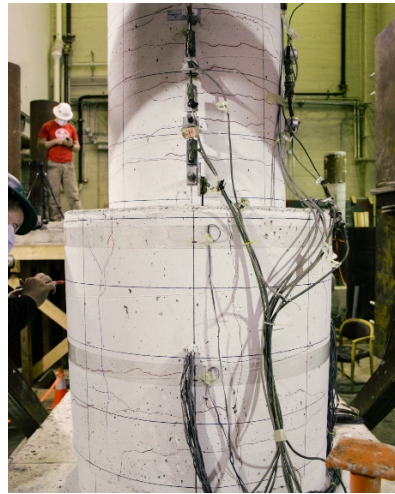


(f)

Figure 5.1 Photographs of damage progression at column–shaft interface (overhead view): (a) 1.0% drift (NW view); (b) 1.8% drift (SE view); (c) 3.6% drift (E view); (d) 5.2% drift (SW view); (e) 7.3% drift (SE view); and (f) 10.5% drift (NE view).



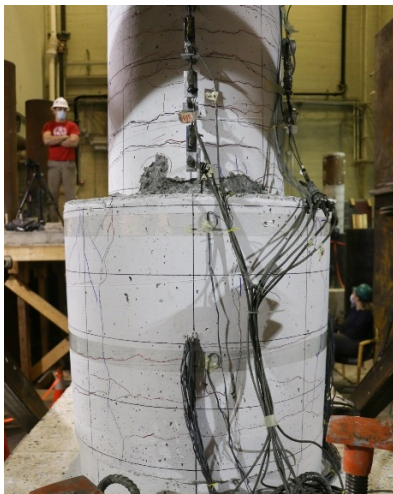
(a)



(b)



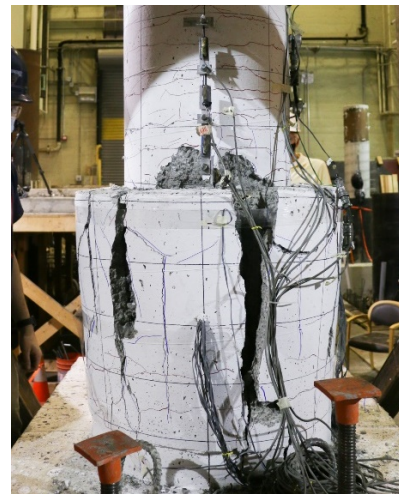
(c)



(d)



(e)



(f)

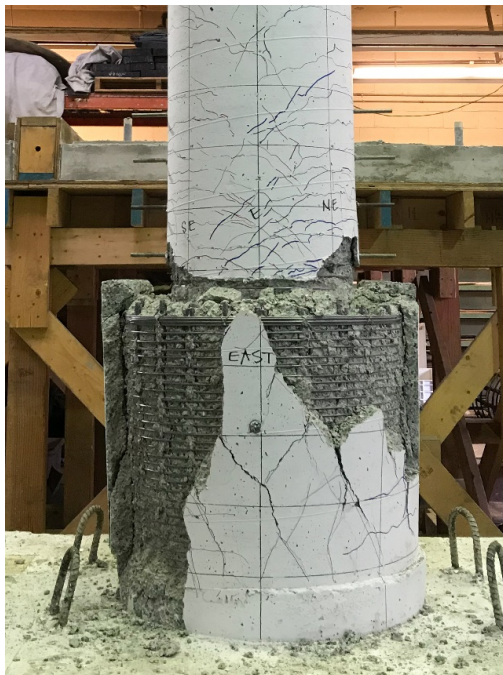
Figure 5.2 Photographs of damage progression in transition region (south view): (a) 1.0% drift; (b) 1.8% drift; (c) 3.6% drift; (d) 5.2% drift; (e) 7.3% drift; and (f) 10.5% drift.



(a)



(b)



(c)



(d)

Figure 5.3 Photographs of specimen at end of test: (a) north view; (b) south view; (c) east view; and (d) transverse reinforcement fractured down to the level of the pencil (height of shaft = 30 in.)



(a)



(b)



(c)

Figure 5.4 Photographs of interface at end of test: (a) north face; (b) south face; and (c) west face.

5.3 GLOBAL MEASURED RESPONSE

The applied force and resulting displacements are reported in this section. These values were then used to calculate the moment-drift response. In each subsection, the methodology for obtaining the response is first described; then, the response is presented and discussed.

5.3.1 Force-Displacement Response

The measured lateral force-displacement response of the specimen is shown in Figure 5.5 (“MTS Force”). The lateral force attributable to the specimen was calculated as the measured load from the MTS actuator load cell minus the friction force from the axial bearing assembly at the top of the column; see Equation (5.1).

$$F_{applied} = V - F_{fric} \quad (5.1)$$

where $F_{applied}$ is the applied lateral load; V is the measured force from MTS actuator load cell; and F_{fric} is the friction force from axial bearing assembly.

The friction force F_{fric} was calculated using a force-displacement relation developed by Brown [2008]. Friction was modeled as a bilinear spring with stiffness k and maximum friction

force F_{max} as defined in Equation (5.2). In this case, k was assumed to be 60 kip/in. and the effective coefficient of friction $\mu_{eff} = 0.016$. Analysis of the initial stiffness of the specimen and the typical coefficient of friction of the various materials acting in parallel confirmed, respectively, that the assumed values of k and μ_{eff} are reasonable.

$$F_{max} = \mu_{eff}P \quad (5.2)$$

where μ_{eff} is the effective coefficient of friction (calculated based on friction properties of individual contact surfaces—see next paragraph), assumed to be 0.016 in this case, and P is the axial load.

The contact surfaces and various materials of the bearing assembly included: the top of bearing (greased dimpled MSM pad) on stainless steel in channel web; the top curved piece of bearing on bottom curved piece of bearing (stainless steel on greased dimpled MSM pad); and the strip of greased dimpled PTFE on stainless steel (per side, for two sides). The first two contact surfaces were the main sliding surfaces. The E–W contact force between the components of the guide system was indeterminate but was expected to be a small fraction of the applied horizontal load, and the resulting N–S friction was expected to be approximately 2% of that. Consequently, that friction was ignored, and the effective coefficient of friction during the experimental test was approximated as:

$$\mu_{eff} = \mu \left(1 + \frac{R}{h} \right) \quad (5.3)$$

where μ is the coefficient of friction between stainless steel and greased dimpled PTFE or MSM pad; R is the radius of spherical surface of the bearing; and h is the height from the column–shaft interface to the spherical bearing.

The top displacement was measured by the string potentiometer at the elevation of the applied load. This measurement from the string potentiometer was verified against measurements from an LVDT in the MTS actuator and another string potentiometer attached to the testing rig at the same height. All measurements across the different instruments at this height were consistent.

The corrected specimen force-displacement response after accounting for friction is shown in Figure 5.5 (“Applied Force”). The outlier force peaks at -5.0 in. and +6.4 in. displacement in Figure 5.5 were attributed to the test apparatus. The outlier peaks can be explained by the incidence of two pieces of the axial bearing assembly coming into contact under large rotations, as described in Section 4.1. The measured lateral load increased as the test system gained stiffness from the pieces in contact, but this load was distributed to both the bearing assembly and the specimen. This similar increase in lateral load can also be seen slightly in two of the negative cycles prior to the -5.0 in. displacement cycle and the final negative displacement cycle. Therefore, these peaks will be neglected in the data interpretation, and it is assumed that the specimen continued to deteriorate in strength and stiffness at these large displacements.

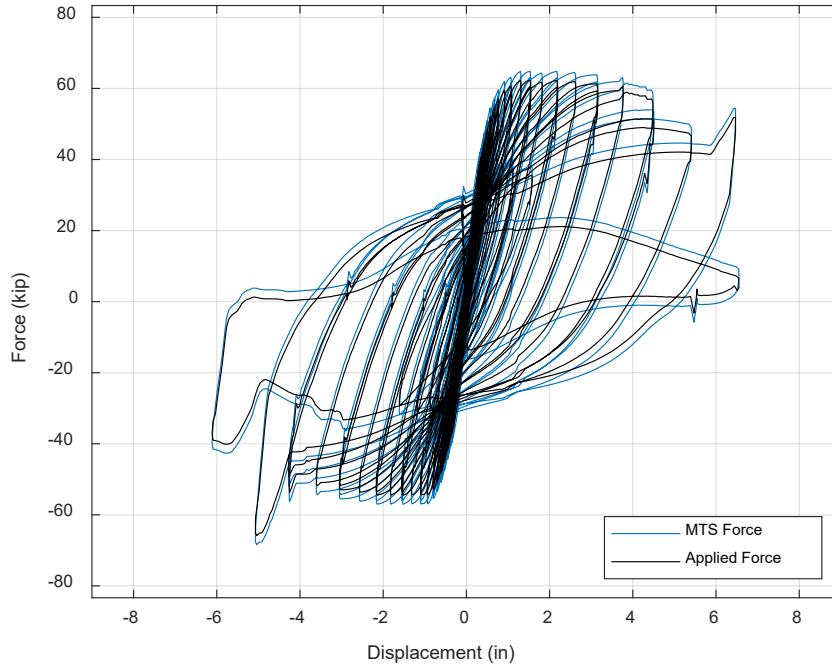


Figure 5.5 Lateral force-displacement response (before and after accounting for friction).

5.3.2 Moment-Drift Response

The moment-drift response of the specimen is shown in Figure 5.7. The moment is defined as the base moment experienced at the column–shaft interface. It is given by Equation (5.4),

$$M = Vh_1 - F_{fric}h_2 + P(\Delta_2 - \Delta_3) \quad (5.4)$$

where (as shown in Figure 5.6) M is the base moment at the column–shaft interface; h_1 is the height from the column–shaft interface to the line of action of the lateral load (60 in.); h_2 is the height from the interface to the top of column where the axial load P is applied (72 in.); Δ_2 is the inferred lateral displacement at the top of column; and Δ_3 is the measured lateral displacement at the column–shaft interface.

Because the value of Δ_2 was not measured, it was approximated by assuming that the column rotated as a rigid body about its base. Therefore,

$$(\Delta_2 - \Delta_3) \approx (\Delta_1 - \Delta_3) \frac{h_2}{h_1} \quad (5.5)$$

where Δ_1 is the lateral displacement at the location of the lateral load, and

$$M = Vh_1 - F_{fric}h_2 + P(\Delta_1 - \Delta_3) \frac{h_2}{h_1} \quad (5.6)$$

The calculated moment-drift response history of the specimen is shown in Figure 5.7, which shows that the peak moment was 4250 kip*in. at 6.3% drift (disregarding the false peaks, see Section 5.3.1). This is 96% of the expected column moment capacity of 4433 kip*in., calculated using the specimen material properties described in Chapter 3. The process to calculate the expected moment is described in Appendix G.

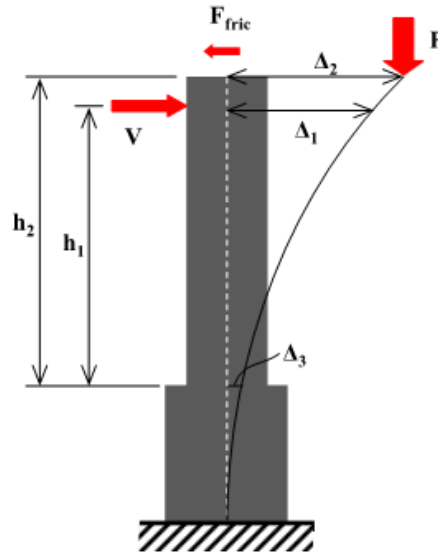


Figure 5.6 Definitions of variables to calculate base moment [Equations (5.4) through (5.6)] [Tran 2015].

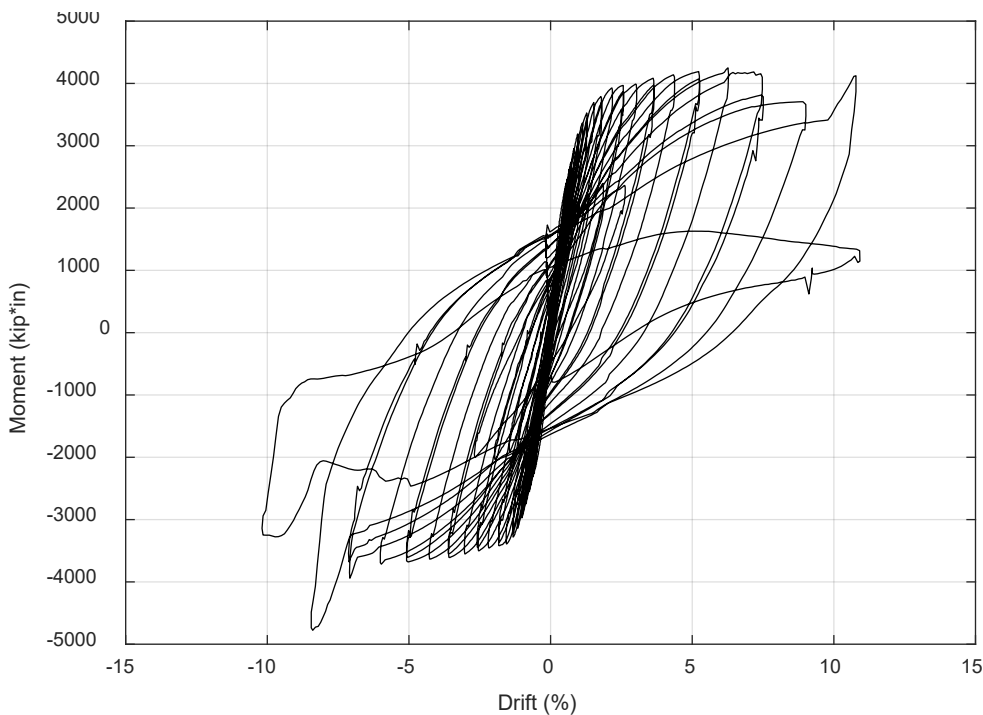


Figure 5.7 Moment-drift response.

5.4 DEFORMATION PROFILES

External deformations were measured by string potentiometers, Duncan potentiometers, inclinometers, and an Optotrak Certus motion capture system, described in Chapter 4. The potentiometers measured displacement, the inclinometers measured absolute rotation, and the Optotrak measured position. From this data, the displacement, rotation, and average curvature of the specimen were calculated.

5.4.1 Displacement Profiles

Specimen displacements were measured by string potentiometers and calculated from the Optotrak position data. The calculated displacement from the Optotrak data was verified against measured displacement from string potentiometers at similar elevations on the shaft; all displacements matched between the two systems. Figure 5.8 shows the specimen displacement vs. height at the peaks and valleys of select cycles, from both sets of instruments. In this figure, the height $y = 0$ refers to the column–shaft interface.

As expected, the displacement over the height of the column steadily increased with an increasing drift ratio. Instruments on the shaft indicated small shaft displacements in most cycles and then up to nearly 2 in. of displacement for the -10.2% drift cycle. This measurement was consistent across all shaft instruments and between the two systems (Optotrak and string potentiometers). This sudden increase in magnitude is consistent with the damage progression described in Section 5.2 in which the shaft quickly pried open between 7.3% and 10.5% drift.

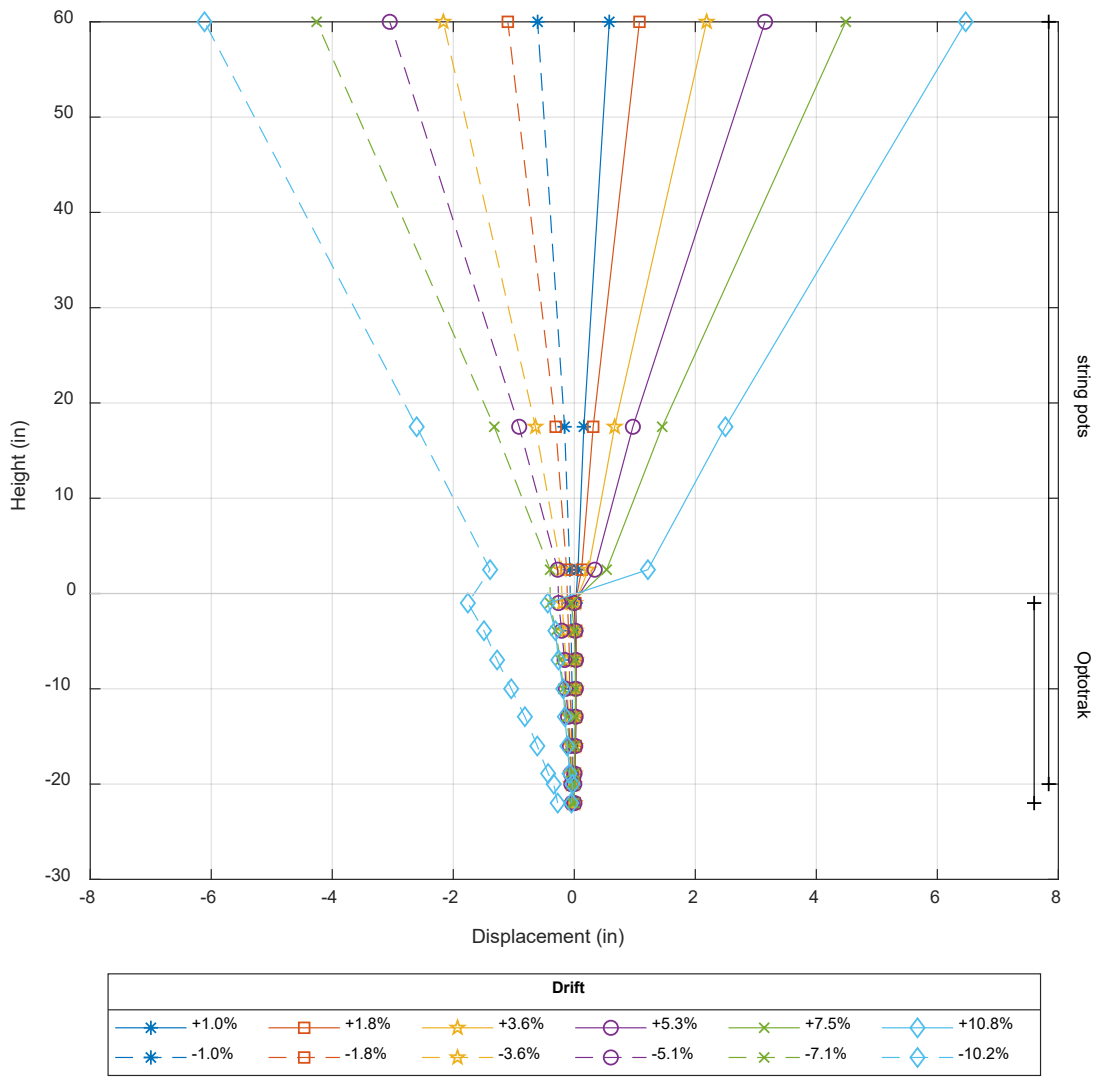


Figure 5.8 Displacement profiles.

5.4.2 Rotation Profiles

Absolute rotations were directly measured from inclinometers, and relative rotations were computed from the Optotrak and Duncan potentiometer measurements; see Figure 5.9. These instruments were closely spaced on the shaft and at the base of the column. They were further spaced in the upper part of the column where rotations and curvatures were not expected to change as quickly. In this subsection, the methodology for obtaining the response is first described; then, the response is presented and discussed.

Near the base of the column, the relative rotations were calculated using the measurements of the vertical Duncan potentiometers. Around 14 in. above the column–shaft interface, there was both an inclinometer and a set of Duncan potentiometers to ensure that measurements from the two systems could be verified against one another. Rotations were calculated from the Duncan potentiometers by determining the deformation of the initially horizontal plane formed by two instruments at the same height. For example, at each height of measurement at the column base, there was one potentiometer on the north side and another on the south side. The displacement measurements from both potentiometers were used in Equation (5.7) to determine a single relative rotation value at that height interval. Because the potentiometers were placed between rods and measured displacement relative to each rod, these rotations are relative rotations.

$$\Delta\theta = \frac{\Delta_{v,N} - \Delta_{v,S}}{B} \quad (5.7)$$

where $\Delta\theta$ is the relative rotation at a given height; $\Delta_{v,N}$ is the vertical displacement on the north side of specimen; $\Delta_{v,S}$ is the vertical displacement on the south side of specimen; and B is the horizontal distance between the two Δ_v measurement locations.

The rotations of the shaft were calculated similarly using vertical positions of the Optotrak markers. The displacements of each marker were first found, and then the rotation of each plane was calculated. These relative rotations $\Delta\theta$ could then be summed to determine the absolute rotation at each measurement location.

Figure 5.9 shows the specimen rotation vs. height at select cycles. The rotations near the base of the column are not plotted for drifts greater than 3.6% because the bottommost Duncan potentiometers, which heavily impact the rotation calculation, reached their maximum stroke at these drifts. The profiles show that rotation steadily increased with increasing drift. Towards the top of the column, from 20 to 60 in. above the column–shaft interface, the rotations were nearly constant, which was expected since the moment in this region was small. This observation also indicates that the largest portion of the column deformation was due to rigid-body rotation about the base of the column.

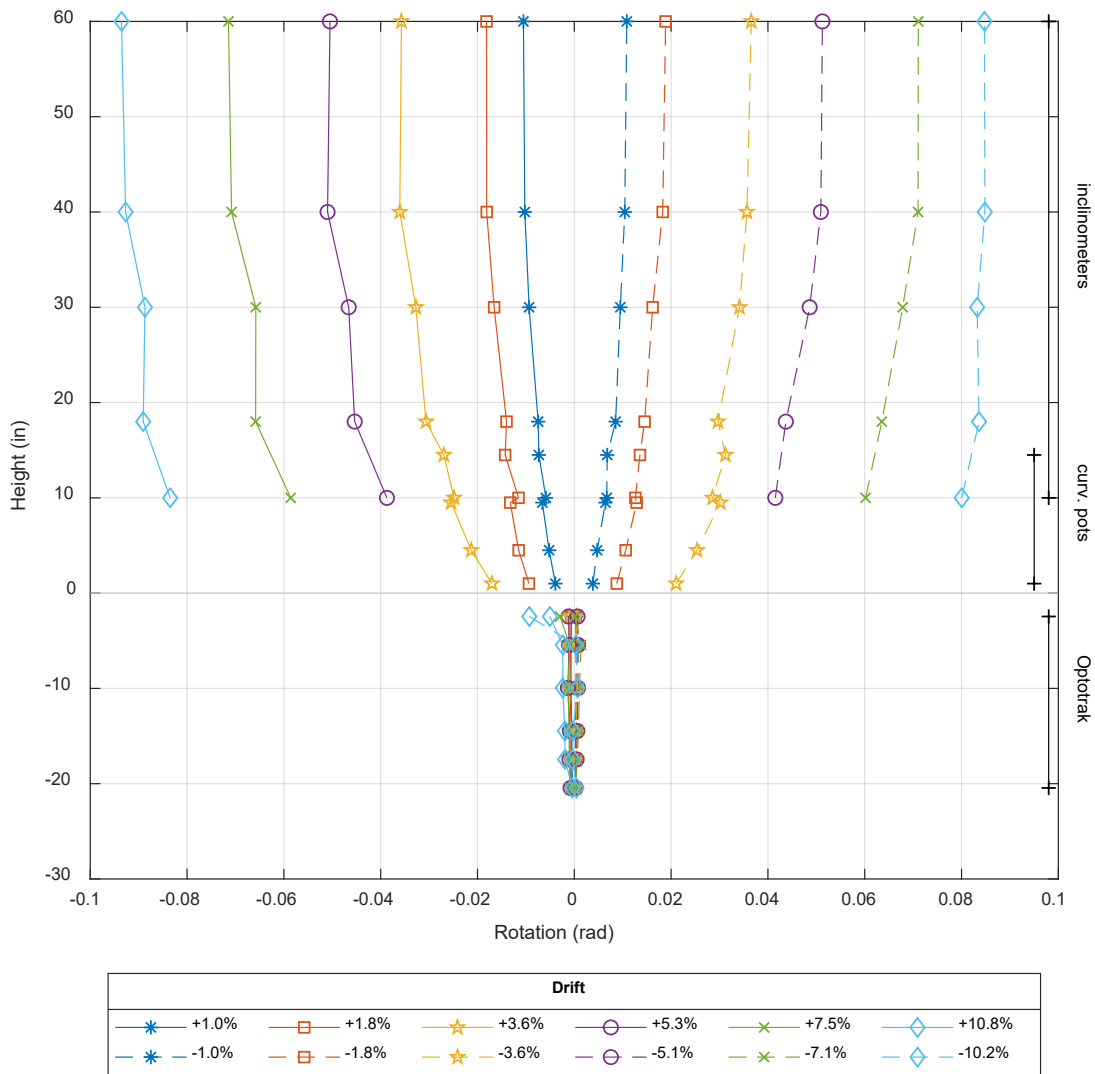


Figure 5.9 Rotation profiles

5.4.3 Curvature Profiles

Average curvatures were computed using the relative rotation results described in Section 5.4.2. Since each curvature measurement represents the average curvature along the segment between two instruments, it is plotted at the midpoint of the segment. The equation is given as:

$$\phi = \frac{\Delta\theta}{\Delta h} \quad (5.8)$$

where ϕ is the average curvature; Δh is the height of the segment (i.e., the vertical distance between the two instrument locations); and $\Delta\theta$ is the relative rotation. For Duncan pot. measurements, this was already calculated per Equation (5.7). For inclinometer data, this is taken as $\Delta\theta = \theta_2 - \theta_1$,

where θ_2 is the rotation from an inclinometer at the top of the segment, and θ_1 is the rotation at the bottom of the segment.

Figure 5.10 shows the average column curvature vs. height at select cycles, combining results from the inclinometer, curvature Duncan potentiometers, and Optotrak data. As expected, the curvatures were smallest within the shaft region, largest at the base of the column, and increased with increasing drift ratios.

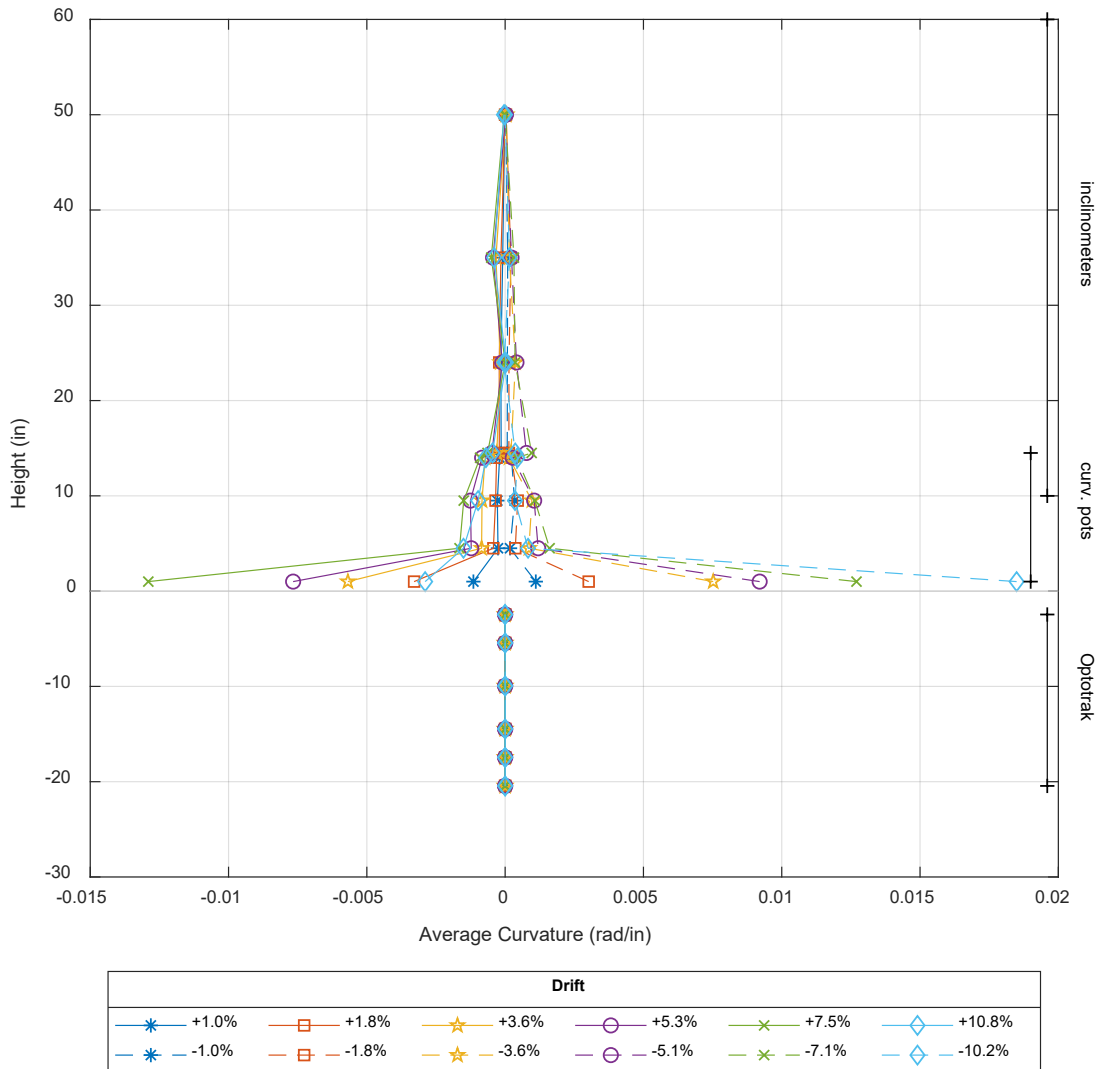


Figure 5.10 Curvature profiles.

5.4.4 Contributions to Total Displacement

The horizontal displacement at the point of load application was broken down into individual contributions from five types of deformations (illustrated in Figure 5.11):

- Shaft bending deformations

- Shaft shear deformations, i.e., pure sliding without rotation
- Column base rotations, i.e., rigid body rotation of the column
- Column bending deformations
- Column shear deformations (expected to be small)

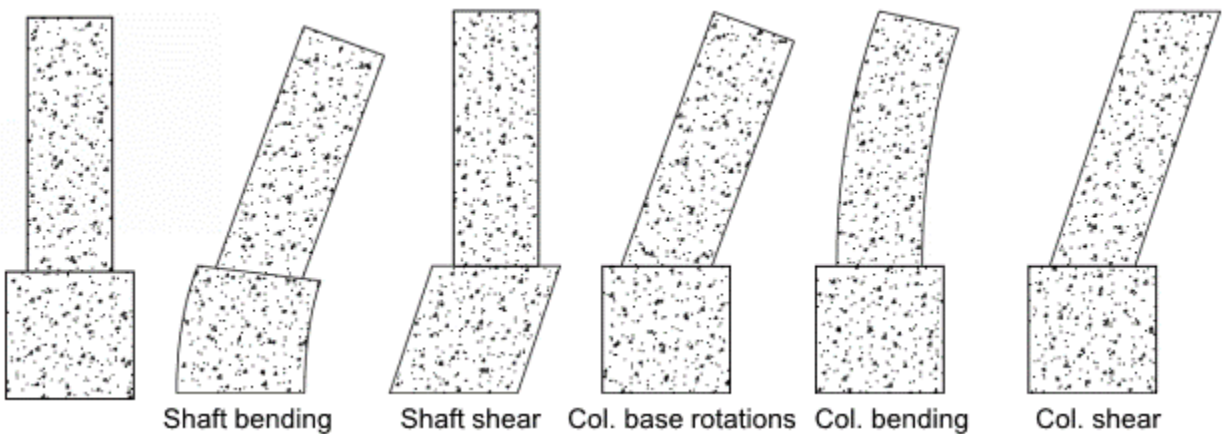


Figure 5.11 Types of deformation [Tran 2015].

This breakdown of contributions assumes that the column and shaft do not split or pry open; this assumption conflicts with the prying action observed during the experimental test; see Section 5.2. However, for comparison with experimental results from other column–shaft connection tests, the prying effect was neglected here.

The contributions were calculated as follows: using the curvature profiles in Figure 5.10 and the Second Moment-Area Theorem, the displacement at the height of loading due to bending deformation of the column (contribution no. 4) was calculated. The displacement due to bending deformation of the shaft (1) was calculated similarly, but at both the height of loading and the top of the shaft. The remainder of shaft displacement at the top of the shaft was attributed to shaft shear deformation (2), and this displacement contribution was assumed to be constant from the column–shaft interface up to the height of loading.

Next, the displacement due to base rotation (3) was found using the calculated rotations at the base of the column (which were previously described and illustrated in Section 5.4.2). Knowing the base rotation and vertical distance from the base to the point of loading, the displacement due to column base rotation was calculated. Finally, the remainder of measured deformations at the point of loading are attributed to column shear deformation and calculation error. The results of this assessment are shown in Figure 5.12. Only results up to 3.6% drift are plotted because the bottommost Duncan potentiometers on the column, which indicated base rotation, reached their maximum stroke at greater drifts.

As shown in Figure 5.12, there was some calculation error in determining the displacement contributions: the individual contributions occasionally sum up to greater than 100%.

Nevertheless, it can be concluded that most of the deformation at the top of the column was due to base rotation and column bending. The contribution from column bending and shaft shear stay relatively constant up to 3.6% drift, whereas the contribution from base rotation increases with increasing drift.

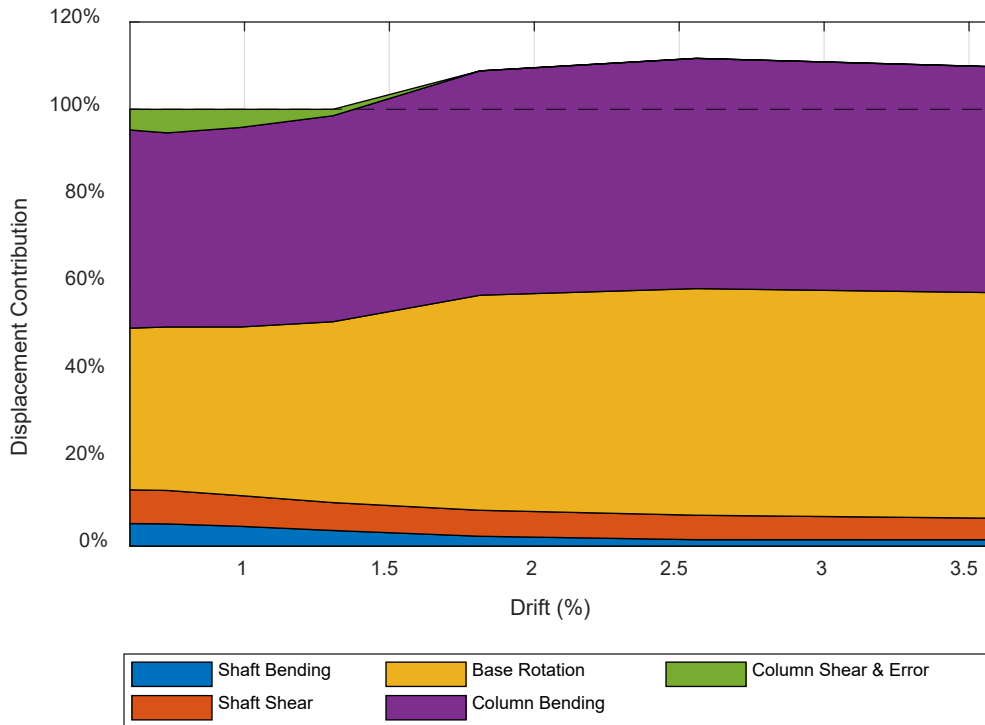


Figure 5.12 Contributions of mechanisms to total displacement.

5.5 STRAIN PROFILES

Strains were measured with strain gauges on both the column and shaft longitudinal reinforcement as well as the transverse reinforcement in the shaft. Concrete surface strains were also determined from two homemade circumferential extensometers and Optotrak position data. These strains were compared with measured crack widths in the shaft.

The following subsections present strain profile envelopes for each type of reinforcement. The strain envelopes for each gauge were determined as follows (and illustrated in Figure 5.13):

1. For each cycle, the data was divided into data recorded during negative drifts and data recorded during positive drifts.
2. For the data from each negative-drift half cycle, the largest-magnitude strain was found. For the first cycle, this strain was recorded as an envelope starting value.
3. Repeat Step 2 for the data from each positive-drift half cycle.

- If the strains from Steps 2 and 3 for a particular half cycle surpassed the previous envelope values, then those newfound strain points were added to envelope values as identified by circles in Figure 5.13. The data points at which strains reached their peak magnitude during each half cycle generally corresponded with the times when peak/valley drifts were reached; see Figure 5.14.

Both negative-drift and positive-drift envelopes were found for each strain gauge. Each unique envelope could then be classified by three identifiers: drift direction (north/south), strain gauge location (north/south/east), and strain gauge elevation (with $y = 0$ as the column–shaft interface). Alternatively, the strain gauge data at a given drift can be defined in terms of strains on the tensile vs. compressive faces. This categorization allows strain readings from different gauges on the tensile and compressive faces to be compared more easily than by only comparing north-face and south-face gauges.

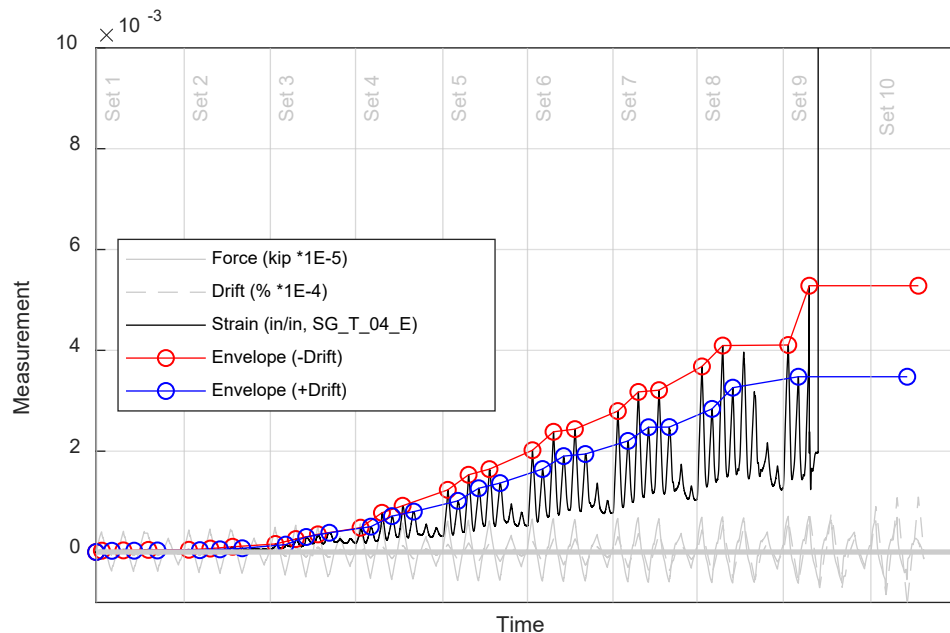


Figure 5.13 Determining strain envelopes: transverse strain vs. frame for the strain gauge on shaft transverse reinforcement at $y = -4$, close to the east face of the specimen (SG_T_04_E).

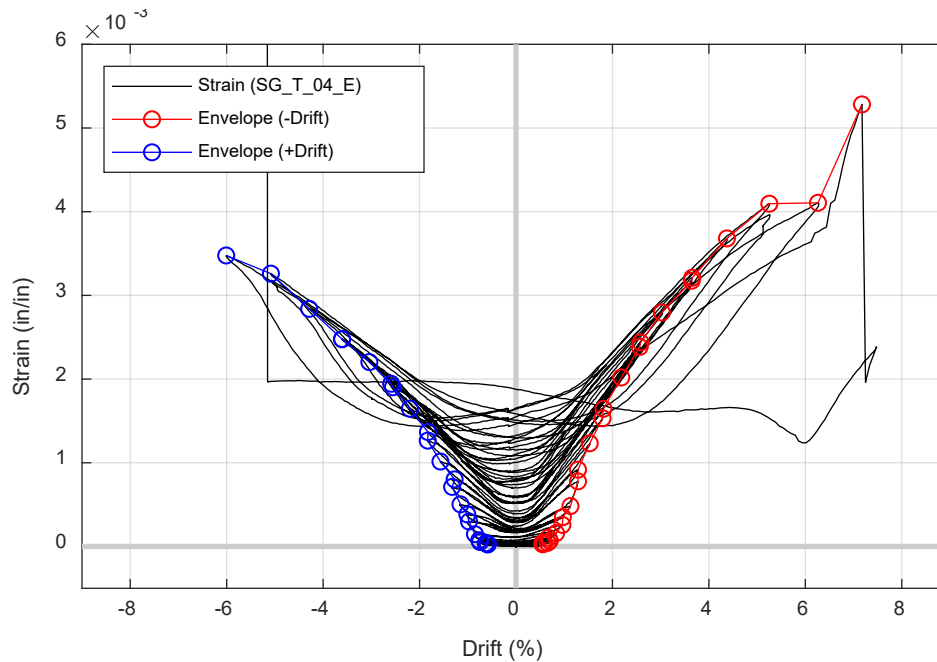


Figure 5.14 Determining strain envelopes: transverse strain vs. drift for the same strain gauge as in Figure 5.13.

In the strain profile envelopes in the following subsections, the color of a curve indicates the drift direction (negative in red, positive in blue, and an averaged envelope between both directions in purple). The curve's line style indicates whether that face was in tension or compression (tension or neutral is solid, compression is dashed). This can also be determined from the names of the curves: the first letter indicates the strain gauge location (N/S/E), and the second letter indicates whether that face was tensioned or compressed (T/C). For example,

- ‘-NT’ represents enveloped strain data from the north-side strain gauges when the north face was in tension. For each cycle, this occurred when the drift was positive.
- ‘-NC’ represents enveloped strain data from the north-side strain gauges when the north face was in compression. For each cycle, this occurred when the drift was negative.
- ‘-ST’ represents enveloped strain data from the south-side strain gauges when the south face was in tension. For each cycle, this occurred when the drift was negative.
- ‘-SC’ represents enveloped strain data from the south-side strain gauges when the south face was in compression. For each cycle, this occurred when the drift was positive.
- ‘-E’ represents the enveloped strain data from the east-side strain gauges, averaged between the positive-drift envelope and negative-drift envelope.

Strain profiles were plotted at four key drift ratios (1.0%, 1.8%, 3.6%, and 5.2%). Note that some of these key drifts did not align exactly with the envelope values (circled in Figure 5.14), so linear interpolation was used to determine the plotted value in the strain profile at any given drift ratio. Thus, the points on the strain profiles do not represent instantaneous strain measurements at the described drift ratio, but rather are interpolated values. The instantaneous strain profiles can be found in Appendix F.

The following subsections summarize the strains in the column longitudinal bars, shaft longitudinal bars, and shaft transverse reinforcement. All three types of reinforcement strains will first be described in writing, and then all strain profiles will be presented in unison after Section 5.5.3.

5.5.1 Strains in Column Longitudinal Bars

Figure 5.15 shows the axial strain distributions of the column longitudinal bars over the depth of the transition region. The bars extended from the column down to 26 in. below the column–shaft interface; the strain gauges were distributed from the height of the interface down to 23 in. below the interface. Each plot in Figure 5.15 corresponds to a specific level of drift and includes enveloped strain data from all functioning column strain gauges in the transition region.

As expected, the profiles show that the maximum column bar strain in the transition region generally occurred at the column–shaft interface. The strains decreased with increasing depth, reaching a value of nearly zero at $y = -23$ in. This indicates that sufficient anchorage was provided through development length, so the addition of mechanical anchorages (e.g., anchor heads) would not have affected the results.

The measured strain between corresponding gauges (e.g., NT and ST; NC and SC) were similar. Compressive strains (NC, SC) were smaller than tensile strains (NT, ST) at all drift ratios. The strains measured on the east face (E) tended to have values between the maximum tensile and compressive strains. First yield in tension occurred at 0.75% drift. Strains at drifts higher than 5.2% were recorded, but some strain gauges reached their maximum strain limit at that point, so only the strains up to 5.2% drift are plotted here.

5.5.2 Strains in Shaft Longitudinal Bars

Figure 5.16 shows the axial strain distributions of the shaft longitudinal bars over the height of the shaft. The bars extended from 0.75 in. below the column–shaft interface down past the transition region; the strain gauges were distributed from 4 in. to 28 in. below the column–shaft interface.

The maximum bar strains were recorded for the bottommost set of strain gauges. It is likely that this strain would have increased with increasing depth past the interface as the shaft moment increased. The strains at $y = -4$ in., the uppermost level of gauges, were nonzero, which indicates that bond stresses developed even above the top longitudinal bar strain gauge.

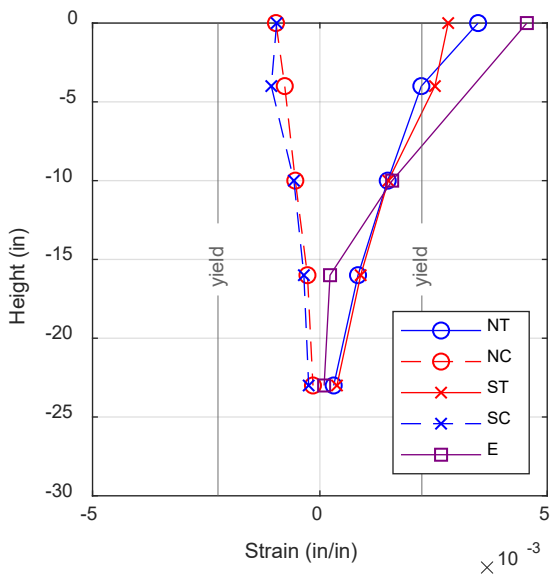
Strains between different gauges were consistent and generally remained small throughout the test. The shaft longitudinal bars first reached yield at 10.5% drift during the last set of testing. The strains measured during this last cycle are not shown in Figure 5.16.

5.5.3 Strains in Shaft Transverse Reinforcement

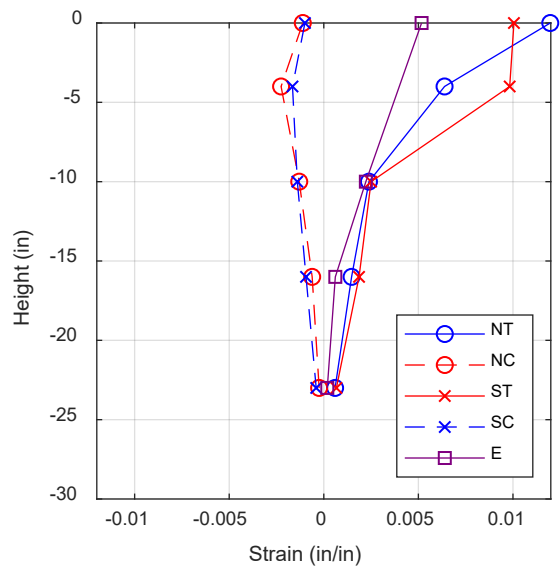
Figure 5.17 shows the hoop strain distributions of the shaft transverse reinforcement over the height of the shaft. The shaft wire spiral extended from about 1.5 in. below the column–shaft interface down past the transition region. At the top of shaft, the spiral was terminated with six full turns in a bundle. This was the scaled-down equivalent of the three turns typically required by AASHTO and other agencies: every two turns of shaft spiral in the specimen represented one turn of #6 spiral at full scale. The strain gauges were distributed from approximately 2 in. to 22 in. below the column–shaft interface. This corresponded with the 1st, 7th, 11th, 15th, 19th, 23rd, and 31st levels of spiral (considering the uppermost revolution in the termination bundle as the first level).

For drift ratios of 1.8%, 3.6%, and 5.2% (not 1.0%), the strains had a distribution that was approximately parabolic along the height of the shaft, with the maximum strain occurring at the top of the shaft. Strains on the compressed face were larger than those on the tensile face, with the east-face strains falling in between the tensile-face and compressive-face envelopes.

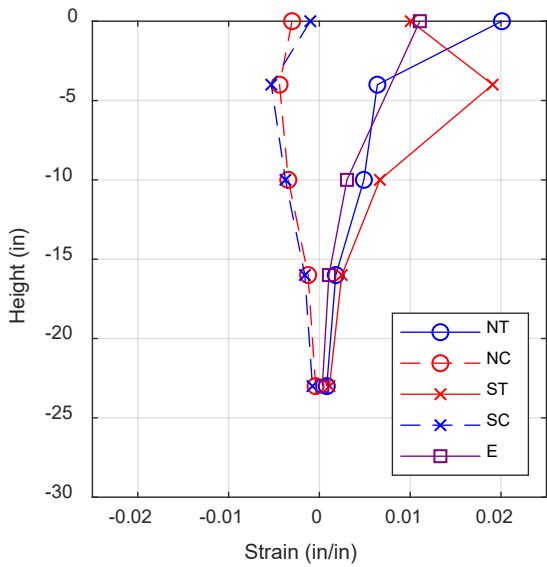
Strains between different gauges were consistent. At drift ratios above 1.0% drift, the ‘ST’ and ‘SC’ strain profiles show a reversal near the top of shaft: this uppermost south strain gauge was located very close to the cut end of the wire (Figure 5.18), so it likely slipped. First yielding of the wire occurred at 2.6% drift.



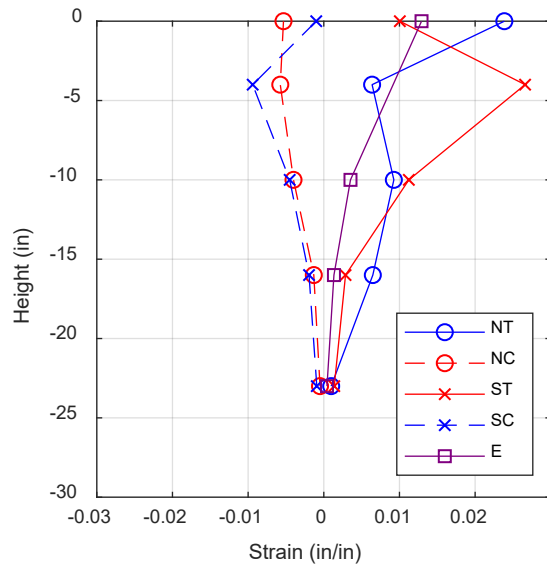
(a)



(b)

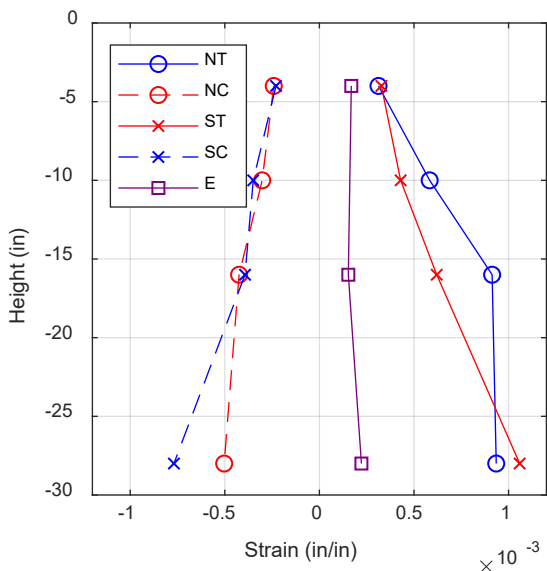


(c)

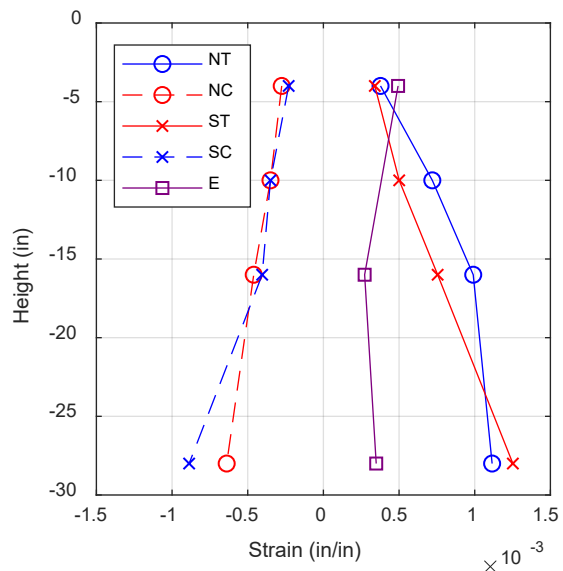


(d)

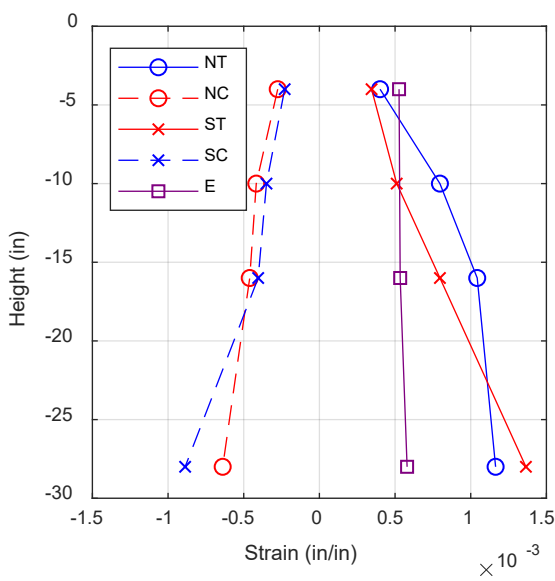
Figure 5.15 Column longitudinal bar strain profiles in transition region: (a) 1.0% drift; (b) 1.8% drift; (c) 3.6% drift; and (d) 5.2% drift. See Section 5.5 for the definition of the envelopes and NT/NC/ST/SC/E.



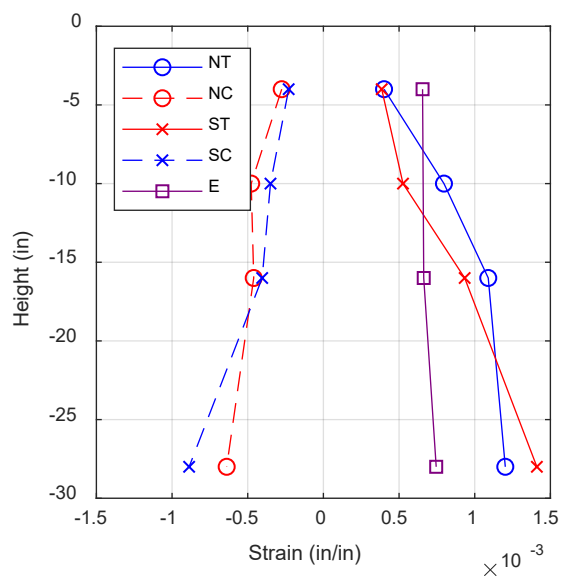
(a)



(b)

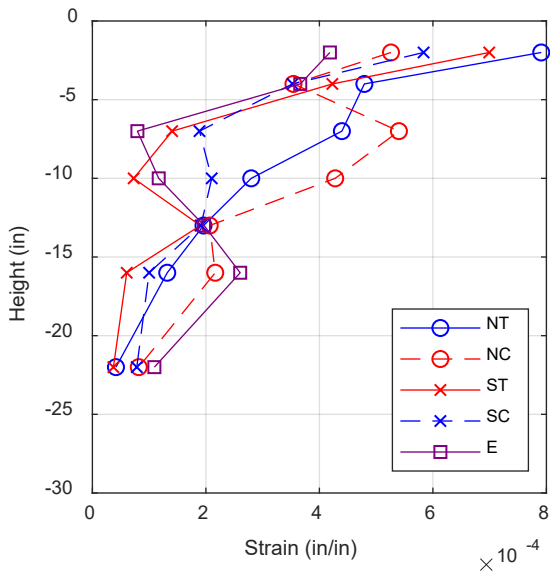


(c)

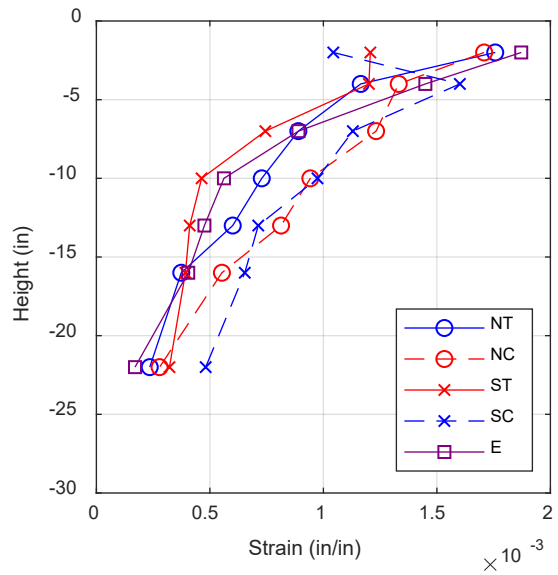


(d)

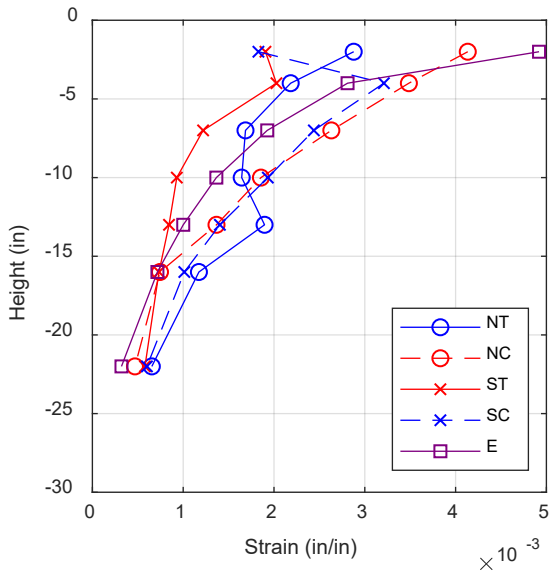
Figure 5.16 Shaft longitudinal bar strain profiles: (a) 1.0% drift; (b) 1.8% drift; (c) 3.6% drift; and (d) 5.2% drift. See Section 5.5 for the definition of the envelopes and NT/NC/ST/SC/E.



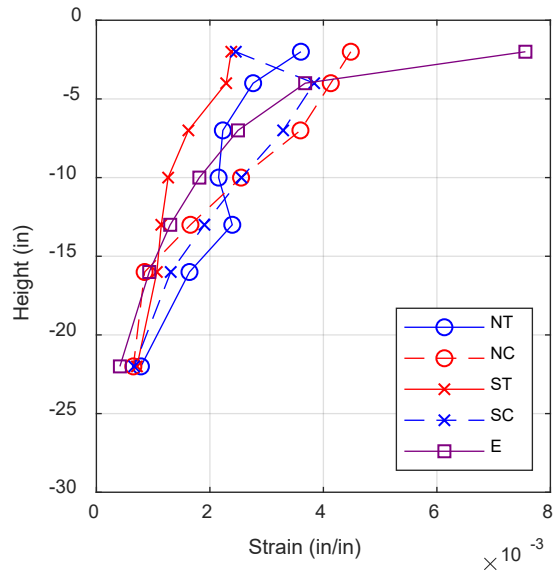
(a)



(b)



(c)



(d)

Figure 5.17 Shaft transverse wire enveloped strain profiles: (a) 1.0% drift; (b) 1.8% drift; (c) 3.6% drift; and (d) 5.2% drift. See Section 5.5 for the definition of the envelopes and NT/NC/ST/SC/E.



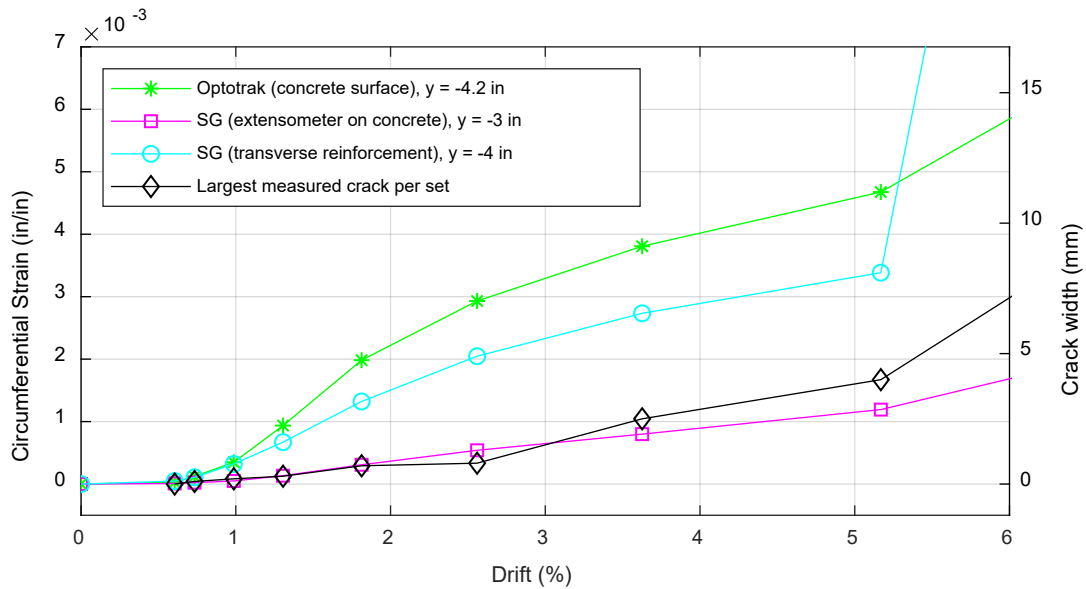
Figure 5.18 Overhead view of uppermost wire strain gauge on the south end of the shaft reinforcement cage (indicated by red arrow; photograph was taken mid-installation).

5.5.4 Circumferential Surface Strains in Shaft Concrete

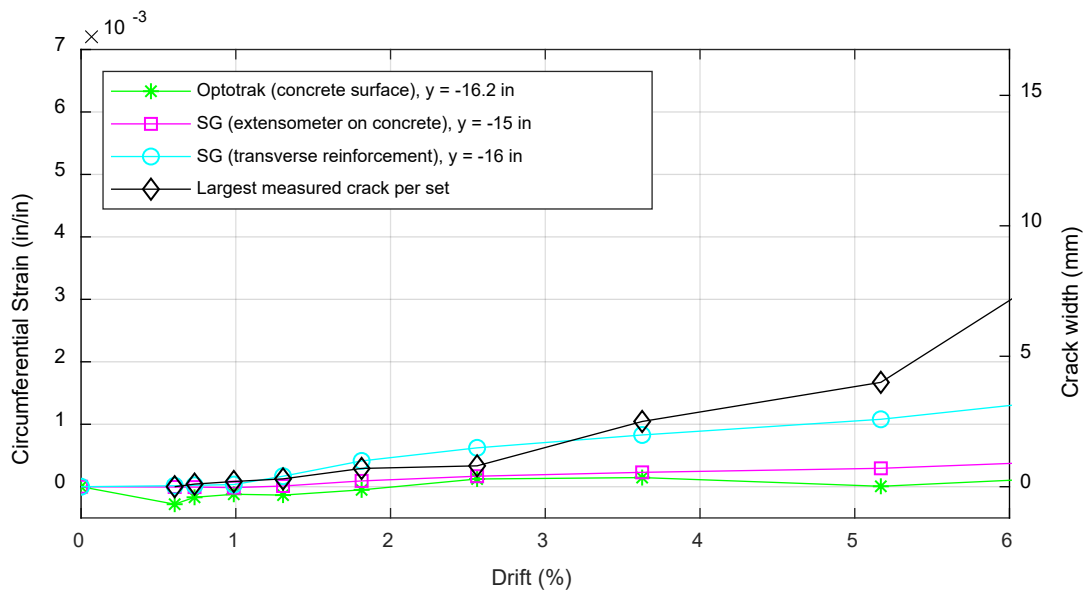
The average shaft hoop strains were calculated (a) using Optotrak position data (which was only obtained in the northwest quadrant of the shaft); (b) from strain gauge measurements on the homemade extensometers (made from tape, Section 4.2.3) and (c) from the average strains measured in the transverse reinforcement. These strains were compared with the strain inferred from the largest measured vertical crack in the shaft at each set of loading (which occurred at the top of the shaft). The strain envelopes for all four measures of circumferential expansion are shown in Figure 5.19.

- All four measures of average circumferential strain showed similar trends. The circumferential strains increased with increasing drift ratio, and the expansion was larger at the top of the shaft than at mid-height.
- At the top of the shaft, the calculated strains from the Optotrak and the average of those measured in the transverse reinforcement were similar. The strains at the concrete surface (Optotrak) were slightly larger than those in the embedded reinforcement, which is consistent with the observed wedge-shaped cracks. This is also consistent with the measured cracks shown in Figure 5.19: the total expected cracking can be calculated from the hoop strains, assuming the concrete cracked rather than elongated when strained (and vice versa as the crack widths can be converted to equivalent hoop strains). Therefore, the largest measured crack per set is a subset of the total expected cracks, and this curve is expected to fall below the strain curves.
- At the top of the shaft, the average strains from the homemade extensometer are much lower than those measured by the Optotrak or strain gauges. These strains were expected to be greater than those in the reinforcement and calculated from the measured cracks, and similar to those calculated from the Optotrak data; however, they were among the lowest strains found between all of the measurement methods. These unexpectedly low strains could be

explained by the components of the homemade extensometer: the strain gauge and glue may have significantly increased the local stiffness of the setup. Therefore, the strain gauges recorded lower local strains, and greater strains may have been experienced by the non-gauged parts of the extensometer (i.e., the tape-only parts). In the future, the researchers recommend using a stiffer tape, perhaps something with fibers in the longitudinal direction, for further iterations of the homemade extensometer.



(a)



(b)

Figure 5.19 Hoop strains at shaft surface and in transverse reinforcement: (a) strains at top of shaft ($y \approx -4$ in.); and (b) strains and height of shaft ($y \approx -15$ in.).

5.6 INFERRED AXIAL AND BOND STRESS PROFILES

The axial and bond stresses along each gauged column and shaft longitudinal bar were inferred from the strains reported in Section 5.5.1 and Section 5.5.2. The process to determine the stresses will first be described, and then the stress profiles will be presented.

5.6.1 Axial Stress-Strain Relation

The axial stress was determined using Raynor et al.'s [2002] stress-strain relation for reinforcing bar. The model consists of a monotonic envelope curve described in Equation (5.9). For this study, the stress-strain curve was assumed to be equal and opposite in either direction of loading. By using this monotonic curve and assuming identical relations in tension and compression, the calculated axial stress does not account for the reduction of bar cross-sectional area under tension (and the opposite under compression), nor any cyclic effects.

$$\sigma = \begin{cases} E\varepsilon, & \varepsilon \leq \varepsilon_y \\ \sigma_y + (\varepsilon - \varepsilon_y)E_y, & \varepsilon_y < \varepsilon \leq \varepsilon_{sh} \\ \sigma_u - (\sigma_u - \sigma_{sh}) \left(\frac{\varepsilon_u - \varepsilon}{\varepsilon_u - \varepsilon_{sh}} \right)^{C_1}, & \varepsilon_{sh} < \varepsilon \leq \varepsilon_u \end{cases} \quad (5.9)$$

where (as shown in Figure 5.20)

$$\varepsilon_y = \frac{\sigma_y}{E} \quad (5.10)$$

$$\sigma_{sh} = \sigma_y + (\varepsilon_{sh} - \varepsilon_y)E_y \quad (5.11)$$

and σ is the stress; ε is the total strain; E is the elastic modulus; σ_y and ε_y are the stress and strain at steel yield, respectively; E_y is the slope of the yield plateau; σ_{sh} and ε_{sh} are the stress and strain at onset of strain hardening, respectively; σ_u and ε_u are the ultimate (peak) stress and strain, respectively; and C_1 is the parameter that defines the curvature of the strain hardening curve, assumed to be 10 herein.

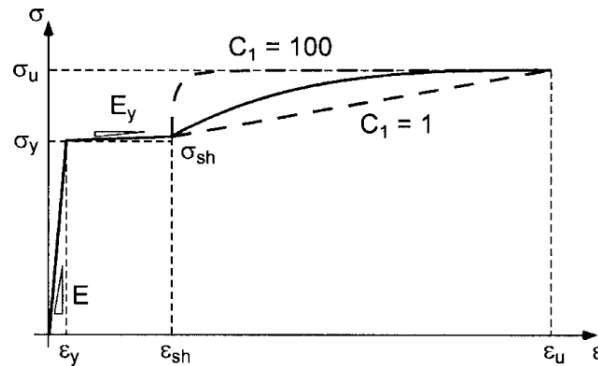


Figure 5.20 Raynor model for monotonic loading on reinforcing bar [Hoehler and Stanton 2006].

5.6.2 Experimental Bond Stress

The bond stresses were approximated using Equation (5.12), which is derived by equating the incremental axial force and the bond force over a segment of bar.

$$\tau = \frac{A}{p} * \frac{d\sigma}{dy} \quad (5.12)$$

where τ is the bond stress; A is the area of bar; p is the perimeter of bar[s] (i.e., the bar circumference for a single bar); and $\frac{d\sigma}{dy}$ is the rate of change in axial stress. For a single reinforcing bar, in which $A = \frac{\pi d_b^2}{4}$ and $p = \pi d_b$, this results in a bond stress of:

$$\tau = \frac{d_b}{4} * \frac{d\sigma}{dy} \quad (5.13)$$

where d_b is the diameter of the reinforcing bar.

Equation (5.13) gives the bond stress in terms of the local rate of change in axial stress. Because the axial stresses could only be inferred from the strain gauge readings at specific locations, Equation (5.13) was used to compute average bond stresses from the finite increments in axial stress. Furthermore, the bond stresses for the shaft bars were computed by scaling up both the area and perimeter of bars by three to reflect the specimen's bundled bars, which results in a bond calculation identical to that for a single bar; in practice, the true perimeter of a three-bar bundle in contact with concrete is less than $3 * \pi d_b$. This overestimation of contact perimeter leads to an underestimation of bond stress. Lastly, the equation assumes that the bond stress is uniform around the perimeter of the bar. While this is likely true for pullout of a bar that is loaded symmetrically, it is questionable for bars in flexure, which might be loaded through struts acting at different orientations on opposite sides of the bar.

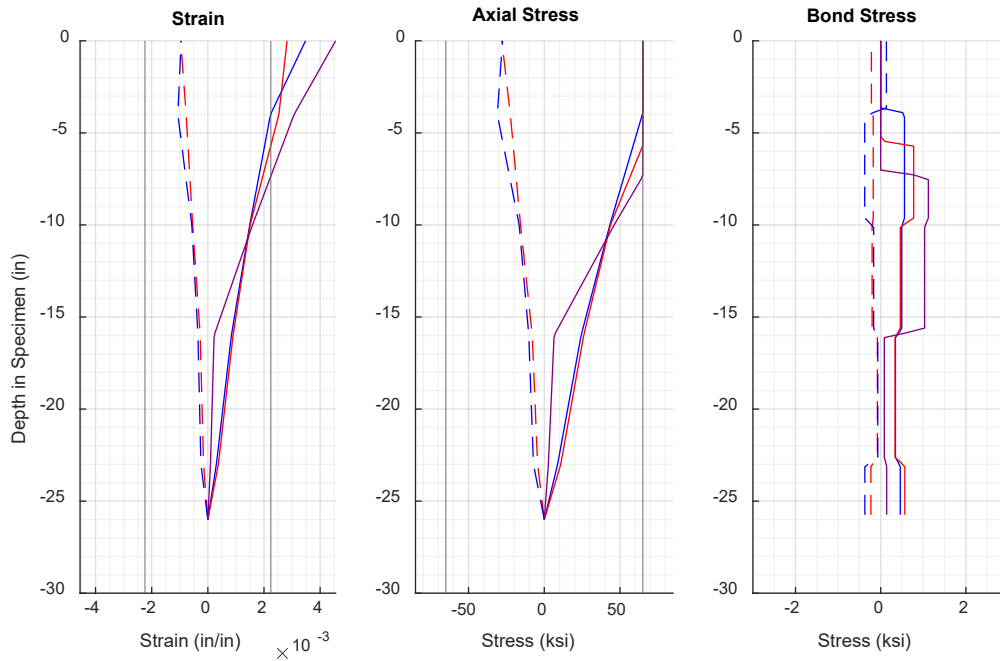
5.6.3 Inferred Axial and Bond Stress Profiles

The experimental axial and bond stress profiles are shown in Figure 5.21, Figure 5.22, and Figure 5.23. For each drift level, the profiles show one curve per loading direction (tension/compression) per gauged bar (north/south). Detailed definitions of the curves' nomenclature (NT/NC/ST/SC) are provided in Section 5.5. As expected, the inferred bond stress profiles tended to be noisy due to the process of derivation; post-yield values were also highly dependent on the axial stress–strain relation. Therefore, the experimental bond stress profiles were most accurate where the reinforcing bar had not yielded, and the profiles were only plotted for drifts of 1.0%, 1.8%, and 3.6%.

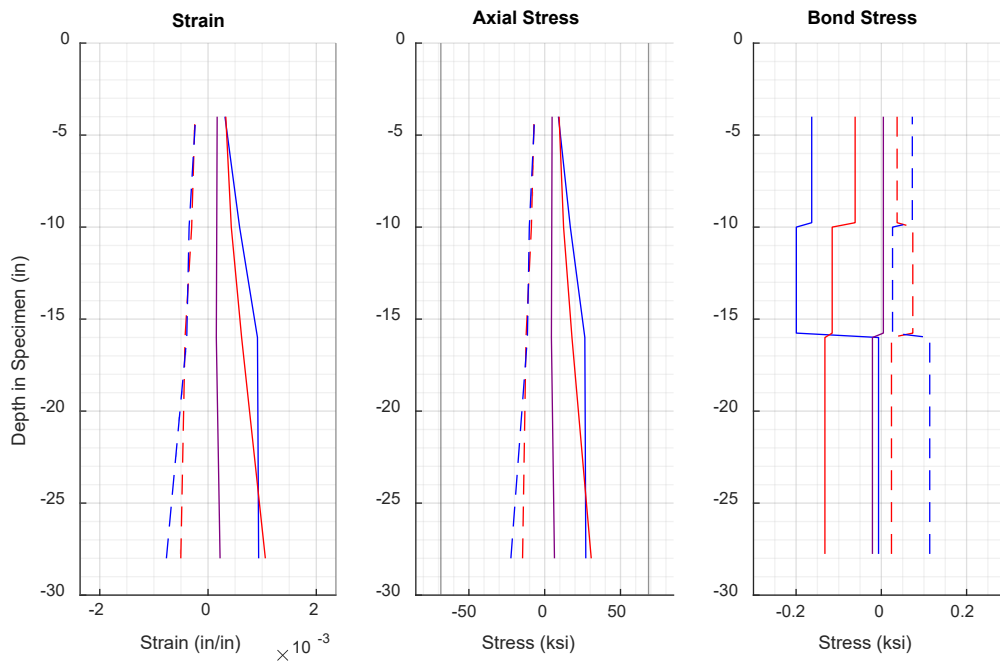
Figure 5.21(a) and Figure 5.22(a) show that the experimental bond stress profile for the column longitudinal bars was roughly constant at low drift ratios, averaging 0.4 ksi in tension and 0.2 ksi in compression along the bar height at both 1.0% drift and 1.8% drift. At higher drift ratios [Figure 5.23(a)] as the column bars yielded near the top of the connection region, the bond stress distribution became nonlinear, and peak bond stresses occurred lower in the bars. This pattern is

consistent with the expectation that yielding leads to bond deterioration; however, conclusions from post-yield calculations should be cautiously drawn, as they are highly dependent on the assumed stress–strain relation for the bar. Additionally, bond stress values were found from the two adjacent strain gauge readings and may not reflect local stresses between the gauges.

Figure 5.21(b), Figure 5.22(b), and Figure 5.23(b) show that the experimental bond stress profile for the shaft longitudinal bars is roughly constant from 1.0% drift to 3.6% drift, averaging 0.1 ksi in tension and 0.05 ksi in compression along the bar height at each drift level shown. The shaft longitudinal bars first reached yield at 10.5% drift, during the last set of testing. The strains measured during this last cycle are not shown in the following figures.



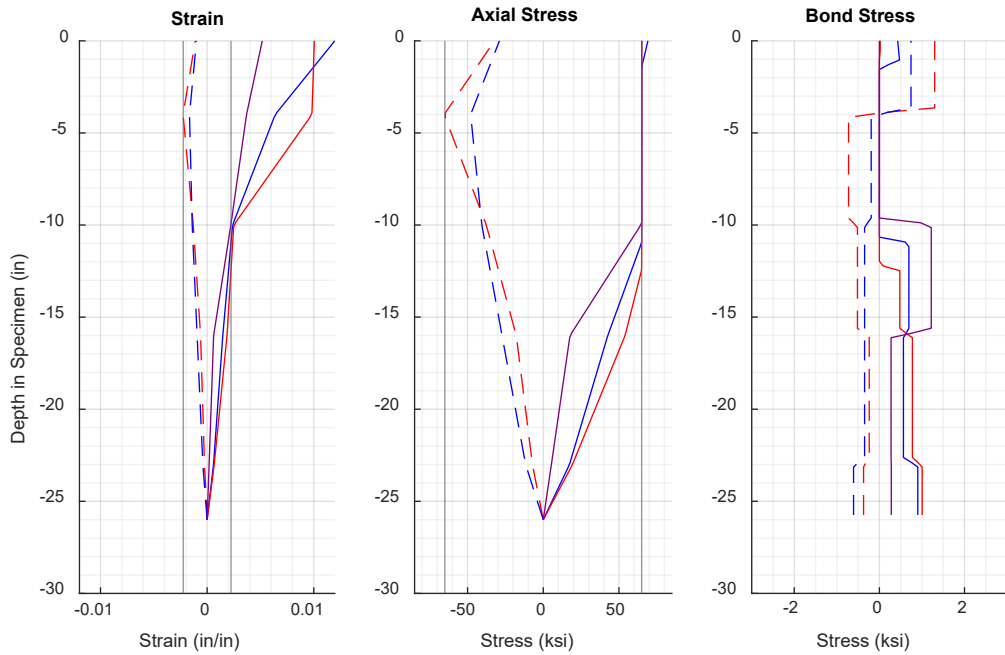
(a)



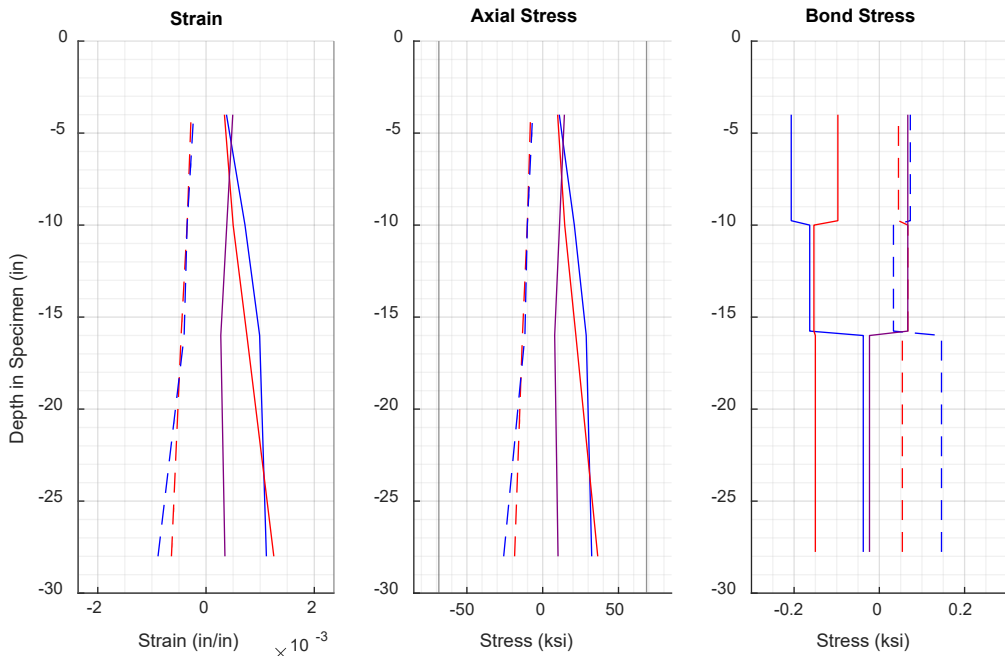
(b)



Figure 5.21 Axial and bond stress profiles at 1.0% drift: (a) column longitudinal bars; and (b) shaft longitudinal bars.



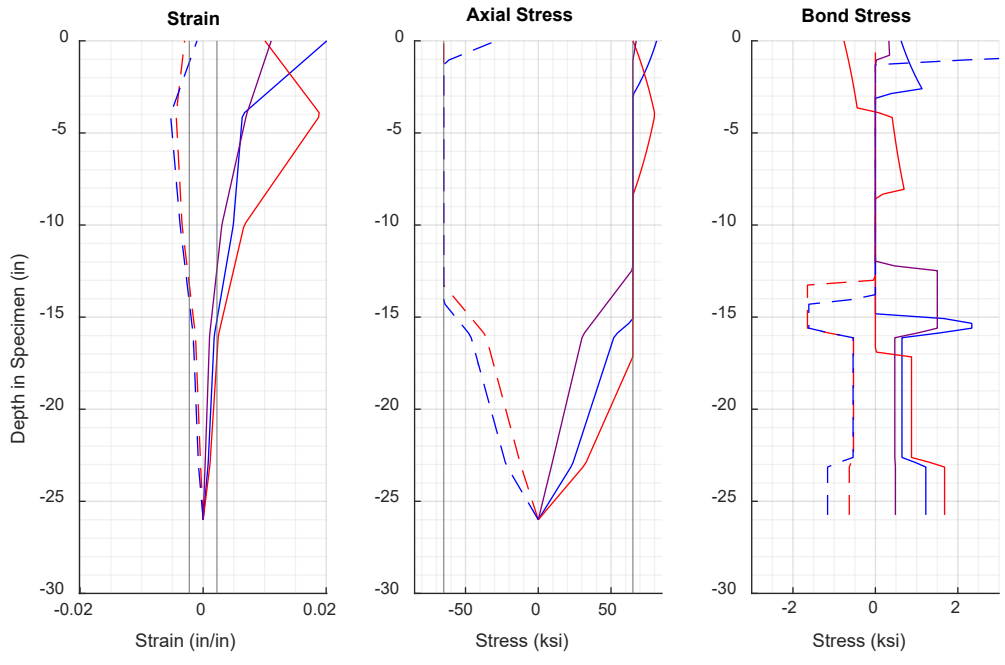
(a)



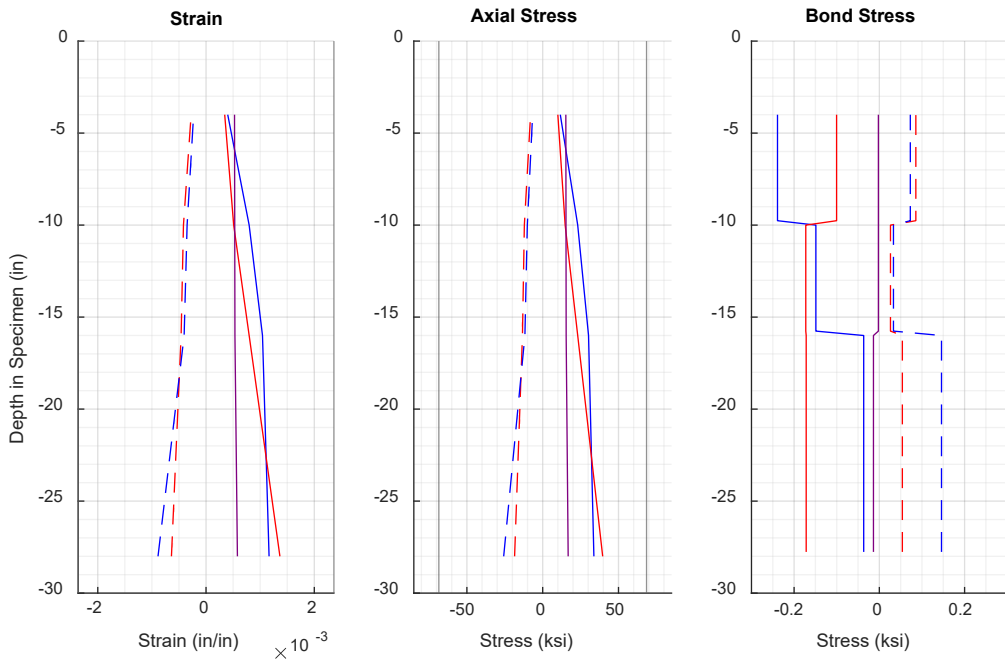
(b)



Figure 5.22 Axial and bond stress profiles at 1.8% drift: (a) column longitudinal bars; and (b) shaft longitudinal bars.



(a)



(b)



Figure 5.23 Axial and bond stress profiles at 3.6% drift: (a) column longitudinal bars; and (b) shaft longitudinal bars.

6 Comparison of Experimental Responses

The experimental results described in Chapter 5 for Specimen DS-4 were compared with results from previous experimental studies of three column–shaft connections (DS-1, DS-2, and DS-3) tested at the University of Washington [Tran 2012; Tran 2015]. This chapter first discusses key parameters that affect the performance of column–shaft connections, then compares the measured results of the four specimens, and finally discusses the influence of selected parameters on the experimental behavior.

6.1 DISCUSSION OF KEY PARAMETERS

Ten key column–shaft specimen parameters were identified from the past experimental and numerical studies outlined in Chapter 2. These parameters can be categorized as parameters relating to specimen geometry (i.e., dimensions), reinforcement, and construction techniques.

Specimen Geometry

1. Column height-diameter ratio H/D_c : this parameter influences the shear span, which is the ratio of the moment demand to the shear demand on the connection region.
2. Shaft-column diameter ratio D_s/D_c : a greater ratio results in a thicker concrete ring around the column core, which might be beneficial for resisting forces in the connection region. It also implies a greater eccentricity of the noncontact lap splice. Note that the eccentricity is also affected by the cover, which is typically larger in the shaft than in the column.

Reinforcement

3. Embedment length-column diameter ratio l_e/D_c : in many design specifications, the required embedment length of the column bars is defined as a function of the column diameter [AASHTO SGS 2015; Caltrans SDC 2019; WSDOT BDM 2020; and AASHTO ABC 2018]. The intent behind this requirement is to ensure sufficient anchorage of the reinforcement and account for possible damage penetration, which would reduce the effective embedment of the column longitudinal bars.

4. Embedment length-bar diameter ratio l_e/d_b : the required tension development length of reinforcing bars is typically described in terms of the bar diameter. In the case of column–shaft connections, the embedment length of the column bars can similarly be described in terms of bar diameter. Through changing this parameter, the column bar tensile capacity could be developed higher or lower in the connection region and thereby potentially change the force-transfer mechanism.
5. Shaft longitudinal reinforcement: in current design, the shaft longitudinal reinforcement is controlled by the peak moments in the shaft, which typically occur below the connection region and are greater than the peak moment demand on the connection. Therefore, it is unlikely that the transition region demands will control the amount of shaft longitudinal reinforcement. However, the inverse is not necessarily true: the amount and size of shaft longitudinal reinforcement may influence the force transfer in the transition region. More reinforcement with a greater surface area can lead to a shorter force-transfer length because each bar needs to develop a lower level of stress.
6. Transverse volumetric reinforcement ratio ρ_{tr} : the variation in the amount of shaft transverse reinforcement clearly influenced the failure mode in Tran’s DS-1 and DS-2 specimens [Tran 2012].
7. Distribution of shaft transverse reinforcement (i.e., variation in spacing of spirals/hoops): typical past specimens and connections used in the field consisted of shafts with uniformly spaced spirals or hoops in the transition region. Tran [2015] suggested that transverse reinforcement could be used more efficiently if it were concentrated at the top of the connection region. If the distribution of spiral were varied more efficiently over the height of the connection region, the connection capacity could be increased.
8. Termination of longitudinal bars (straight or headed bars in column and/or shaft): mechanical anchor heads can provide anchorage where bar embedment is insufficient for development, especially in precast columns; however, where embedment is sufficient, anchor heads are an unnecessary expense.

Construction Techniques

9. Precast vs. CIP columns: past experiments have been conducted on both precast column-CIP shaft specimens and entirely CIP specimens, but studies have not directly addressed whether there a significant difference in the shear transfer mechanism and capacity between the two types of connections.
10. Intentional debonding of longitudinal bars: Tran’s strut-and-tie model (STM) indicated that the location of the STM nodes [Tran 2015] plays a key role in the connection region. The node locations are influenced by the development length of the bars and any debonding of them. By debonding part of the

longitudinal bars, the force-transfer region could be shifted to improve performance in the connection region.

Two main parameters were studied during this series of experimental tests at the University of Washington in order to investigate the force-transfer behavior. They included: the transverse volumetric reinforcement ratio (parameter #6 in the aforementioned list of key parameters), which was studied primarily by varying the amount of spiral A_{tr}/s over the transition region; and precast vs. CIP (parameter #9), which was studied through changing the column construction method between specimens. The influence of each of these parameters based on experimental results will be discussed in Section 6.8.

6.2 SPECIMEN CHARACTERISTICS

A summary of the key characteristics of all four specimens can be found in Table 6.1. Specimens DS-1 through DS-3 consisted of three precast columns with CIP shafts [Tran 2012; Tran 2015]. They included: a reference specimen based on a column–shaft connection with reinforcement typical of that used in Washington (DS-1); a “weak-shaft” specimen with a 50% reduction in the shaft transverse reinforcement in the transition region (DS-2); and a “strong-column” specimen with increased column flexural strength, increased shaft transverse reinforcement, and decreased shaft diameter compared to the first two specimens (DS-3). Specimen DS-4’s column was nearly identical to the column in DS-3, with the following exceptions:

- It was CIP, not precast.
- The column longitudinal reinforcement was not terminated with mechanical anchor heads. Specimen DS-4’s shaft (which contains the transition region) was designed as a hybrid of the DS-1 and DS-3 shafts.

The design rationale for all specimens is described in more detail in Chapter 3. All specimens were loaded under the same axial load of 159 kips and cyclic lateral displacements described in Chapter 4.

Table 6.1 Key characteristics of Specimens DS-1 through DS-4.

		DS-1	DS-2	DS-3	DS-4
Column	Column diameter (in.)	20	20	20	20
	Column height (in.)	60	60	60	60
	Column height-to-diameter ratio	3.0	3.0	3.0	3.0
	Column longitudinal reinforcement (reinf. ratio)	10 #5 (0.98%)	10 #5 (0.98%)	16 #5 (1.56%)	16 #5 (1.56%)
	Column transverse reinforcement (volumetric ratio)	gauge-3 wire (0.244 in. dia.) at 1.25 in.	gauge-3 wire (0.244 in. dia.) at 1.25 in.	gauge-3 wire (0.244 in. dia.) at 1.25 in.	gauge-3 wire (0.244 in. dia.) at 1.25 in.
	Volumetric ratio of col. transverse reinforcement	0.81%	0.81%	0.81%	0.81%
	Clear side cover to column spiral (in.)	0.6	0.6	0.6	0.75
Shaft	Shaft diameter (in.)	30	30	26	30
	Shaft height (in.)	30	30	30	30
	Shaft-column diameter ratio	1.5	1.5	1.3	1.5
	Shaft longitudinal reinforcement (reinf. ratio)	30 2#3 (0.94%)	30 2#3 (0.94%)	24 3#4 (2.66%)	24 3#4 (1.58%)
	Embedment length of column reinforcement into shaft (in.)	26 (42 <i>d_b</i>)	26 (42 <i>d_b</i>)	26 (42 <i>d_b</i>)	26 (42 <i>d_b</i>)
	Shaft transverse reinforcement in transition region	2 gauge-9 wire (0.148 in. dia.) at 3 in.	gauge-9 wire (0.148 in. dia.) at 3 in.	3 gauge-9 wire (0.148 in. dia.) at 1.5 in.	gauge-9 wire (0.148 in. dia.) at 0.75 in.
	Volumetric ratio of shaft transverse reinforcement in transition region	0.17%	0.09%	0.61%	0.35%
	Clear side cover to shaft spiral (in.)	1.70	1.70	1.70	1.75
	Shaft-column diameter ratio	1.5	1.5	1.3	1.5
	Column construction method	precast	precast	precast	CIP

6.3 DAMAGE PROGRESSION

The damage progressions for all specimens are compared in Figure 6.1 and Figure 6.2. Figure values are also reported in Table 6.2 and Table 6.3. Photographs of the damage progressions are shown at the end of this section (Figure 6.3, Figure 6.4, Figure 6.5, and Figure 6.6). The results at each level of displacement are reported in terms of drift ratio, which is defined as the lateral

displacement at the actuator level divided by the vertical distance from the actuator centerline to the column–shaft interface (60 in.).

All four specimens developed flexural cracks in the columns, which remained open after unloading as the imposed displacements increased. The column longitudinal reinforcement yielded at drift ratios ranging from 0.6% to 0.9% for the four tests. At larger deformations, the columns for all but DS-2 experienced first spalling around 1.2% to 2.6% and significant spalling from 3.1% to 5.2%. The shaft of each of the four specimens also cracked and experienced some spalling starting at 1.6% to 3.9% drift.

After that, at higher levels of applied displacement (up to 11% drift), most of the additional damage for Specimens DS-1 and DS-3 occurred in the columns. Failure occurred by plastic hinging in the column base (just above column–shaft interface), which consisted of a sequence of exposure of the longitudinal reinforcement, buckling of the longitudinal reinforcement, fracture of the transverse reinforcement, and fracture of the longitudinal reinforcement. The shafts of these two specimens sustained little additional damage.

In contrast, the additional damage for Specimens DS-2 and DS-4 at higher levels of displacement occurred mainly in the shafts. Neither the longitudinal nor transverse column reinforcement buckled or fractured. Instead, failure occurred through prying in the connection region: large vertical cracks formed in the shaft (which propagated from radial cracks at the column–shaft interface), a circumferential crack formed around the column confined core and the annular region of the shaft separated from it, the shaft was stretched circumferentially, and the shaft transverse reinforcement burst, resulting in a loss in moment capacity. At the same time, the column behaved essentially as a rigid body and sustained only minor damage.

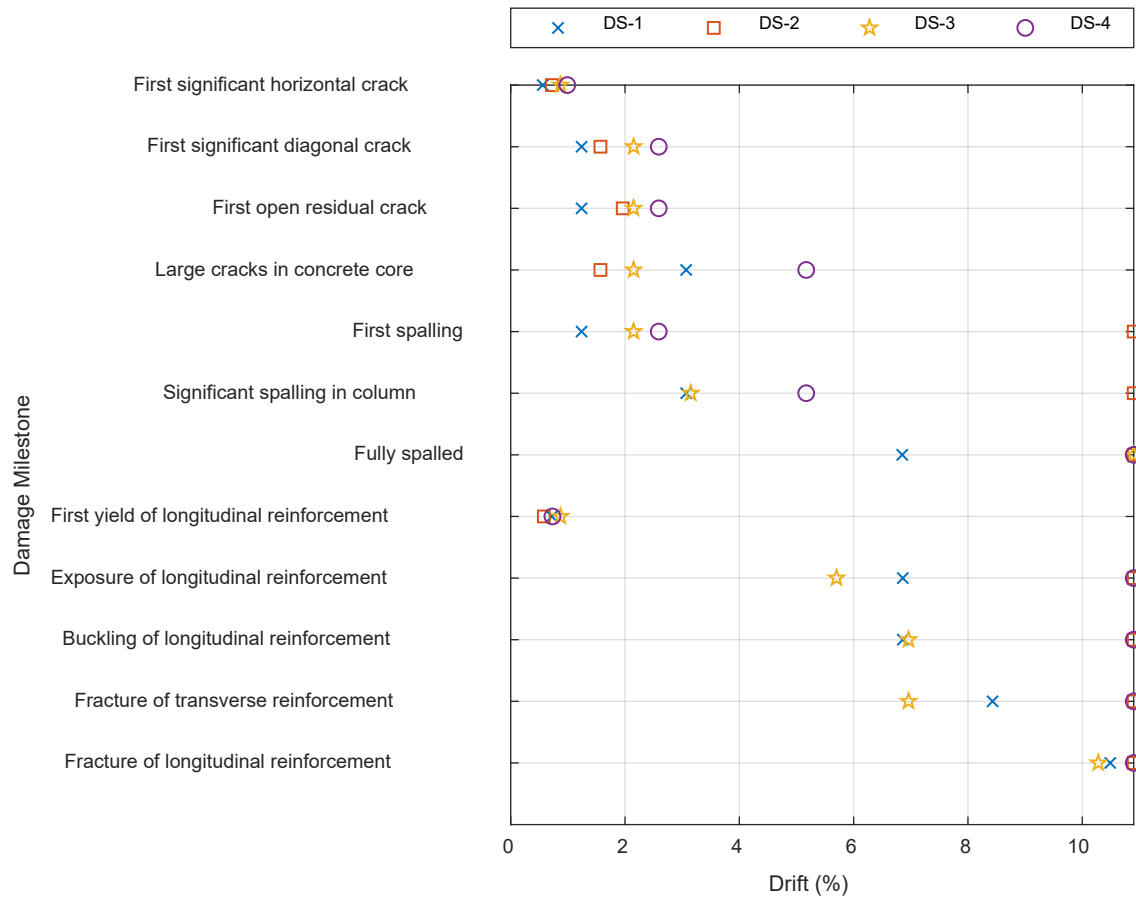


Figure 6.1 Damage progression in the column for Specimens DS-1 through DS-4. Note: any points on the right-side axis indicate that the milestone did not occur by the end of testing. Figure values are reported in Table 6.2.

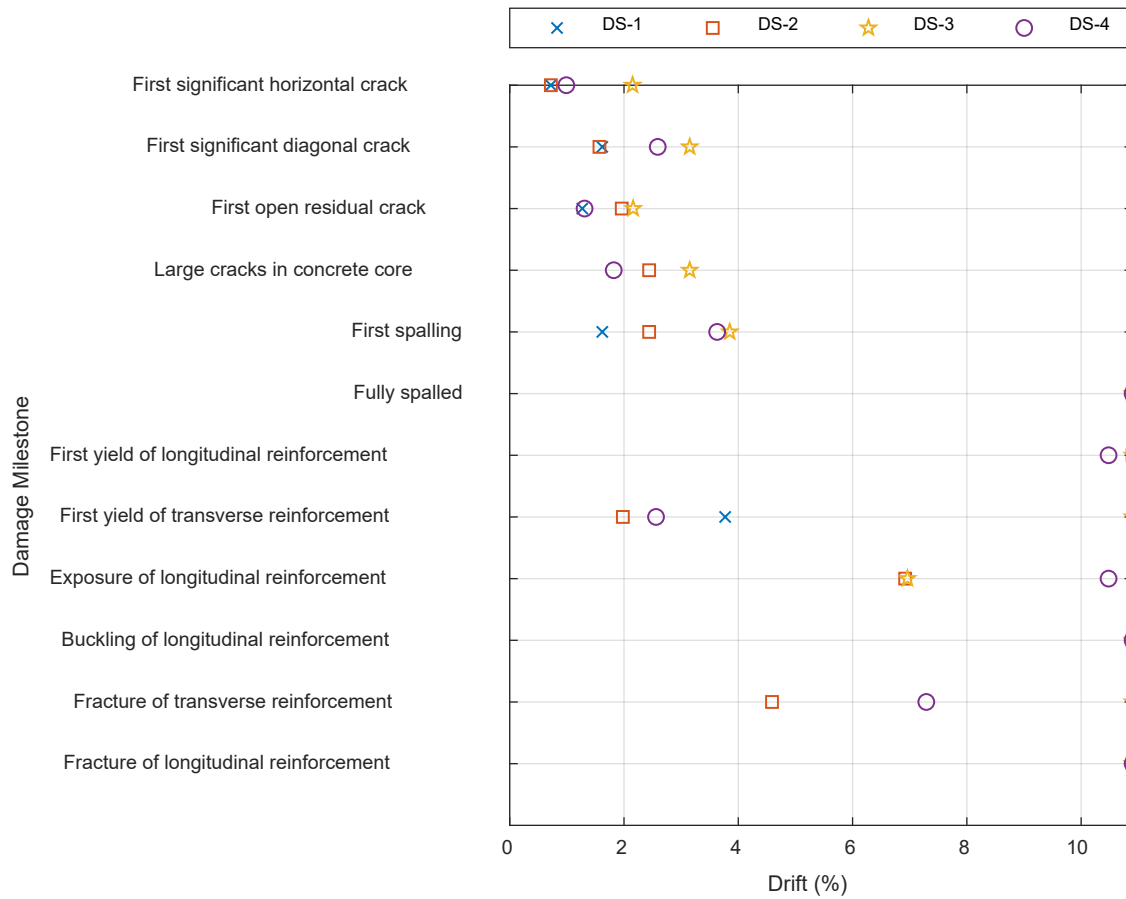


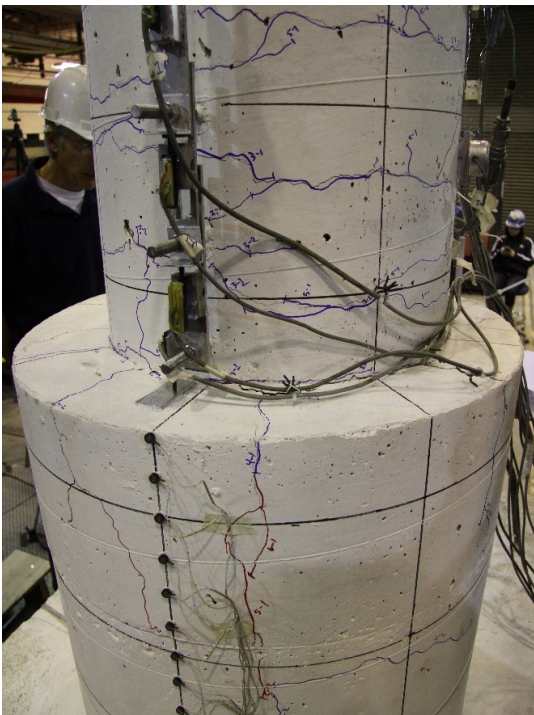
Figure 6.2 Damage progression in the shaft for Specimens DS-1 through DS-4. Note: any points on the right-side axis indicate that the milestone did not occur by the end of testing. Figure values are reported in Table 6.3.

Table 6.2 Damage progression in the column for Specimens DS-1 through DS-4. Milestones are defined in Table 5.2.

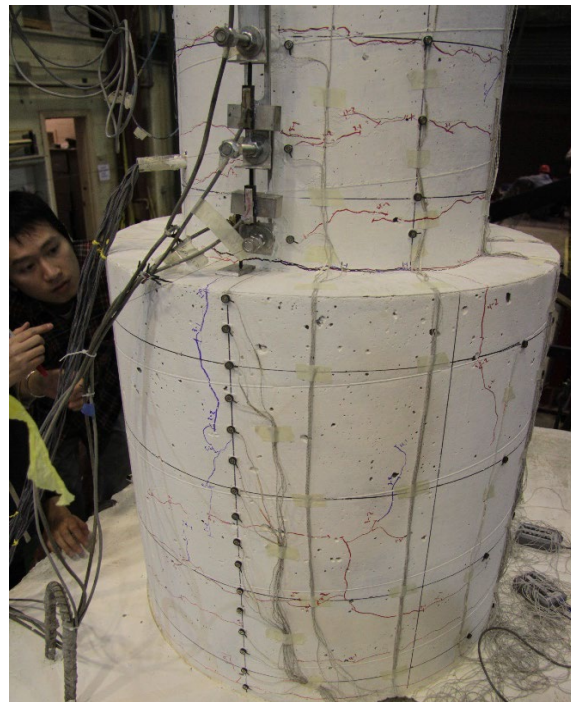
Damage Milestone	Drift Ratio at which Milestone Occurred			
	DS-1	DS-2	DS-3	DS-4
First significant horizontal crack	0.56%	0.72%	0.87%	0.99%
First significant diagonal crack	1.24%	1.57%	2.15%	2.59%
First open residual crack	1.24%	1.96%	2.15%	2.59%
Large cracks in concrete core	3.07%	1.57%	2.15%	5.17%
First spalling	1.24%	-	2.15%	2.59%
Significant spalling	3.07%	-	3.15%	5.17%
Fully spalled	6.85%	-	-	-
First yield of longitudinal reinforcement	0.72%	0.58%	0.87%	0.73%
First yield of transverse reinforcement	not measured			
Exposure of longitudinal reinforcement	6.86%	-	5.7%	-
Buckling of longitudinal reinforcement	6.86%	-	6.96%	-
Fracture of transverse reinforcement	8.43%	-	6.96%	-
Fracture of longitudinal reinforcement	10.49%	-	10.28%	-

Table 6.3 Damage progression in the shaft for Specimens DS-1 through DS-4. Milestones are defined in Table 5.2.

Damage Milestone	Drift Ratio at which Milestone Occurred			
	DS-1	DS-2	DS-3	DS-4
First significant horizontal crack	0.72%	0.72%	2.15%	0.99%
First significant diagonal crack	1.62%	1.57%	3.15%	2.59%
First open residual crack	1.27%	1.96%	2.16%	1.31%
Large cracks in concrete core	-	2.44%	3.15%	1.82%
First spalling	1.62%	2.44%	3.85%	3.63%
Significant spalling	not recorded			
Fully spalled	-	-	-	-
First yield of longitudinal reinforcement	-	-	-	10.48%
First yield of transverse reinforcement	3.77%	1.98%	-	2.56%
Exposure of longitudinal reinforcement	-	6.92%	6.96%	10.48%
Buckling of longitudinal reinforcement	-	-	-	-
Fracture of transverse reinforcement	-	4.59%	-	7.29%
Fracture of longitudinal reinforcement	-	-	-	-



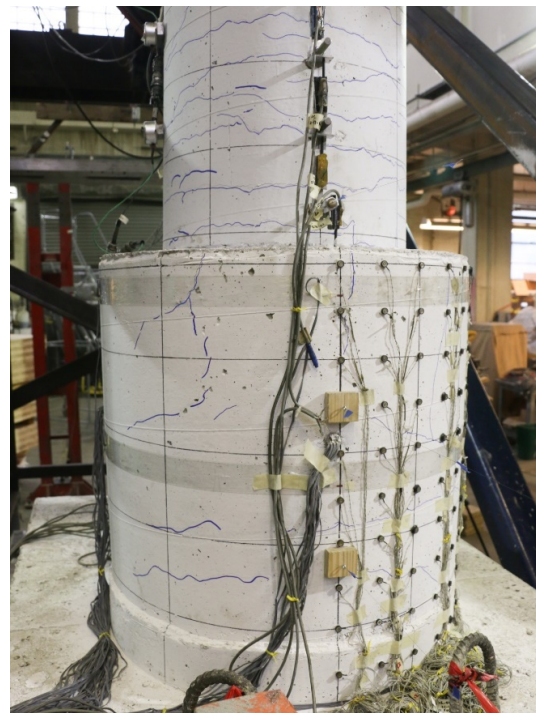
(a)



(b)

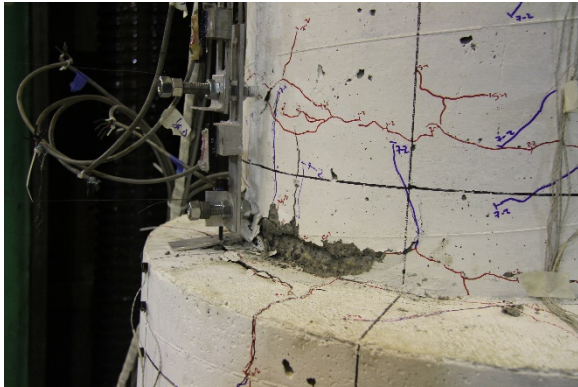


(c)



(d)

Figure 6.3 Photographs of Specimens DS-1 through DS-4 at 1.6%-1.8% drift: (a) DS-1, (b) DS-2, (c) DS-3, and (d) DS-4.



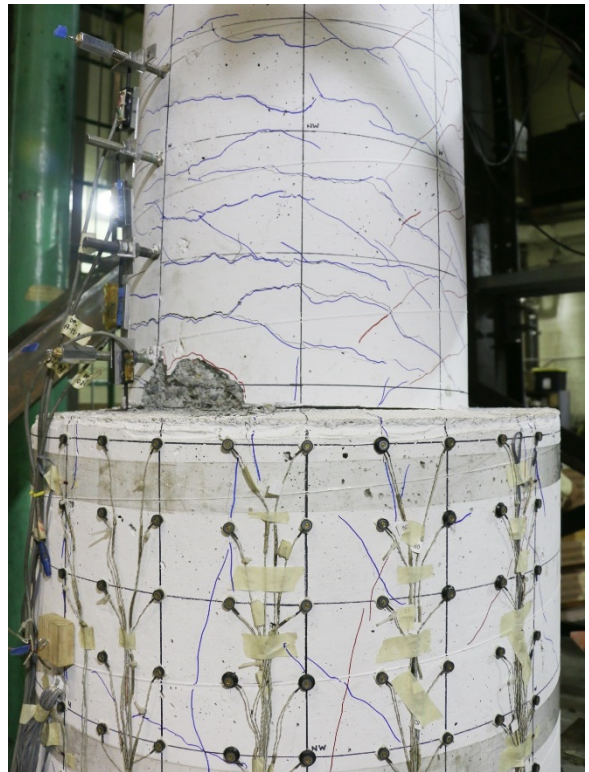
(a)



(b)



(c)

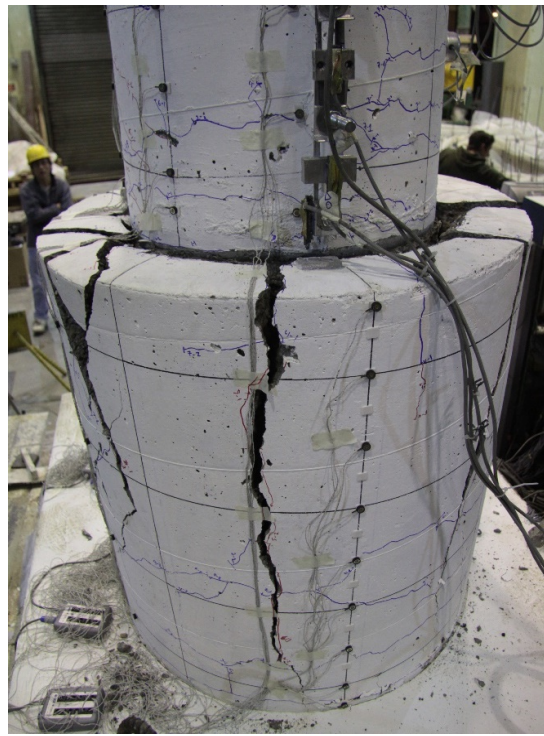


(d)

Figure 6.4 Photographs of Specimens DS-1 through DS-4 at 3.6-3.9% drift: (a) DS-1, (b) DS-2, (c) DS-3, and (d) DS-4.



(a)



(b)



(c)



(d)

Figure 6.5 Photographs of Specimens DS-1 through DS-4 at 6.8-7.4% drift: (a) DS-1, (b) DS-2, (c) DS-3, and (d) DS-4.



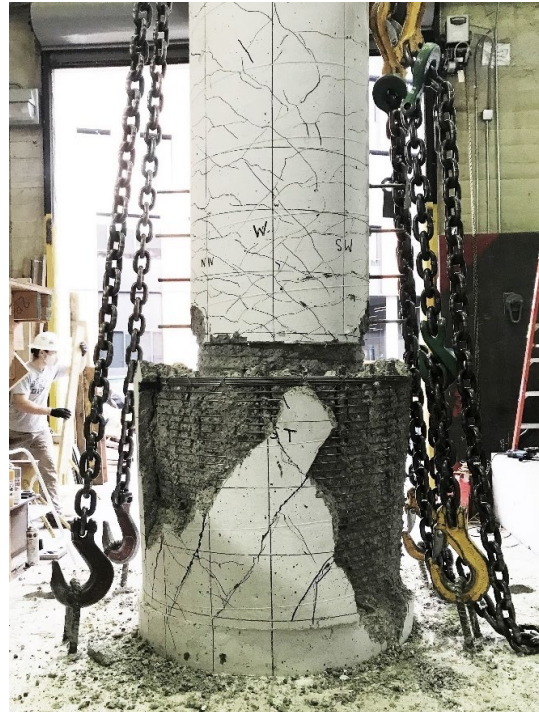
(a)



(b)



(c)



(d)

Figure 6.6 Photographs of Specimens DS-1 through DS-4 after experimental testing: (a) DS-1, (b) DS-2, (c) DS-3, and (d) DS-4.

6.4 MOMENT-DRIFT RESPONSE

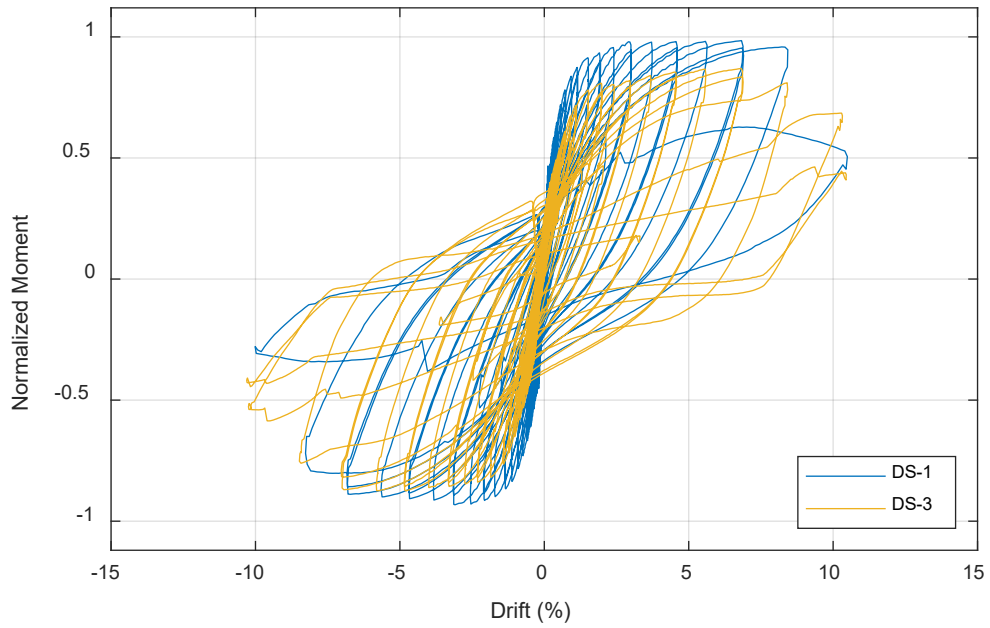
The failure modes varied among the specimens, but all four of the column–shaft connections were strong enough to develop the yield moment of the columns. Figure 6.7 shows the normalized moment vs. drift envelopes for four specimens, in which the normalized moments were calculated as the measured moment divided by the expected maximum moment. The calculated expected moment capacities (Table 6.4) were computed using measured properties (Section 3.4), the Kent and Park [1971] concrete model, and Raynor et al. [2002] model for the longitudinal steel. More moment-curvature analysis details are described in Appendix G.

The measured moments were within 4% of the expected values for DS-1, DS-2, and DS-4, but the maximum measured moment for DS-3 was 13% lower than the calculated value. This discrepancy was also observed by Tran [2015].

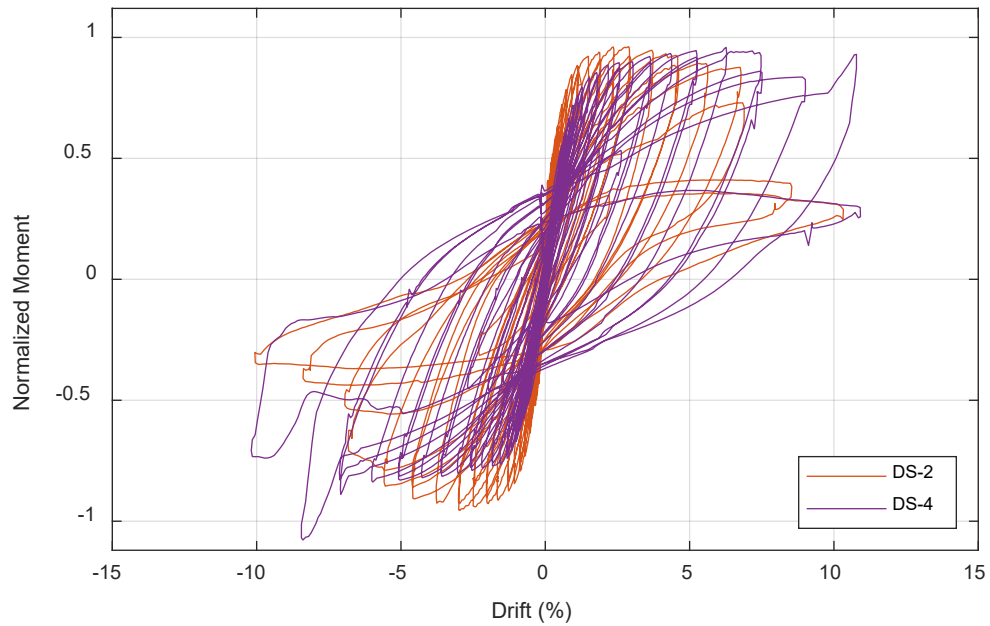
In Table 6.4, failure was defined as the point when maximum moment in a post-yield cycle dropped below of 80% of the maximum resistance measured during the test. For Specimen DS-4, the outlier peaks in the moment-drift response [Figure 6.7(b)] were ignored in determining the maximum moment; see Section 5.3 for discussion on the outlier peaks. As expected, DS-2 reached failure at the lowest drift ratio, but for the other specimens, the drift ratios at failure did not correlate consistently with the failure mode.

Table 6.4 Comparison of maximum moments and imposed drifts during testing.

	DS-1	DS-2	DS-3	DS-4
Expected max. moment (kip*in.)	3530	3530	4165	4433
Measured max. moment (kip*in.)	3476	3393	3622	4250
Ratio of measured to calculated maximum moment	0.98	0.96	0.87	0.96
Drift at failure	8.2%	6.8%	10.3%	10.2%
Maximum drift imposed during test	10.7%	10.7%	10.7%	10.8%



(a) DS-1 and DS-3



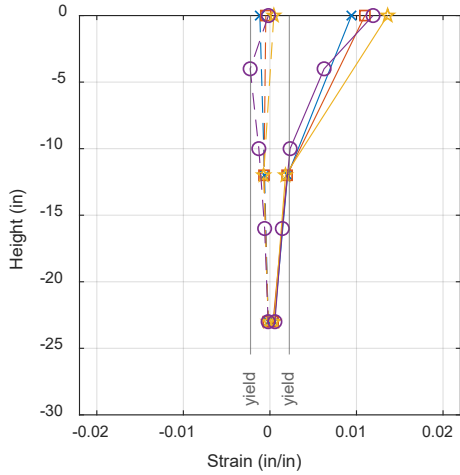
(b) DS-2 and DS-4

Figure 6.7 Normalized moment vs. drift curves for all DS specimens. See Appendix F for non-normalized curves. See Section 5.3 for an explanation of the DS-4 outlier peaks.

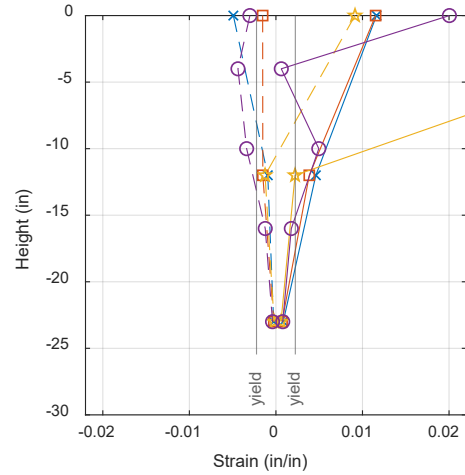
6.5 STRAINS IN COLUMN LONGITUDINAL BARS

Figure 6.8 shows the axial strain distributions of the column longitudinal bars over the height of the transition region at drift ratios of 1.8% and 3.6%. Strains were plotted up to a value of 0.02, which roughly corresponds to a strain ductility of 10. Beyond this point, the strain measurements might not be reliable. The measured strains were generally consistent with expectations.

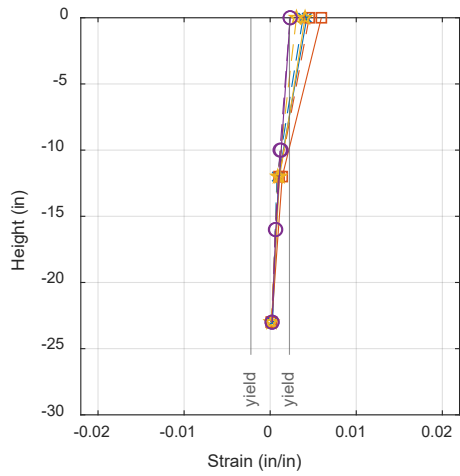
- In all four specimens, the column bars extended down to 26 in. below the column–shaft interface. The DS-3 strain gauge data at a depth of 12 in. is omitted because it appears that this strain gauge failed.
- The north bar experienced tensile strains for positive drifts, and the south bar experienced tensile strains for negative drifts. For the east bars, the strains were tensile for both positive and negative drifts.
- The maximum column bar strains in the transition region generally occurred at the shaft–column interface.
- The column bars in all specimens reached first yield in tension at about 0.6–0.9% drift.
- The maximum strains in the column bars for all specimens eventually exceeded the strain gauge reading limit (0.011 in./in. for DS-1 through DS-3, and 0.05 in./in. for DS-4; DS-4 used strain gauges with a greater measurement range).
- The column bars in Specimens DS-1, DS-2, and DS-3 were terminated with mechanical anchor heads, but those in DS-4 were not; they had straight ends. The strains in all specimens decreased with increasing depth, reaching a value of nearly zero at an elevation of $y = -23$ in. These measurements suggest that the anchor heads in DS-1, DS-2, and DS-3 did not significantly contribute to the anchorage of the column longitudinal bars.



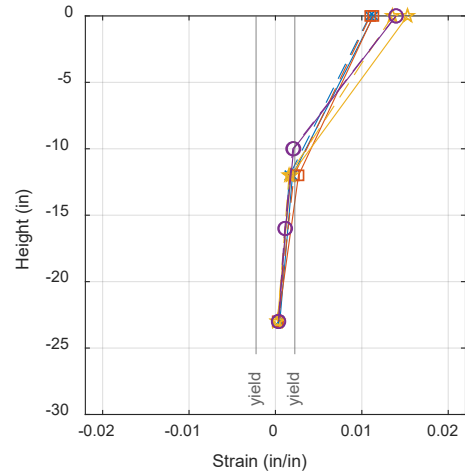
(a) 1.8% drift, north bar



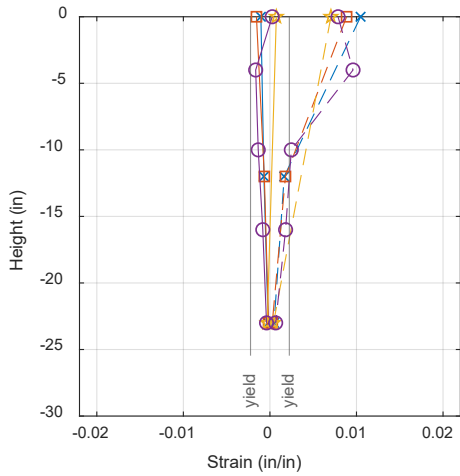
(b) 3.6% drift, north bar



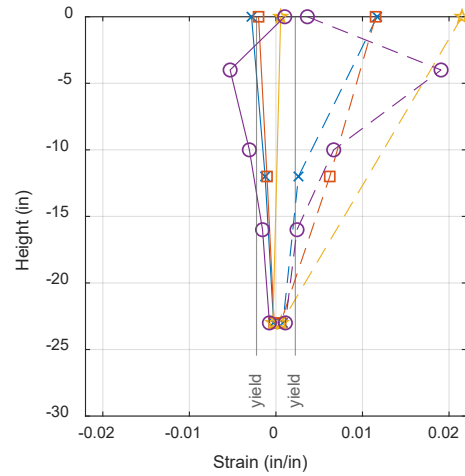
(c) 1.8% drift, east bar



(d) 3.6% drift, east bar



(e) 1.8% drift, south bar



(f) 3.6% drift, south bar



Figure 6.8 Column longitudinal bar strain profiles.

6.6 STRAINS IN SHAFT LONGITUDINAL BARS

The strain profiles for the shaft longitudinal bars at 1.8% and 3.6% drift are shown in Figure 6.9. The strains increased with increasing depth, and the maximum shaft bar strain was usually measured at the bottommost strain gauge in all specimens. This trend was expected due to the increasing shaft moment demand with depth. At the drift ratios shown, the strain distributions for the north and south bars were approximately linear along the height of the shaft.

The strain values at drift ratios of 1.8% and 3.6% were similar, which is consistent with the observation that the column capacity appeared to limit the force transferred to the connection. For these two levels of drift, the maximum strain never exceeded 70% of the yield strain of the reinforcement. The shaft strains only increased marginally for the two specimens that suffered primarily column damage. Over the full duration of testing (beyond the drift ratios shown in the figure), the shaft bars in Specimens DS-1 and DS-3 reached 58% and 54% of the yield strain, respectively. In contrast, the strains in Specimens DS-2 and DS-4 reached 91% and 104% of yield strain, respectively. These maximum strains occurred at the end of testing, at about 9–10% drift, for all specimens.

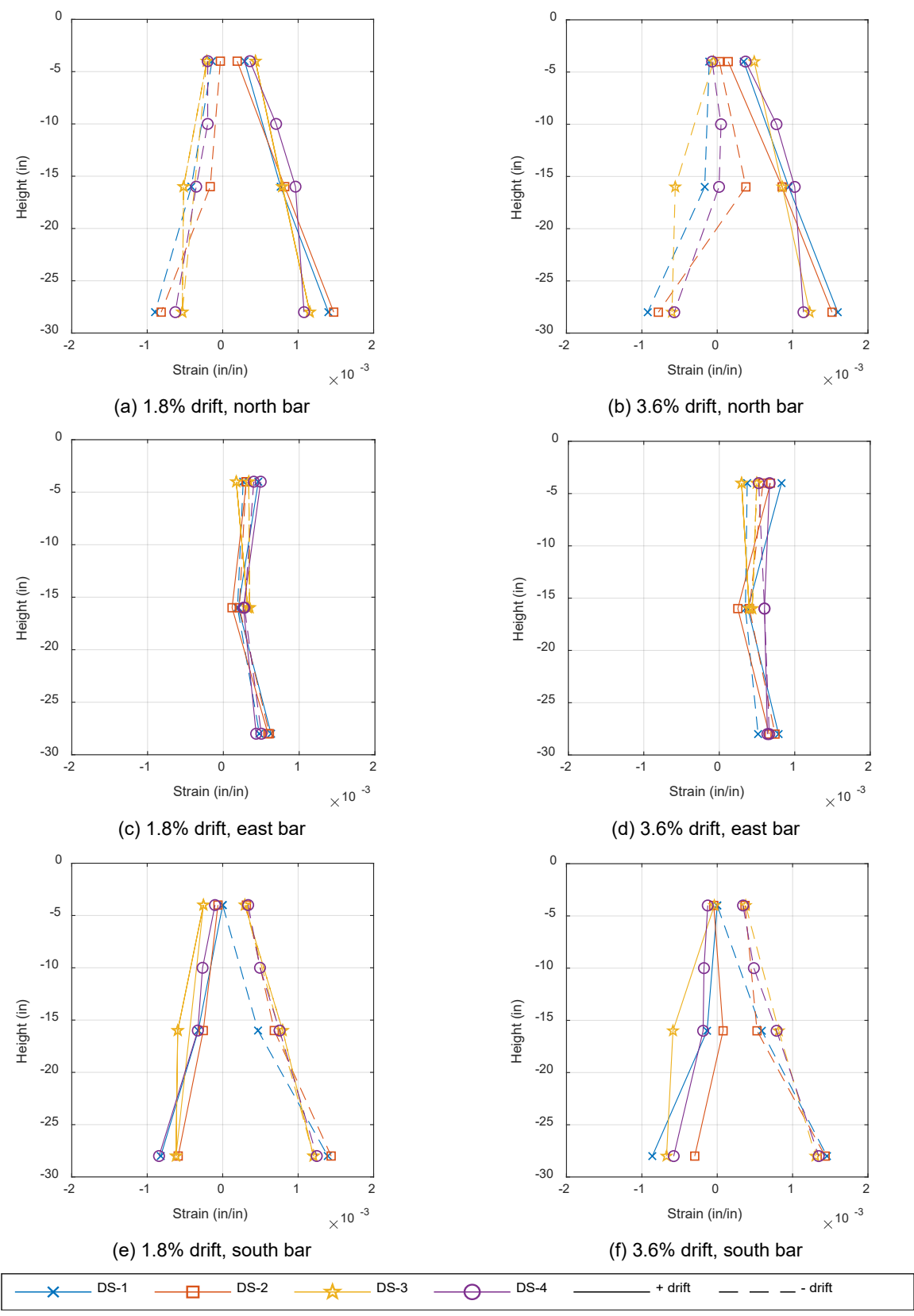


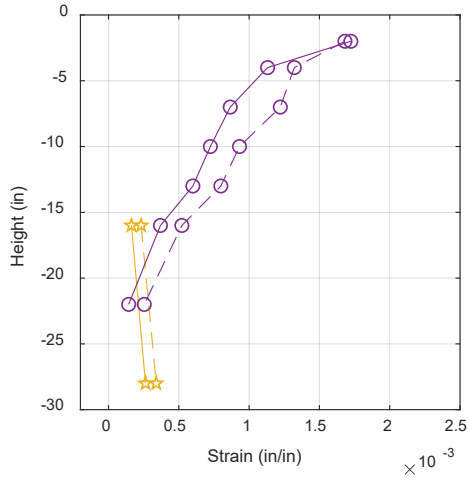
Figure 6.9 Shaft longitudinal bar strain profiles.

6.7 STRAINS IN SHAFT TRANSVERSE REINFORCEMENT

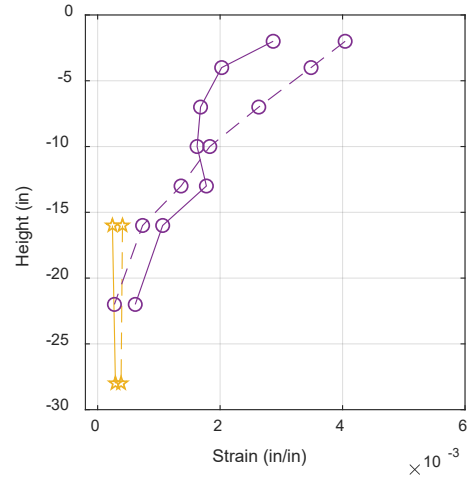
Figure 6.10 shows the hoop strain distributions of the shaft transverse reinforcement at 1.8% and 3.6% drift. For Specimens DS-1, DS-2, and DS-3, strain gauges were installed at three levels along the height of the shaft (top, middle, and bottom). For Specimen DS-4, strain gauges were installed at seven levels. On the north side [Figure 6.10(a) and Figure 6.10(b)], Specimens DS-1 and DS-2 were not gauged. The uppermost strain gauge in Specimen DS-3 on the north side and all strain gauges in DS-1 on the south side broke before testing.

- The strain gauge measurements were consistent with each other.
- The maximum strains were similar for the positive and negative cycles.
- The largest strains occurred in the highest strain gauges, near the column–shaft interface.
- The strains decreased with increasing depth, reaching a value of nearly zero between $y = -22$ in. and $y = -28$ in. for all specimens at both 1.8% and 3.6% drift.
- The strain distributions were approximately parabolic along the height of the shaft.

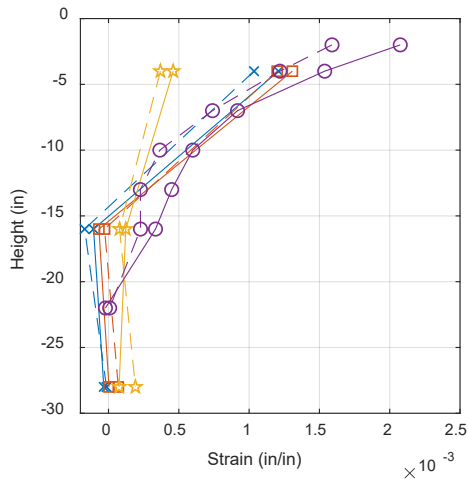
The peak transverse strain envelopes are plotted against drift in Figure 6.11. The plot shows a bifurcation in strains: the transverse reinforcement strains in DS-1 and DS-3 barely reached 0.0024 strain (approximate yield) by 3% drift, while those in DS-2 and DS-4 reached over twice that amount by 3% drift. The bifurcation began around 1.5% drift, at which point all of the measured strains were still within the elastic range, and the split grew with increasing drift. This bifurcation is consistent with the failure modes of each specimen, implying that there is a correlation between transverse reinforcement strains and failure mode.



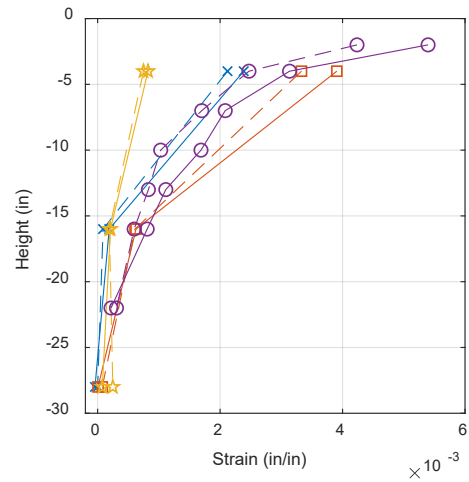
(a) 1.8% drift, north wire



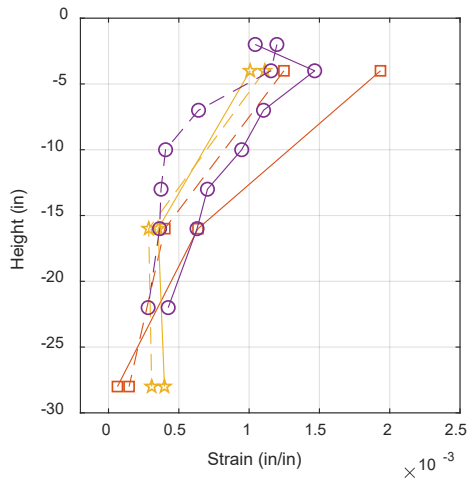
(b) 3.6% drift, north wire



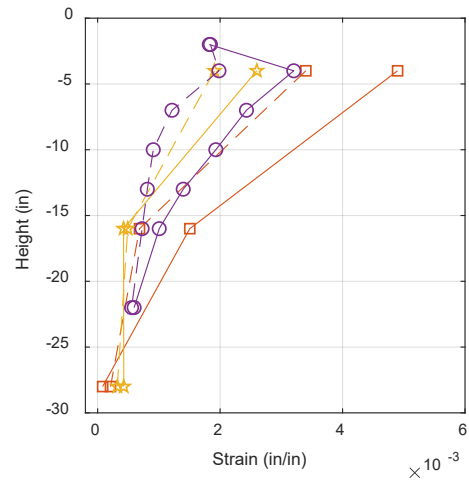
(c) 1.8% drift, east wire



(d) 3.6% drift, east wire



(e) 1.8% drift, south wire



(f) 3.6% drift, south wire



Figure 6.10 Shaft transverse reinforcement strain profiles.

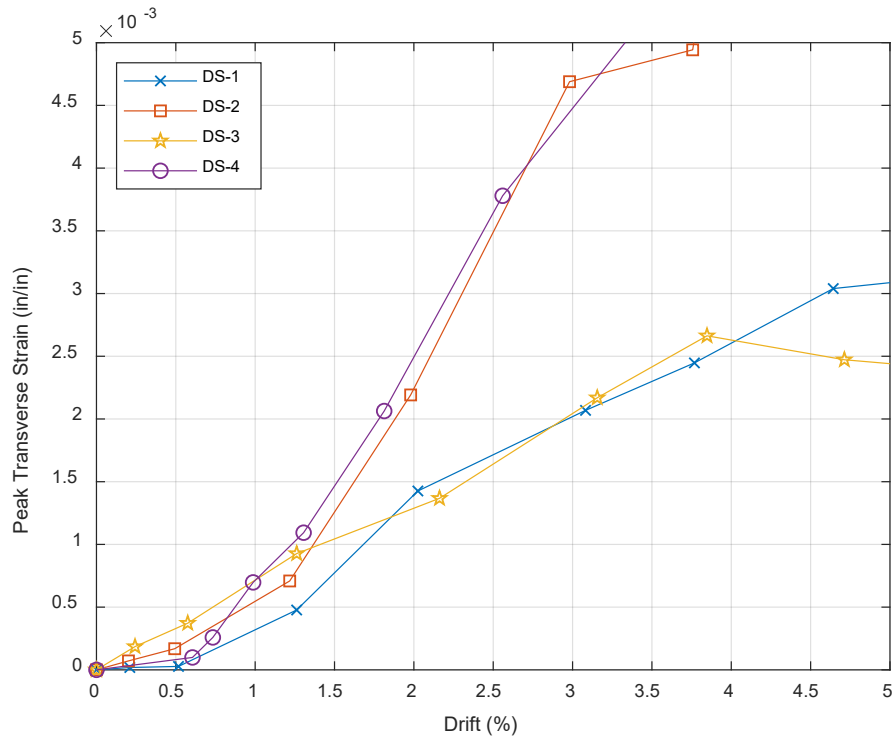


Figure 6.11 Transverse strain vs. drift envelopes.

6.8 DISCUSSION OF EXPERIMENTAL RESPONSES

This chapter first discussed key parameters and then compared results from four column-drilled-shaft specimen experiments at the University of Washington. Results indicated that the construction method (precast vs. CIP) did not significantly impact the behavior of the specimens: DS-4’s behavior demonstrated that a prying failure, in which the column confined core and the annular region of the shaft separated, was possible even in a CIP connection with proper embedment. This prying behavior has not been addressed in models of column–shaft connections [Tran 2015; Murcia-Delso et al. 2013; and McLean and Smith 1997].

The similar moment-drift envelopes across all specimens indicate that the failure mode cannot be determined solely from moment-drift curves. It is not sufficient to design each component to resist overstrength moment demands; reinforcement in the connection region must be detailed in order to avoid an undesirable prying failure in the shaft. As discussed in Section 6.7, transverse reinforcement and transverse strains are essential in determining the failure modes of column–shaft connections.

7 Evaluation of Models and Design Equations

Several models have been proposed to describe the force-transfer behavior and to proportion the shaft transverse reinforcement in a column–shaft connection; see Chapter 2. In this chapter, three models that have been proposed to detail the shaft transverse reinforcement in the transition region are evaluated: McLean and Smith’s noncontact lap splice model [1997], Murcia-Delso et al.’s bond-based model [2013], and Tran’s strut-and-tie model [2015].

The evaluation procedure is based on the amount of transverse reinforcement required by each model. Therefore, in this chapter, each model is only summarized in the context of the evaluation; more information on the basis of each model can be found in Chapter 2. The evaluation procedure is described in the following section, then each model is evaluated, and finally the performances of all of the models are compared at the end of the chapter.

7.1 STRATEGY FOR EVALUATING MODEL ACCURACY

The expected performance determined from the model was compared to the experimental strains from eight test specimens (three of which were precast, and the other five were CIP). The expected performance was represented by the ratio of $\frac{A_{tr}}{s}$ required by the model to $\frac{A_{tr}}{s}$ used in the specimen, where A_{tr} is the cross-sectional area of the shaft transverse reinforcement in the transition region, and s is the transverse reinforcement spacing (also known as pitch). For the four specimens with bundled spiral at the top of the shaft, the amount of “ $\frac{A_{tr}}{s}$ used” in the required-to-used ratio was taken as the average $\frac{A_{tr}}{s}$ in the specimen’s shaft, i.e., the bundled area was smeared along the full height of the shaft. For the four specimens, including the bundled turns resulted in an increase of 0.001–0.003 in. (about 13%) in the value of $\frac{A_{tr}}{s}$. On the “required” side of the required-to-used ratio, none of the three models explicitly prescribed a different or altered design procedure for connections with a nonuniform distribution of spiral. Therefore, the “ $\frac{A_{tr}}{s}$ required” in the required-to-used ratio was taken as the $\frac{A_{tr}}{s}$ prescribed by each of the design procedures, which inherently assumed a uniform distribution of transverse reinforcement in the transition region. A required-to-used ratio less than one indicates that favorable performance should be expected (failure at the column base), while a ratio greater than one indicates an expectation of poor performance (failure in the shaft).

The measured strains used in the comparison correspond to the peak transverse strain developed at 2.0% drift, normalized by the nominal yield strain of the transverse reinforcement. The drift ratio of 2.0% was chosen for comparison because the transverse strains in most specimens were at or below the nominal yield strain, so the measured strains were more likely to be reliable, and stresses and forces could more accurately be inferred from measured strains. The measured moment at the column base at this drift ratio was near the maximum moment measured over the duration of testing for all specimens. Additionally, the analysis in Figure 6.11 shows that the bifurcation in measured strains began prior to this drift ratio, and the relative performance of each specimen (from most to least favorable) stayed consistent from 2.0% drift through the end of the experiments. Nominal steel yield strains were used for the normalization because actual yield strains were not measured. The yielding of the spirals or hoops was also influenced by residual stresses from bending straight rods into a circular shape, which are described in Appendix D.

If the expected and measured behaviors matched, then the model is considered adequate. If the model predicted prying failure but measured transverse strains were relatively low, then the model is overly conservative. If the model did not predict failure but measured transverse strains were relatively high, then the model is unsuitable, because it dangerously fails to predict poor behavior.

The properties of the specimens used for model evaluation are summarized in Table 7.2 and Table 7.2. They include the four specimens tested at the University of Washington (Specimens DS-1 through DS-4), as well as four CIP, full-scale specimens tested at UCSD. Specimen UCSD-3 was omitted from the model evaluation because it had a steel casing around the shaft in addition to the shaft transverse reinforcement.

The measured strains used in the model evaluation (strains at 2.0% drift) are shown in Table 7.3. For completeness, strains at some other drift ratios are also recorded in the table. These strains were obtained from the strain–drift ratio envelope for the specimens, interpolated as necessary for cases when no loading cycle to exactly 2.0% drift was used. For Specimen UCSD-4, the strain gauge readings at 25 in. below the column–shaft interface on the north and south sides were far greater than those in adjacent strain gauges (placed above and below -25 in.) and in other specimens; see Figure 7.1. Therefore, two measured strain values are listed for each drift ratio in Table 7.3: the upper value is the maximum measured strain extracted using the same method as for all the other specimens; and the lower value is the maximum measured strain when omitting the outlier strain gauge readings at -25 in. The maximum measured strain after omitting the outlier strains occurred at the top of the shaft, which is consistent with the strain profiles seen in the other specimens. In the model evaluations, both strain values for UCSD-4 are plotted as separate points: “UCSD-4 (T)” for the measured strain at the top gauges, and “UCSD-4 (M)” for the maximum measured strain.

Table 7.1 Key characteristics of specimens used in model evaluation.

	Reduced-scale specimens (Tran [2015] and current study)				Full-scale specimens [Murcia-Delso et al. 2013; Loffizadeh and Restrepo 2019]			
	DS-1	DS-2	DS-3	DS-4	UCSD-1	UCSD-2	UCSD-4	UCSD-5
Column diameter (in.)	20	20	20	20	48	48	48	48
Column height (in.)	60	60	60	60	192	216	192	216
Shaft diameter (in.)	30	30	26	26	72	72	60	72
Shaft height (in.)	30	30	30	30	108	96	72	96
Shaft-column diameter ratio	1.5	1.5	1.3	1.5	1.5	1.5	1.25	1.5
Column longitudinal reinforcement (reinf. ratio)	10 #5 (0.98%)	10 #5 (0.98%)	16 #5 (1.56%)	16 #5 (1.56%)	18 #11 (1.55%)	18 #14 (2.24%)	32 #8 (1.40%)	14 #14 (1.74%)
Shaft longitudinal reinforcement (reinf. ratio)	30 2#3 (0.94%)	30 2#3 (0.94%)	24 3#4 (2.66%)	24 3#4 (1.58%)	28 #14 (1.55%)	26 #18 (2.55%)	40 #11 (2.21%)	20 #18 (1.96%)
Embedment length of column reinf. (in.)	26 (42d _b)	26 (42d _b)	26 (42d _b)	26 (42d _b)	90 (64d _b)	72 (43d _b)	37 (37d _b)	90 (53d _b)
Shaft transverse reinf. in transition region (vol. ratio)	2 gauge-9 wire at 3 in. (0.17%)	gauge-9 wire at 3 in. (0.09%)	3 gauge-9 wire at 1.5 in. (0.61%)	gauge-9 wire at 0.75 in. (0.35%)	2#6 at 6.5 in. (0.82%)	2#7 at 7 in. (1.04%)	2#7 at 5.5 in. (1.62%)	#7 at 5 in. (0.74%)
Average A_{tr}/s (in.)	0.0138	0.0069	0.0378	0.0258	0.1359	0.1718	0.2187	0.1203
Transverse reinforcement in plastic-hinge region of column (vol. ratio)	gauge-3 wire at 1.25 in. (0.81%)	gauge-3 wire at 1.25 in. (0.81%)	gauge-3 wire at 1.25 in. (0.81%)	gauge-3 wire at 1.25 in. (0.81%)	2#5 at 6.5 in. (0.87%)	2#5 at 4 in. (1.41%)	#6 at 4 in. (1.00%)	2#5 at 5 in. (1.14%)
Clear side cover to column reinf. cage (in.)	0.60	0.60	0.60	0.75	2.0	2.0	2.0	2.0
Clear side cover to shaft reinf. cage (in.)	1.70	1.70	1.70	1.75	3.0	3.0	3.0	3.0
Construction method	precast column	precast column	precast column	CIP column	CIP column	CIP column	CIP column	CIP column

Table 7.2 Material properties of specimens used in model evaluation.

	Reduced-scale specimens (Tran [2015] and current study)				Full-scale specimens [Murcia-Delso et al. 2013; Loffizadeh and Restrepo 2019]			
	DS-1	DS-2	DS-3	DS-4	UCSD-1	UCSD-2	UCSD-4	UCSD-5
f'_c (ksi), column	7.8	7.2	7.2	7.1	4.9	5.6	5.1	5.2
f'_c (ksi), transition region	7.4	6.5	8.4	6.7	5.0	5.4	5.3	4.9
f_y (ksi), column longitudinal reinforcement	68	68	62	65	65	67	66	87
f_u (ksi), column longitudinal reinforcement	106	106	86	96	91	92	94	114
f_y (ksi), shaft longitudinal reinforcement	66	66	67	69	70	67	64	82
f_u (ksi), shaft longitudinal reinforcement	101	101	92	98	97	93	92	110
f_y nominal (ksi), shaft transverse reinforcement	70	70	70	70	60	60	60	80
f_u (ksi), shaft transverse reinforcement	110	110	110	98	-	-	-	-

Table 7.3 Maximum measured strains in shaft transverse reinforcement at given drift ratios.

Drift Ratio	Reduced-scale specimens (Tran [2015] and current study)				Full-scale specimens [Murcia-Delso et al. 2013; Lotfizadeh and Restrepo 2019]			
	DS-1	DS-2	DS-3	DS-4	UCSD-1	UCSD-2	UCSD-4	UCSD-5
1.0% drift	0.0003	0.0005	0.0007	0.0007	0.0006	0.0005	0.0016 0.0007	0.0005
2.0% drift	0.0014	0.0022	0.0013	0.0025	0.0012	0.0010	0.0158 0.0009	0.0011
3.0% drift	0.0020	0.0047	0.0020	0.0045	0.0017	0.0015	0.0213 0.0012	0.0015
4.0% drift	0.0026	0.0068	0.0026	0.0061	0.0020	0.0018	0.0213 0.0017	0.0020
End of test	0.0035	0.012+	0.0028	0.050+	0.0025	0.0033	0.0226 0.0021	0.0029

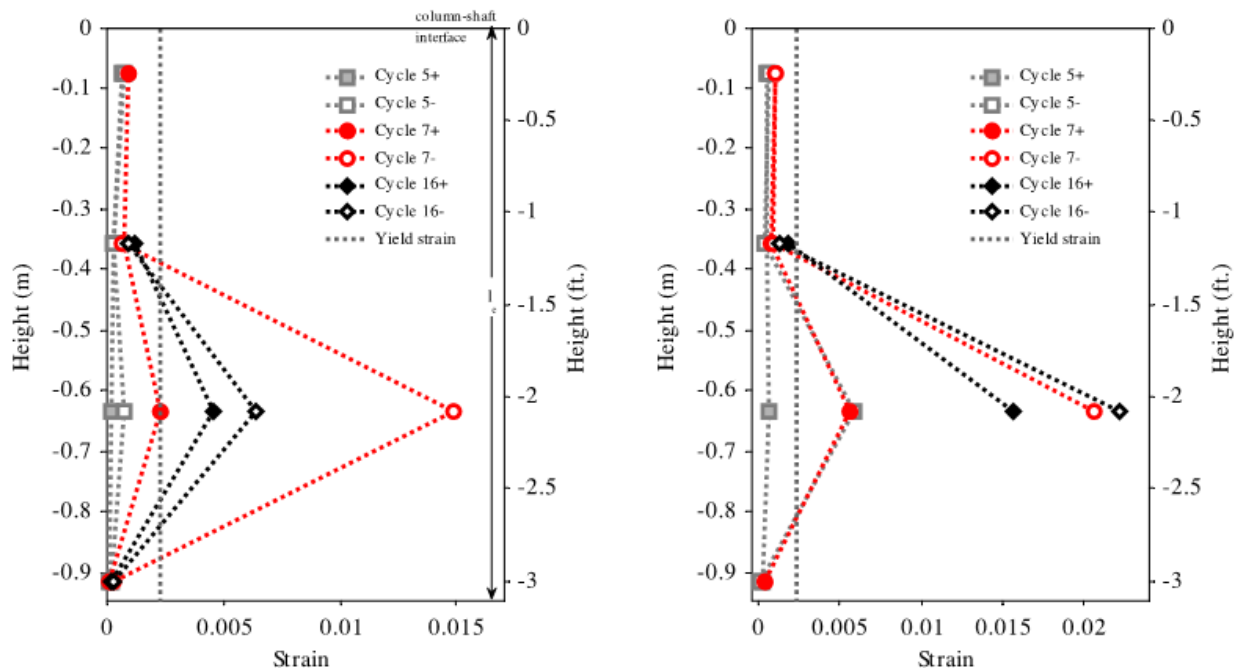


Figure 7.1 Strains in shaft hoops for Specimen UCSD-4: (a) north face and (b) south face [Murcia-Delso et al. 2013].

7.2 NONCONTACT LAP SPLICE MODEL: MCLEAN AND SMITH [1997]

McLean and Smith’s [1997] model required that the shaft transverse reinforcement be at least:

$$\frac{A_{tr}}{s} = \frac{A_l f_{u,l}}{2\pi f_{y,tr} l_s} \quad (7.1)$$

where A_{tr} is the cross-sectional area of transverse reinforcement in transition region; s is the pitch (i.e., center-to-center spacing) of transverse reinforcement; A_l is the total area of column longitudinal reinforcement; $f_{u,l}$ is the ultimate strength of column longitudinal reinforcement; $f_{y,tr}$ is the yield strength of transverse reinforcement; and l_s is the required typical (in-contact) Class C lap splice length for the larger of the shaft and column longitudinal bars per *AASHTO LRFD Bridge Design Specifications* [2010]. The AASHTO lap splice length requirements remained unchanged from 1995 through 2010. Hence, AASHTO BDS [2010] is cited here even though it was published after McLean and Smith's study.

McLean and Smith assumed that the load transfer between noncontact column and shaft longitudinal bars is uniform along the splice length, and that it is achieved using struts oriented at 45°. The model was developed for applied tension rather than bending.

Some of the eight specimens did not provide the minimum required Class C lap splice length l_s assumed in McLean and Smith's model. Therefore, when using McLean and Smith's model to determine the $\frac{A_{tr}}{s}$ required, the lap splice length l_s in Equation (7.1) was taken as:

$$l_s = \min \left\{ \begin{array}{l} 1.7l_d \\ l_{ns,provided} - e \end{array} \right. \quad (7.2)$$

The top term in Equation (7.2) represents the required lap splice length, and the bottom term represents the provided equivalent in-contact lap splice length. The top term in Equation (7.2) is the required Class C lap splice length per AASHTO BDS [2010], where l_d is the required shaft or column bar tension development length specified in AASHTO BDS [2010], per McLean and Smith's model. The lap splice length l_s used in Equation (7.1) to determine the transverse reinforcement should never be less than that physically provided in the specimen. The bottom term includes the provided noncontact lap splice length $l_{ns,provided}$ between the column and shaft bars, minus the eccentricity of the bars (e). This procedure is consistent with McLean and Smith's determination of the equivalent in-contact lap splice length for noncontact bars; the subtraction of the eccentricity (e) is consistent with McLean and Smith's assumption of 45° struts.

The results of the model evaluation, using the process described in Section 7.1, are summarized in Table 7.4 and plotted in Figure 7.2. Both axes use a logarithmic scale. Expected and achieved performance decrease respectively upwards and to the right in the plot. Hence, if the model is a good indicator of performance, the results should lie in a band from bottom left to top right. The data point for UCSD-4 (M) was plotted with a y -value of 2.0 to avoid distorting the plot scale. Its true y -value ($\frac{\epsilon_{tr}}{\epsilon_{y,tr}}$) is 7.64. For all specimens, the provided noncontact lap splice length was less than that required by McLean and Smith, so the bottom term in Equation (7.2) controlled. The evaluation results will be discussed at the end of this section following the presentation of the other force-transfer models.

Table 7.4 Evaluation of McLean and Smith’s [1997] model.

	Reduced-scale specimens (Tran [2015] and current study)				Full-scale specimens [Murcia-Delso et al. 2013; Lotfizadeh and Restrepo 2019]			
	DS-1	DS-2	DS-3	DS-4	UCSD-1	UCSD-2	UCSD-4	UCSD-5
l_d (in.) (controlling bar)	17.0 (col.)	17.0 (col.)	15.5 (col.)	16.3 (col.)	84.6 (shaft)	77.9 (shaft)	54.7 (shaft)	99.9 (shaft)
l_s (in.)	21.2	21.2	23.2	21.2	72.3	58.0	29.0	76.0
A_{tr}/s required (in.)	0.035	0.035	0.041	0.051	0.089	0.171	0.217	0.089

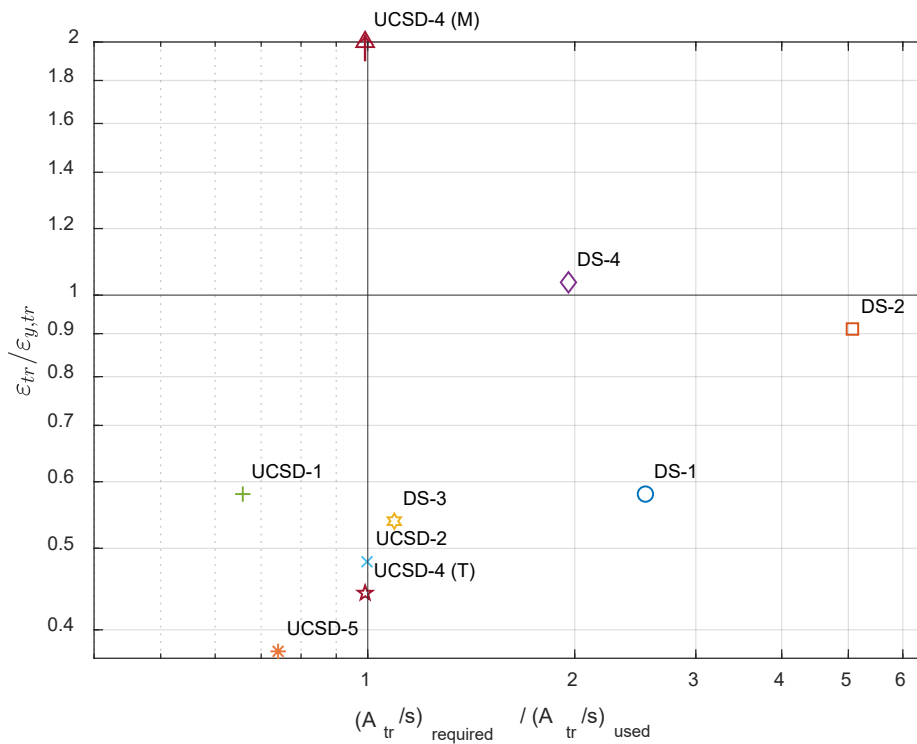


Figure 7.2 Evaluation of McLean and Smith’s [1997] model.

7.3 BOND-BASED MODEL: MURCIA-DELISO ET AL. [2013]

Murcia-Delso et al. [2013] suggested that the minimum shaft transverse reinforcement be:

$$\frac{A_{tr}}{s} = \frac{N_{col} d_{b,col} \tau_{max}}{2\pi f_{y,tr}} \quad (7.3)$$

where N_{col} = number of column longitudinal bars; $d_{b,col}$ = diameter of column longitudinal bars; and τ_{max} = maximum bond strength capacity of the column longitudinal bars. For 5 ksi concrete,

Murcia-Delso et al. took this value to be 2.4 ksi. For other concrete strengths, they recommended that this value be scaled proportionally to $f_c^{3/4}$.

Murcia-Delso's model is based purely on the bond of the column bars, and it does not depend on a particular strut-and-tie model configuration nor the embedment length of the column bars. Equation (7.3) conservatively assumes that the column bar bond demand is equivalent to the maximum bond capacity (τ_{max}), as a higher bond demand leads to a higher demand on the shaft transverse reinforcement. The results of the model evaluation, using the process described in Section 7.1, are summarized in Table 7.5 and plotted in Figure 7.3.

Table 7.5 Evaluation of Murcia-Delso et al.'s [2013] model.

	Reduced-scale specimens (Tran [2015] and current study)				Full-scale specimens [Murcia-Delso et al. 2013; Lotfizadeh and Restrepo 2019]			
	DS-1	DS-2	DS-1	DS-2	DS-1	DS-2	DS-1	DS-2
τ_{max} (ksi)	3.2	2.9	3.5	3.0	2.4	2.5	2.5	2.4
A_{tr}/s required (in.)	0.046	0.042	0.081	0.068	0.162	0.206	0.213	0.106

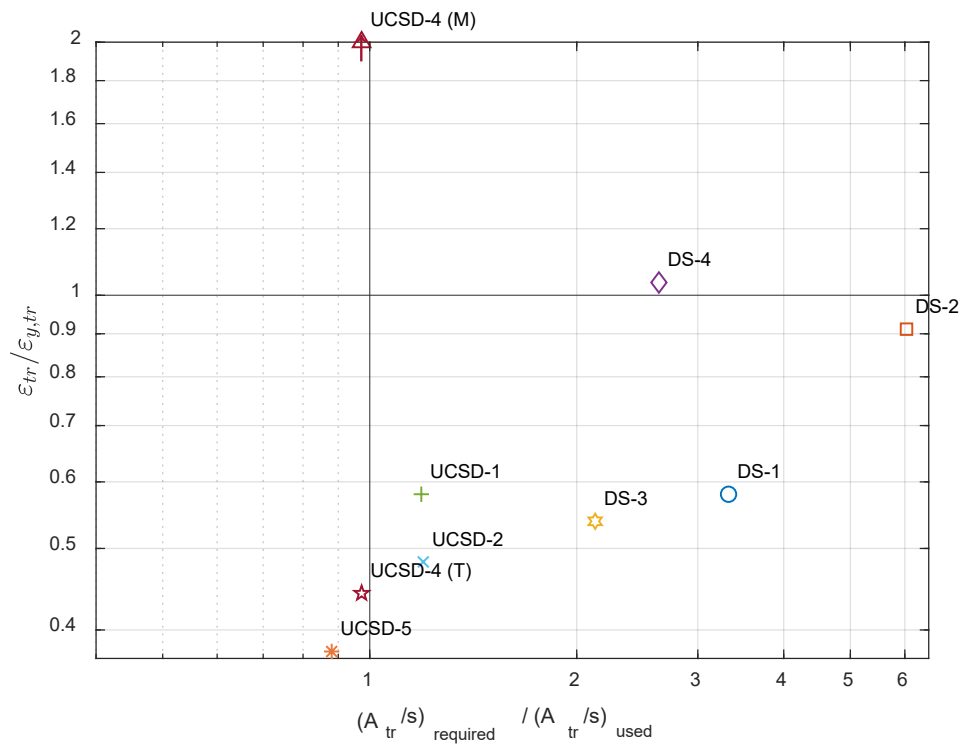


Figure 7.3 Evaluation of Murcia-Delso et al.'s [2013] model.

7.4 STRUT-AND-TIE MODEL: TRAN [2015]

Tran's design process [2015] was based on a strut-and-tie model of the transition region; see Figure 7.4. The design procedure for the shaft transverse reinforcement involves moment-curvature analysis to obtain the bar forces at the boundary of the region and solving for truss forces. As shown in Figure 7.4, the force resisted by the transverse reinforcement (force in Tie BC, F_{BC}) depends entirely on the magnitude of the resultant tension force in the shaft reinforcement (T_s), and the angle of the compression strut, θ .

$$F_{BC} = T_s / \tan \theta \quad (7.4)$$

To obtain a required-to-used reinforcement ratio, Tran distributed this force along the transverse reinforcement in depth L using the following equation.

$$\frac{\left(\frac{A_{tr}}{S}\right)_{required}}{\left(\frac{A_{tr}}{S}\right)_{used}} = \frac{F_{BC}}{\sum_{i=1}^{\frac{L}{S}} \left(2A_{tri} * f_{y,tr} \left(\frac{y_i}{L}\right)^2\right)} \quad (7.5)$$

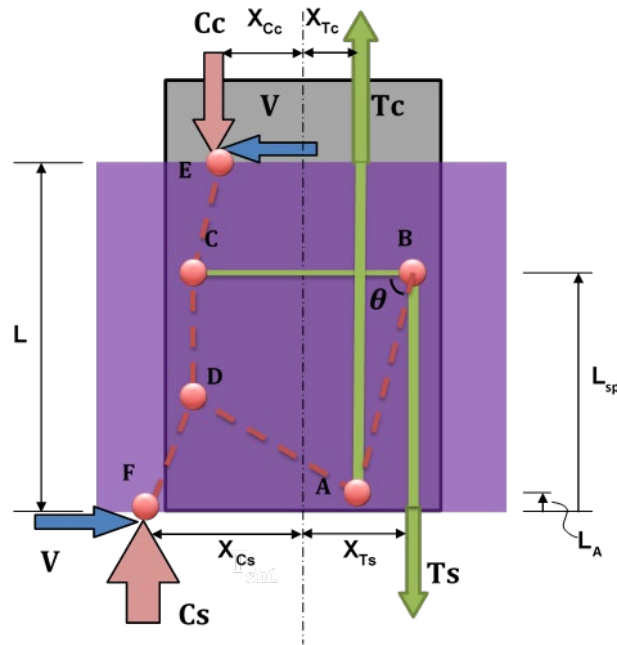


Figure 7.4 Tran [2015] strut-and-tie model for force transfer.

In Equation (7.5), the denominator represents the effective force capacity of the transverse reinforcement, with the assumptions that the stresses are distributed parabolically and the stress in the top hoop or turn of spiral is limited to a maximum of f_y . Each layer/turn of transverse reinforcement (layer i) in the transition region (which has a depth L) is expected to resist a stress of $f_{y,tr} \left(\frac{y_i}{L}\right)^2$; y_i is the vertical distance from the bottom of the transition region to layer i . The

numerator is the force demand on the transverse reinforcement. Therefore, if this required-to-used ratio is less than one, then the uppermost hoop or turn of spiral is below yield. If it is greater than one, the top turn cannot resist the force demand at that location without yielding.

The results of the model evaluation using Tran’s procedure are summarized in Table 7.6 and shown in Figure 7.5. Some of the values are different from those reported in Tran [2015] because errors were found in Tran’s assumed inputs. Additionally, Tran did not consider the bundled turns of spiral at the top of the shaft in his model evaluation; for this evaluation, the bundled turns were considered.

Table 7.6 Evaluation of Tran’s [2015] model.

	Reduced-scale specimens (Tran [2015] and current study)				Full-scale specimens [Murcia-Delso et al. 2013; Loffizadeh and Restrepo 2019]			
	DS-1	DS-2	DS-1	DS-2	DS-1	DS-2	DS-1	DS-2
L (in.)	28	28	28	28	56	72	37	72
L_A (in.)	2	2	2	3	8	9	5	11
L_{sp} (in.)	23	23	20	21	42	54	27	54
Tie BC Force (kips)	36	36	67	58	377	447	491	454
A_{tr}/s required	0.018	0.018	0.052	0.045	0.167	0.153	0.341	0.161

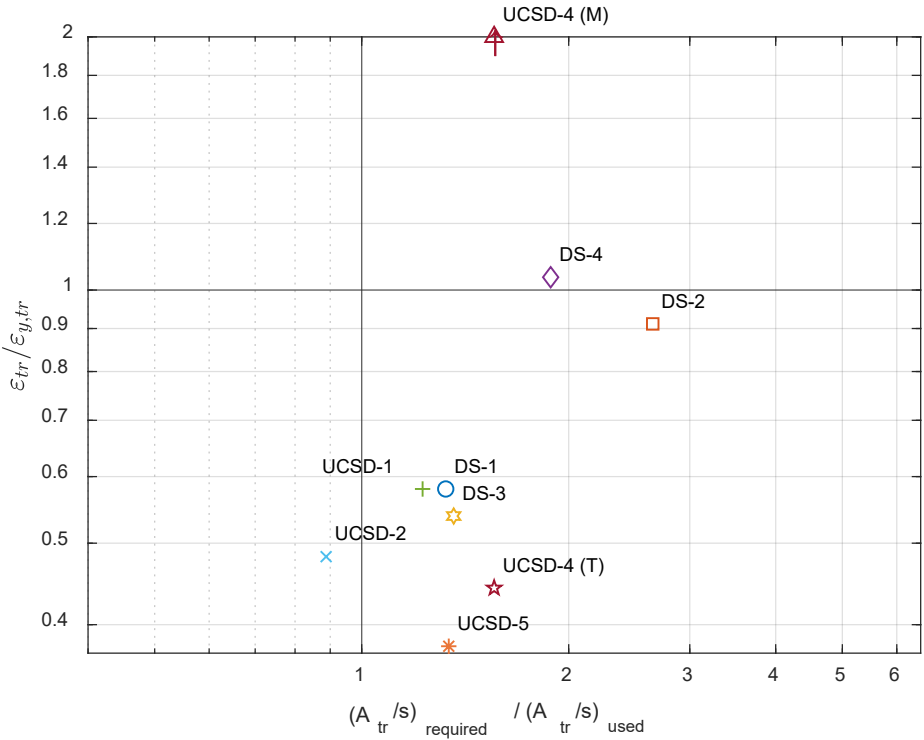


Figure 7.5 Evaluation of Tran’s [2015] model.

7.5 DISCUSSION OF MODEL EVALUATION RESULTS

All three design methodologies identified Specimen DS-2 as having inadequate transverse reinforcement, with used-to-required steel ratios of 0.16, 0.14, and 0.31 for the McLean and Smith, Murcia-Delso et al., and Tran methodologies, respectively. These results are consistent with the observed poor performance of this specimen; see Figure 6.6.

The performance of the McLean and Smith and Murcia-Delso et al. methodologies were similar. The amount of transverse reinforcement required by the two methodologies can be compared using the following equations.

$$\frac{A_{tr}}{S_{Murcia-Delso}} = \frac{N_{col}d_{b,col}\tau_{max}}{2\pi f_{y,tr}} = \left(\frac{A_l f_u}{2\pi f_{y,tr} l_s} \right) \left(\frac{4l_s \tau_{max}}{\pi d_b f_u} \right) \quad (7.6)$$

This relationship can also be written as:

$$\frac{A_{tr}}{S_{Murcia-Delso}} = \left(\frac{A_{tr}}{S_{McLean \& Smith}} \right) \left(\frac{4l_s \tau_{max}}{d_b f_u} * \frac{1}{\pi} \right) \quad (7.7)$$

The factor of $\frac{4l_s \tau_u}{d_b f_u}$ is equivalent to the bond capacity-to-axial capacity ratio for the column longitudinal bars. The values of this ratio for the eight specimens are listed in Table 7.7.

Both methodologies predicted that the performance of the USCD specimens would be adequate, which is consistent with the experimental response. Both methodologies incorrectly predicted that DS-4 would perform better than DS-1. The two models mainly differed in their performance estimates for DS-3 and UCSD-1. The Murcia-Delso et al. procedure predicted that DS-3 would perform poorly (A_{tr}/s required-to-used ratio = 2.13), whereas the McLean and Smith procedure predicted that DS-3 would perform more adequately (ratio = 1.09). A similar pattern is seen in UCSD-1. From Table 7.7, it can be seen that these two specimens had bond-to-axial capacity ratios significantly greater than those of other specimens. In DS-3, this ratio was larger than in other specimens due to the higher concrete strength ($f'_c = 8.4$ ksi) and consequently higher bond stress (τ_u), as well as lower ultimate strength of the column bars ($f_u = 86$ ksi). In UCSD-1, the bond-to-axial capacity ratio was large due to the long lap splice length, especially relative to the column bar diameter (l_s/d_b). The other specimens had bond-to-axial capacity ratios of approximately π , which led to similar results from both methodologies.

McLean and Smith's and Murcia-Delso et al.'s models were found to be overly conservative for Specimen DS-1. The specimen damage was concentrated at the column base with little damage in the shaft, and the shaft transverse strains barely exceeded yield by the end of the experiment, indicating that the shaft transverse reinforcement used was just short of sufficient. However, these models indicate that the shaft transverse reinforcement was only about 35% of that required.

Table 7.7 Bond-to-axial capacity ratios.

	Reduced-scale specimens (Tran [2015] and current study)				Full-scale specimens [Murcia-Delso et al. 2013; Lotfizadeh and Restrepo 2019]			
	DS-1	DS-2	DS-3	DS-4	UCSD-1	UCSD-2	UCSD-4	UCSD-5
$\tau_{max}l_s\pi d_b$ (kips)	134	122	161	124	769	784	228	960
$\pi d_b^2 f_u/4$ (kips)	33	33	26	29	142	208	74	257
$\frac{\text{bond capacity}}{\text{axial capacity}}$	4.1	3.7	6.1	4.2	5.4	3.8	3.1	3.7
$\frac{\text{bond cap.}}{\text{axial cap.}} * \frac{1}{\pi}$ [the factor in Eq. (7.7)]	1.3	1.2	1.9	1.3	1.7	1.2	1.0	1.2

Tran’s model, in contrast, might be overly conservative for Specimen UCSD-4 relative to the other specimens. The transverse strains in UCSD-4 throughout the experiment were low relative to those in the DS specimens; however, the model predicts worse behavior in UCSD-4 than in DS-1, DS-3, and DS-4. Additionally, Tran’s model appears to be generally conservative, as it implies that all of the specimens were under-reinforced, with a required-to-used ratio greater than one. Experimental evidence showed that the transverse reinforcement strains reached a maximum of about 0.002–0.003 among all UCSD specimens throughout the experiments, so it is not true that all specimens were under-reinforced.

Murcia-Delso et al.’s model is based on bond stress alone, and it does not assume any particular strut-and-tie configuration. In the development of an equation to determine the shaft transverse reinforcement [Equation (7.3)], the researchers took a conservative approach so that the transverse reinforcement would be designed to resist the maximum possible bond strength τ_{max} in the longitudinal reinforcement. The researchers noted that the true peak bond stress would be lower than τ_{max} due to tensile yielding of the bars. Additionally, the model does not address a possible difference in bond strength on each face of the longitudinal bars. The bond at the column and shaft bar faces that intersect with the transverse reinforcement is potentially different from the bond at the bar faces that are in direct contact with concrete. Therefore, if there is a bond constraint on the force transfer in the connection region, it may also be influenced by this difference. This concept is potentially supported by the observation of different behaviors on the two faces of the column bars in Specimens DS-2 and DS-4. On the outer face, at the split, the bars lost contact with (i.e., debonded from) the concrete, while inside the column cage, the concrete remained intact and in full contact with the bars.

Tran’s strut-and-tie model consisted of separate processes to analyze precast and CIP connections; however, because the model was developed based on precast specimens and later adapted for CIP connections, it did not explicitly compare the two types of connections or explore the reasoning for two separate processes. The analysis in Chapter 6 showed that the construction method (precast vs. CIP) did not significantly impact the behavior of the specimens, so a force-

transfer model should be applicable to both types of connections with no need for separate processes.

In developing, implementing, and verifying his model, Tran did not consider the band of bundled spiral used for termination at the top of shaft in Specimens DS-1 through DS-3; the spiral was assumed to be uniformly spaced for modeling purposes. However, the effect of the bundled spiral is potentially significant, as evidenced by large spiral strains in the uppermost turn of spiral immediately before termination, and thus this bundling should be accounted for during the evaluation process.

Finally, Tran referenced two methods for finding the tension development length of a reinforcement bar [Priestley 1993; Ingham 1995]. Both methods were used in Tran's proposed methodology, but their results were intended to represent the same parameter. This led to the use of two inconsistent numbers that both represented the development length of a bar. Ingham [1995] calculated development lengths are about half that of the Priestley development lengths, so this difference made a significant impact on the strut-and-tie model; therefore, a new model is needed to better predict the experimental behavior of all eight specimens.

8 Strut-and-Tie Model for Column–Shaft Connections

As discussed in Chapter 7, existing models do not consistently predict the relative behavior, from most to least favorable, observed in eight experimental column–shaft connection specimens. This chapter proposes a new strut-and-tie model to describe the force-transfer behavior in column–shaft connections. It also introduces design recommendations based on both McLean and Smith’s [1997] noncontact lap splice model and the strut-and-tie model.

8.1 INTRODUCTION OF PROPOSED MODEL

The proposed force-transfer model and methodology is adapted from Tran’s [2015] methodology. It assumes that the force-transfer mechanism in the connection region can be described by a 2D strut-and-tie model; see Figure 8.1. This strut-and-tie configuration underlies a statically consistent, reasonable methodology to evaluate and design the reinforcement layout within a column–shaft connection.

First, the transition region depth, node locations, and boundary forces on the transition region need to be determined. Then, the strut-and-tie forces in the model, as shown in Figure 8.1, can be calculated. The tie forces represent the resultant demands on the longitudinal and transverse reinforcement in the transition region. Therefore, upon determining the forces, the reinforcement can be properly detailed to resist the expected peak loading. The analysis procedure is described in detail in the next section.

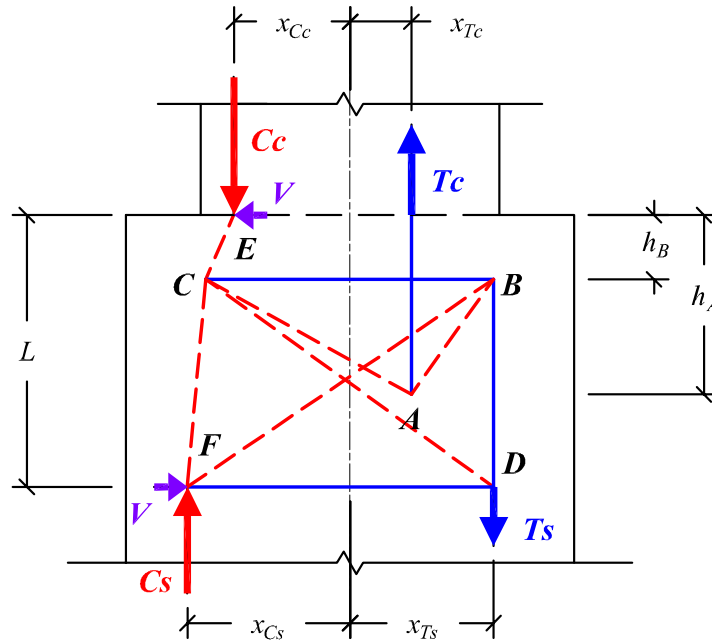


Figure 8.1 Proposed strut-and-tie model.

The boundary forces and dimensions in Figure 8.1 are defined as follows. The process to find these forces and dimensions, as well as definitions for nodes, struts, and ties, will be defined within the analysis procedure.

C_c = compressive resultant force from the column

T_c = tensile resultant force from the column

x_{Cc} = distance from column compressive resultant force to the centroid of column

x_{Tc} = distance from column tensile resultant force to the centroid of column

C_s = compressive resultant force from the shaft

T_s = tensile resultant force from the shaft

x_{Cs} = distance from shaft compressive resultant force to the centroid of shaft

x_{Ts} = distance from shaft tensile resultant force to the centroid of shaft

V = column base shear force

While the truss in Figure 8.1 is statically indeterminate, it can be separated into two statically determinate modes, one of which will control over the other in a connection under a given load combination; see Figure 8.2. The configurations are named V and M , representing shear-dominant and moment-dominant modes, respectively. The only difference between the two configurations is the orientation of the shaft diagonal strut. In the V -Configuration, the strut connects nodes F and B , whereas in the M -Configuration, the strut connects nodes C and D . In the V -Configuration, DF is always a zero-force member.

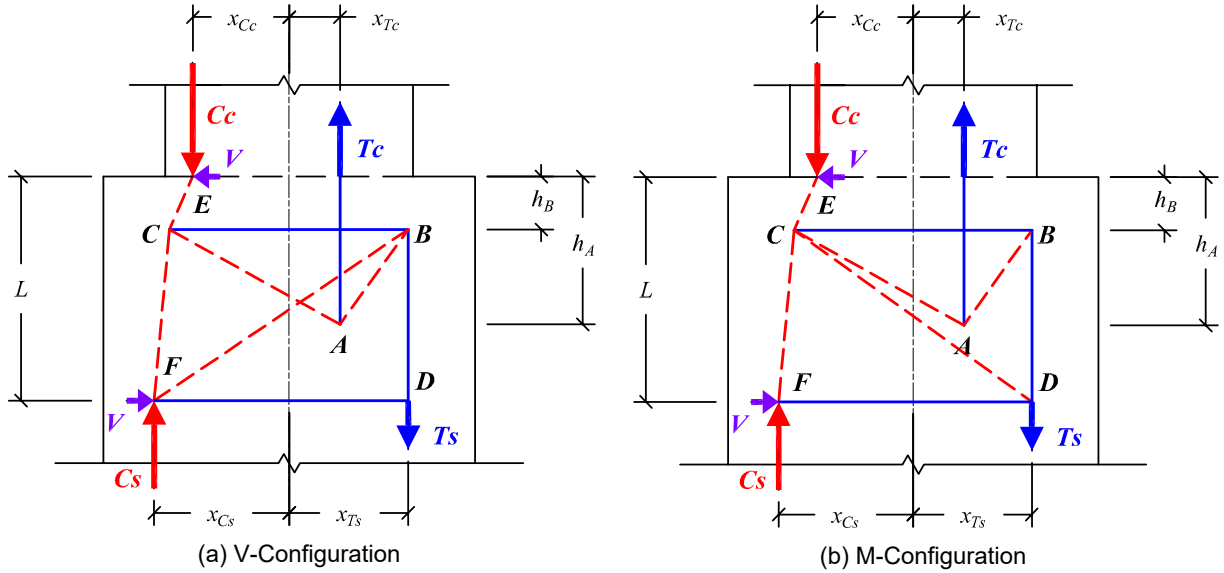


Figure 8.2 Strut-and-tie configuration modes.

The controlling configuration can be identified by considering horizontal equilibrium of Node F. If one assumes that struts can only resist compression, then the V-Configuration will control if the shear, V , exceeds the horizontal component of strut CF . For example, the V-Configuration will always control if the connection is subjected to a pure shear force in the absence of flexural forces, C_c and T_c . In this special case, strut members AC and AB would carry no force (because of equilibrium at Node A). Similarly, member DF would not carry any force because of vertical equilibrium considerations at Node D. For pure shear, the tie force can be computed as:

$$F_{BC} = V \quad (8.1)$$

The M-Configuration will always control if the connection is subjected to pure bending with no shear force. In this special case, an inclined compressive strut force, F_{CF} , is needed to balance the horizontal reaction at Node F. Considering equilibrium at Nodes A and B, the tie force can be computed as the following, where θ is the strut angle measured from the horizontal:

$$F_{BC} = \frac{T_c}{\tan \theta_{AB} + \tan \theta_{AC}} \quad (8.2)$$

Of course, most connections are subjected both to shear and flexural bending, so until one checks the relative magnitudes of the horizontal component of F_{CF} and shear, V , it is not clear a priori which configuration will control. The controlling configuration is dependent on the shear-to-moment-demand ratio, axial load, and connection geometry. The following section will describe the full analysis procedure to solve the strut-and-tie model, which can then be used to assess whether the provided transverse reinforcement is sufficient for the reinforcement stresses to remain under a certain threshold, such as the nominal yield stress.

8.2 MODELING AND ANALYSIS PROCEDURE

The analysis procedure is as follows:

1. Column moment-curvature analysis:

- Perform moment-curvature analysis for the column to find the moment demand on the transition region and the boundary force locations. In bridge substructures, the column is designed to be the critical member in which a plastic hinge develops; the shaft is capacity-protected. Therefore, the moment capacity of the column based on actual or expected material properties will control the moment demand on the transition region.
- From the column moment-curvature analysis, determine the resultant compressive and tensile forces C_c and T_c , along with their locations x_{Cc} and x_{Tc} . All locations in the model (e.g., x_{Cc} and x_{Tc}) are taken as dimensions and do not carry a positive or negative sign.
- Using the column moment capacity and distance to the inflection point, find the corresponding column shear force V .

2. Approximate the transition depth:

Approximate the transition depth L using Equation (8.3). This is a rough estimate in order to proceed with the next step; the revised depth of the transition region L is calculated later in the analysis procedure.

$$L \approx 1.5l_{d,c} \quad (8.3)$$

where $l_{d,c}$ = tension development length of column longitudinal bar per AASHTO BDS [2017] Section 5.10.8, including all modification factors (λ). In particular, the reinforcement confinement factor λ_{rc} will significantly influence the development length. Assuming that $\lambda_{rc} = 0.4$ (which assumes well-confined bars and is the lower limit of λ_{rc}) and all other $\lambda = 1.0$, $l_{d,c}$ required by AASHTO BDS [2017] is 1.2 times that required by Priestley [1993].

The 1.5 factor in the equation was empirically derived. L represents the depth of the transition region and the depth of the effective transverse reinforcement that will resist the connection demand. Since it depends on the effective eccentricity of the column and shaft bars, which is determined from the column and shaft moment-curvature analyses, and the latter moment-curvature analysis is dependent on L , the process is iterative.

3. Shaft moment-curvature analysis:

- Perform a moment-curvature analysis for the shaft section at the approximate transition depth L to determine its state when the column is at its maximum moment capacity. Because the shaft dimensions and reinforcement are likely controlled by the larger moment demand below grade, the stresses in the shaft at this stage may be in the elastic range.
- L is the height of the D-region of the strut-and-tie model, in which beam theory might not apply and the moment and shear strengths cannot be evaluated separately. However, below

the D-region, the shear and moment behaviors are essentially independent, so moment-curvature analysis is appropriate at the transition depth L .

- From the shaft moment-curvature analysis, determine the resultant forces C_s and T_s , along with their locations x_{C_s} and x_{T_s} .

4. Find the revised transition depth:

Calculate the revised elevation of L using Equation (8.4). This equation is consistent with McLean and Smith's [1997] truss analogy for the force transfer between the column and shaft bars, with the exception that Equation (8.4) assumes 60° struts (to the horizontal) rather than the 45° struts assumed by McLean and Smith. While the strut-and-tie model overall does not presuppose a strut angle for strut AB , this assumption of 60° struts is used in this step to achieve a close approximation for L . Otherwise, iteration through the majority of the analysis procedure would be necessary to find both the strut angle and transition depth. It was found that even with iteration, the angle of strut AB in seven of the eight specimens was approximately 60° .

$$L = \min \begin{cases} l_{d,c} + \sqrt{3}e_{ef} + c \\ l_e \end{cases} \quad (8.4)$$

where $l_{d,c}$ is the tension development length of column longitudinal bars per AASHTO BDS [2017] Section 5.10.8, including all modification factors (λ); e_{ef} is the horizontal distance between T_c and T_s , i.e., $x_{T_s} - x_{T_c}$; and c is the top cover from column–shaft interface to shaft longitudinal bars.

In theory, another iteration loop between steps 3 and 4 would be necessary to determine L , due to the interactive relationship between e_{ef} and L (even with the assumption of 60° struts). However, the solution quickly converges in one loop or less. The values of e_{ef} and the boundary forces are not very sensitive to changes in L , so it is sufficient to proceed without iteration.

5. Find the node locations:

- The node locations remain the same regardless of which configuration (Figure 8.2) controls. In the strut-and-tie model, each node or truss member represents the centroid or resultant of several nodes, struts, or ties in the force-transfer mechanism. For simplicity, they are described as points or one-dimensional members in these steps.
- Node A depth L_A is found using Equation (8.5).

$$h_A = \begin{cases} \frac{l_{d,c}}{2} + \sqrt{3}e_{ef} + c, & l_e \geq l_{d,c} + \sqrt{3}e_{ef} + c \\ \frac{1}{2}(l_e - \sqrt{3}e_{ef} - c), & l_e < l_{d,c} + \sqrt{3}e_{ef} + c \end{cases} \quad (8.5)$$

The effective force-transfer length of the column longitudinal bars is assumed to start at a depth of approximately $\sqrt{3}e_{ef} + c$ below the column–shaft interface (based on McLean

and Smith's [1997] model for noncontact lap splices {Section 2.1.1}, but using a strut angle of 60° rather than 45°), and end when the bars are fully developed or at the end of the bars, whichever occurs first. The depth of Node A is located at the center of this effective force-transfer length. Equation (8.5) expresses this concept. Laterally, Node A is placed in line with boundary force T_c .

- Node B is the location at which the tensile force is transferred to the shaft longitudinal bars and shaft spiral or hoops. Its depth h_B is located at the centroid of the transverse resultant force, assuming that the shaft longitudinal bars are developed by that point. If the shaft longitudinal bars are not able to be developed at the transverse force centroid, then Node B is located at the center of the effective force-transfer length for the shaft longitudinal bars. This condition is described in Equation (8.6).

$$h_B = \max \left\{ \begin{array}{l} \text{centroid of transverse resultant force} \\ c + \frac{l_{d,s}}{2} * \frac{\varepsilon_s}{\varepsilon_{y,s}} \end{array} \right. \quad (8.6)$$

where $l_{d,s}$ = tension development length of shaft longitudinal bars per AASHTO BDS [2017] Section 5.10.8, including all modification factors (λ) besides the excess reinforcement factor (λ_{er}); ε_s = maximum strain in shaft longitudinal bars at the transition depth L , at the instant when the column is at its peak moment capacity—this can be found from moment-curvature analysis of the shaft; and $\varepsilon_{y,s}$ is the yield strain of shaft longitudinal bars

The $\frac{\varepsilon_s}{\varepsilon_{y,s}}$ factor accounts for the fact that the shaft bars will not reach yield at the instant when the column is at its peak moment capacity, so less than the full tension development length is required. This is analogous to the excess reinforcement factor (λ_{er}) in AASHTO BDS [2017].

The centroid location is dependent on the assumed transverse strain distribution along the transition depth L and the transverse reinforcement spacing. The transverse strain distribution is assumed to be parabolic based on experimental results; see Chapter 5 and Chapter 6. If the spiral is designed to remain elastic throughout loading (per AASHTO SGS 4.7.1), then the stress distribution profile is also parabolic. The transverse reinforcement spacing can be uniform, as in Specimens UCSD-1 through UCSD-5, or nonuniform, as in Specimens DS-1 through DS-4 (which each had three turns of bundled spiral at the top of the transition region).

Laterally, Node B is placed in line with boundary force T_s .

- Node C is located at the same depth as Node B to form horizontal tie BC . Laterally, it is located at the intersection of tie BC and strut EC (whose angle is defined by the ratio of V/C_c).

- Nodes D, E, and F are located at the top and bottom boundaries of the transition region. Laterally, they are placed in line with the boundary forces at x_{Ts} , x_{Cc} , and x_{Cs} (respectively, measured from the centerline of the corresponding section (column or shaft)).

6. Determine the strut and tie forces in the STM:

- Because the truss in Figure 8.1 is statically indeterminate, an additional assumption is necessary to solve the system quickly without the use of structural analysis software. It is assumed that the truss has two possible configurations; see Figure 8.2. Depending on the shear, moment, and axial load applied to the connection, the configuration with compressive diagonal struts will control. Therefore, the procedure is as follows:
- Determine which configuration controls (Figure 8.2) by first assuming that the M-Configuration controls, finding the magnitude of the horizontal component of strut CF , and comparing it to the shear force, V . Equation (8.7) describes this component based on vertical and horizontal equilibrium at Node F (the superscript M refers to the assumed moment-dominant mode). In the equation, C_s , C_c , and V are the magnitudes of the compressive and shear forces.

$$F_{CF,H}^M = \frac{C_s}{L - h_B} \left(x_{Cs} - x_{Cc} - h_B \frac{V}{C_c} \right) \quad (8.7)$$

If $F_{CF,H}^M < V$, then the V-Configuration controls. The true magnitude of $F_{CF,H}$ will be different than that found in Equation (8.7) since the equation was developed based on the M-Configuration.

If $F_{CF,H}^M > V$, then the M-Configuration controls.

If $F_{CF,H}^M = V$, then the members BF , CD , and DF are zero-force members, and the two configurations are identical.

- Solve for the forces in the controlling strut-and-tie configuration.
- Strut AB represents the noncontact lap splice force-transfer mechanism between the column and shaft tension reinforcement. This (2D) strut is the resultant of all compressive struts acting (in 3D) between the longitudinal bars.
- Tie BC is a 2D representation of the 3D resultant force acting on all the shaft transverse reinforcement in the transition region.

7. Distribute the transverse tie force among the reinforcement:

- Calculate the effective force demand on the shaft transverse reinforcement F_{tr} using Equation (8.8). The tie force F_{BC} represents all transverse ties acting radially in an arc around the cross-section of the connection; F_{tr} represents the component of the tie force in the transverse direction (i.e., in the direction perpendicular to loading).

$$F_{tr} = V + \frac{F_{BC} - V}{\pi/2} \quad (8.8)$$

In Equation (8.8), the first term represents the shear demand on the spiral or hoop reinforcement, all of which occurs in the transverse direction. The remainder of the load in tie BC is $F_{BC} - V$, which is attributed to the moment and axial loads. The transverse component of this remaining load is related to the total remaining load by a factor of $1/(\pi/2)$ based on circular geometry.

Specifically, the 3D force in the spiral per unit length (i.e., height) for half of the shaft (cut vertically through its diameter, Figure 8.3) is:

$$\frac{F}{l} = \frac{\pi D}{2} p \quad (8.9)$$

where p is the confinement pressure from the concrete, which acts around half of the circumference of the confined core.

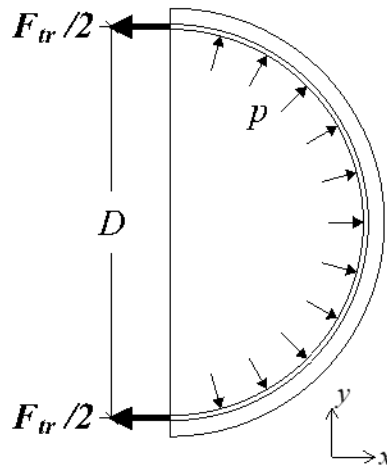


Figure 8.3 Determination of transverse component factor.

The component of F in the direction parallel to the loading is illustrated as F_{tr} in Figure 8.3. Based on equilibrium in the x -direction, it can be expressed as the following. The confinement force per unit height in the horizontal direction is Dp .

$$\frac{F_{tr}}{l} = Dp \quad (8.10)$$

Therefore, the transverse component of the load on the hoops or spirals due to moment and axial load is related to the total load in the hoops or spirals due to moment and axial load by a factor of $1/(\pi/2)$.

- Distribute F_{tr} among the provided shaft transverse reinforcement using the stress and reinforcement distribution assumed in Step 5.
- If the stress in each level of spiral or hoop exceeds $f_{y,tr}$, then the reinforcement is considered to be inadequate per AASHTO SGS 4.7.1 because it does not

prevent yielding in the shaft. Agencies recommend that the reinforcement in below-ground elements remain elastic to lessen the need for underground repairs.

Sample results from this analysis procedure, including moment-curvature results and STM forces, are summarized in the next section.

8.3 VERIFICATION OF PROPOSED MODEL

The strut-and-tie analysis procedure was completed for each specimen. The magnitudes and locations of the boundary forces were calculated using an in-house moment-curvature analysis program [Stanton 2010] and are summarized in Table 8.1. Key strut-and-tie node locations and results are reported in Table 8.2.

Table 8.2 also shows the results of the calculations to verify the strut-and-tie model, which was evaluated following the procedure described in Section 7.1. In the table, positive force values indicate that the force directions were consistent with the assumed strut-and-tie configuration (i.e., struts were compressive, and ties were tensile). Negative force values indicate that the member carried force in the direction opposite to the one assumed (e.g., an assumed tie was actually in compression). The measured vs. expected performance of the specimens, represented by $\frac{\epsilon_{tr}}{\epsilon_{y,tr}}$ vs. the force demand-to-capacity ratio (which is an analogous ratio to $\left(\frac{A_{tr}}{s}\right)_{required} / \left(\frac{A_{tr}}{s}\right)_{used}$), is plotted in Figure 8.4. The measured strains used in the comparison correspond to the peak transverse strain developed at 2.0% drift. The force demand-to-capacity ratio was calculated similarly as in Equation (7.5) (which was used to evaluate the Tran [2015] model), with a substitution of F_{tr} in place of F_{BC} . The modified equation is as follows.

$$\frac{\text{Force demand}}{\text{Force capacity}} = \frac{F_{tr}}{\sum_{i=1}^{\frac{L}{s}} \left[2A_{tri} * f_{y,tr} \left(\frac{y_i}{L} \right)^2 \right]} \quad (8.11)$$

In Equation (8.11), the denominator represents the effective force capacity of the transverse reinforcement, assuming that the stresses are distributed parabolically, and the stress in the top hoop or turn of spiral is limited to a maximum of $f_{y,tr}$. Each layer/turn of transverse reinforcement (layer i) in the transition region is expected to resist a stress of $f_{y,tr} \left(\frac{y_i}{L} \right)^2$; y_i is the vertical distance from the bottom of the transition region to layer i . The numerator is the force demand on the transverse reinforcement. Therefore, if this demand-to-capacity ratio is less than one, then none of the hoops or spirals have yielded. If it is greater than one, the top turn(s) cannot resist the force demand without yielding.

Table 8.1 Calculated boundary forces and locations in the transition region.

	Reduced-scale specimens (Tran [2015] and current study)				Full-scale specimens [Murcia-Delso et al. 2013; Loffizadeh and Restrepo 2019]			
	DS-2	DS-3	DS-2	DS-3	DS-2	DS-3	DS-2	DS-3
Axial load (kips)	159	159	159	159	800	800	800	800
Column base moment (kip*in)	3530	3530	4165	4433	54,041	72,640	61,061	69,893
Shear force V (kips)	59	59	70	74	281	336	318	364
Transition depth L (in.)	23.1	24.1	21.1	25.3	63.9	71.5	37.0	88.2
C_c (kips)	364	364	434	462	2443	3206	2656	3011
T_c (kips)	205	205	275	303	1643	2406	1856	2211
x_{Cc} (in.)	7.4	7.4	7.2	6.9	16.0	15.9	16.0	16.9
x_{Tc} (in.)	4.1	4.1	3.8	4.1	9.1	9.0	10.0	8.6
C_s (kips)	317	320	401	382	1870	2416	2209	2511
T_s (kips)	158	161	242	223	1070	1616	1409	1711
x_{Cs} (in.)	11.3	11.3	9.1	10.9	26.2	25.7	21.8	26.4
x_{Ts} (in.)	8.3	8.3	8.1	9.6	21.5	21.5	17.5	20.9

Table 8.2 Strut-and-tie model results.

	Reduced-scale specimens (Tran [2015] and current study)				Full-scale specimens [Murcia-Delso et al. 2013; Loffizadeh and Restrepo 2019]			
	DS-2	DS-3	DS-2	DS-3	DS-2	DS-3	DS-2	DS-3
h_A (in.)	15.6	16.1	14.7	17.8	44.2	48.0	10.5	56.3
h_B (in.)	5.1	5.4	5.0	5.8	18.2	21.1	18.2	28.2
$F_{CF,H}^M$	53	51	28	60	331	362	426	254
STM mode/ configuration	V	V	V	V	M	M	M	V
θ_{AB}	68°	68°	66°	66°	64°	65°	-46°	66°
θ_{AC}	41°	41°	39°	45°	44°	45°	-15°	44°
F_{BC} (kips)	68	70	134	111	538	763	-1426	806
F_{tr} (kips)	64	66	110	97	445	608	-792	646
$f_{y,tr}$ (ksi)	70	70	70	70	60	60	60	80
$\varepsilon_{y,tr}$	0.0024	0.0024	0.0024	0.0024	0.0021	0.0021	0.0021	0.0028
$\frac{\text{Force demand}}{\text{Force capacity}}$	3.29	6.51	2.76	3.00	1.27	1.22	-2.51	1.10
A_{tr}/s required	0.045	0.045	0.104	0.078	0.172	0.209	-0.446	0.132

As shown in Table 8.2, analysis of Specimen UCSD-4 using the strut-and-tie procedure results in a shaft node (Node B) that is deeper than the column node (Node A), leading to negative values for strut angles, compressive forces in the ties, and tensile forces in the struts, all of which are the opposite of what should be expected. This can be explained by the following phenomena observed in UCSD-4:

- Specimen UCSD-4 consisted of #8 column bars and #11 shaft bars. The column bars were embedded in the shaft a much shorter distance than in any other UCSD specimen. Because of their smaller diameter, they were also able to be developed much faster (shallower) than the shaft bars, leading the STM to generate negative strut angles.
- The strains in the shaft transverse reinforcement in UCSD-4 were not distributed parabolically; see Figure 7.1. This conflicts with the assumed distribution of strains in the STM.
- While large vertical splitting cracks were observed in the shaft throughout much of testing, the specimen still ultimately failed at the base of the column. This damage progression was unique to UCSD-4 and implies that some other force-transfer mechanism was in effect.

The strut-and-tie procedure performed adequately for all other specimens. Figure 8.4 shows the evaluation results for the proposed model. Overall, the model is conservative, but it successfully predicts the relative behavior of most of the specimens. It suggests that the demand-to-capacity ratio was higher for the DS specimens than the UCSD specimens and was highest of all for Specimen DS-2. These results are consistent with the observed behavior of the specimens.

While the model did not predict worse behavior in Specimen DS-4 compared to Specimen DS-1, which was observed in the experiments, it still performs better than McLean and Smith's [1997] model and Murcia-Delso et al.'s [2013] model in this regard; see Chapter 7. The evaluation suggests that this strut-and-tie model might be more suitable than previous models for describing the force-transfer behavior in a column–shaft connection.

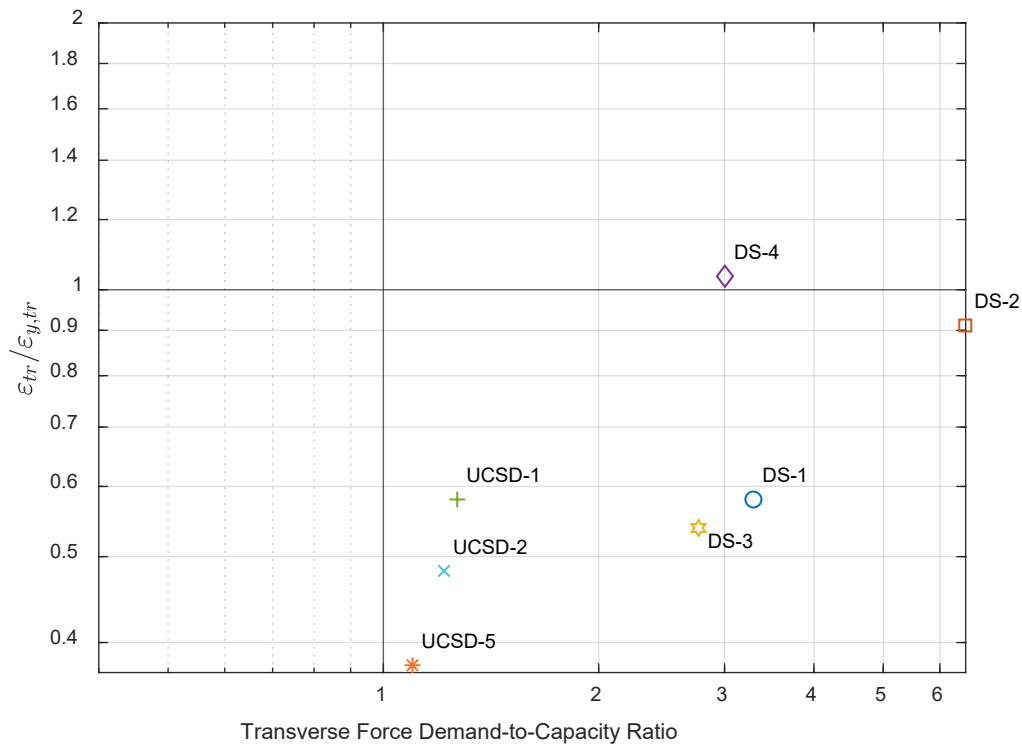


Figure 8.4 Evaluation of proposed strut-and-tie model

8.4 CONCRETE CONTRIBUTION TO SHEAR TRANSFER

Figure 8.4 shows that the proposed strut-and-tie model is conservative compared to the observed behavior of the specimens. For example, all of the UCSD specimens failed favorably, with most of the damage concentrated at the base of the column and less damage in the shaft. Some of the conservatism in the prediction might be explained by any contribution of the concrete to the total shear resistance. This concrete contribution was not considered in the model evaluation shown in Figure 8.4.

The concrete shear resistance can be described as (adapted from Equation 5.7.3.3-3 in AASHTO BDS [2017]):

$$V_c = 0.0316\beta\sqrt{f'_c}A_v \quad (8.12)$$

where V_c is the concrete contribution to shear resistance (kips); β is the factor indicating the ability of diagonally cracked concrete to transmit tension and shear, taken as 2.0 in this case with column–shaft connections; f'_c is the concrete strength of transition region (ksi); A_v is the effective shear area (in.²) = $0.8\pi D_s^2/4$ for a round shaft, where the 0.8 factor represents the assumption that the effective shear area is 80% of the section area; and $0.0316 = 1/\sqrt{1000}$ is the conversion factor between $\sqrt{\text{ksi}}$ and $\sqrt{\text{psi}}$. Therefore, the shear demand on the transverse reinforcement becomes:

$$V_{u,s} = V - V_c \geq 0 \quad (8.13)$$

where $V_{u,s}$ is the shear demand on the steel; and V is the total shear demand as determined from the column moment-curvature analysis.

The shear demand on the reinforcement ($V_{u,s}$) can then be used as a boundary force in the STM. In seven of the specimens used in the evaluation, the concrete shear resistance exceeds the total shear demand, so $V_{u,s} = 0$ and the M-Configuration controls. After accounting for the concrete shear resistance, the M-Configuration is always expected to control in typical column–shaft connections. Exceptions occur in connections in which the column shear span is very small, or the shaft-to-column-diameter ratio is large. The model evaluation results, considering a concrete component per Equation (8.12) and Equation (8.13), are shown in Table 8.3 and Figure 8.5.

Figure 8.5 shows that by considering the concrete shear resistance, the procedure better correlates with the measured results. Note that transfer of shear through the concrete in the transition region implies diagonal compression (in the direction of strut BF) and simultaneous tension in the perpendicular direction (i.e., some tension force carried by the concrete in the direction of strut CD). Since the strut-and-tie model was developed to predict the connection behavior when the column is at its peak moment capacity, and shaft cracks at this instant were small in all specimens, this diagonal concrete tension is plausible. However, after cracks grow, the shear transfer mechanism must change, as the concrete is no longer able to carry diagonal tension. This post-cracking behavior lies outside the scope of the strut-and-tie model.

Table 8.3 Concrete shear contribution results. See Section 8.3 for an explanation of UCSD-4.

	Reduced-scale specimens (Tran [2015] and current study)				Full-scale specimens [Murcia-Delso et al. 2013; Lotfizadeh and Restrepo 2019]			
	DS-1	DS-2	DS-3	DS-4	UCSD-1	UCSD-2	UCSD-4	UCSD-5
V (kips)	59	59	70	74	281	336	318	364
V_c (kips)	97	91	78	93	460	478	329	457
$V_{u,s}$ (kips)	0	0	0	0	0	0	0	0
F_{tr} (kips)	33	33	48	51	289	409	N/A	360
$\frac{\text{Force demand}}{\text{Force capacity}}$	1.95	3.74	1.40	1.81	0.95	0.94	N/A	0.71
A_{tr}/s required	0.027	0.026	0.053	0.047	0.129	0.162	N/A	0.085

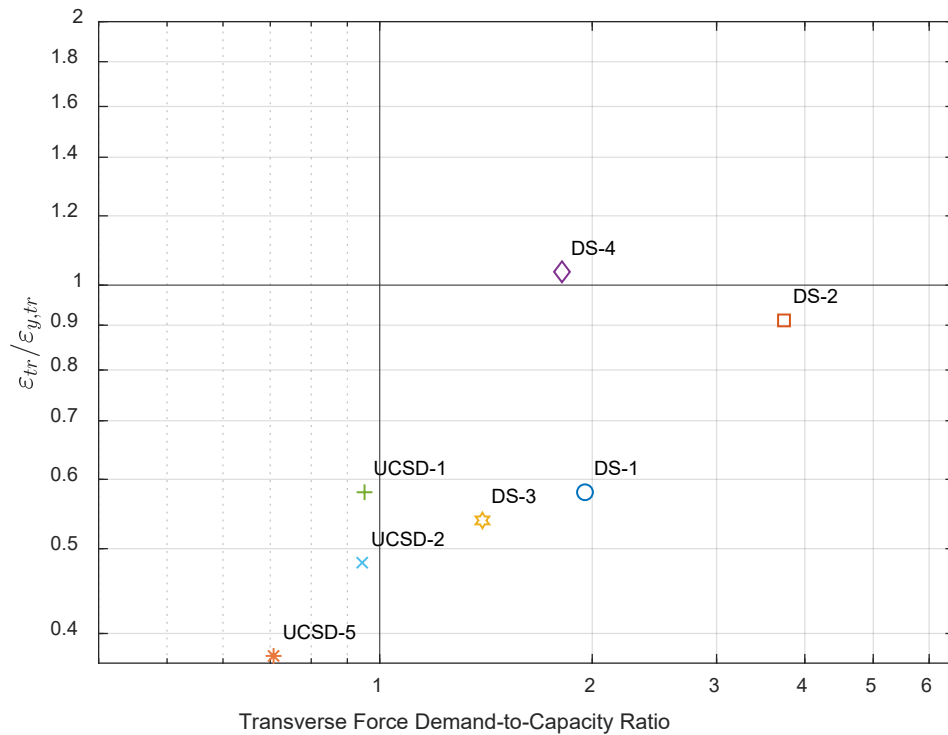


Figure 8.5 Evaluation of strut-and-tie model considering concrete shear resistance.

8.5 ADDITIONAL CONCRETE CONTRIBUTION

The model with consideration of the concrete shear resistance, using Equation (8.12), still does not accurately predict worse behavior in Specimen DS-4 compared to Specimen DS-1. Additionally, it remains conservative for all specimens. Some of the remaining difference between the predicted and measured behavior might be explained by a tensile concrete force, parallel to the tie force F_{tr} , in addition to the concrete shear resistance outlined in Section 8.4. The specific mechanism of this

component is unknown, but the component would transfer some force between the column and the shaft outside of the realm of the proposed strut-and-tie model. This would reduce the force demand on the transverse reinforcement (F_{tr}).

The concrete component can be hypothesized as a function of the effective concrete shear area and tensile stress. One possible form of this is:

$$F_c = D_s L * 0.35 * 0.0316 \sqrt{f'_c} \quad (8.14)$$

where F_c is the force in concrete component (kips); D_s is the shaft diameter (in.); L is the depth of transition region (in.); and f'_c is the concrete strength of transition region (ksi).

In Equation (8.14), 0.35 is an empirical factor that was chosen to give a demand-to-capacity ratio of approximately one for Specimens DS-1 and DS-3, which both performed favorably with little damage in the shaft. $D_s L$ assumes that the effective tensile concrete area is the area of a vertical plane cut through the middle of the shaft. The component F_c can then be subtracted from the force demand on the transverse reinforcement (F_{tr}), and a new ratio of force demand-to-capacity can be found.

Similarly to the concrete shear resistance component V_c described in Section 8.4, the use of F_c assumes that concrete can carry horizontal or diagonal tension. This concrete tension is plausible in the realm of the strut-and-tie model, in which shaft cracks remain small. After the cracks in the shaft grow, the use of F_c can no longer be justified.

The model evaluation results, considering a concrete component per Equation (8.14) in addition to the concrete shear resistance, are shown in Table 8.3 and Figure 8.6.

Figure 8.6 shows that by considering an additional concrete component, the analysis procedure can predict the observed performance of the specimens. The specific mechanism of the concrete component is unknown, so more investigation is needed in order to take advantage of it in design.

Table 8.4 Additional concrete contribution results. See Section 8.3 for an explanation of UCSD-4.

	Reduced-scale specimens (Tran [2015] and current study)				Full-scale specimens [Murcia-Delso et al. 2013; Lotfizadeh and Restrepo 2019]			
	DS-1	DS-2	DS-1	DS-2	DS-1	DS-2	DS-1	DS-2
F_c (kips)	21	20	18	22	114	132	N/A	156
$F_{tr} - F_c$ (kips)	17	17	38	37	220	340	N/A	260
$\frac{\text{Force demand}}{\text{Force capacity}}$	0.89	1.71	0.96	1.14	0.63	0.68	N/A	0.44
A_{tr}/s required	0.012	0.012	0.036	0.029	0.085	0.117	N/A	0.053

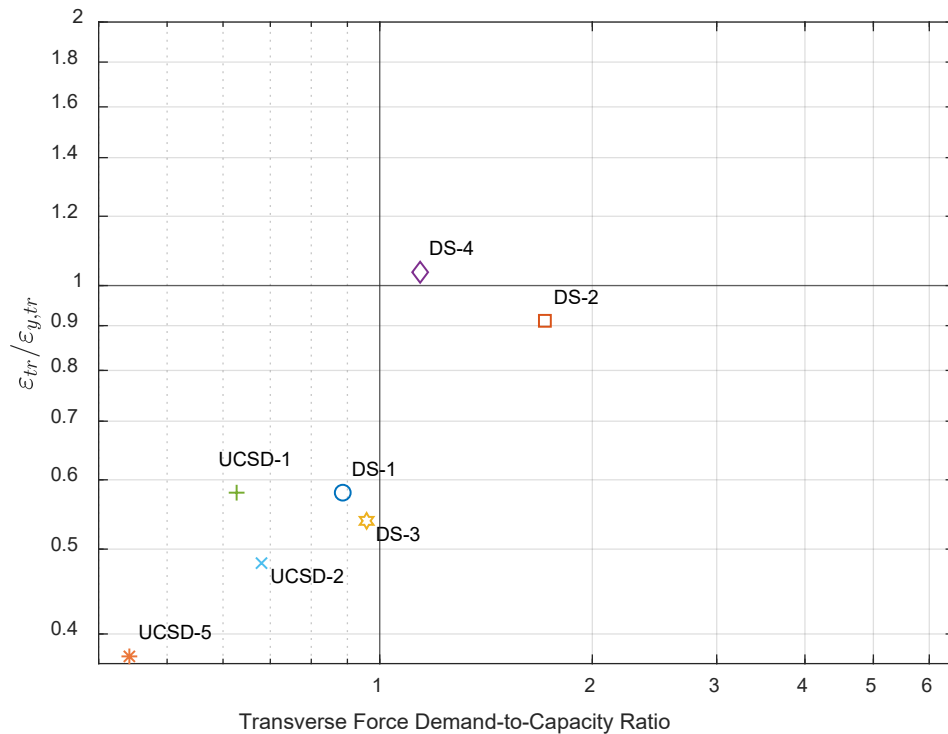


Figure 8.6 Evaluation of strut-and-tie model considering additional concrete component.

8.6 DISCUSSION

The strut-and-tie model results are consistent with the observed and measured behavior of the specimens. The model assumes a parabolic profile of strains in the transverse reinforcement, which was seen in the experiments; see Chapter 5 and Chapter 6. Such a profile indicates that the reinforcement would be used most efficiently if it were concentrated at the top of the shaft. The strut-and-tie model reflects this finding, showing that the force-transfer angle between the shaft and column longitudinal bars—and thus the transverse force demand—is most advantageous when Node B is shallow. By concentrating the transverse reinforcement at the top of the shaft, rather than using a uniform distribution of spiral or hoops, Node B is shifted upwards.

While the proposed model appears to be the most successful in predicting the relative failure modes and damage in the experimental specimens, it neglects some experimental and theoretical issues.

Firstly, the strut-and-tie model is based on forces, while cracking and the experimental strains that were used for evaluation are displacement-based. The evaluation was performed at a drift ratio lower than the maximum reached during the experiments so that forces could be inferred from the elastic strains and vice versa; however, this implies that the model can no longer accurately predict strains at higher drift ratios.

The model is also unable to accurately describe general behavior at higher drift ratios if the vertical column core-shaft annular region interface splits open, as seen in Specimens DS-2 and DS-4. The model depends on struts (represented by resultant strut AB) carrying loads across the interface, which cannot occur if there is an open gap.

After the formation of the split, shear stress cannot easily be carried across the open gap, so the moment from the column must be transmitted to the shaft largely by a force couple consisting of horizontal forces, one at the column–shaft interface, and another about at the bottom of the column. The horizontal force couple causes shear stresses with opposite signs in the column and the shaft annular region, so diagonal cracks in those two elements should be expected in opposite directions. That phenomenon suggests that after splitting, a 2D model of the system is not feasible, because it would require struts crossing each other at about 90° . Thus, a 3D model is needed to represent the behavior after split formation.

Finally, a 2D model would be unable to capture the shaft transverse strains in the direction perpendicular to loading. Experimental evidence showed nearly uniform strains around the circumference of the transverse reinforcement, regardless of spiral or hoop location (Chapter 6, Murcia-Delso et al. [2013]); this evidence remains unexplained by analytical means.

In summary, the model cannot explain all of the mechanisms leading up to failure. Nonetheless, evaluations show that the proposed model performs better than existing models in predicting the relative behavior of column–shaft connections. Therefore, the proposed model can be considered for design to protect against the undesirable shaft-prying failure mode.

8.7 DESIGN RECOMMENDATIONS

The strut-and-tie model was used to determine a new design procedure to proportion the shaft transverse reinforcement in a column–shaft connection; see Appendix H. However, the procedure requires detailed moment-curvature analysis results, some of which might not be provided by typical moment-curvature software.

While the proposed strut-and-tie methodology more accurately describes the observed behavior of the specimens, it is suggested that a modified version of McLean and Smith's [1997] equation [Equation (7.1)] be used as a simpler way to proportion the shaft transverse reinforcement. The model evaluations demonstrated that McLean and Smith's model (Figure 7.2) performed similarly to (albeit with slightly more scatter than) the strut-and-tie methodology with consideration of the concrete shear resistance (Figure 8.4), except for Specimen UCSD-4. McLean and Smith's model is also much easier to implement because it does not require moment-curvature analysis or finding the centroids of the tensile and compressive forces acting on the boundary of the transition region. Section 7.5 compared McLean and Smith's model results to Murcia-Delso et al.'s [2015] model results, which were similar. Therefore, it is adequate to use McLean and Smith's model, with (1) an additional condition to qualify its applicability for UCSD-4; and (2) some other modifications based on the strut-and-tie model findings, for design. The development of the additional condition will first be described, and then a set of design equations will be proposed.

McLean and Smith’s equation was developed for a column in direct tension rather than bending, but the authors advised that the same equation could be used under either load case. In calculating the force demand on the transverse reinforcement due to the force transfer between longitudinal bars, it is conservative to assume direct tension rather than a pure moment loading. At the same time, this assumption still neglects the shear load, which is not discussed in McLean and Smith [1997]. As seen in Section 8.4 and Table 8.3, the concrete shear resistance exceeded the shear demand in all of the column–shaft connections (besides UCSD-4, for which the STM is not valid). Therefore, it can be safely assumed that the concrete is able to carry the shear in typical column–shaft connections. Exceptions occur in connections in which the column shear span is very small, or the shaft-to-column-diameter ratio is large.

McLean and Smith developed their equation based on experiments in which the shaft and column bars were the same size. However, if the shaft and column bars are different sizes, then they have different development lengths (due to different bond areas, axial stresses, and confinement of the bars), and thus the force-transfer angle is not necessarily 45° as assumed by McLean and Smith. For example, if the shaft longitudinal bar development length is greater than that of the column bars [Figure 8.7(c)], the column bars will develop quicker than the shaft bars. Any additional column bar length provided beyond the development length will not be effective for force transfer without some plasticity occurring in the below-ground transition region. Thus, if the transition region is designed to remain elastic per AASHTO SGS [2015] recommendations, then the centroid of force transfer on the column bars will be relatively shallow, and the force-transfer angle is less than 45°. With an angle shallower than 45°, Equation (7.1) is unconservative and should not be used. This condition is described by Equation (8.15).

$$l_{d,c} \geq \alpha l_{d,s} \quad (8.15)$$

where $l_{d,c}$ is the tension development length of column longitudinal bar per AASHTO BDS [2017]; $l_{d,s}$ is the tension development length of shaft longitudinal bar per AASHTO BDS [2017]; and $\alpha = \frac{\epsilon_s}{\epsilon_{y,s}}$ is the shaft bar strain factor.

The α factor in Equation (8.15) represents the ratio of $\frac{\epsilon_s}{\epsilon_{y,s}}$ in the outermost shaft bar at the instant when the column is at its peak moment capacity. It is similar to the excess reinforcement factor λ_{er} on development length. Therefore, $\alpha l_{d,s}$ is the development length of the shaft bars when the connection is subjected to the column peak moment loading. α can be determined using moment-curvature analysis on the shaft, or it can be conservatively taken as 1.0.

Equation (8.15) can be rearranged as:

$$\frac{l_{d,c}}{\alpha l_{d,s}} \geq 1 \quad (8.16)$$

The $\frac{l_{d,c}}{\alpha l_{d,s}}$ ratio for each specimen is listed in Table 8.5. The results indicate that Specimen UCSD-4 does not satisfy Equation (8.16). Therefore, McLean and Smith’s equation [Equation (7.1)] cannot be used to proportion the necessary shaft transverse reinforcement in this specimen.

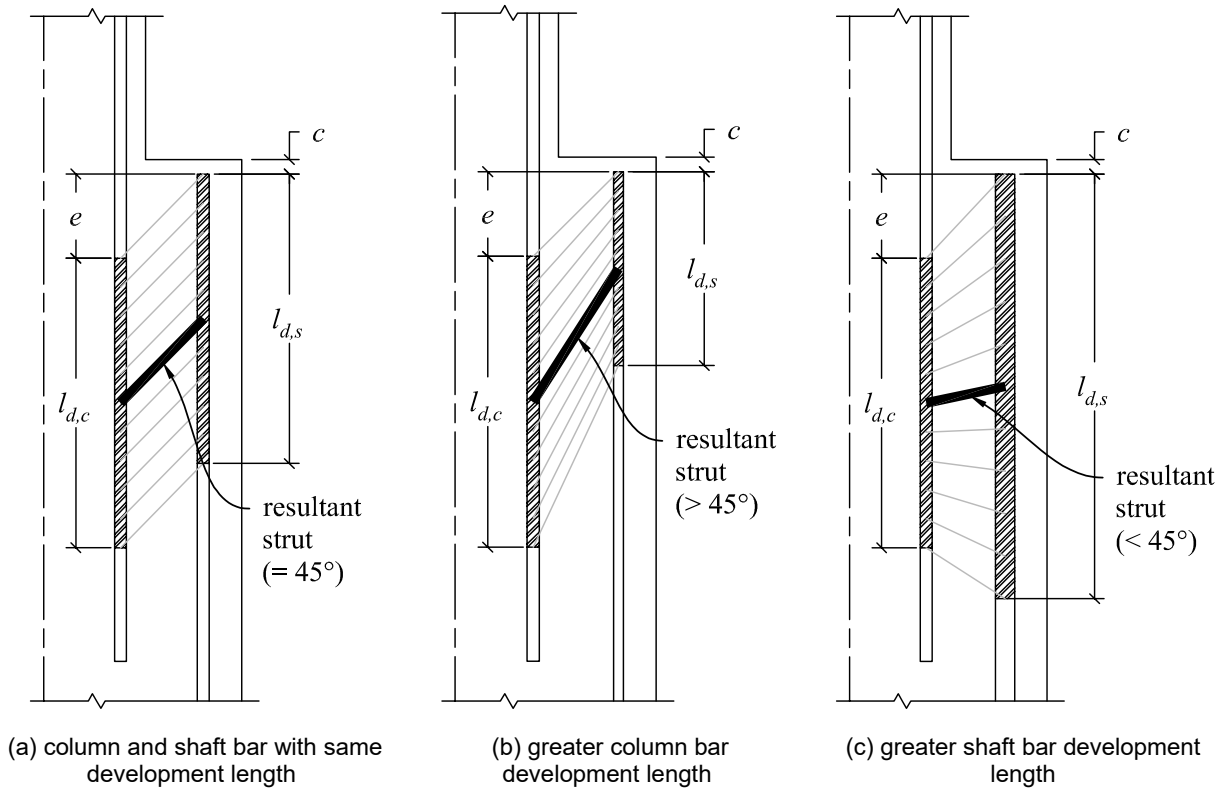


Figure 8.7 Force-transfer lengths of column and shaft bars.

Table 8.5 Column-to-shaft longitudinal bar development length ratio.

	Reduced-scale specimens (Tran [2015] and current study)				Full-scale specimens [Murcia-Delso et al. 2013; Lotfizadeh and Restrepo 2019]			
	DS-1	DS-2	DS-3	DS-4	UCSD-1	UCSD-2	UCSD-4	UCSD-5
$l_{d,c}$ (in.)	15	16	12.8	15.1	39.3	46.9	27.7	63.9
α	0.82	0.83	0.64	0.57	0.59	0.58	0.90	0.63
$\alpha l_{d,s}$ (in.)	8.6	9.3	8.4	8.7	30.3	36.2	40.7	50.4
$l_{d,c}/\alpha l_{d,s}$	1.75	1.72	1.52	1.74	1.30	1.29	0.82	1.27
Eq. (8.16) satisfied?	Yes	Yes	Yes	Yes	Yes	Yes	No	Yes

In summary, it is recommended that for design, a modified version of McLean and Smith's equation can be used, provided that the following conditions are met. The conditions will first be explained, and then the modified equation to proportion the shaft transverse reinforcement will be introduced. It can be used in both CIP and precast applications.

$$\frac{l_{d,c}}{\alpha l_{d,s}} \geq 1 \quad (8.17)$$

$$l_e \geq l_{d,c} + e + c \quad (8.18)$$

where $l_{d,c}$ is the tension development length of column longitudinal bar per AASHTO BDS [2017]; $l_{d,s}$ is the tension development length of shaft longitudinal bar per AASHTO BDS [2017]; and α equals $\frac{\varepsilon_s}{\varepsilon_{y,s}}$, where ε_s is the strain in the outermost shaft bar, at the bottom of the transition region (which can be assumed as l_e) at the instant when the column is at its peak moment capacity. It can be calculated from moment-curvature analysis of the shaft, or α can be conservatively assumed as 1.0; l_e = embedment depth of column longitudinal bars; e is the eccentricity between column and shaft longitudinal bars; and c is the cover from top of shaft-to-shaft longitudinal bar.

The first condition indirectly limits the column and shaft bars' relative sizes to avoid an undesirable force-transfer angle and determines the applicability of McLean and Smith's model. The second condition ensures that the longitudinal bars have a sufficient force-transfer length, and the column bars will not prematurely pull out. It is similar to McLean and Smith's required column longitudinal bar embedment depth but uses $l_{d,c}$ rather than l_s (which equals $1.7l_d$, where l_d is the greater of the shaft and column bar development lengths). Murcia-Delso et al. [2013] determined that McLean and Smith's embedment depth of $l_s + e + c$ was unwarranted, and $l_{d,c} + e + c$ was proven to be sufficient through experimental tests, FE analysis, and reliability analysis to account for material and construction uncertainties. Note that Murcia-Delso et al.'s conclusions were based on AASHTO BDS [2010] rather than AASHTO BDS [2017].

Then, if the conditions in Equation (8.17) and Equation (8.18) are met, the shaft transverse reinforcement in the transition region can be proportioned as:

$$\frac{A_{tr}}{s} \geq \frac{A_l f_{u,l}}{2\pi f_{y,tr} l_{d,s}} \quad (8.19)$$

where A_{tr} is the area of shaft transverse reinforcement in transition region; s is the pitch (i.e., center-to-center spacing) of transverse reinforcement; A_l is the total area of column longitudinal reinforcement; $f_{u,l}$ is the ultimate strength of column longitudinal reinforcement; $f_{y,tr}$ is the yield strength of shaft transverse reinforcement; and $l_{d,s}$ is the tension development length of shaft longitudinal bar per AASHTO BDS [2017].

$\frac{A_{tr}}{s}$ is to be distributed over the shaft development length $l_{d,s}$. Equation (8.19) is similar to McLean and Smith's equation [Equation (7.1)] but uses $l_{d,s}$ rather than l_s (which = $1.7l_d$). Consistent with McLean and Smith's equation, it is based on equilibrium requirements between forces in the longitudinal and transverse reinforcement (Figure 2.1, Section 2.1.1). The force transfer occurs over length $l_{d,s}$ in the shaft, where equilibrium is calculated. Additionally, it is unconservative to use a lap splice factor in Equation (8.19) or Equation (7.1). Therefore, Equation (8.19) is based on $l_{d,s}$.

Equation (8.19) was evaluated following the procedure described in Section 7.1, with the exception that in specimens with bundled spiral at the top of the shaft, “ A_{tr}/s used” was taken as the average A_{tr}/s over length $l_{d,s}$ rather than over the full length of the shaft. The evaluation results are shown in Figure 8.8.

The evaluation shows that the modified McLean and Smith model [Equation (8.19)] correlates with the measured results from seven experimental specimens with some conservatism. The model assumes 45° force-transfer struts; the strut-and-tie procedure indicated that the true strut angles in these seven specimens were in the range of 60–70° (θ_{AB} in Table 8.2). If 60° struts were assumed instead in the modified McLean and Smith model, then the A_{tr}/s required would be $1/\sqrt{3}$, or 58%, of that calculated by Equation (8.19) and implied in Figure 8.8. Therefore, all data points would shift to the left, and the model would more closely represent the behavior of the specimens.

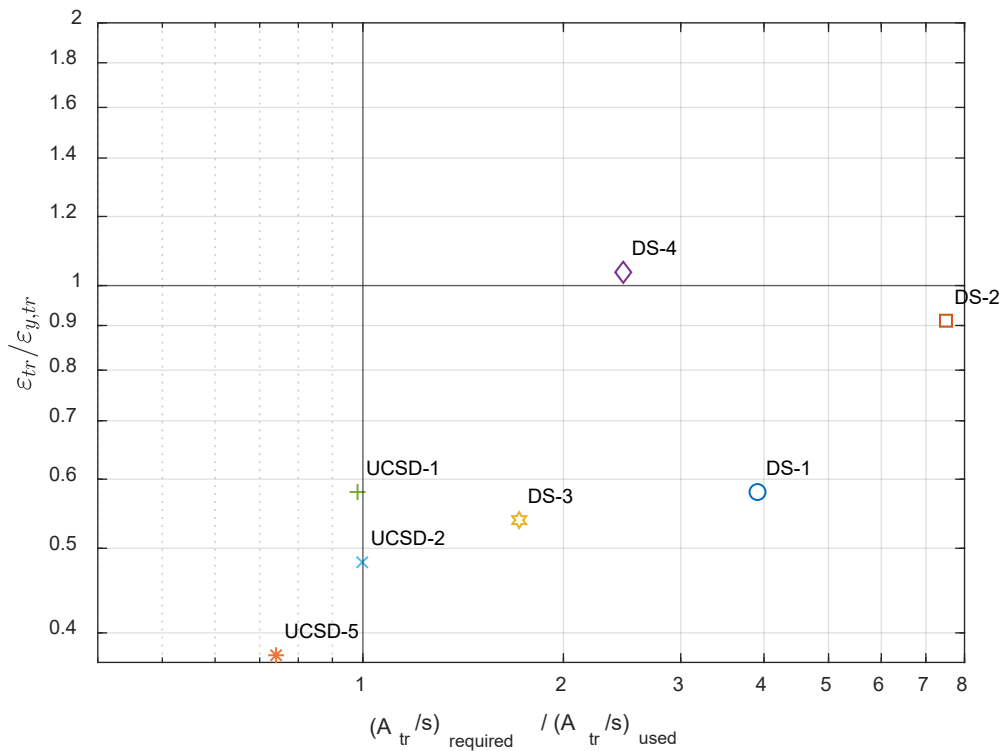


Figure 8.8 Evaluation of modified McLean and Smith model [Equation (8.19)].

9 Summary and Conclusions

9.1 SUMMARY

An experimental and analytical research program was conducted to investigate the force-transfer mechanism within the connection between a reinforced concrete column and a drilled shaft under seismic loads. One experimental specimen (DS-4) was loaded under constant axial and cyclic lateral loads. Testing continued until the lateral load resistance dropped to nearly zero, which occurred at a drift ratio of 11%. Experimental results were compared with those of three previous specimens tested at the University of Washington (DS-1, DS-2, and DS-3). Based on the comparison of results and modeling using the strut-and-tie method, a new analysis procedure was developed to predict the force-transfer mechanism in a column–shaft connection.

The experimental specimen failed through prying open of the annular part of the shaft surrounding the column. At 5.2% drift, a circumferential split opened between the column and shaft, allowing the column to start rocking inside the connection. Vertical, radial cracks in the shaft widened significantly, so the originally vertical shaft face visibly sloped outwards. This behavior continued throughout the remainder of the test at increasing drift ratios, and the shaft transverse reinforcement fractured at about 7.3% drift. No other reinforcement had buckled or fractured by the end of testing.

By the end of testing, an annular gap had opened up between the column confined core and the surrounding shaft shell; it measured about 4-in. wide \times at least 12-in. deep. The shaft transverse reinforcement was fractured from the top of shaft down to 22 in. below the column–shaft interface. The column remained intact, although the cover spalled at the column–shaft interface and the column longitudinal bar experienced strains greater than 0.05.

The test series of Specimens DS-1 through DS-4 demonstrated two modes of failure for column–shaft connections: (1) flexural failure of the column (DS-1 and DS-3), accompanied by relatively little damage to the shaft; or (2) prying and splitting failure in the transition region (DS-2 and DS-4). Other failure modes are possible but were not part of the scope of this study and were not seen in any specimen in the DS test series. A comparison of the experimental test inputs and results indicated that the failure mode was primarily related to the amount of transverse reinforcement provided in the shaft and the strains that the transverse reinforcement experienced. An evaluation of existing design procedures to detail the shaft transverse reinforcement revealed that existing procedures did not consistently predict the behavior of eight experimental specimens

(DS-1 through DS-4 and four specimens from the University of California, San Diego). Therefore, a new analysis and design procedure was developed for use with both CIP and precast applications.

The new procedure was based on a strut-and-tie model of the observed experimental behavior. It was evaluated against measured results from eight specimens and compared to procedures developed by other researchers. The proposed strut-and-tie methodology appeared to correlate better with experimental results than did the other procedures.

9.2 CONCLUSIONS

Identification of Failure Modes

- Current design procedures for the amount of spiral reinforcement required in column–shaft connections do not consistently predict the observed failure modes and relative transverse strains in the eight experimental specimens for which data was available (DS series and the UCSD series). The shaft prying failure mode of Specimen DS-2 was expected, both because the column was precast (providing a cold joint between the shaft and column), and the spiral reinforcement in the shaft was very light. However, the same failure mode was not expected in Specimen DS-4, as the specimen was cast-in-place; based on current design recommendations, it was expected to fail similarly to Specimens DS-1 and DS-3 (both of which failed in the column).
- Prying behavior has not been well-studied, but Specimen DS-4 demonstrated that it is possible for it to occur even in a CIP connection with adequate embedment of the longitudinal reinforcement.

Role of Shaft Spiral Reinforcement

- The experimental investigation of Specimens DS-1 through DS-4 showed that the failure mode correlated with shaft transverse reinforcement strains.
- The vertical distribution of strains in the shaft transverse reinforcement was approximately parabolic, except in Specimen UCSD-4.
- The configuration of the shaft spiral consisted of six turns concentrated at the top and a uniform distribution below that. The uppermost turns experienced the largest strains. This behavior shows that the largest demand occurs at the top, in which case the most efficient design is to intentionally concentrate hoops or spirals, or use a permanent steel casing, at the top of a drilled shaft.

Effects of Column Spiral Reinforcement

- The existence of circumferential tensile strains in the spiral in Specimen DS-4 implies radial tensile strain in the surrounding concrete. Eventually, the concrete could not resist the tension, so a vertical split formed between the column core and the shaft annular region. In the transition region, the column was equipped with a relatively heavy spiral, which might have caused a concentration in the radial stress field there. Thus, the

existence of column spiral through the transition region might have actually promoted the splitting and subsequent shaft prying failure mode. The observed behavior suggests that, for a given total quantity of spiral steel in the transition region, the connection might have performed better if the column spiral had been reduced and the shaft spiral increased.

Modeling

- The proposed strut-and-tie model predicted the observed behavior in the specimens better than did previous design methodologies. The proposed model is more versatile than previous ones, but it has some limitations:
 - The model was developed for response prior to the formation of a split at the vertical column core-shaft annular region interface. Once that split forms, the behavior changes, and a different model is needed to describe the subsequent behavior.
 - Bar bond is needed not only to anchor the column and shaft bars, but also to transfer load between them. If the column bars are encased in a spiral, the bond capacity on the inner and outer faces of the bar might differ because of the different levels of confinement.
 - The model was based on 2D concepts, so it is not capable of explaining some of the true 3D effects, such as the distribution of tensile strains around the circumference of the spiral.

9.3 RECOMMENDATIONS FOR FUTURE WORK

- A number of complex failure models were observed in the tests of column–shaft connection specimens. Additional tests and analyses would be needed to identify all possible failure modes and develop accurate models of each of them.
- In practice, enlarged drilled shafts are often preferred over smaller-diameter shafts to allow for greater construction tolerances, especially with respect to column location within the shaft. While eccentricity of the column with respect to the shaft may be acceptable for the column and shaft individually, it could adversely affect the column–shaft connection resistance. The behavior in a column–shaft subassembly with eccentric column and shaft reinforcement cages should be studied.
- Past efforts to model column–shaft connections using FE software [Murcia-Delso et al. 2013; Tran 2015; and Saiidi et al. 2020] have had mixed results in reproducing observed behavior. Numerical and analytical investigations, particularly using 3D simulation tools, should be continued until they can reproduce the measured results consistently.
- Once a numerical model has been verified against experimental results, a parametric study could be performed to study the influence of the shaft transverse reinforcement, column longitudinal bar embedment depth, column–shaft diameter ratio, and anchorage of longitudinal reinforcement. The relationship between column longitudinal bar embedment

depth and required shaft transverse reinforcement for favorable behavior (flexural failure in the column) should also be studied.

REFERENCES

- AASHTO (2015). *Guide Specifications for LRFD Seismic Bridge Design with 2012, 2014 and 2015 Interim Revisions*, American Association of State Highway and Transportation Officials, Washington, DC.
- AASHTO (2017). *AASHTO LRFD Bridge Design Specifications*, American Association of State Highway and Transportation Officials, Washington, DC.
- AASHTO (2010). *AASHTO LRFD Bridge Design Specifications*, American Association of State Highway and Transportation Officials, Washington, DC.
- AASHTO (2018). *LRFD Guide Specifications for Accelerated Bridge Construction*, American Association of State Highway and Transportation Officials, Washington, DC.
- ACI (2014). *Building Code Requirements for Structural Concrete (ACI 318-14)*, American Concrete Institute, Farmington Hills, MI.
- Berry M., Eberhard M.O. (2003). Performance models for flexural damage in reinforced concrete columns, *PEER Report No. 2008/13*, Pacific Earthquake Engineering Research Center, University of California, Berkeley, CA.
- Berry M., Parrish M., Eberhard, M.O. (2004). *PEER Structural Performance Database User's Manual (Version 1.0)*. Pacific Earthquake Engineering Research Center, University of California, Berkeley, CA.
- Building Seismic Safety Council. (2004). *NEHRP Recommended Provisions for Seismic Regulations for New Buildings and Other Structures (FEMA 450)*. National Institute of Building Sciences, Washington, DC.
- California Department of Transportation (Caltrans). (2010). *Seismic Design Criteria*. Sacramento, CA.
- California Department of Transportation (Caltrans). (2019). *Seismic Design Criteria*. Sacramento, CA.
- Cohagen L.S., Pang J.B.K., Eberhard M.O., Stanton J.F. (2008). *A Precast Concrete Bridge Bent Designed to Re-center after an Earthquake*. Washington State Department of Transportation, Olympia, WA.
- Dassault Systèmes. (2010). *Abaqus*. Dassault Systèmes Simulia Corp.
- Dassault Systèmes. (2014). *Abaqus/Explicit*. Dassault Systèmes Simulia Corp.
- Freytag D.M. (2006). *Bar Buckling in Reinforced Concrete Bridge Columns*, Master's thesis, Department of Civil and Environmental Engineering, University of Washington, Seattle, WA.
- Haraldsson O. (2015). *A Pre-Tensioned Bridge Bent System for Accelerated Bridge Construction*, PhD Thesis, Department of Civil and Environmental Engineering, University of Washington, Seattle, WA.
- Hoehler M.S., Stanton J.F. (2006). Simple phenomenological model for reinforcing steel under arbitrary load, *J. Struct. Eng.*, 132(7):1061–1069, [https://doi.org/10.1061/\(ASCE\)0733-9445\(2006\)132:7\(1061\)](https://doi.org/10.1061/(ASCE)0733-9445(2006)132:7(1061)).
- Ingham J. (1995). *Seismic Performance of Bridge Knee Joints*, Ph.D. Thesis, Department of Structural Engineering, University of California, San Diego, La Jolla, CA.
- Janes T.M. (2011). *Precast Column Socket Connections for Thin Spread Footings*, Department of Civil and Environmental Engineering, University of Washington, Seattle, WA.
- Kent D.C., Park R. (1971). Flexural members with confined concrete, *Journal of the Structural Division*, 97:1969–1990.
- Liu Y. (2012). *Lateral Behavior of Reinforced Concrete Columns Supported on Type II Shafts*, Master's Thesis, Department of Structural Engineering, University of California, San Diego, La Jolla, CA.
- Lotfizadeh K.H., Restrepo J.I. (2019). *High-Strength Steel Reinforcement in Critical Regions of Earthquake-Resistant Bridges*. California Department of Transportation, Sacramento, CA.
- Mander J.B., Priestley M.J.N., Park R. (1988). Theoretical stress-strain model for confined concrete, *J. Struct. Eng.*, 114(8):1804–1826, [https://doi.org/10.1061/\(ASCE\)0733-9445\(1988\)114:8\(1804\)](https://doi.org/10.1061/(ASCE)0733-9445(1988)114:8(1804)).
- McLean D.I., Smith C.L. (1997). *Noncontact Lap Splices in Bridge Column-Shaft Connections*. Washington State Department of Transportation, Olympia, WA.

- Murcia-Delso J., Shing P.B. (2015). Bond-slip model for detailed finite-element analysis of reinforced concrete structures, *J. Struct. Eng.*, 141(4), [https://doi.org/10.1061/\(ASCE\)ST.1943-541X.0001070](https://doi.org/10.1061/(ASCE)ST.1943-541X.0001070).
- Murcia-Delso J., Liu Y., Shing P.B. (2016). Development of bridge column longitudinal reinforcement in oversized pile shafts, *J. Struct. Eng.*, 142(11), [https://doi.org/10.1061/\(ASCE\)ST.1943-541X.0001591](https://doi.org/10.1061/(ASCE)ST.1943-541X.0001591).
- Murcia-Delso J., Shing P.B. (2018). Numerical study of bond and development of column longitudinal reinforcement extended into oversized pile shafts, *J. Struct. Eng.*, 144(5), [https://doi.org/10.1061/\(ASCE\)ST.1943-541X.0002024](https://doi.org/10.1061/(ASCE)ST.1943-541X.0002024).
- Murcia-Delso J., Shing P. B., Savridis A., Liu Y. (2013). *Required Embedment Length of Column Reinforcement Extended into Type II Shafts*, California Department of Transportation, Sacramento, CA.
- Priestley M.J.N. (1993). *Assessment and Design of Joints for Single-Level Bridges with Circular Columns*, Department of Applied Mechanics and Engineering Sciences, University of California, San Diego, La Jolla, CA.
- Priestley M.J.N., Calvi G.M., Seible F. (1996). *Seismic Design and Retrofit of Bridges*. John Wiley & Sons, New York.
- Raynor D.J., Lehman D.E., Stanton J.F. (2002). Bond-slip response of reinforcing bars grouted in ducts, *ACI Struct. J.*, American Concrete Institute, 99(5):568–576.
- Saiidi M.S., Mehraein M., Shrestha G., Jordan E., Itani A., Tazarv M., Sanders D., Murphy T.P., Reno M.L., Pohll M.N. (2020). Proposed *AASHTO* seismic specifications for ABC column connections, *NCHRP Report No. 935*, National Academies of Sciences, Engineering, and Medicine, Transportation Research Board, Washington, DC.
- Stanton J.F. (2010). *Mphi18*, Department of Civil and Environmental Engineering, University of Washington, Seattle, WA.
- Stanton J.F. (2021). *Mphi18*, Department of Civil and Environmental Engineering, University of Washington, Seattle, WA.
- Tran H.V. (2012). *Drilled Shaft Socket Connections for Precast Column in Seismic Regions*, Master's Thesis, University of Washington.
- Tran H.V. (2015). *Drilled Shaft Socket Connections for Precast Columns in Seismic Regions*, PhD Thesis, Department of Civil and Environmental Engineering, University of Washington, Seattle, WA.
- WSDOT (2020). *Bridge Design Manual (LRFD) M 23-50*, Washington State Department of Transportation, Olympia, WA.

APPENDIX A Specimen Design Drawings

The specimen design and instrumentation drawings are included in the next pages. As-built dimensions and changes during construction are marked in red. This appendix is a supplement to the information provided in Chapter 3 and Chapter 4.

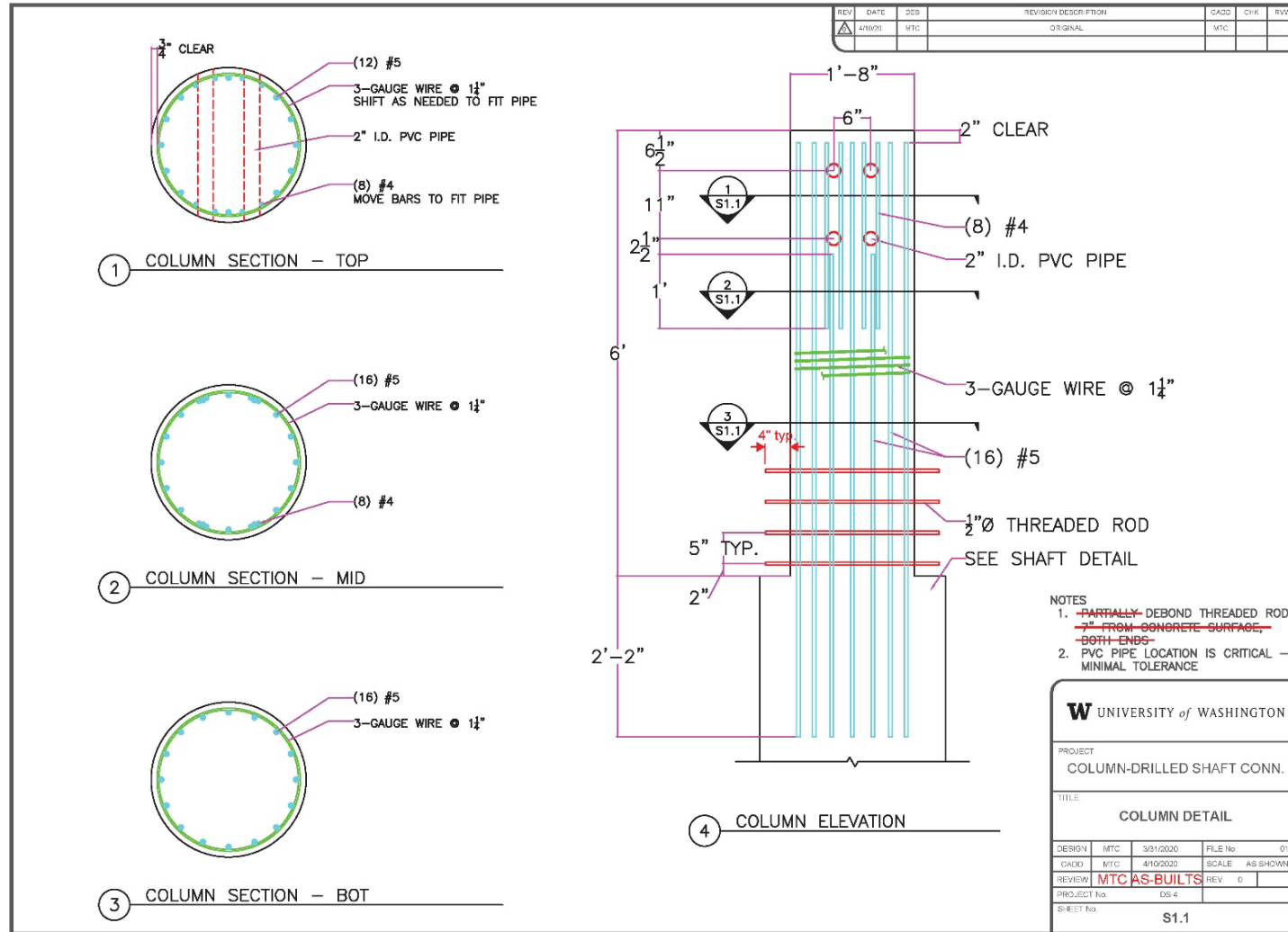


Figure A.1 Column detail.

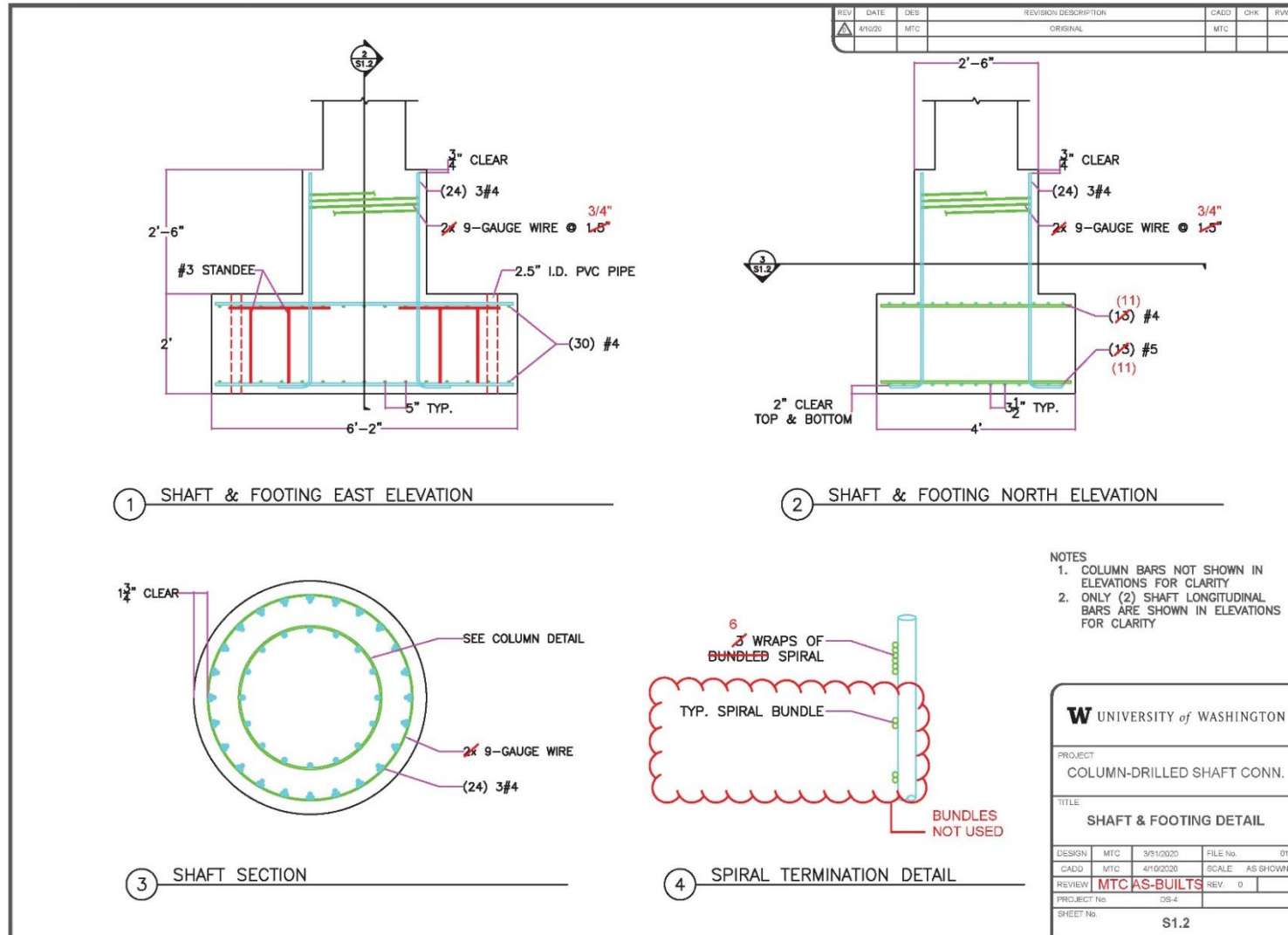


Figure A.2 Shaft and footing detail.

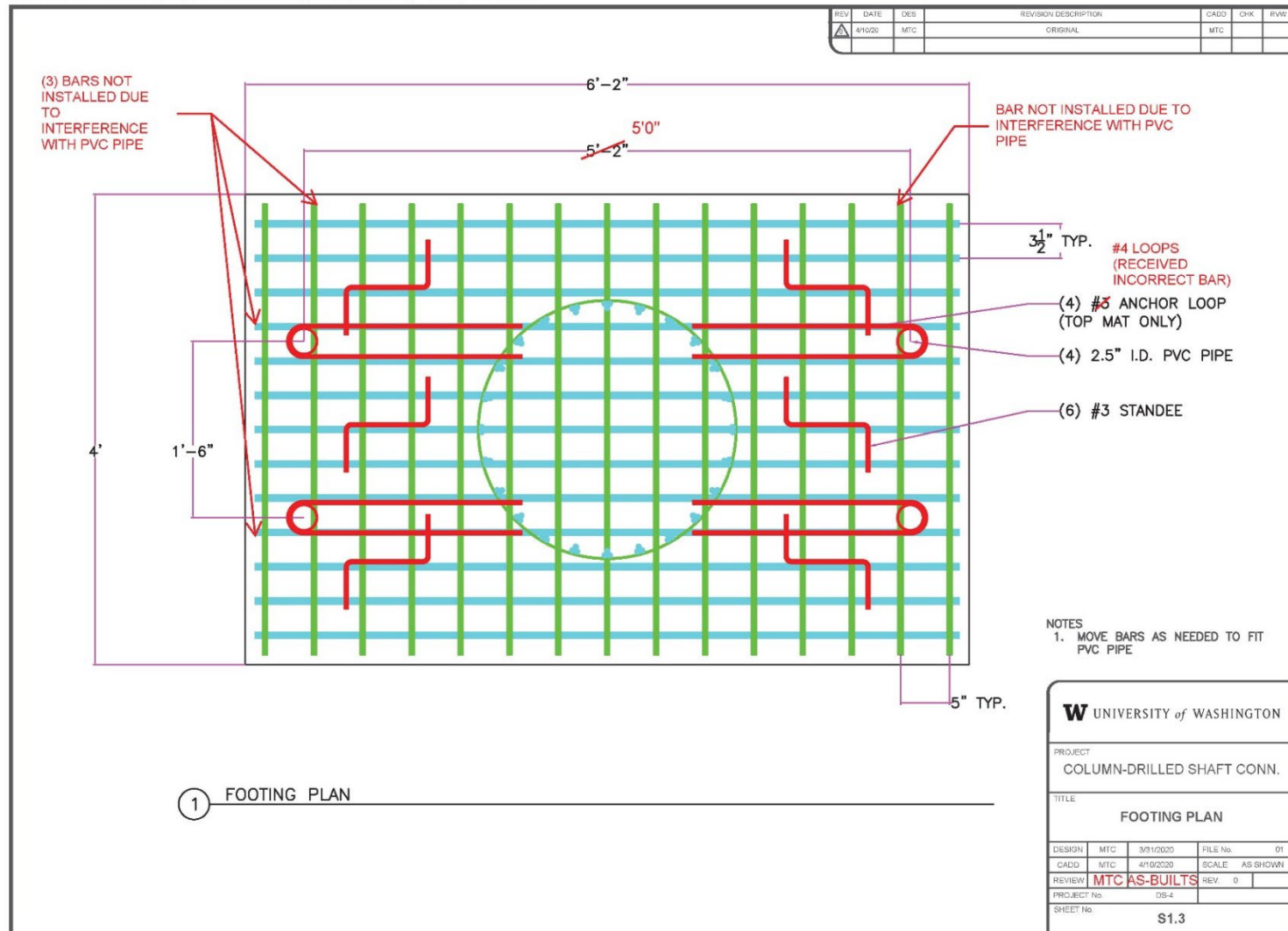


Figure A.3 Footing plan.

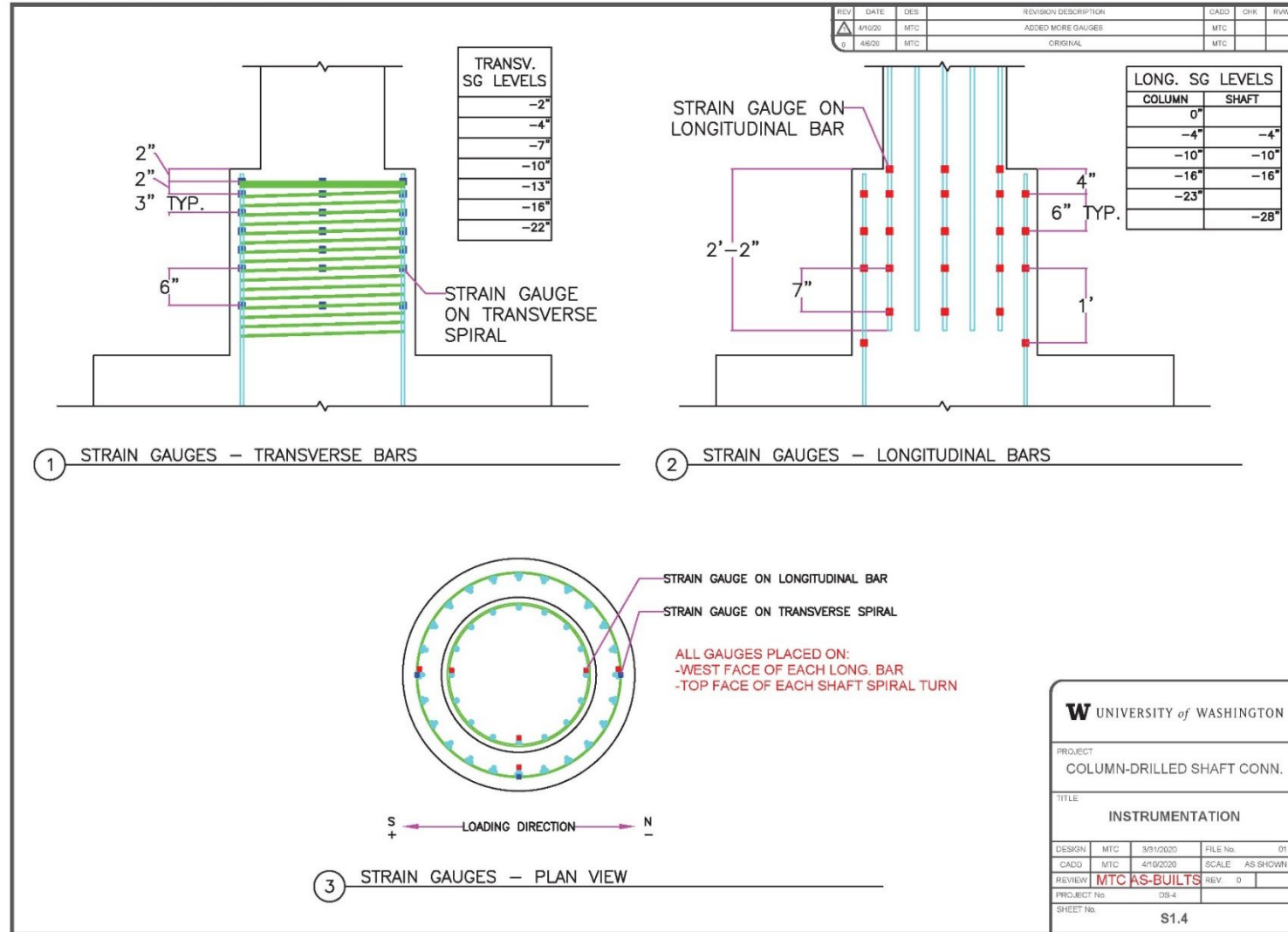


Figure A.4 Instrumentation.

APPENDIX B Specimen Construction and Setup Photographs

This appendix includes construction photographs of Specimen DS-4 as a supplement to the information provided in Chapter 3 and strain gauge installation description in Chapter 4. It also contains photographs of the experimental setup described in Chapter 4. Photographs will be introduced in the order in which they were captured.



Figure B.1 Shaft reinforcement cage in progress.



Figure B.2 Column reinforcement cage in progress.



Figure B.3 End of first concrete placement (base and shaft starter stub).



Figure B.4 Sonotube formwork for the shaft, with strain gauge leads routed out.

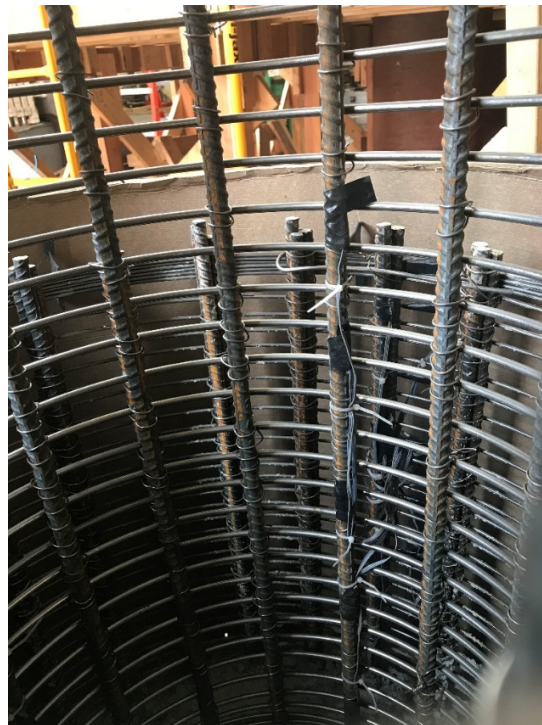


Figure B.5 Covered strain gauges on column longitudinal bar (north bar).



Figure B.6 Concrete placement for the shaft (pour #2).

Threaded rods, nuts, and screws were all covered with masking tape to avoid concrete splatter. Holes around the PVC pipes at the top of column and threaded rods at the bottom of column were caulked.



Figure B.7 Formwork and embedded items for the column.

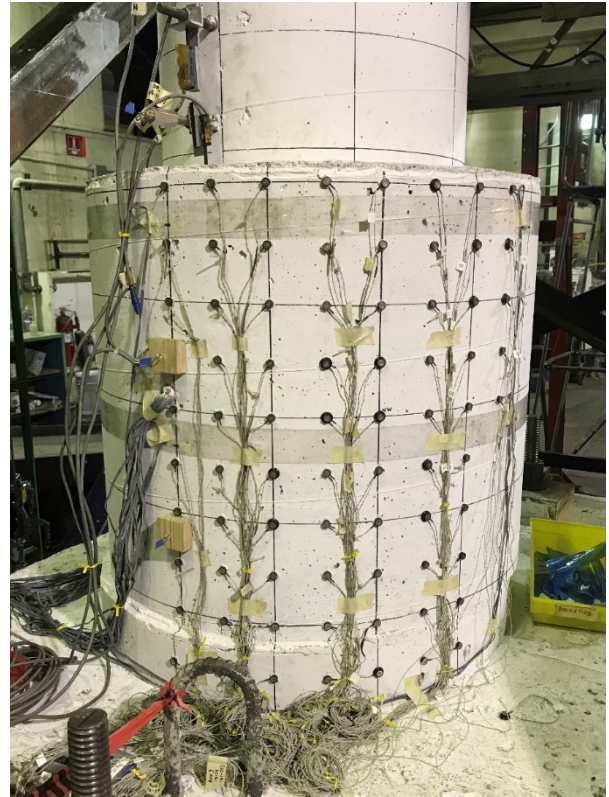
The lumber resting on the test frame anchor block acted as a dam. A flowable Hydrostone mix was poured into the dam, and then the specimen was lowered into the liquid and plumbed. This ensured that there was a level bearing surface between the specimen and the anchor block prior to post-tensioning, and the specimen was vertical under the Baldwin UTM.



Figure B.8 Move-in of the specimen onto the test frame.



(a)



(b)

Figure B.9 Instruments attached to the specimen: (a) inclinometers, Duncan potentiometers, and string potentiometers at the column base (north side); and (b) Optotrak marker installation in progress.

APPENDIX C Material Tests

This appendix includes material test procedures and details for Specimen DS-4. For DS-1, DS-2, and DS-3 material tests, see Tran [2015]. Strengths from these material tests were summarized in Section 3.4.

C.1 CONCRETE

The concrete was supplied by Stoneway Concrete and specified to be 5000 psi, 3/8-in. aggregate, 5 to 7 in. slump (mix #458374) for the entire specimen. A retarder was added to the concrete mix for the base and column placements. It is recommended that a retarder be added to all placements (base, shaft, and column) when using this concrete mix in warm temperatures.

For each concrete placement, eighteen 4-in. × 8-in. cylinders were taken for material testing: three each for 7-day, 14-day, 28-day, and test-day compressive tests, and the remaining six as backup or for possible modulus of elasticity testing. Cylinders were filled, rodded with a tamping rod, and compacted on a vibrating table according to ASTM C31 standards. Cylinders were stored in a lime bath until the day of the material test.

Compressive tests were performed in accordance with ASTM C39 compressive strength testing standards. Results of compressive tests are summarized in the following table.

Table C.1 Concrete compressive test results for DS-4.

	7-day (psi)	14-day (psi)	28-day (psi)	Testday (psi)	Test day age (days)
Column	4456	5307	6283	7093	57
Shaft	4249	5392	5857	6705	78
Base	4650	5361	6325	-	106

C.2 STEEL

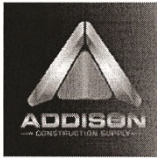
All reinforcing bars in the specimen were A706 Grade 60 and were supplied by Addison Construction Supply. The Western Group supplied the A82 Bright Basic (plain steel) wire for the transverse reinforcement. Wire was supplied as bundled coils (one coil per size of wire). The thicker 3-gauge wire was then coiled tighter by Concrete Technology Corporation to the desired diameter for installation. The thinner 9-gauge wire coil was already provided at approximately the desired diameter for the test specimen, so no additional reworking of the wire was needed.

It is expected that the stress–strain curve for the plain steel wire will not have a distinct yield plateau. Additionally, the available material testing equipment at the University of Washington was unable to measure the elongation of small-diameter wire during a tensile test, and mill certificates only reported the ultimate fracture stress, so there was no measured yield stress value. Lastly, the fabrication and shipping process might have left residual stresses on the coiled wire. Namely, the A82 wire is assumed to be cold-drawn as a straight rod, and then coiled on a spiral bending machine for shipping and final installation. In bending a straight rod into a round spiral, the process leaves residual stresses on the bent spiral. This complicates the wire stress-strain relation. These residual stresses are described in detail in Appendix D.

In conclusion, the yield stress of the spiral reinforcement used for calculations in this report was assumed as the nominal A82 yield stress, 70 ksi. This neglects the residual stresses from coiling the wire. All other steel material properties used in this report (Table C.2) were based on mill certificates, all of which are attached in the following pages.

Table C.2 Steel material properties for DS-4.

Property		Strength (ksi)
f_y [column longitudinal reinforcement (#5)]	Nominal	60
	Actual	65
f_u [column longitudinal reinforcement (#5)]	Nominal	80
	Actual	96
f_y [shaft longitudinal reinforcement (#4)]	Nominal	60
	Actual	69
f_u [shaft longitudinal reinforcement (#4)]	Nominal	80
	Actual	98
f_y [shaft transverse reinforcement (9GA)]	Nominal	70
	Actual	-
f_u [shaft transverse reinforcement (9GA)]	Nominal	80
	Actual	98



Addison Construction Supply, Inc.
 PO Box 9066
 Tacoma, WA 98490-0066
 800-474-0711
 F: 253-474-0714
 addisonsupply.com

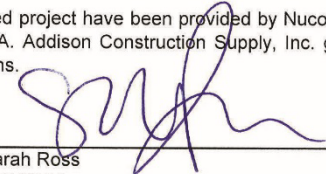
FABRICATORS CERTIFICATE OF COMPLIANCE

CONTRACTOR: UNIVERSITY OF WASHINGTON
JOB NAME: MORE HALL
P.O. NUMBER: _____
RELEASE NO: _____

REBAR SIZE	WEIGHT (in lbs.)	HEAT NUMBER	FILE NO.
#2	_____	_____	_____
#3	_____ 19	_____ 145320	_____ CS8193
#4	_____ 286	_____ 482119	_____ CS8049
#5	_____ 315	_____ 68420	_____ CS8155
#6	_____ 46	_____ 67220	_____ CS8156
#7	_____	_____	_____
#8	_____	_____	_____
#9	_____	_____	_____
#10	_____	_____	_____
#11	_____	_____	_____
#14	_____	_____	_____
#18	_____	_____	_____
TOTAL:	_____ 666 lbs.		

The reinforcing steel covered by this certification was manufactured and fabricated in compliance per the CRSI Manual of Standard Practice and per the standard specification of the Washington State Department of Transportation, AASHTO M31, ASTM A-615-09a/ Grade 60, ASTM A-706/A-706M and ASTM A-767/A-767M. Based on the rolling mills documentation, it is certified that the representative samples of the materials have been tested and the test results conform to the applicable requirements listed above.

Materials used for the above referenced project have been provided by Nucor Steel Seattle Inc. and/or Cascade Steel Rolling Mills and are made in the USA. Addison Construction Supply, Inc. guarantees that the rebar was fabricated according to the plans and specifications.

SIGNED: 
 Sarah Ross
DATE: 12/1/2020

CUSTOMER ADDISON CONSTRUCTION SUPPLY, INC.
 P. O. BOX 9066
 6201 SO ADAMS
 TACOMA, WA 98409



CERTIFIED MILL TEST REPORT
 (CMTR)
 3200 NORTH HIGHWAY 99W
 McMinnville, Oregon 97128
 (503) 472-4181 FAX (503) 434-5739

CS8049
 DATE 1-22-20
 BILL OF LADING 10286790

PAGE 1 OF 1

HEAT NO. / PRODUCT / GRADE	YIELD PSI	TENSILE PSI	ELONG. % 8 INCHES	NOM. WT %	TEST NAME / UNIT OF MEASURE				Melted Rolled	Shipped Lbs/Tons	Melt Lbs Roll Lbs
					BEND DEGREES	DEF.					
*482119 #4 706/60 GRADE REBAR ASTM A706-16 Grade 60 AASHTO M31-19	68,500	98,000	14	96	180 OK	OK		12/18/19 01/04/20	18,276 9.1	224,997 221,115	
*445319 #5 706/60 GRADE REBAR ASTM A706-16 Grade 60 AASHTO M31-17	64,500	93,500	15	96	180 OK	OK		11/21/19 12/02/19	29,915 15.0	212,121 209,779	
*375119 #6 706/60 GRADE REBAR ASTM A706-16 Grade 60 AASHTO M31-17	64,500	95,500	17	96	180 OK	OK		10/05/19 10/12/19	6,128 3.1	224,224 220,248	
*001920 #6 706/60 GRADE REBAR ASTM A706-16 Grade 60 AASHTO M31-19	68,000	100,000	15	96	180 OK	OK		01/02/20 01/10/20	11,445 5.7	227,409 220,106	

CHEMICAL ANALYSIS													
HEAT NO.	C %	Mn %	P %	S %	Si %	Cu %	Ni %	Cr %	V %	Mo %	Sn %	CE %	
482119	.28	1.24	.022	.017	.25	.33	.08	.21	.024	.02	.020	.52	
445319	.29	1.22	.013	.022	.25	.27	.08	.13	.022	.02	.025	.52	
375119	.28	1.24	.017	.018	.24	.25	.07	.17	.023	.02	.014	.51	
001920	.28	1.21	.021	.018	.26	.28	.08	.19	.024	.02	.022	.51	

PO NUMBER(S): MASTER

CERTIFIED BY: 
 Jeff Kramer
 Quality Assurance Manager

* ALL MELTING AND MANUFACTURING PROCESSES FOR THE MATERIALS OCCURRED IN THE UNITED STATES.

F016-1.02

CUSTOMER ADDISON CONSTRUCTION SUPPLY, INC.
 P. O. BOX 9066
 6201 SO ADAMS
 TACOMA, WA 98409



CERTIFIED MILL TEST REPORT
 (CMTR)
 3200 NORTH HIGHWAY 99W
 McMINNVILLE, OREGON 97128
 (503) 472-4181 FAX (503) 434-5739

CS8193
 DATE 4-24-20
 BILL OF LADING 12693710

PAGE 1 OF 1

DESCRIPTION	TEST NAME / UNIT OF MEASURE								
HEAT NO. / PRODUCT / GRADE	YIELD PSI	TENSILE PSI	ELONG. % 8 INCHES	NOM. WT %	BEND DEGREES	DEF.	Melted Rolled	Shipped Lbs/Tons	Melt Lbs Roll Lbs
*145420 #3 COILED REBAR 60D GRADE ASTM A615-18/A706-16 Gr60 AASHTO M31-19	67,000	105,000	15	101	180 OK	OK	04/15/20 04/22/20	31,922 16.0	226,044 219,008
*145320 #3 COILED REBAR 60D GRADE ASTM A615-18/A706-16 Gr60 AASHTO M31-19	68,000	106,000	16	101	180 OK	OK	04/15/20 04/22/20	27,336 13.7	216,626 127,486
*145420 #3 COILED REBAR 60D GRADE ASTM A615-18/A706-16 Gr60 AASHTO M31-19	67,000	105,000	15	101	180 OK	OK	04/15/20 04/22/20	31,922 16.0	226,044 219,008
*145320 #3 COILED REBAR 60D GRADE ASTM A615-18/A706-16 Gr60 AASHTO M31-19	68,000	106,000	16	101	180 OK	OK	04/15/20 04/22/20	27,336 13.7	216,626 127,486

CHEMICAL ANALYSIS													
HEAT NO.	C %	Mn %	P %	S %	Si %	Cu %	Ni %	Cr %	V %	Mo %	Sn %	CE %	
145420	.29	1.22	.010	.020	.25	.26	.07	.11	.032	.02	.024	.51	
145320	.29	1.23	.009	.020	.25	.25	.06	.10	.033	.02	.022	.51	
145420	.29	1.22	.010	.020	.25	.26	.07	.11	.032	.02	.024	.51	
145320	.29	1.23	.009	.020	.25	.25	.06	.10	.033	.02	.022	.51	

PO NUMBER(S): 30006 30013

CERTIFIED BY: 
 Jeff Kramer
 Quality Assurance Manager

* ALL MELTING AND MANUFACTURING PROCESSES FOR THE MATERIALS OCCURRED IN THE UNITED STATES.

FM16-1.02



A HEICO WIRE GROUP COMPANY

Davis Wire Corporation
 19411 80th Avenue South
 Kent, WA 98032
 USA
 Tel: (800) 872-8920
 Fax: (253) 395-3729

Ship to:
 PACIFIC NW WIRE
 253-964-6201, James B
 3250 INTERNATIONAL PLACE
 Du Pont, WA 98327

Certificate of Compliance

Page	Page 1 of 3
Cert Number	MCA0002443
Order	S067050
Ship Date	4/17/2020
Packing Slip	PS071353
Customer Req	45547
Customer Ref	James Bennett

<u>Item</u>	<u>Item Name</u>
1000252	BB .2430 3GA XCLN STD
1000255	BB .1920 6GA XCLN STD

Quality test results

<u>Item number</u>	<u>Description</u>		
1000252	BB .2430 3GA XCLN STD		
<u>Batch</u>	<u>Diameter</u>	<u>Break</u>	<u>Tensile</u>
0004656746	0.2440	4830.00	103
0004656748	0.2440	4880.00	104
UOM	in	lb	kpsi
Min	0.2440	4830.00	103
Max	0.2440	4880.00	104
Avg	0.2440	4855.00	104
Lower limit	0.2420	1.00	80
Upper limit	0.2460	0.00	110



A HEICO WIRE GROUP COMPANY

Davis Wire Corporation
19411 80th Avenue South
Kent, WA 98032
USA
Tel: (800) 872-8920
Fax: (253) 395-3729

Ship to:
THE WESTERN GROUP - PORTLAND
(503)222-1644
4025 N.W. EXPRESS AVENUE
Portland, OR 97210

Certificate of Compliance

Page	Page 5 of 6
Cert Number	MCA0000791
Order	S056824
Ship Date	10/22/2018
Packing Slip	PS059842
Customer Req	34839
Customer Ref	Steve Jewell

Quality test results

Item number	Description		
1000259	BB .1483 9GA XCLN STD		
Batch	Diameter	Break	Tensile
0003972521	0.1480	1628.00	95
0003972520	0.1480	1689.00	98
0003972519	0.1480	1698.00	99
0003972518	0.1480	1744.00	101
UOM	in	lb	kpsi
Min	0.1480	1628.00	95
Max	0.1480	1744.00	101
Avg	0.1480	1689.75	98
Lower limit	0.1470	1.00	75
Upper limit	0.1490	0.00	105

APPENDIX D Effect of Residual Stress on Premature Spiral Yielding

This appendix describes the residual stresses induced in spiral or hoop reinforcement when the reinforcement is bent into shape. The residual stresses are first computed, and then their implications are described.

D.1 THE PHENOMENON

The transverse reinforcement in a circular column or shaft typically consists of a continuous circular spiral or separate circular hoops. These must be bent into a circular shape before installation. Cold bending, which is usual, results in plastic action and residual stresses. During the forming process, the bar is bent plastically, but it springs back elastically to reach its final diameter. When the bar or wire is subsequently stressed axially, for example due to column bending, the residual stresses from cold bending will alter the average stress at any given axial strain. Two important outcomes are that:

- Yielding will start at an average imposed axial strain that is less than the yield strain.
- The average stress, when the imposed strain is equal to the yield strain, will be less than the yield stress.

The characteristics that control the effect are the material properties and the ratio D_{sp}/d_b , where D_{sp} is the diameter of circular arc into which the bar is bent; and d_b is the diameter of the bar diameter.

D.2 METHOD OF CALCULATION

First, the residual stress profile that corresponds to the bent shape must be computed. Then, the axial load vs. deflection, or average imposed stress vs. average imposed strain, can be computed. Finding the residual stress profile is necessarily iterative and requires the following sequence of steps:

- Impose on the section a user-selected curvature, ϕ_{pp} , and find the corresponding stress profile and moment, M_{pp} .

- Compute the elastic curvature, ϕ_{sb} , corresponding to M_{pp} , i.e. $\phi_{sb} = M_{pp}/EI$.
- Find the net curvature after springback, $\phi_{net} = \phi_{pp} - \phi_{sb}$.
- If the error, $|\phi_{net} - \phi_{target}| > \text{tolerance}$, choose a new ϕ_{pp} and repeat the cycle.

The subscripts are defined as follows: *sb* is springback; and *pp* is partially plastic.

For a cross section of arbitrary shape, the partially plastic moment must be computed numerically by dividing the section up into fine trapezoidal layers. For certain elementary shapes, such as a rectangle or a circle, the calculations can be done in closed form. For a circular cross section in which the central elastic core is $2R \sin \alpha$ high, the partially plastic moment is given by

$$M_{pp} = R^3 g(\alpha) f_0 \quad (D.1)$$

where

$$g(\alpha) = \frac{4}{3} \cos^3 \alpha + \frac{4\alpha - \sin 4\alpha}{8 \sin \alpha} \quad (D.2)$$

which varies from $\pi/4$ (i.e., S/R^3) to $1/6$ (i.e., Z/R^3), as α varies from 0 to $\pi/2$.

The curvature is given by

$$\phi = \frac{2}{D_{sp}} \quad (D.3)$$

Figure D.1 shows the residual stress patterns for $E = 29000$ ksi, $f_y = 60$ ksi, and two example values of $D_{sp}/d_b = 48$ and 384 . For $D_{sp}/d_b = 384$, the residual stress is highest at the exterior, while for $D_{sp}/d_b = 48$, it is highest in the interior.

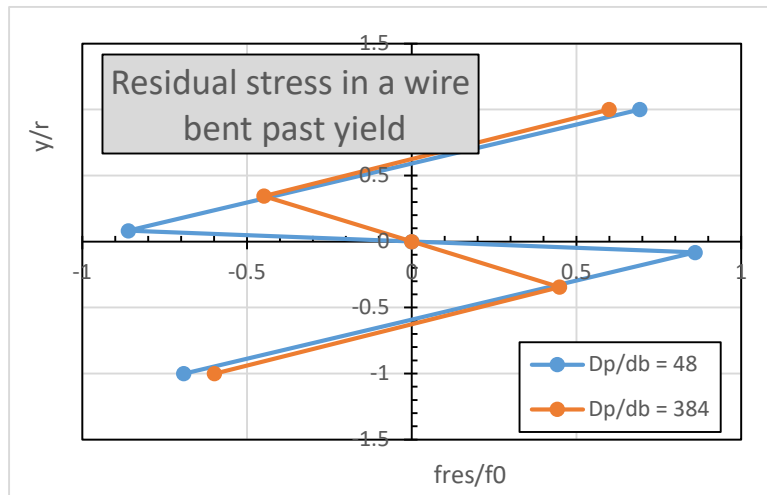


Figure D.1 Normalized residual stress profiles.

The load-deflection curve is most easily obtained numerically. The strain is incremented in steps of $\Delta\varepsilon$. At each step, the total stress at each interface between trapezoidal layers is given by

$$\sigma(y) = \max[-\sigma_0, \min(\sigma_0, \sigma_{res}(y) + E * \Delta\varepsilon)] \quad (D.4)$$

The force is then obtained by integrating the stresses over the trapezoidal layers.

The result for $D_{sp}/d_b = 48$ is shown in Figure D.2, where it is shown as a normalized average stress vs. strain. As seen in Figure D.2, the section starts to yield before the average imposed strain reaches the yield strain. Also, the average stress is less than the yield stress when the imposed strain is equal to the yield strain.

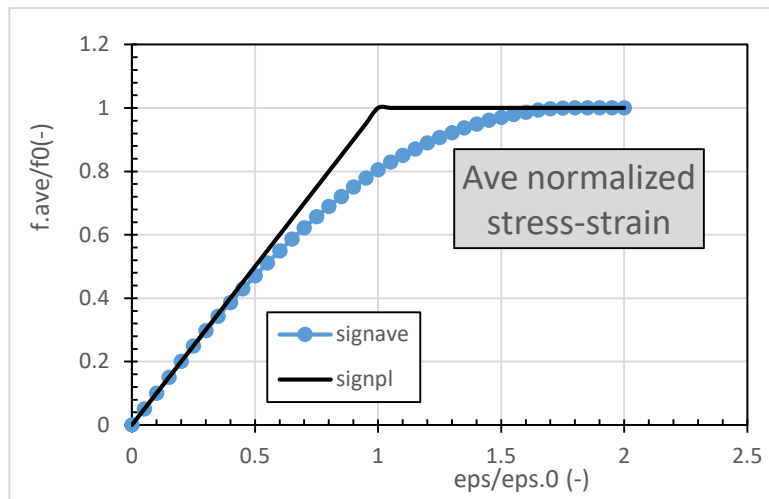


Figure D.2 Normalized average (ave) axial stress-strain curves, with and without residual stress (dotted blue and solid black lines, respectively).

D.3 RESULTS

Figure D.3 shows how the residual stresses vary with the D_{sp}/d_b ratio. For reference, the UCSD specimens had D_{sp}/d_b in the range of 64 to 90, and all the DS specimen had $D_{sp}/d_b = 162$. For $D_{sp}/d_b > 150$, the largest residual stress is at the exterior, and for $D_{sp}/d_b < 150$, it is in the interior. Figure D.4 shows the normalized strains at which the axial stress-strain curve departs from linearity and reaches the yield stress, as functions of D_{sp}/d_b . For larger D_{sp}/d_b , the strains approach the yield strain, meaning that the stress-strain curve that includes the residual stresses approaches the virgin elasto-plastic stress-strain curve. Table D.5 shows the average normalized axial stress at an imposed axial strain equal to the yield strain, for different D_{sp}/d_b ratios.

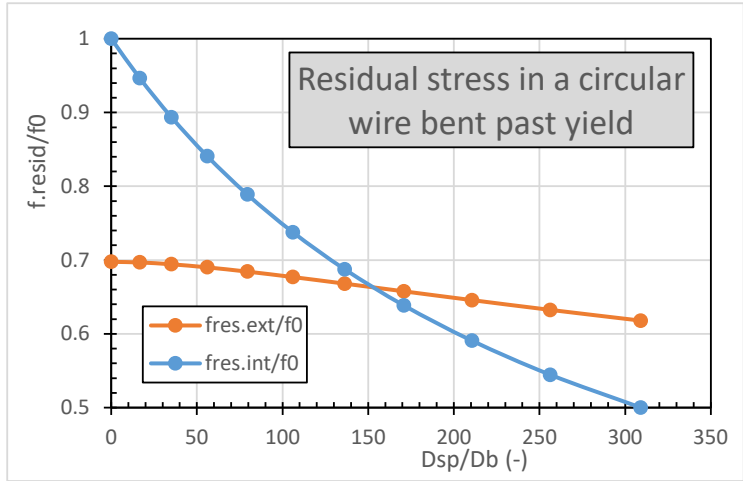


Figure D.3 Normalized residual stresses at the exterior and interior of the spiral.

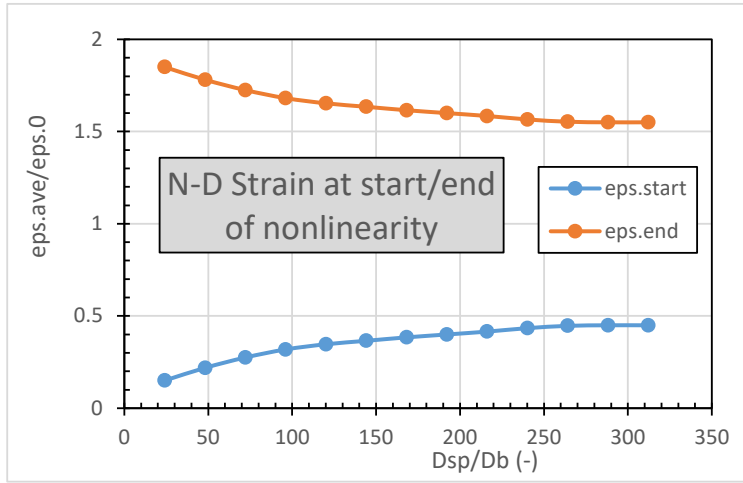


Figure D.4 Normalized strain at the departure from linearity.

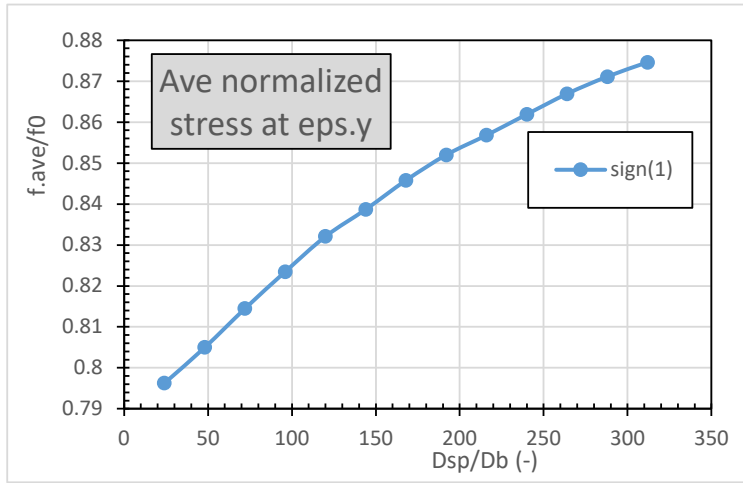


Figure D.5 Normalized axial stress when axial yield strain.

D.4 IMPLICATIONS IN PRACTICE

In the present application, the most important effects of the residual stresses due to cold bending are that the true stresses in the spiral are lower than those inferred from measured strains in the range $0 < \varepsilon < 2\varepsilon_y$, where ε is the measured strain. The reduction is never greater than 20% and lies in the same range, 15.5% to 18.5%, for all DS and UCSD specimens. Thus, while residual stresses make a difference to models' abilities to predict the absolute forces vs. strains in a column–shaft connection, they should make little difference to the models' abilities to rank experimental specimens in order of their performance.

APPENDIX E Damage Progression Photographs

This appendix is a supplement to the damage progression photographs provided in Chapter 5. Photographs in this appendix will be presented in the order in which they were captured.

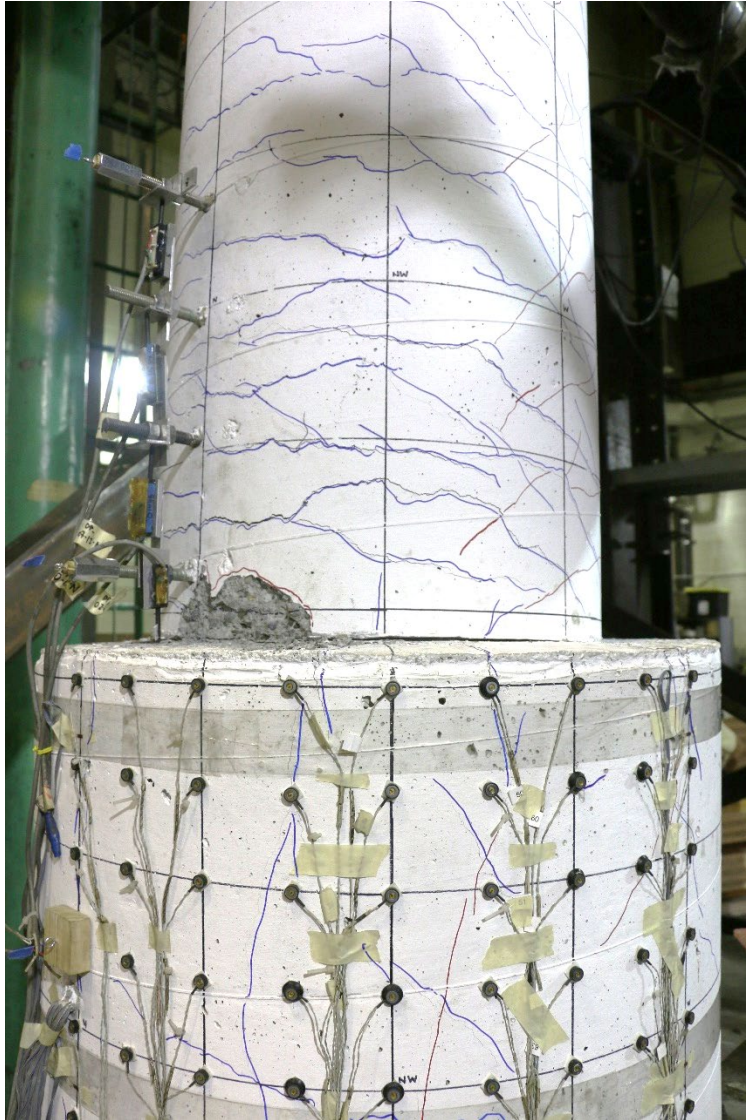


Figure E.1 Crack opening at column–shaft construction joint at 3.6% drift (peak).

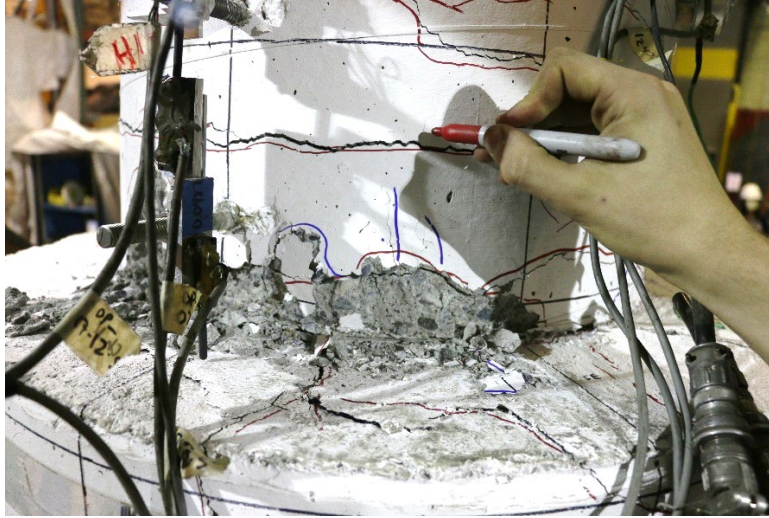


Figure E.2 Spalling and cracks at base of column at 5.2% drift.



Figure E.3 Close-up photographs of shaft transverse reinforcement fracture (at end of test): (a) uppermost spiral fracture on southwest side; and (b) Line of spiral fracture on southside.



Figure E.4 Southwest view of specimen (at end of test).



Figure E.5 Overhead angled view of specimen from southwest (post-test).

APPENDIX F Additional Experimental Results

This appendix is a supplement to Chapter 5 and Chapter 6. It contains additional experimental results from Specimens DS-1 through DS-4.

F.1 RAW MOMENT-DRIFT RESPONSE (DS-4)

The raw and adjusted moment-drift responses for Specimen DS-4 are presented in Figure F.1. The raw moment is defined as the measured MTS actuator force multiplied by the height from column–shaft interface to the actuator mid-height (60 in.). The moment was first adjusted to account for the $P-\Delta$ effect and then adjusted for friction (per processes described in Section 5.3.2). The moment after each of these adjustments is shown in the following figure.

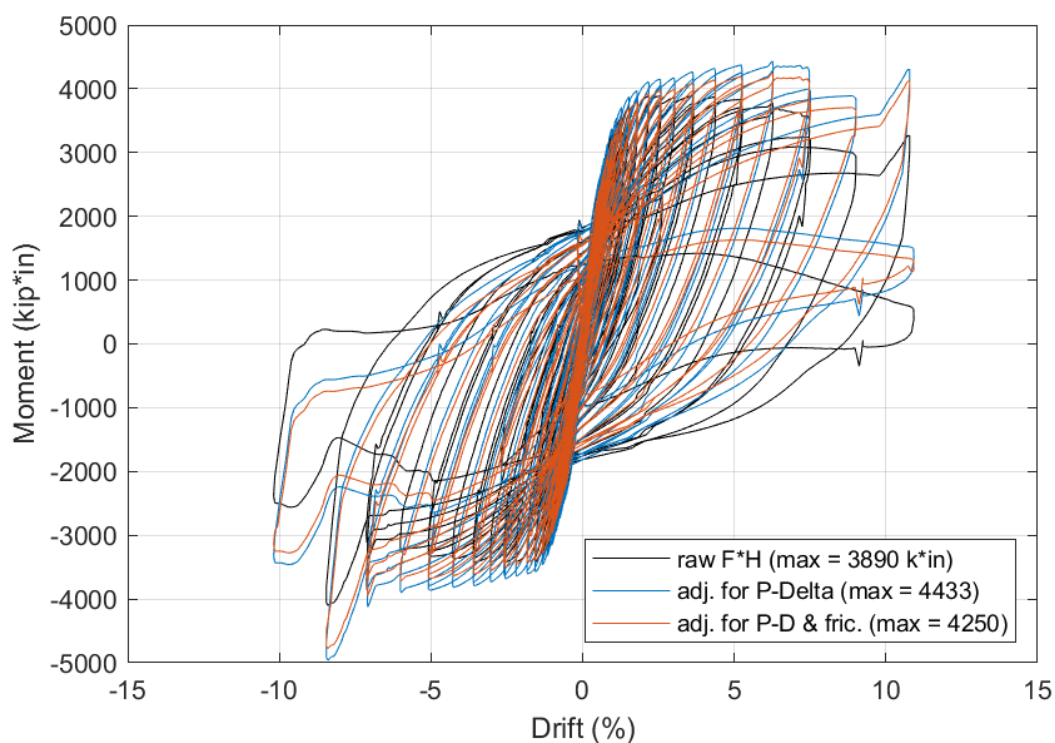
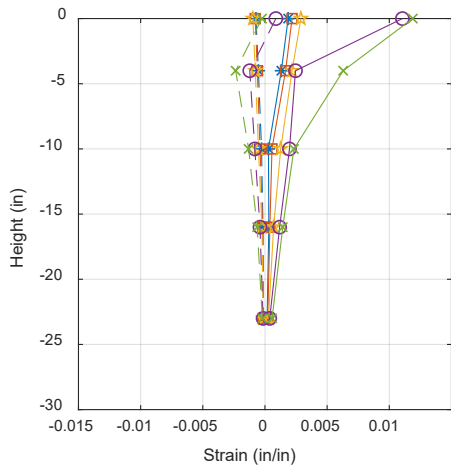


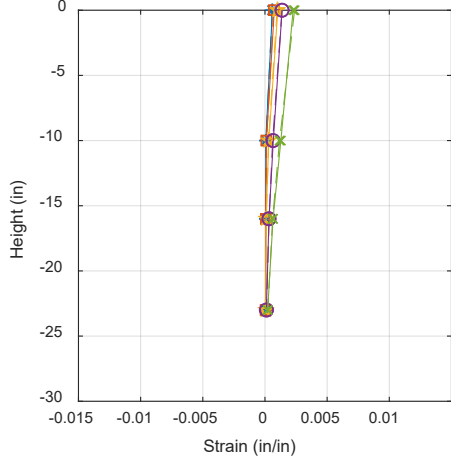
Figure F.1 Raw vs. adjusted moment-drift response.

F.2 INSTANTANEOUS STRAIN PROFILES (DS-4)

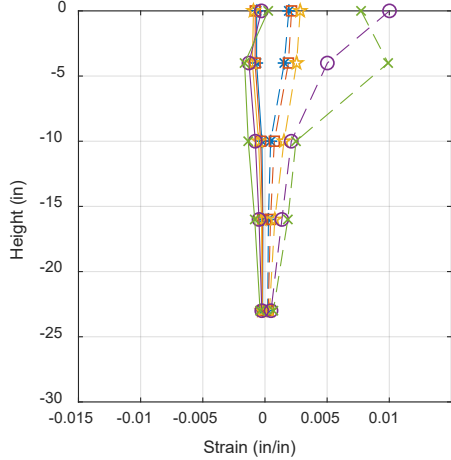
Strain profile envelopes for Specimen DS-4 were provided in Section 5.5. The corresponding instantaneous strain profiles are provided in this appendix section. Solid curves refer to measurements recorded at peak drift ratios, while dashed curves refer to measurements recorded at valley drift ratios.



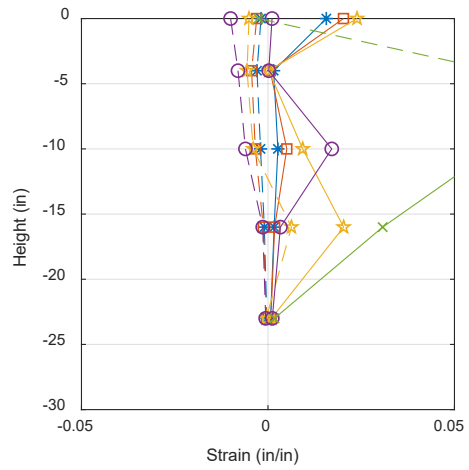
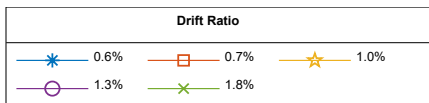
(a) north bar, early cycles



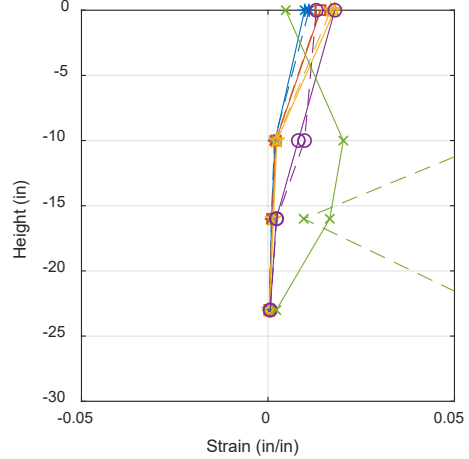
(c) east bar, early cycles



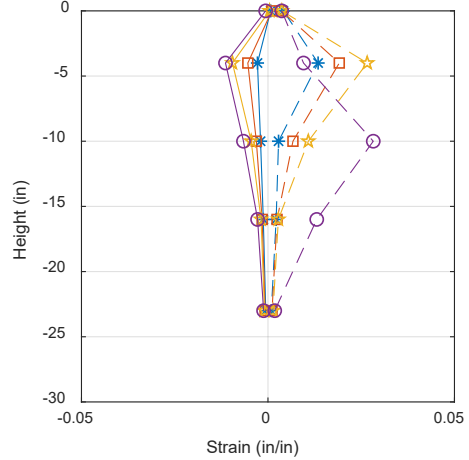
(e) south bar, early cycles



(b) north bar, final cycles



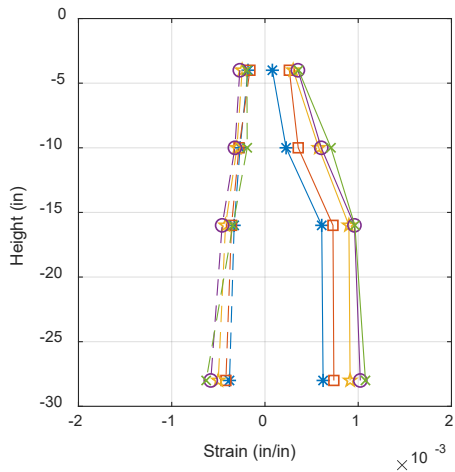
(d) east bar, final cycles



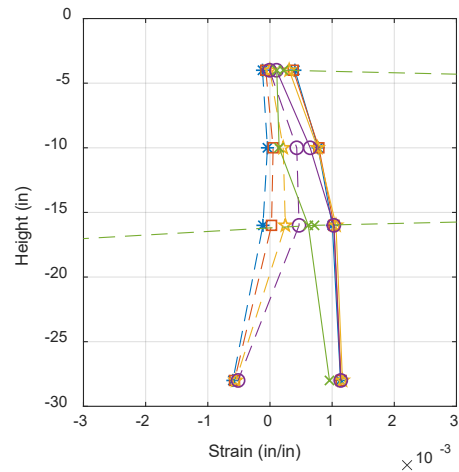
(f) south bar, final cycles



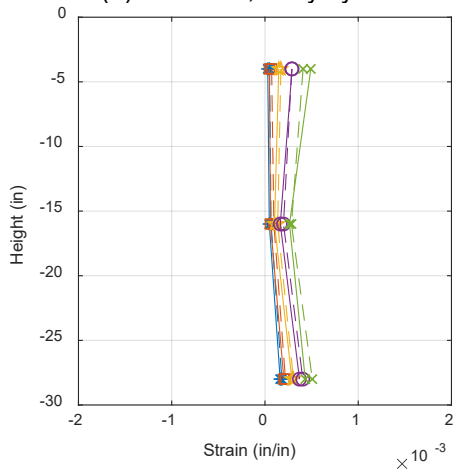
Figure F.2 Column longitudinal bar instantaneous strain profiles.



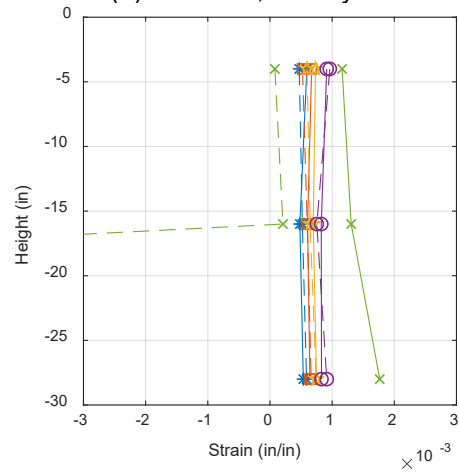
(a) north bar, early cycles



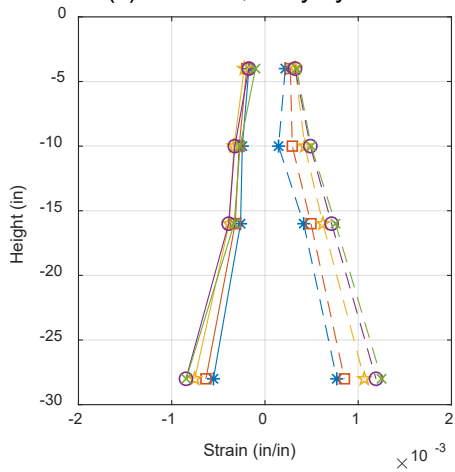
(b) north bar, final cycles



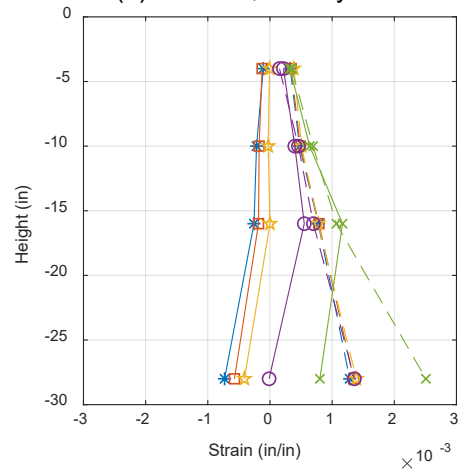
(c) east bar, early cycles



(d) east bar, final cycles



(e) south bar, early cycles

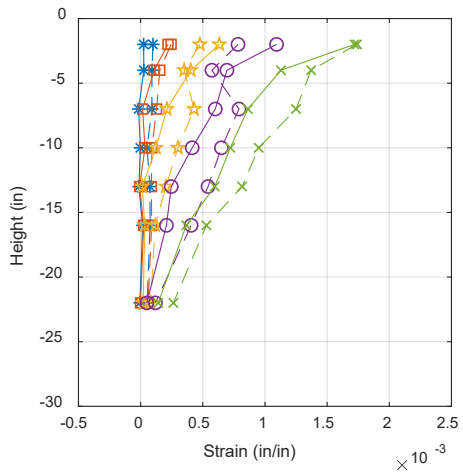


(f) south bar, final cycles

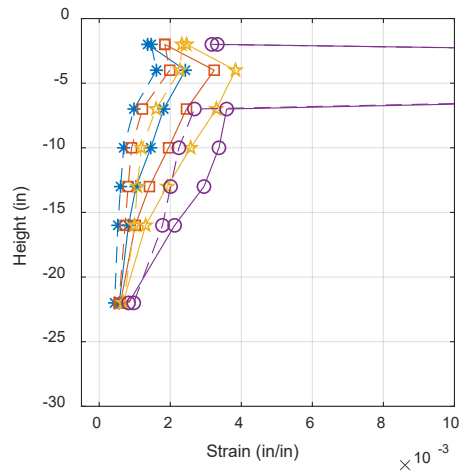
Drift Ratio		
* 0.6%	□ 0.7%	☆ 1.0%
○ 1.3%	× 1.8%	

Drift Ratio		
* +2.6%	□ +3.6%	☆ +5.3%
○ +7.5%	× +10.8%	

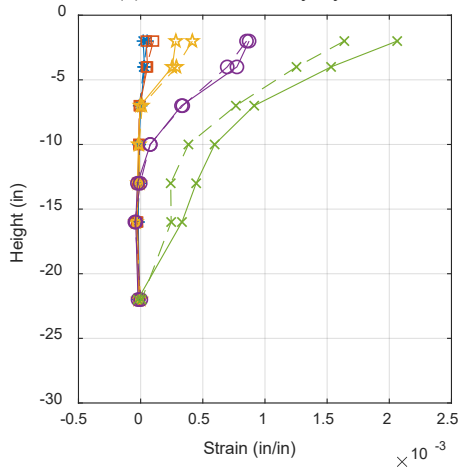
Figure F.3 Shaft longitudinal bar instantaneous strain profiles.



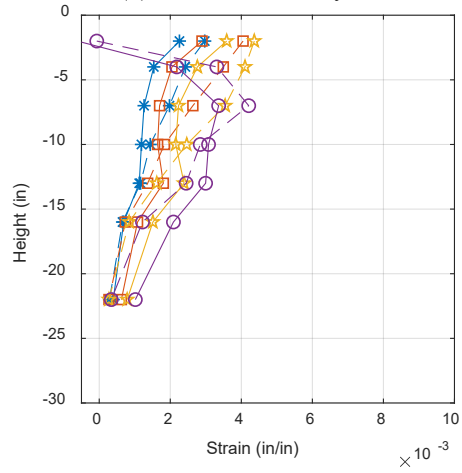
(a) north bar, early cycles



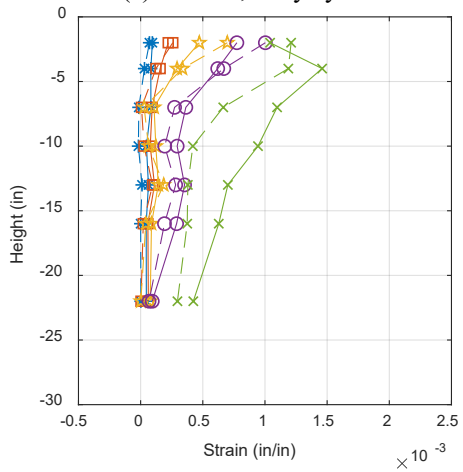
(b) north bar, final cycles



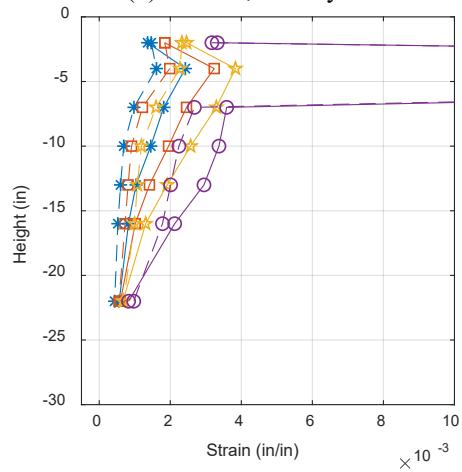
(c) east bar, early cycles



(d) east bar, final cycles



(e) south bar, early cycles



(f) south bar, final cycles

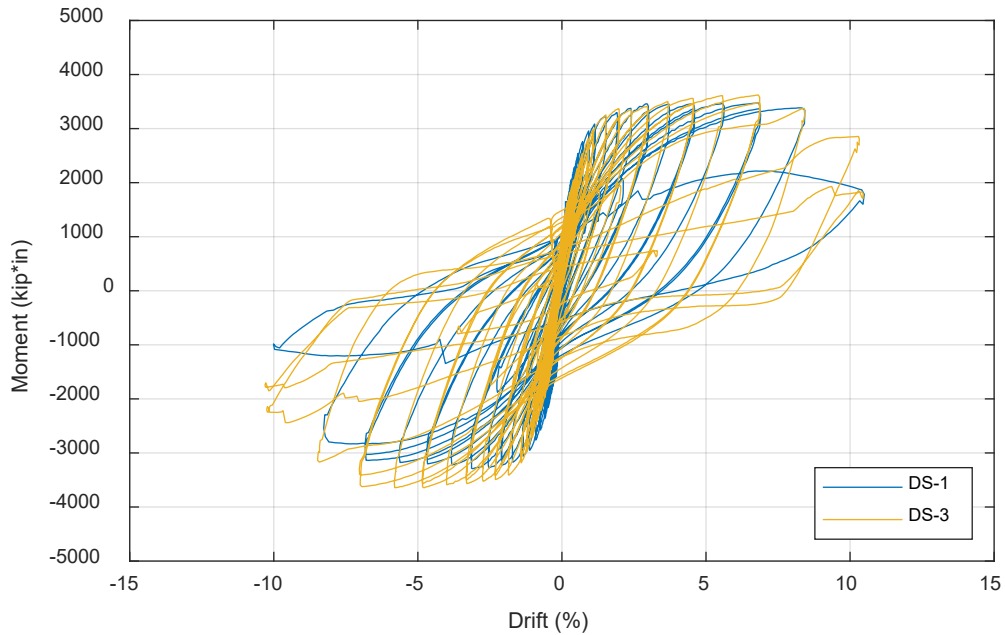
Drift Ratio		
	0.6%	
	1.3%	
	1.0%	

Drift Ratio		
	+2.6%	
	+7.5%	
	+5.3%	

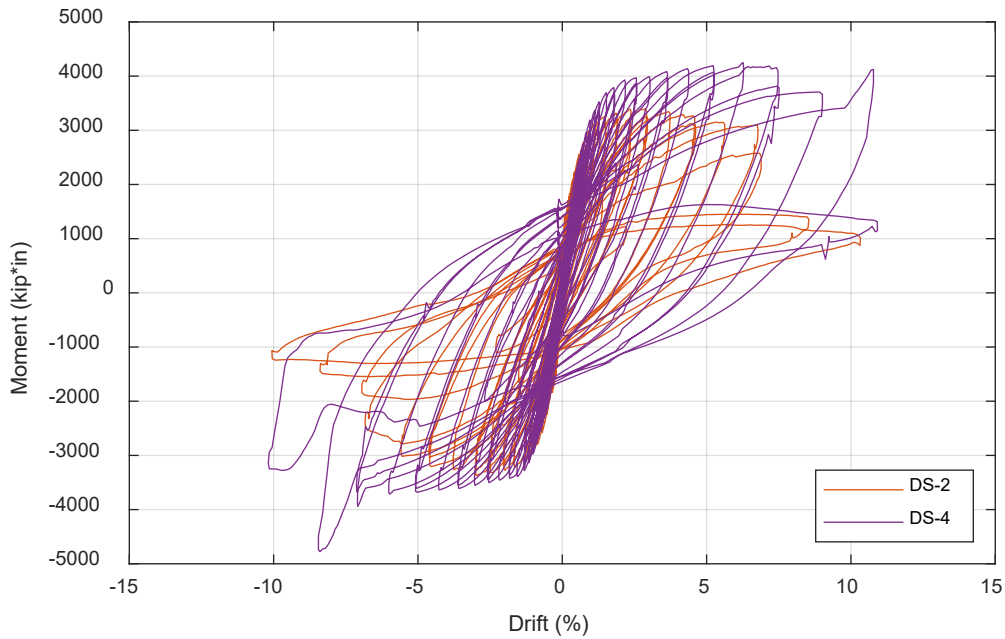
Figure F.4 Shaft transverse reinforcement instantaneous strain profiles.

F.3 MOMENT-DRIFT RESPONSE FOR SPECIMENS DS-1 THROUGH DS-4

Chapter 6 included normalized moment-drift curves for Specimens DS-1, DS-2, DS-3, and DS-4. The non-normalized curves are shown in the following figures. Specimens DS-1 and DS-2 were expected to have a lower moment capacity than DS-3 and DS-4; see Table 6.4.



(a) DS-1 and DS-3



(b) DS-2 and DS-4

Figure F.5 Moment vs. drift curves for all DS specimens.

APPENDIX G Flexural Analysis

This appendix describes the methodology for flexural analysis on Specimens DS-1 through DS-4 and UCSD-1 through UCSD-5. It also contains a justification for the approximations used in Appendix H to find the location of the tensile and compressive resultant forces.

G.1 MOMENT-CURVATURE RELATIONSHIP

Moment-curvature analyses were executed with a University of Washington in-house program. The Kent and Park [1971] concrete model was used as the base model for the analyses; see Figure G.1. The values of the confined concrete strength f'_{cc} and ultimate compression strain ϵ_{cu} were computed using Mander confinement properties [Mander et al. 1988; Priestley et al. 1996] based on the transverse reinforcement, rather than using the values recommended by Kent and Park. The concrete model for Specimens DS-4's column is shown in Figure G.2(a). In the figure, tension is defined as positive, and the axes are reversed so they descend to the right and up.

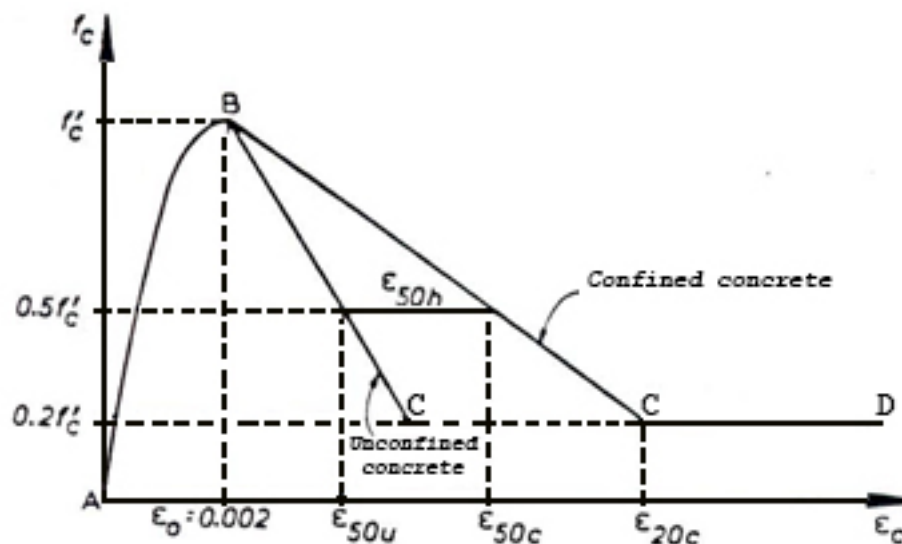


Figure G.1 Kent and Park model for concrete confined concrete [Kent and Park 1971].

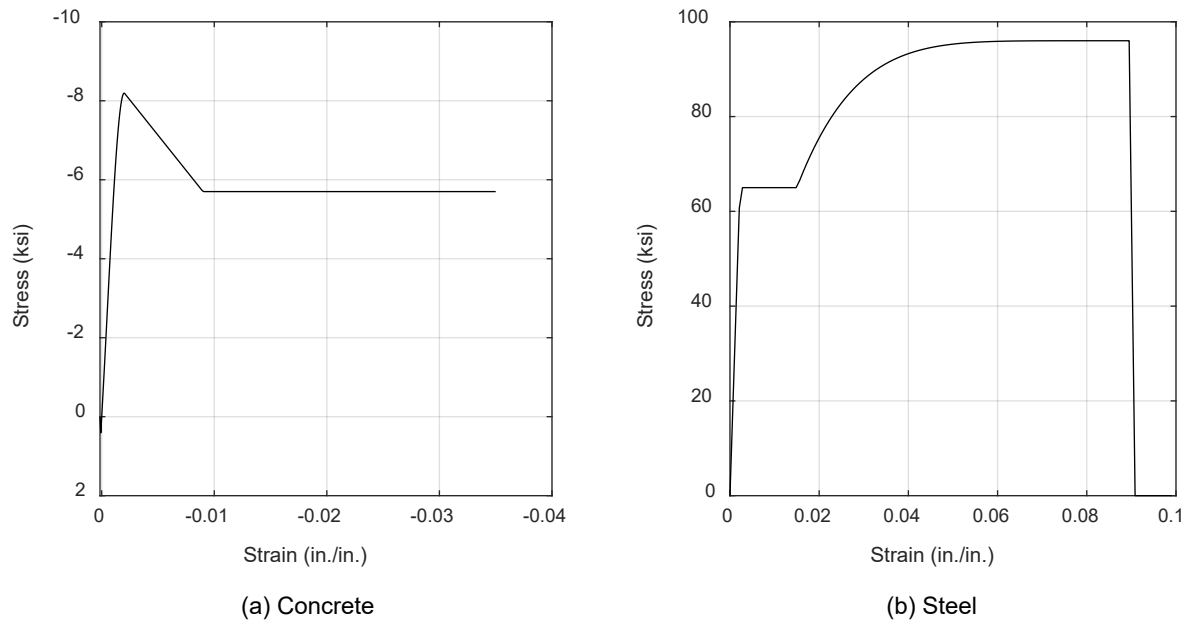


Figure G.2 Material stress-strain relationships for Specimen DS-4 column flexural analysis.

The peak moment determined from moment-curvature analysis is particularly sensitive to the slope of the descending branch of the concrete stress–strain curve. In terms of the parameters defined in Kent and Park [1971] (Figure G.1), the descending branch is characterized by ϵ_{20c} and the post-peak constant stress value of segment *CD* (which may be assumed as $0.2f'_c$ as in Kent and Park, or a different value). Designers and modelers should use a concrete model that reflects this increased ductility due to confinement. The authors of this report found that accounting for confined concrete in this manner, versus using a more brittle, unconfined concrete model, resulted in an approximately 20% difference in the calculated peak moment capacity of an element (e.g., column or shaft).

The steel model in the program is based on the Raynor model [Raynor et al. 2002; Hoehler and Stanton 2006] and consists of three regions: an elastic segment, a yield plateau, and a strain-hardening region with a user-defined curvature; see Figure G.2(b). The measured reinforcement properties were used in the program.

The moment-curvature curve for the column of Specimen DS-4 is shown in Figure G.3 as a sample result.

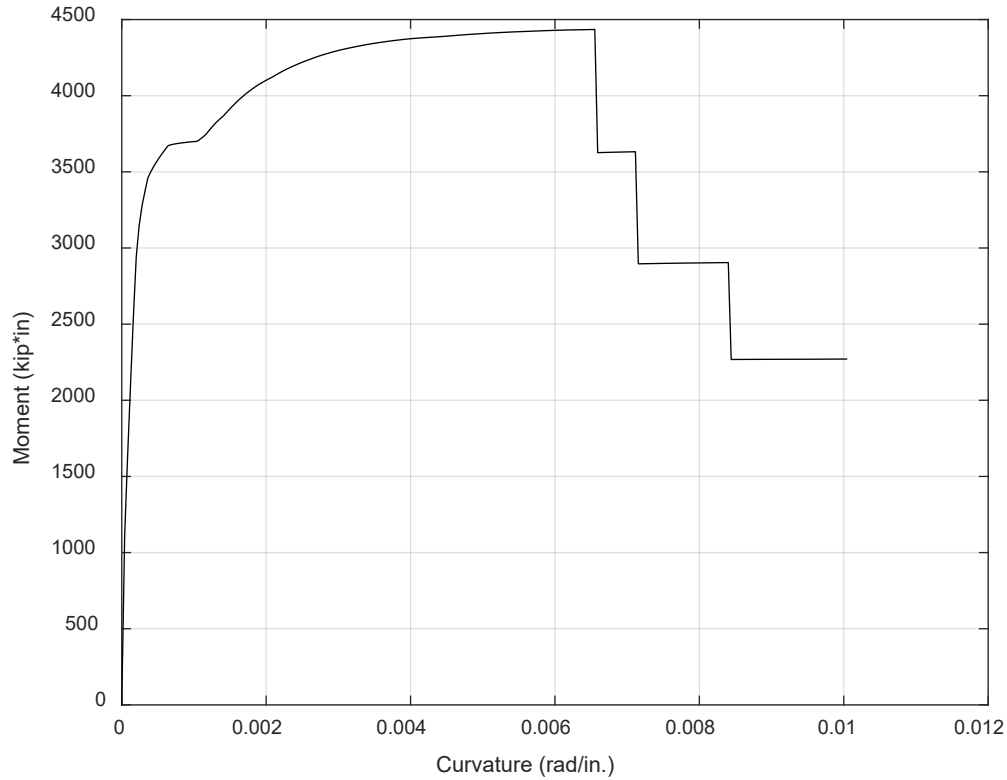


Figure G.3 Moment-curvature results for Specimen DS-4 column.

G.2 TRENDS IN NEUTRAL AXIS AND RESULTANT LOCATIONS

The neutral axis and force resultant locations can be approximated using observed trends so that these locations can be determined without a moment-curvature analysis. Berry and Eberhard [2003] found an equation to approximate the location of the plastic neutral axis, which can be used for both round and rectangular columns:

$$\frac{D}{c} = 5.3 \left(1 + 9.4 \frac{P}{A_g f'_c} \right)^{-1} \quad (\text{G.1})$$

where D is the diameter or width of the cross section; c is the distance from compression face to neutral axis; P is the axial load; A_g is the gross area of concrete; and f'_c is the compressive strength of concrete.

The location of the tensile resultant relative to the neutral axis can be defined as:

$$\text{resultant location} = \gamma(D - c) \quad (\text{G.2})$$

where γ is a constant factor. This is shown in Figure G.4; if strains were elastic, and thus forces were elastic, and the reinforcement was distributed along a continuum in a rectangular section

rather than being placed at discrete heights and in a circular section, then $\gamma = 0.67$ (the centroid of a triangular force distribution).

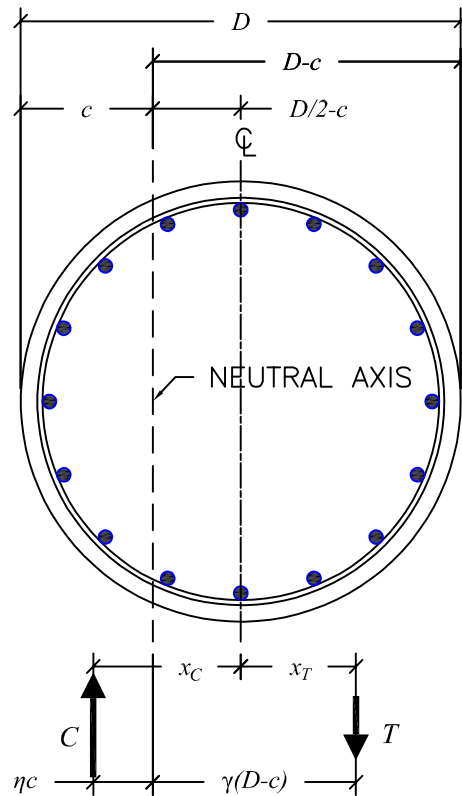


Figure G.4 Neutral axis and resultant locations.

The tensile resultant location relative to the center of the section (x_T , as used in Chapter 8 and Appendix H), is then:

$$X_T = \gamma(D - c) - \left(\frac{D}{2} - c\right) \quad (\text{G.3})$$

Substituting Equation (G.1) into Equation (G.3) and dividing by D ,

$$\frac{X_T}{D} = C_1 + C_2 \left(\frac{P}{A_g f'_c}\right) \quad (\text{G.4})$$

where $C_1 = 0.81\gamma - 0.31$ and $C_2 = 1.77(1 - \gamma)$.

Equation (G.3) contains γ , a factor, which can be calibrated using the exact locations of the shaft and column tensile resultants from moment-curvature analysis. Two values were found for γ based on eight shaft sections and eight column sections: $\gamma = 0.55$ for a column at its peak moment capacity, and $\gamma = 0.73$ for the shaft state when the column is at its peak moment capacity. The lower γ factor for the column indicates that the tensile resultant centroid is located closer to

the neutral axis. Since the column is at its peak moment capacity, much of the longitudinal reinforcement is beyond yield, and the tensile force distribution is more trapezoidal/bilinear than triangular/linear. In contrast, the shaft is elastic at the instance of peak column moment, so the tensile resultant centroid is located closer to the tensile face of the section. $\gamma > 0.67$ in the shaft due to the physical placement of longitudinal bars around an arc. Additionally, Equation (G.1) was developed for a plastic state, whereas the shaft, in this case, is elastic. Nonetheless, a single γ value for all shaft sections was able to be calibrated with a minimal variance. The values of C_1 , C_2 , and $\frac{x_T}{D}$ are as shown in Table G.1 (column) and Table G.2 (shaft).

Table G.1 Tensile resultant location in the column.

	Reduced-scale specimens (Tran [2015] and current study)				Full-scale specimens [Murcia-Delso et al. 2013; Lotfizadeh and Restrepo 2019]			
	DS-1	DS-2	DS-1	DS-2	DS-1	DS-2	DS-1	DS-2
C_1	0.13	0.13	0.13	0.13	0.13	0.13	0.13	0.13
C_2	0.80	0.80	0.80	0.80	0.80	0.80	0.80	0.80
$\frac{P}{A_g f'_c}$	0.07	0.07	0.07	0.07	0.09	0.08	0.08	0.09
$\frac{x_{TC} 1}{D_c}$	0.19	0.19	0.19	0.19	0.21	0.20	0.20	0.20
$\frac{x_{TC} 2}{D_c}$	0.21	0.21	0.19	0.21	0.19	0.19	0.21	0.18

¹ From Equation (G.3).

² From $M - \phi$ analysis.

Table G.2 Tensile resultant location in the shaft.

	Reduced-scale specimens (Tran [2015] and current study)				Full-scale specimens [Murcia-Delso et al. 2013; Lotfizadeh and Restrepo 2019]			
	DS-1	DS-2	DS-1	DS-2	DS-1	DS-2	DS-1	DS-2
C_1	0.28	0.28	0.28	0.28	0.28	0.28	0.28	0.28
C_2	0.49	0.49	0.49	0.49	0.49	0.49	0.49	0.49
$\frac{P}{A_g f'_c}$	0.03	0.03	0.04	0.03	0.04	0.04	0.05	0.04
$\frac{x_{TS} 1}{D_s}$	0.29	0.29	0.29	0.29	0.30	0.29	0.30	0.30
$\frac{x_{TS} 2}{D_s}$	0.28	0.28	0.31	0.32	0.30	0.30	0.29	0.29

¹ From Equation (G.3).

² From $M - \phi$ analysis.

The results show that for all specimens, $\frac{x_{Tc}}{D_c} \cong 0.2$ and $\frac{x_{Ts}}{D_s} \cong 0.3$ through both methods (moment-curvature analysis and using the approximations from Berry and Eberhard [2003]). The consistency in results between the methods indicates that the procedures were performed correctly, and the approximation procedure sheds light on the engineering basis for some of the constants. Ultimately, x_{Tc} was approximated as $0.2D_c$ and x_{Ts} as $0.3D_c$ in Appendix H.

A similar calculation and approximation can be used to find the location of the compressive resultant. The compressive resultant location relative to the center of the section (x_c) is:

$$x_c = \eta c + \left(\frac{D}{2} - c \right) \quad (G.5)$$

Substituting Equation (G.1) into Equation (G.5) and dividing by D ,

$$\frac{x_c}{D} = C_3 + C_4 \left(\frac{P}{A_g f'_c} \right) \quad (G.6)$$

where $C_3 = 0.19\eta + 0.31$, and $C_4 = 1.77(\eta - 1)$.

Calibrating η using the exact locations of the shaft compressive resultants from moment-curvature analysis results in $\eta_{column} = 0.54$. The full results of the approximation are shown in Table G.3. Ultimately, x_{Cc} was approximated as $0.35D_c$ in Appendix H. x_{Cs} was not needed.

Table G.3 Compressive resultant location in the column.

	Reduced-scale specimens (Tran [2015] and current study)				Full-scale specimens [Murcia-Delso et al. 2013; Lotfizadeh and Restrepo 2019]			
	DS-1	DS-2	DS-3	DS-4	UCSD-1	UCSD-2	UCSD-4	UCSD-5
C_3	0.41	0.41	0.41	0.41	0.41	0.41	0.41	0.41
C_4	-0.82	-0.82	-0.82	-0.82	-0.82	-0.82	-0.82	-0.82
$\frac{x_{Cc}^1}{D_c}$	0.36	0.35	0.35	0.35	0.34	0.35	0.34	0.34
$\frac{x_{Cs}^2}{D_s}$	0.37	0.37	0.36	0.35	0.33	0.33	0.33	0.35

¹ From Equation (G.3).

² From $M - \phi$ analysis.

APPENDIX H Design Equations for Transverse Reinforcement based on Strut-and-Tie Modeling

This appendix describes a set of design equations for proportioning the shaft transverse reinforcement in a column–shaft connection. The design procedure is based on the strut-and-tie analysis procedure described in Chapter 8. This procedure and equations are not recommended for typical design but might be useful to future researchers.

As described in Section 8.3, the force demand-to-capacity ratio is analogous to the required-to-used transverse reinforcement ratio.

$$\frac{A_{tr}/s \text{ used}}{A_{tr}/s \text{ required}} = \frac{\text{force capacity of transverse reinf. used}}{\text{transverse force demand}} \quad (\text{H.1})$$

Substituting in for the force capacity and demand, and rearranging,

$$A_{tr}/s \text{ required} = \frac{F_{tr}}{\sum_{i=1}^{\frac{L}{s}} \left[2A_{tri} * f_{y,tr} \left(\frac{y_i}{L} \right)^2 \right]} * A_{tr}/s \text{ used} \quad (\text{H.2})$$

A_{tr}/s used can be described as $\sum_{i=1}^{\frac{L}{s}} A_{tri} / L$, which leads to

$$A_{tr}/s \text{ required} = \frac{F_{tr}L}{2f_{y,tr}} * \frac{\sum_{i=1}^{\frac{L}{s}} A_{tri}}{\sum_{i=1}^{\frac{L}{s}} A_{tri}y_i^2} \quad (\text{H.3})$$

The summations in Equation (H.3) refer to the individual levels of spiral, which can be found for both connections with uniformly spaced spiral or those with nonuniform distributions. To simplify Equation (H.3), approximations can be made for the summation terms.

By approximating $\sum_{i=1}^{\frac{L}{s}} A_{tri}$ as $\frac{A_{tr}}{s} * L$, and $\sum_{i=1}^{\frac{L}{s}} A_{tri}y_i^2$ as $A_{tr} * \frac{L^3}{3s}$ (based on the area under a parabola), the minimum transverse reinforcement becomes

$$A_{tr}/s \text{ required} = \frac{3F_{tr}}{2Lf_{y,tr}} \quad (\text{H.4})$$

F_{tr} is found using the strut-and-tie procedure described in Section 8.2. Namely,

$$F_{tr} = F_{tr}^V + F_{tr}^M \quad (\text{H.5})$$

where F_{tr}^V is the transverse force demand on the hoops or spiral due to shear, and F_{tr}^M is the demand due to pure moment and axial load. F_{tr}^V can be assumed as

$$F_{tr}^V = V - V_c \quad (\text{H.6})$$

where V is the total shear demand as determined from the column moment-curvature analysis, and V_c is the concrete contribution to shear resistance (kips), Equation (8.9).

F_{tr}^M is taken as the tie force in F_{BC} in the M-Configuration of the strut-and-tie model multiplied by a factor of $\frac{2}{\pi}$ to account for the transverse component only.

$$F_{tr}^M = T_c * \frac{\cot \theta_{AB}}{1 + \cot \theta_{AB} \tan \theta_{AC}} * \frac{2}{\pi} \quad (\text{H.7})$$

This can also be written as:

$$F_{tr}^M = T_c * \frac{x_{Ts} - x_{Tc}}{h_A - h_B} * \frac{x_{Tc} + x_{Cc}}{x_{Ts} + x_{Cc}} * \frac{2}{\pi} \quad (\text{H.8})$$

In summary, the minimum shaft transverse reinforcement in the transition region can be determined using Equations (H.4), (H.5), (H.6), and (H.8). This first involves moment-curvature analyses for both the shaft and column, finding the centroids of the resultant forces, and calculating L per the procedure described in Chapter 8. Then, the results from the moment-curvature analyses can be substituted into Equations (H.4), (H.5), (H.6), and (H.8).

This process might be undesirable to designers, so approximations can be made for F_{tr}^M and L to eliminate some of these steps. F_{tr}^M can be simplified using approximations for h_A and h_B based on empirical evidence, and for x_{Ts} , x_{Tc} , and x_{Cc} per Appendix G. By approximating the values of h_A as $0.7L$ and h_B as $0.25L$, and using the approximations of x_{Ts} , x_{Tc} , and x_{Cc} as $0.3D_s$, $0.2D_c$, and $0.35D_c$, respectively, Equation (H.8) becomes:

$$F_{tr}^M = 0.78T_c * \frac{D_c}{L} * \frac{D_s - \frac{2}{3}D_c}{D_s + \frac{7}{6}D_c} \quad (\text{H.9})$$

Note that the approximation of $h_B \approx 0.25L$ assumes that the shaft longitudinal bars are able to be developed at the transverse force centroid [i.e., the upper term in Equation (8.6) controls].

Also, the value of L can be approximated as:

$$L = \frac{l_{db}}{3} + 0.3D_s - 0.2D_c + c \quad (\text{H.10})$$

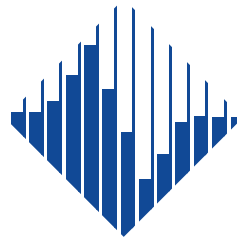
where l_{db} is the basic tension development length of column bars per AASHTO BDS [2017].

Equation (H.9) still requires the designer to find the tensile resultant in the column (T_c). It also has significantly more terms than other proposed design equations, and it overestimates the required steel in Specimens DS-1 and DS-2. Therefore, this set of equations is not recommended for use in design.

The Pacific Earthquake Engineering Research Center (PEER) is a multi-institutional research and education center with headquarters at the University of California, Berkeley. Investigators from over 20 universities, several consulting companies, and researchers at various state and federal government agencies contribute to research programs focused on performance-based earthquake engineering.

These research programs aim to identify and reduce the risks from major earthquakes to life safety and to the economy by including research in a wide variety of disciplines including structural and geotechnical engineering, geology/seismology, lifelines, transportation, architecture, economics, risk management, and public policy.

PEER is supported by federal, state, local, and regional agencies, together with industry partners.



PEER Core Institutions

University of California, Berkeley (Lead Institution)
California Institute of Technology
Oregon State University
Stanford University
University of California, Davis
University of California, Irvine
University of California, Los Angeles
University of California, San Diego
University of Nevada, Reno
University of Southern California
University of Washington

Pacific Earthquake Engineering Research Center
University of California, Berkeley
325 Davis Hall, Mail Code 1792
Berkeley, CA 94720-1792
Tel: 510-642-3437
Email: peer_center@berkeley.edu

ISSN 2770-8314
<https://doi.org/10.55461/MZFA9360>